ANNUAL REPORT

University Research Initiative

Contract No.: N00014-92-J-1808

March 1993 - April 1994

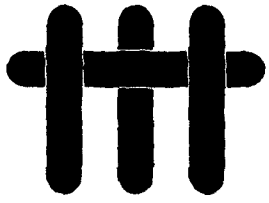

The Processing and Mechanical Properties of High Temperature/ High Performance Composites

by

A.G. Evans & F. Leckie
University of California,
Santa Barbara

University of Pennsylvania
Harvard University
Washington State University
Carnegie Mellon University
University of Virginia

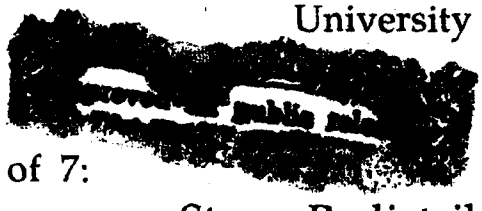

Book 2 of 7:

Stress Redistribution and Notch Properties

SUMMARY

OF

TABLE OF CONTENTS

EXECUTIVE SUMMARY

BOOK 1: MECHANISM-BASED CONSTITUTIVE LAWS AND DESIGN

BOOK 2: STRESS REDISTRIBUTION AND NOTCH PROPERTIES

BOOK 3: FATIGUE AND CREEP

BOOK 4: PROCESSING/PROPERTY CORRELATIONS

BOOK 5: INTERFACE EFFECTS

BOOK 6: DELAMINATION AND COMPRESSIVE BEHAVIOR

BOOK 7: *IN-SITU* MEASUREMENTS OF STRESS AND DAMAGE

KJS 4/27/94

KJS 4/27/94

BOOK 2

STRESS REDISTRIBUTION AND NOTCH PROPERTIES

KJS 4/27/94

28.	On the Strength of Fiber Reinforced Ceramic Composites Containing an Elliptic Hole	Y. L. Cui
29.	On the Theoretical Toughness and Strength of Ceramic Composites	B. Budiansky
30.	Microlaminated High Temperature Intermetallic Composites	R. G. Rowe D. W. Skelly M. Larsen J. Heathcote G. R. Odette G. E. Lucas
31.	Fracture Toughness of Al-4%Mg/Al_2O_3p Composites	R. H. Pestes S. V. Kamat J. P. Hirth

EXECUTIVE SUMMARY

The general emphasis for 1994 would be on increased software development, testing of subelements and design calculations. For these purposes, the constitutive law coding and development would be coordinated by Nick Aravas, and implemented in ABAQUS. The initial implementation would be the elastic/plastic model for MMCs with interface debonding developed in 1993 (Leckie). This would be extended in 1994 to include creep and some aspects of thermomechanical cycling. The code would be used for design calculations concerned with MMC rotors, actuators and vanes (Leckie). A plan is being formulated to collaborate with Pratt and Whitney to acquire MMC sub-elements representative of these components during 1994. Experimental tests on these subelements would be capable of providing a direct validation of the code capabilities.

Constitutive law and fatigue lifing software would be created for CMCs using continuum damage mechanics (CDM) approaches (Leckie, McMeeking). The approach has been motivated by micromechanics models developed in 1993 (Hutchinson, Zok, Evans). These codes would be used to calculate stress redistribution effects and fatigue life on simple sub-elements, such as center notched and pin-loaded plates. Comparison with experimental measurements needed to test the fidelity of the models will be based on moiré interferometry and thermoelastic emission. This effort is coordinated with the NASA EPM program through both General Electric and Pratt and Whitney. A plan for acquiring sub-elements from DuPont Lanxide is being formulated.

A new emphasis for 1994 would be on the transverse properties of CMCs. The measurements and calculations performed in 1993 have indicated a strategy for curved sections and junctions that would establish a consistent design approach. The basic approach for resisting failures from combinations of interlaminar shear and transverse tension involves the use of stitching and angle ply weaving patterns that inhibit major reductions in stiffness when matrix cracks are induced by transverse loads and bending moments. For this purpose, calculations would be performed that combine

the mechanics of delamination cracks with models of bridging by inclined fiber bundles (Hutchinson, Ashby, Evans, McMeeking). The insight gained from these calculations would be used to design and acquire sub-elements, such as C sections and T junctions.

Additional software development will be for creep and creep rupture (McMeeking). The models devised in 1993 and test data relevant to MMCs will be combined into a code that predicts the creep and rupture of unidirectional MMCs subject to multiaxial loads. Some aspects of this code will also be applicable to CMCs.

Two new activities will be introduced in 1994: thermal properties and damping. The thermal properties will be studied on both CMCs and MMCs (Ashby, Hutchinson). Measurements of thermal diffusivity will be made by the laser flash method and related to the properties of the interface and the density of matrix damage in the material. Thermal expansion measurements will also be performed with emphasis on determining hysteresis effects, which can be related to the temperature dependence of the interfaces properties, through cell models. The latter might evolve into a diagnostic for establishing relationships between the interface properties and thermomechanical fatigue.

The processing activities in the program will have newly established goals in 1994. The principal emphasis will be on concepts for affordable manufacturing. The issues selected for investigation will be consistent with manufacturing processes that allow near-net shape consolidation while still yielding reasonable combinations of longitudinal and transverse properties. Performance models developed in the program would be used as an initial test of concept viability.

Beyond these general trends, specific activities are planned for 1994. These are elaborated below. The status of understanding and development in each of these areas is summarized in Table I. Increasing magnitudes between 0 and 1 designate a knowledge range from limited to comprehensive.

TABLE 1A

Status of Design Knowledge for MMCs

	$[0°]_n$ MMC				$[0°/90°]_n$	
	LONG.		TRANS.			
	P	S	P	S	P	S
Tensile Strength	3/4	1	1	1/2	1/4	~0
Creep and Creep Rupture	3/4	0	1	0	0	0
Cyclic Flow (Isothermal, TMF)	1/4	0	1	1/2	0	0
Crack Growth (Isothermal Fatigue)	1	1	0	1/2	0	0
Crack Growth (TMF)	1/2	1/2	0	0	0	0
Compressive Strength	3/4	0	0	0	0	0

TABLE 1B

Status of Design Knowledge for CMCs

	[0/90]		[45/45]	
	P	S	P	S
Stress/Strain	3/4	1/4	1/2	0
Fatigue	3/4	0	0	0
TMF	1/4	0	0	0
Creep and Rupture	1/2	0	0	0
Compression Strength	3/4	1/4	0	0
Transverse Properties	3/4	1/2	—	—
Thermal Properties	1/4	0	—	—

P Primary Structure

S Secondary Structure

2. CONSTITUTIVE LAWS

Two approaches will be used to create a formulation capable of representing the in-plane properties of CMCs. One would be based on Continuum Damage Mechanics (CDM) (Leckie). The other would use concepts analogous to those used in plasticity theory (Hutchinson). The CDM approach uses damage parameters that relate explicitly to micromechanics models. A potential function has already been identified as the state variable which separately represents the strain from the elastic compliance change caused by the matrix cracks and the inelastic strains associated with the debonding and sliding interfaces. Derivatives of the potential with regard to strain and damage give the relationships between variables, such as stress, interface sliding resistance, matrix crack density, etc.

The first version of the CDM model would use the minimum number of damage variables potentially capable of representing the behavior of laminated or woven composites. Cross terms between the damage variables would not be considered at this stage. Moreover, matrix cracks would be introduced normal to the maximum principal tensile stress, consistent with the experimental observations.

The plasticity theory approach would seek a formulation based on matrix cracks occurring normal to the maximum principal tension. It would introduce parameters that reflect the inelastic strain caused by interface sliding upon off-axis loading which would be calibrated from tests performed in tension in 0/90 and 45/45 orientations.

The insight needed to characterize off-axis loading effects will be gained from cell models (Hutchinson) in a manner analogous to that previously used for axial loads. The principal objective will be to understand trends in matrix crack opening and interface debonding/sliding with applied loads. The stress on the fibers will be calculated with the intent of predicting effects of loading orientation on fiber failure. The models will be compared with measurements made in 45/45 tension, using various CMCs (Evans).

Calibration of the damage parameters for each material would be made from hysteresis loop measurements in accordance with procedures developed in 1993. Experimental results obtained in 0/90 tension, 45/45

tension and in-plane shear will be used. In future work, it is hoped that shear tests will not be necessary.

The validation of the constitutive laws will be achieved by comparing calculations with measurements made on sub-elements, especially pin-loaded holes (Evans). The experimental results include residual strains obtained by Moiré interferometry (Fig. 2.1), ultimate loads for either tensile or shear failure and principal strain trajectories delineated by matrix cracking patterns. Acoustic methods will also be developed to probe the local values of the elastic modulus (Clarke, Wadley) which could be compared directly with the CDM predictions.

3. FATIGUE LIFING

3.1 CMCs

A software program for isothermal low cycle fatigue (LCF) of CMCs, developed in 1993 (Fig. 3.1) will be extended in 1994. The present program asserts that fatigue is associated with cyclic degradation of the interface sliding resistance, τ, which can be characterized by analyzing hysteresis loops measured periodically during a fatigue test. With this methodology, S-N curves have been predicted for both unidirectional and woven 0/90 composites tested in cyclic tension as well as changes in compliance and permanent strain. Some additional effort is required to analyze data on 0/90 laminates in order to validate the model predictions. The extensions envisaged for 1994 include thermomechanical fatigue (TMF), strain controlled LCF and off-axis fatigue (Zok, Evans). Experiments are planned which would assess the effects of temperature cycling and of inclined fibers on τ degradation, measured from hysteresis loops. Various cell model calculations (Hutchinson) will be used to interpret the experiments. The results will be used to establish general *rules* for interface degradation in CMCs.

The off-axis experiments will also give insight into the fiber failure criterion that replaces the global load sharing (GLS) results successfully used for 0/90 loadings. This study will coordinate with the cell calculations described above, and the 45/45 tensile experiments.

Notch fatigue studies will be initiated. These will examine cyclic stress redistribution and notch sensitivity (Evans).

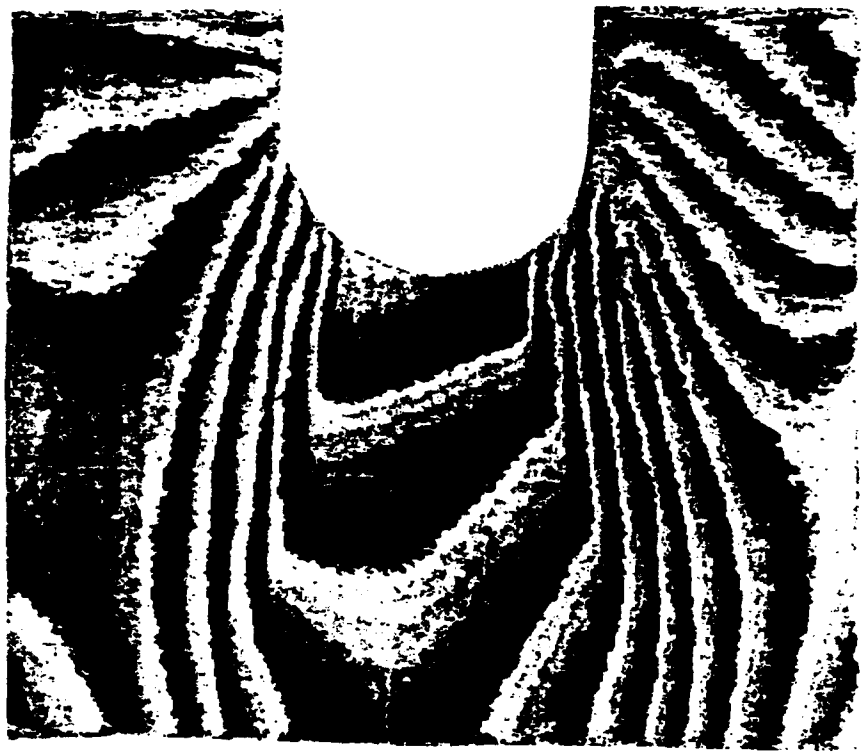

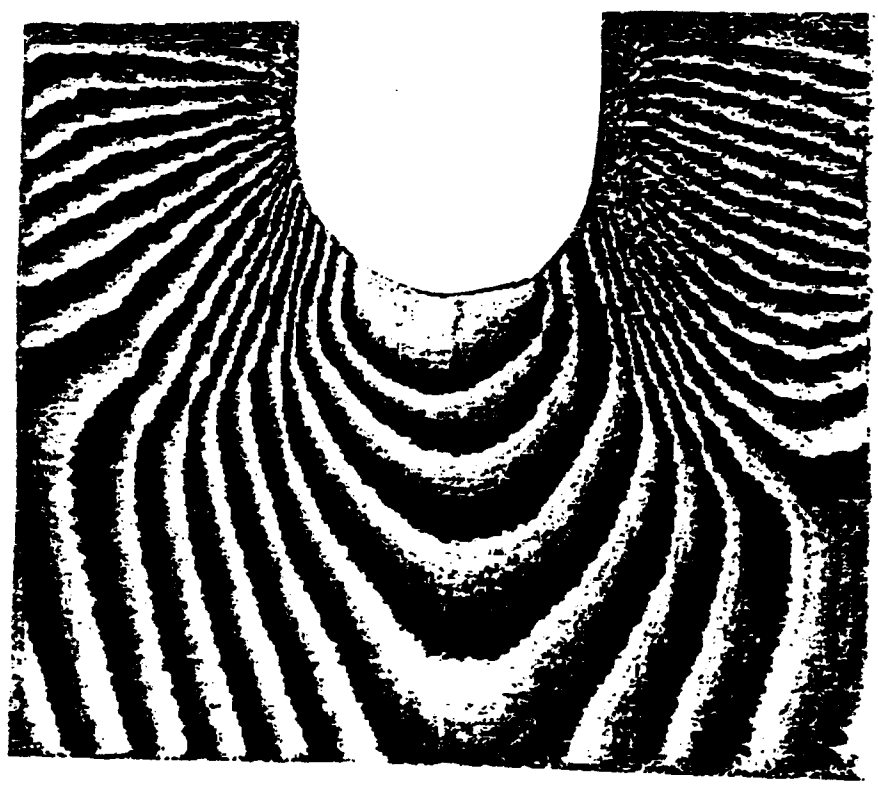

Figure 2.1

Fatigue Methodology

CMC Life Program

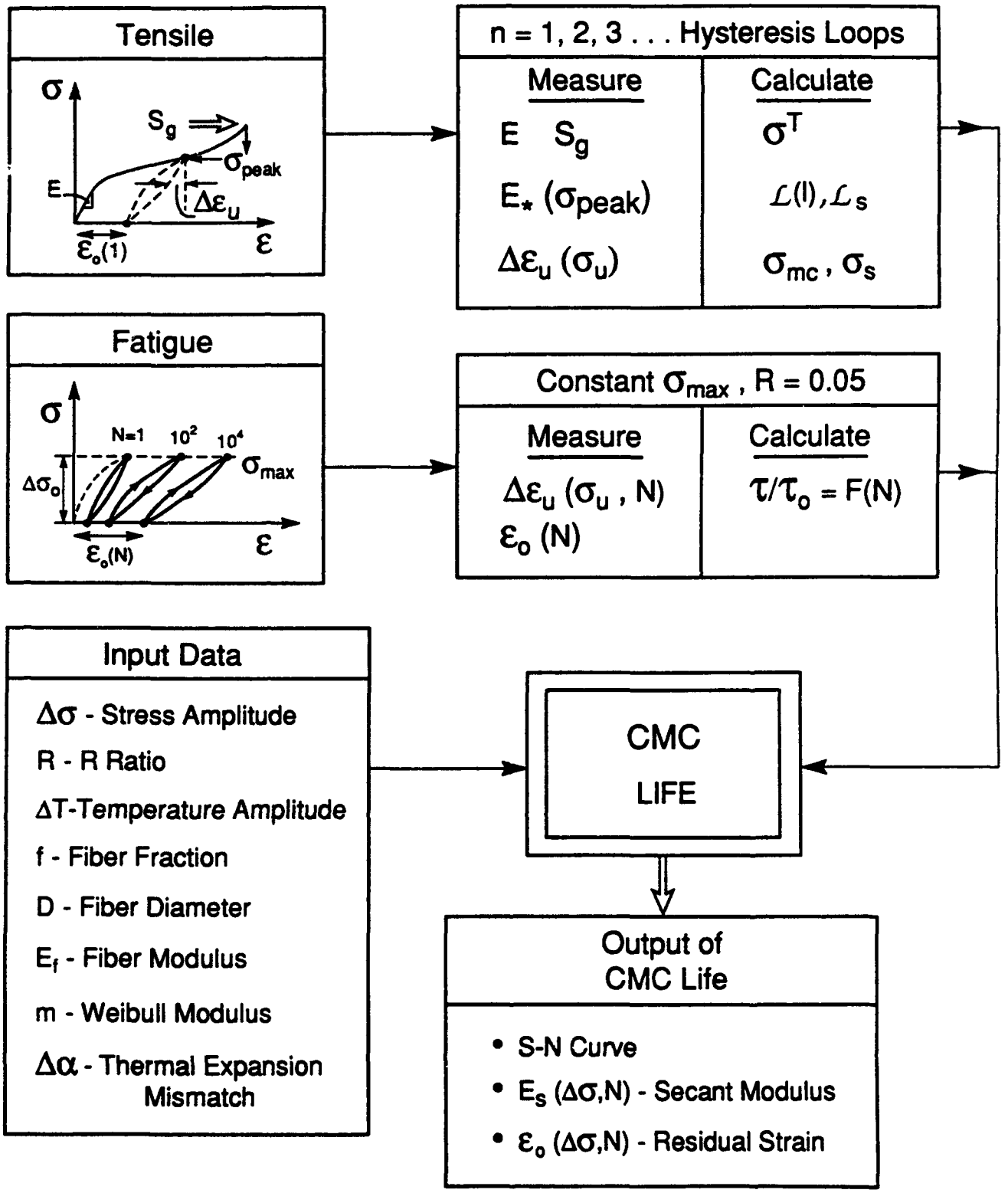

Figure 3.1

3.2 MMCs

Fatigue crack growth and notch strength studies in MMCs will be extended to 0/90 laminates (Zok, Suo). The experiments concerned with crack growth will be interpreted using crack bridging models. The utility of such models has been validated in previous years through studies on unidirectional MMCs. It is envisaged that the fatigue crack growth characteristics of the unidirectional and 0/90 configurations will be related through the volume fraction of fibers aligned with the loading direction. The notch strength behavior will also be interpreted using crack bridging models. Such models have been developed in 1993 and found to be useful in rationalizing the behavior of unidirectional materials (Zok, Suo). In all cases, the mechanical measurements will be augmented by *in-situ* observations to identify changes in damage mechanisms with temperature, fiber architecture, etc. Plans to study the influence of panel thickness on fatigue and fracture resistance are also being developed, as well as tests to understand the potential for crack growth in mixed mode loadings (Hirth, Zok).

Studies of the TMF response of MMCs loaded parallel to the fiber axis will be initiated (Zok, Leckie). Experiments will evaluate both in-phase and out-of-phase loadings. Models of load shedding (matrix-fibers) will be used to interpret the hysteresis loops and to develop fatigue life models applicable to low cycle, high strain TMF.

4. CREEP AND RUPTURE

4.1 MMCs

The considerable progress made in 1993 towards identifying and understanding the mechanisms of creep and rupture in unidirectional MMCs containing non-creeping fibers (McMeeking, Zok) will be used to develop creep rupture software. The longitudinal creep model to be used incorporates stochastic fiber fracture and interface sliding in a format amenable to the prediction of primary and tertiary creep in terms of matrix creep strength, interface sliding resistance, fiber strength, Weibull modulus, etc. The concepts would be visualized in a rupture mechanisms map

(Fig. 4.1). The transverse creep behavior would include interface debonding, which greatly accelerates the creep, leading to marked anisotropy. A constitutive law for creep that includes these effects will be developed (Aravas, McMeeking).

Additional experiments and calculations will be conducted to assess the effects of notches and holes on creep rupture (Zok, Suo). Experience with MMCs at ambient temperature indicates that the notch sensitivity is largely dictated by matrix properties (i.e., strength and ductility). The reduction in matrix properties at elevated temperatures may lead to a substantial elevation in notch sensitivity. However, this behavior may be complicated by the development of alternate damage processes, such as shear bands.

4.2 CMCs

Studies of the creep and rupture of CMCs will continue with emphasis on materials containing creeping fibers. A particular emphasis will be on matrix cracking that arises as fiber creep relaxes fiber bridging tractions (McMeeking, Evans). The experimental studies will be performed on SiC/SiC composites. Hysteresis loop measurements will be used to monitor matrix damage during composite creep, using procedures devised in 1993. Models will be developed based on time dependent fiber bridging concepts (McMeeking, Cox).

It is envisioned that the lifetime of some CMCs will be dictated by time-dependent rupture of the fibers. A lifetime prediction tool for such a composite *must* incorporate the knowledge of fiber strength degradation over time. A new activity will be initiated to address this problem (Suo, Evans). The initial work will involve a survey of data in the existing literature, and a comparison with available models. A new model is being developed for single crystal fibers. This model involves a residual pore inside a fiber which changes shape, under stress, via surface diffusion, to become a crack. These issues will be viewed in the broad context of fiber and composite manufacture.

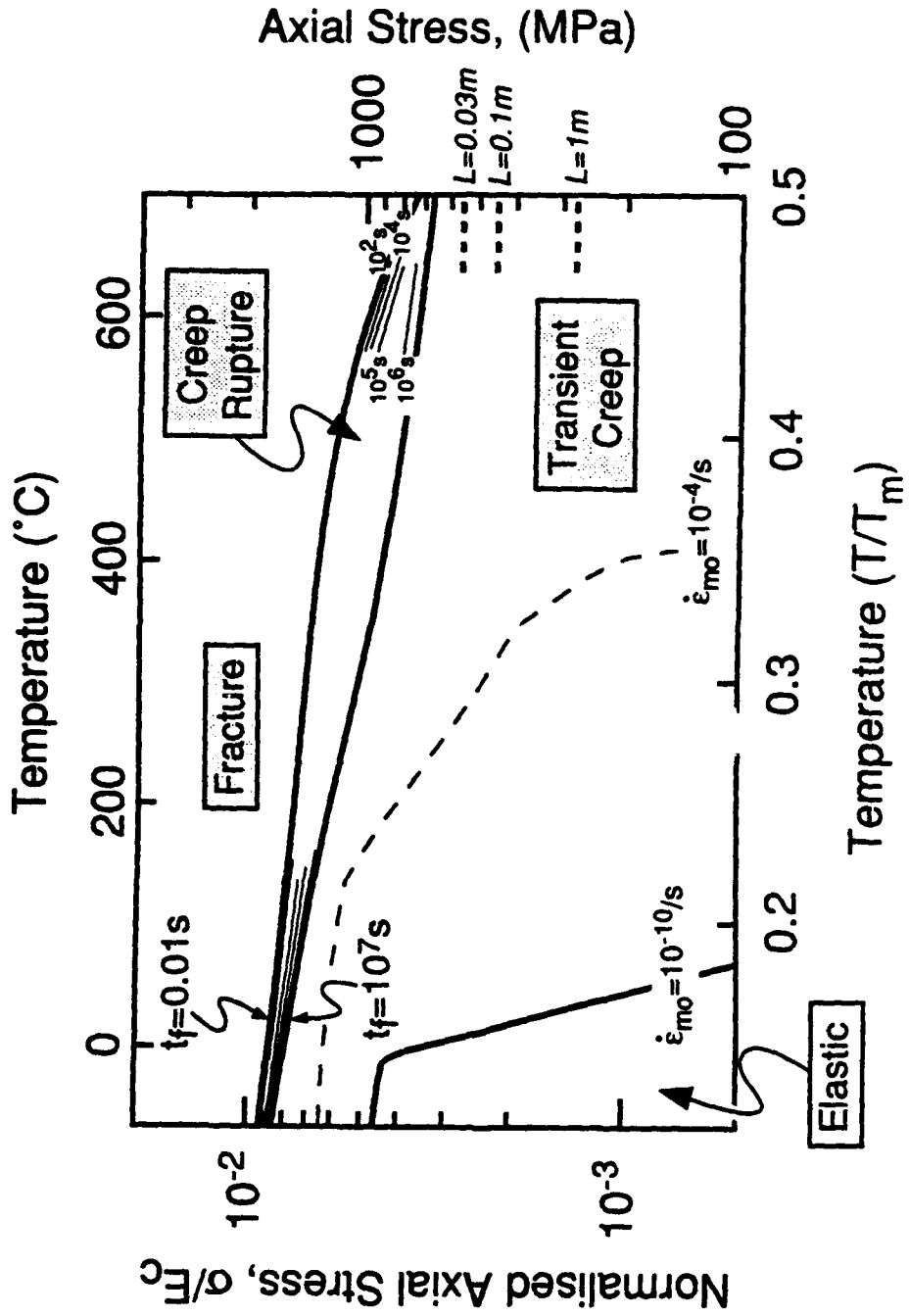
Axial Stress, (MPa)
1000
100
L=0.03m
L=0.1m
L=1m
0.5
0.4
0.3
0.2
Temperature (T/T_m)
Creep Rupture
Transient Creep
Fracture
Elastic
10^2s
10^4s
10^5s
10^6s
ε̇_mo=10^-4/s
ε̇_mo=10^-10/s
t_f=0.01s
t_f=10^7s
600
400
200
0
Temperature (°C)
10^-2
10^-3
Normalised Axial Stress, σ/E_C

Figure 4.1

5. TRANSVERSE PERFORMANCE OF CMCs

Analyses and tests performed in 1993 (Ashby, Hutchinson, Bao) have highlighted the essential issues related to components that experience combinations of transverse tension and interlaminar shear. In both loadings, matrix cracks form at manufacturing flaws at low stresses, of order 10-100 MPa. These cracks extend across the plies and interact minimally with the fibers. Although the crack configurations differ for transverse tension and interlaminar shear loadings, multiple cracks always form. This multiplicity of cracking causes a major reduction in stiffness, which can cause unacceptably large displacements and also redistribute stress into other areas. The formation of the matrix cracks is probabilistic in nature and governed by the size distribution of manufacturing flaws. Design based on the prevention of such transverse cracks must rely on weakest link statistics, usually with a low Weibull modulus. Alternatively, it may be assumed that cracks *inevitably* form and, instead, reliance is placed on *controlling* the diminished modulus of the material, after matrix cracking has occurred. This approach relies on having 3-D architectures, with transverse fibers introduced locally either by stitching or by using angle plies. To explore this possibility, calculations will be performed (Hutchinson, Evans) to examine fiber architectures that lead to minimum stiffness loss, subject to acceptable in-plane properties. Based on these calculations, sub-elements will be designed that test out the concepts.

6. COMPRESSIVE BEHAVIOR

The studies completed in 1993 on the compressive failure of polymer matrix composites by the growth of kink bands (Budiansky, Fleck) will be extended to metal matrix composites, through a coordination with 3M. Compressive failure of Al and Ti MMCs with small diameter fibers has been observed by 3M to occur in accordance with the same kink band mechanism known to operate in PMCs and in C/C composites. The theory should thus extend to the MMCs, with the fiber misalignment, the shear yield strength of the matrix and its work hardening coefficient as the principal variables. A comparison between the theory and experimental

results would provide the basis for specifying the compressive properties of MMCs.

Compression failure of CMCs occurs by different mechanisms (Ashby). The dominant failure modes are similar to those that operate in porous brittle solids such as monolithic ceramics, concrete and rocks. The theory is well established and validated for these materials. Applications of the theory to various CMCs will be made and applied to the understanding of a behavior of pin-loaded holes (Evans, Ashby).

7. THERMAL PROPERTIES

A new focus on the thermal properties of CMCs and MMCs will be initiated in 1994. Calculations of the effects of matrix cracks in the thermal expansion of CMCs will be made (Hutchinson). These will be compared with data obtained from TMF testing (Zok). The effects of such cracks on the in-plane thermal conductivity will also be calculated (Hutchinson). Measurements will be performed using the laser flash method (Ashby).

Thermal conductivity measurements will be initiated on Ti MMCs (Ashby). These will be used to understand the effects of the fiber/matrix interphases and of matrix damage on the transverse and in-plane thermal conduction.

8. MATERIALS SELECTION

The Cambridge Materials Selector software will be expanded in 1994 to include high temperature creep design with the corresponding data base (Ashby). This expanded version will permit estimates to be made of temperature limits for MMCs based on creep controlled TMF and on the transverse creep of components with unidirectional reinforcements.

9. DESIGN CALCULATIONS AND SUB-ELEMENT TESTS

A larger fraction of the effort in 1994 will be on design and sub-element testing, particularly for MMCs. Discussions are now in progress with Pratt and Whitney, Textron and 3M to perform design calculations using the

constitutive equations developed at UCSB and to produce sub-elements for testing.

The design emphasis for MMCs will be on various diffusion bonded joints with Ti matrices and monolithic Ti attachments. Two specific subelements are envisaged. The first involves unidirectionally reinforced rods (or plates), clad with monolithic metal. The purpose of the cladding is to prevent exposure of the fibers to the environment and to mechanical abrasion. The design of clad MMC structures requires consideration of (i) the residual stresses resulting from thermal mismatch between the cladding and the composites section, (ii) the potential for fatigue cracks to initiate and grow through the monolithic material, and (iii) the interaction of such cracks with the composite section and their influence on the strength and life of the structure. The design and testing of such subelements (Zok, Leckie) will be augmented by calculations of crack growth and fracture, incorporating the effects of thermal and elastic mismatch between the cladding and the composite (McMeeking). The clad structures will also be used to initiate studies on the reinforcement of holes in composite sections with monolithic metal patches, as drawn in Fig. 9.1 (Zok, Suo). The second subelement involves the attachment of a MMC actuator rod to a pin-loaded monolithic section (Fig. 9.2). The critical design issues relate to the strength and fatigue resistance of the interfaces between the composite and monolithic matrices. Design studies shall also be completed on rotor rings with special efforts made to produce rule-based design procedures which would be used by industry at the conceptual level of design to determine sizes and the efficient disposition of material.

For CMCs, the sub-element studies would be based on the calculations described above in Section 5. These would include C sections and T junctions (Fig. 9.3) Negotiations for manufacturing these sub-elements will be initiated and tests performed at UCSB.

10. AFFORDABLE MANUFACTURING

As our understanding of composite mechanics and its interplay with design and performance has evolved, it has become increasingly evident that *cost* and *reproducibility*, are major constraints. Even as processing

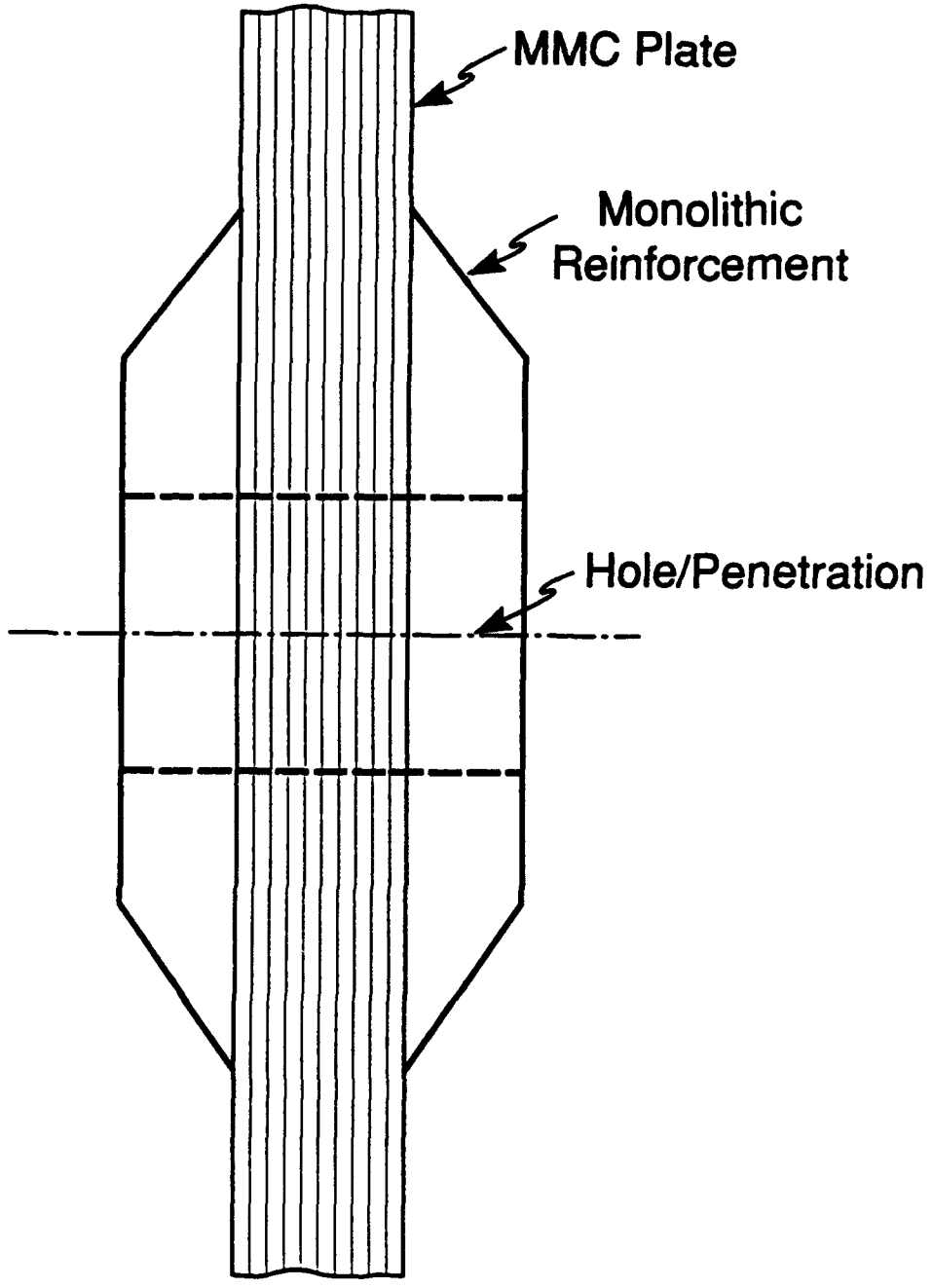

Figure 9.1

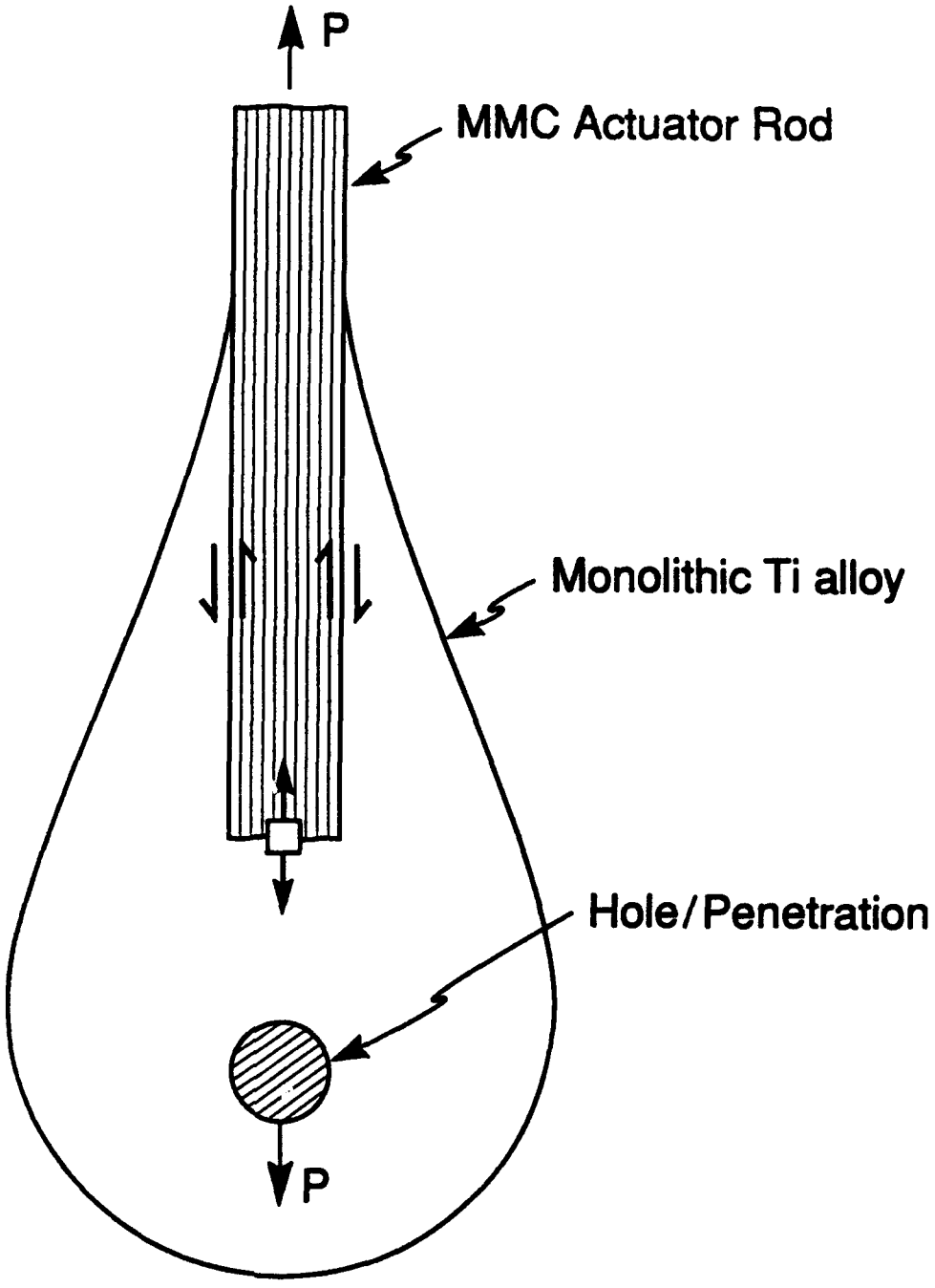

Figure 9.2

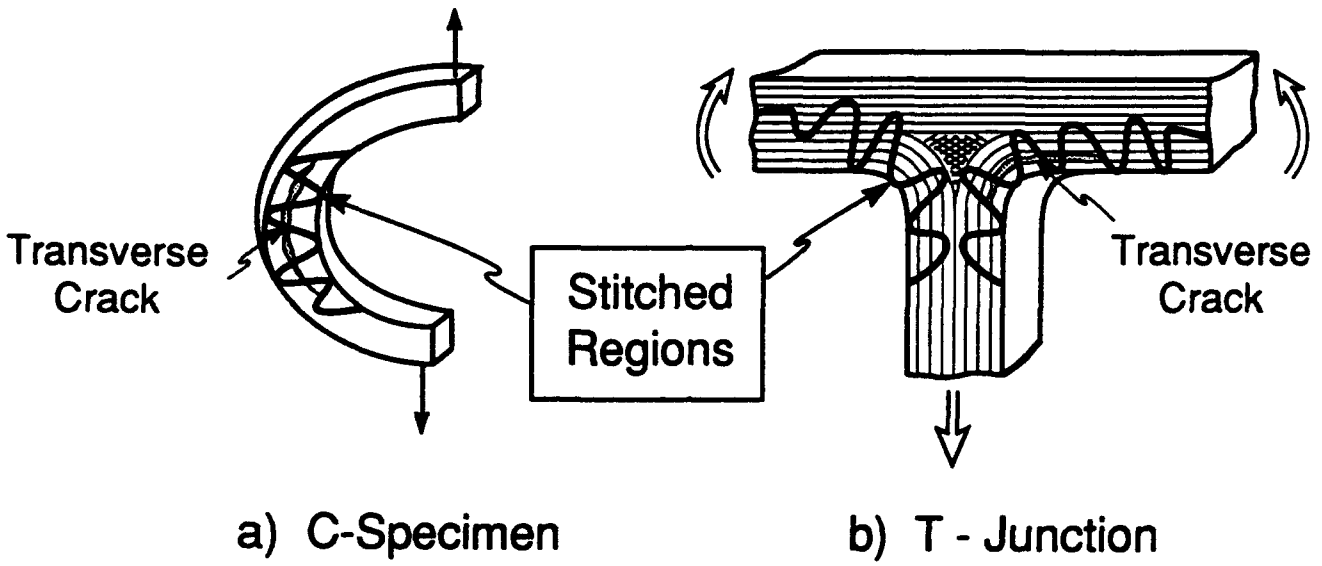
Transverse
Crack
Stitched
Regions
Transverse
Crack
a) C-Specimen
b) T - Junction

Figure 9.3

developments make the prospect of affordable high temperature fibers more realistic, evolving knowledge on the mechanical and thermochemical functions of interfaces have led to design concepts involving carefully tailored interphase layers, with unfavorable impact on cost. Moreover, if affordable coated fibers were available today, fabrication costs associated with consolidation and pressure densification would often remain prohibitive. Future processing and manufacturing activities are predicated on these issues, especially the need for new ideas, and the related knowledge base.

10.1 MMCs

Melt processing methods provide the more affordable options in composite synthesis with the added benefit of near-net shape capability. For continuous fiber composites melt infiltration also enables full density while minimizing the consolidation stresses that typically cause premature reinforcement failure in solid state processes. However, melt processing requires a high degree of thermochemical compatibility between matrix and reinforcement since deleterious diffusional interactions would be accelerated by the liquid phase. Conventional melt processing also exhibits limited ability to control the volume fraction and spatial uniformity of the reinforcements.

Among metal matrices, Ti alloys epitomize unsuitability for direct melt infiltration owing to aggressive reactivity. Fiber clustering is also a concern, even in solid state processes based on powder or foil matrices. Composite consolidation by vapor deposition (PVD) of the matrix on the fibers provides an avenue for improving *homogeneity of fiber spacing*. However, present schemes require expensive pressure densification with its many problems. A potential solution involves a hybrid manufacturing route wherein part of the matrix is first applied to the fibers by PVD. The pre-metallized fibers are then assembled into a preform having the desired shape and then infiltrated with the remaining matrix in liquid form.

Direct infiltration with Ti alloys could be feasible owing to the protection of the fiber by the PVD layer, but the high temperatures involved would exacerbate the diffusional interactions at the fiber-matrix interface. An alternate approach involves depositing the more refractory constituents of

the matrix (e.g., Ti, Nb, Mo, etc.) by PVD and then infiltrating with the lower melting point constituents (e.g. Al). Based on stoichiometric considerations, the latter approach would be suitable for matrices with $\geq$ 25 at.% Al, notably the orthorhombic and α_2 alloys. The obvious problem with this approach is the homogenization of the matrix after consolidation, which may require lengthy high temperature treatments in the solid state. However, a significant part of the matrix synthesis reaction could be effected in the presence of molten Al, followed by a final heat treatment in the solid state. While this lower temperature infiltration approach is evidently desirable from a manufacturing viewpoint, it is not clear that matrix homogenization can be achieved.

A program involving modeling and experimental work will be initiated in 1994 to generate the knowledge base appropriate to hybrid approaches for Ti matrix composites (Levi, Evans). Cell models (single fiber environment) would be developed to study diffusional interactions and remelting/solidification phenomena as a function of processing cycle (temperature-time history). Experiments would be performed to elucidate the relevant aspects of microstructural evolution and provide the reaction and interdiffusion kinetics needed to calibrate the models. Initial experiments would be performed by infiltrating pure Ti-wire preforms with molten Al and subjecting the "composite" to different treatments in the semi-solid state. Subsequent experiments would focus on developing a metallization route for Ti-Nb alloys on SiC fibers and on the relevant interactions with infiltrated Al. Larger scale modeling issues would be tackled in 1995 if the proposed approach appears promising.

Ongoing activities on the understanding of microstructure evolution and its relationship to properties in *in-situ* TMC systems based on TiB reinforcements would be continued (Levi). These are by nature affordable composites which exhibit inherent thermochemical stability and may be cast into shapes using conventional Ti processing techniques. A potential application of these materials would be in joints with unidirectionally reinforced composites, wherein their higher modulus and creep resistance combined with acceptable toughness and isotropic properties could be advantageous. It is also anticipated that these materials could be used for cladding in PVD or plasma-sprayed form, thereby reducing the potential for fatigue crack initiation in the cladding. Since TiB is thermochemically stable

with practically all Ti matrices of interest in fiber composites, such strengthening concepts may be readily implemented.

10.2 CMCs

Measurements and observations in 1993 have shown that strong, high strain to failure CMCs can be fabricated using an inexpensive method that involves a) packing a powder around fibers within a fiber preform using pressure filtration and b) making the powder matrix strong by heat treatment followed by infiltration with a liquid precursor that decomposes to an inorganic material. A composite made this way, with polycrystalline alumina fibers in a silicon nitride matrix, demonstrated that the *matrix* deflects the crack. This observation is significant since it suggest that a class of CMCs can be processed without needing weak fiber/matrix interfaces. The potential of this observation will be explored (Lange, Evans), by processing a composite with strong, polycrystalline alumina fibers in a mullite matrix because the thermomechanical properties of mullite minimize thermal stresses and resist creep. In addition, the thermal expansion mismatch is relatively small. Mixed Al, Si metal alkoxide precursors which can be gelled *in-situ*, prior to decomposition, will be used to strengthen the matrix.

Manufacturing studies would initiate with understanding the precursor infiltration into mullite power compacts. The densification of the matrix would be determined as a function of the cyclic infiltration. Microstructure changes would be controlled to avoid flaw populations during densification. The fracture toughness and the strength of the matrix would be determined as a function of the number of precursor infiltration cycles. Composite processing would initiate with precursor infiltration into alumina fiber preforms by pressure filtration, with emphasis on the colloidal aspects of this processing step. The goal would be to determine the processing conditions needed to produce a matrix that optimizes the ability to deflect cracks without degrading fiber strength. To optimize composite processing, panels for testing under conditions of both strain and stress control would be manufactured.

11. STRESS AND DAMAGE SENSORS

The extensive exploitation of the optical fluorescence method of measuring stresses in sapphire fiber and alumina-containing ceramic composites begun in 1993 will be continued in 1994 (Clarke, Wadley). The emphasis is on using the method to understand basic, unresolved issues in stress redistribution in composites by the direct measurement, with high spatial resolution, of the stresses themselves. Particular attention will be paid to determining the stress distribution associated with interfacial sliding. One of the problems to be addressed relates to new concepts for oxidation resistant interfaces within MMCs and CMCs, particularly the concomitant roles of fiber roughness and sintering on interface sliding and debonding, after exposure to high temperatures and cyclic loadings. For this purpose, fibers with fugitive, low modulus coatings will be explored and fluorescence measurements used to understand stress evolution and its connection with fiber durability within the composite. A second problem relates to the distinction between the line spring and large scale sliding models for fiber bridging (Budiansky, Hutchinson), so as to determine the range of applicability of the two models. The two competing models predict different distributions of stresses in the fibers within the bridging zone and hence are amenable to validation on the basis of the measured stress distribution.

Two approaches to measuring local damage are under development and will be the focus of the sensor activities. One is the use of acoustic methods (Wadley) to probe local variations in the elastic modulus of CMCs as a function of load. This should provide a means of mapping the distribution of damage which can be compared directly with the predictions of continuum damage mechanics models. The second approach (Clarke) is to detect the third harmonic signal generated by the presence of local damage. Preliminary experimental results obtained in 1993 concerned with the detection of crack-like voids in thin metal lines, together with computer simulation studies, have demonstrated the viability of the technique. This work will be extended in order to detect damage accumulation in CMCs and MMCs.

Materials Science and Engineering, A167 (1993) 57–64

Cracking and stress redistribution in ceramic layered composites

K. S. Chan
Southwest Research Institute, San Antonio, TX 78238-5100 (USA)

M. Y. He
Materials Department, University of California, Santa Barbara, Santa Barbara, CA 93106 (USA)

J. W. Hutchinson
Division of Applied Sciences, Harvard University, Cambridge, MA 02138 (USA)

(Received November 16, 1992)

Abstract

Problems are analyzed that have bearing on cracking and survivability in the presence of cracking of layered composite materials composed of brittle layers joined by either a weak interface or a thin layer of a well-bonded ductile metal. The problems concern a crack in one brittle layer impinging on the interface with the neighbouring brittle layer and either branching, if the interface is weak, or inducing plastic yielding, if a ductile bonding agent is present. For the case of a weak interface, the effect of debonding along the interface is analyzed and results for the stress redistribution in the uncracked layer directly ahead of the crack tip are presented. Debonding lowers the high stress concentration just across the interface, but causes a small increase in the tensile stresses further ahead of the tip in the uncracked layer. A similar stress redistribution occurs when the layers are joined by a very thin ductile layer that undergoes yielding above and below the crack tip, allowing the cracked layer to redistribute its load to the neighbouring uncracked layer. The role of debonding and yielding of the interface in three-dimensional tunnel cracking through an individual layer is also discussed and analyzed. Residual stress in the layers is included in the analysis.

1. Introduction

When layered, thin sheets of a brittle material may have toughness and strength properties far superior to those of the material in bulk form [1–6]. To enable good strength and toughness, the interface between adjoining layers must counteract the stress concentration effect of any crack that occurs in an individual layer, reducing the likelihood that it will propagate into the next layer. Depending on the nature of the interface, this may occur by debonding, when the interface is brittle and relatively weak, or by yielding and sliding for systems composed of brittle layers alternating with thin ductile adhesive layers. The latter category is represented by sheets of Al_2O_3 joined by thin layers of aluminum [2] and by the model system with sheets of Al_2O_3 bonded by epoxy [3]. Some of the issues related to the design of layered brittle materials are similar to those encountered in the design of fiber-reinforced brittle matrix composites, such as the selection of interface toughness to prevent matrix cracks from penetrating the fibers. Other issues are unique to the layered geometry, and this paper addresses a few of them. In particular, the role of yielding or debonding of the interface in defeating cracks in individual layers is analyzed by consideration of the stress redistribution in the adjoining uncracked layer that accompanies these processes. Results are given for the energy release rate of three-dimensional cracks tunneling through an individual layer. This release rate, which is influenced by interface yielding or debonding, provides the essential information needed to predict the onset of widespread layer cracking in terms of the thickness of the brittle layer material and its toughness.

The geometries of the problems to be studied are shown in Fig. 1. Figure 1(a) shows a cracked layer of width $2w$ with zones of either yielding or debonding in the interface extending a distance d above and below the crack tips. The interface is taken to be either a very thin ductile layer of an elastic–perfectly plastic material with shear flow stress τ or a weak plane that debonds and slips under conditions such that the layers remain in contact and exert a friction stress τ on each other. The ductile adhesive layer allows relative slipping of the layers it joins by plastic yielding, but it is assumed that debonding does not occur. In this case, the condition $K_2 = 0$ must be enforced, leading to well-behaved shear stresses at the end of the yielding zone and estab-

0921-5093/93/$6.00

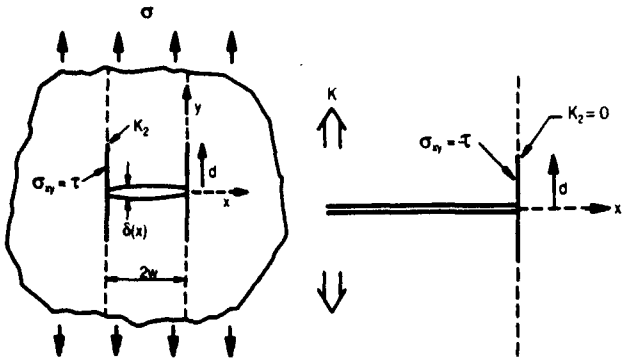

Fig. 1. Specification of the plane strain problems: (a) finite layer crack; (b) asymptotic problem.

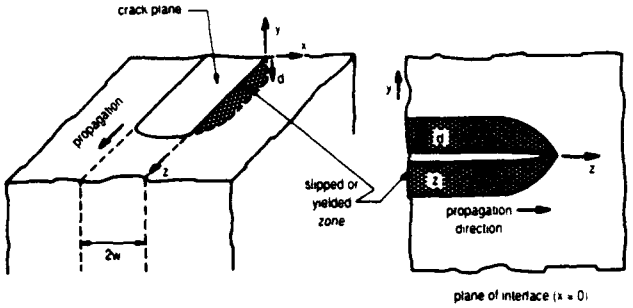

Fig. 2. Specification of the three-dimensional tunneling crack problem.

lishing the zone length d. In the case where the interface debonds, the interface crack is fully closed for $d/w > 0.71$ [7]. The mode 2 stress intensity factor K_2 at the end of the slipped zone will be nonzero, and must attain the mode 2 toughness of the interface for the debond to spread. Results for K_2 are given below.

Cracks in individual layers spread as three-dimensional tunnel cracks propagating through the layer (Fig. 2). Once the crack has spread a distance of at least several layer thicknesses in the z direction it approaches a steady state wherein the behavior at the propagating crack front becomes independent of the length of the crack in the z direction. Under these steady-state conditions, the energy release rate of the propagating front can be computed by use of the plane strain solution associated with the geometry of Fig. 1(a) (other examples of tunnel cracks are given in ref. 8). The steady-state energy release rate can be computed in terms of the average of the opening $\delta(x)$ of the plane strain crack. The zone of yielding or debonding increases the tunneling energy release rate, thereby lowering the overall stress at which widespread layer cracking can occur. Results for the tunneling energy release rate are given below. The role of residual stresses in the layers are readily accounted for: this is discussed in the final section.

When the interface is weak and debonding occurs, the interface crack is fully open with mixed mode intensity factors when $d/w < 0.24$ [7]. This case can be approximated well by the asymptotic problem for a semi-infinite crack impinging the interface where the remote field is the K-field associated with the problem in Fig. 1(a), with $d = 0$. The stress redistribution in the next layer ahead of the impinging crack tip is given, with a correction of previous energy release rate results for the doubly-deflected interface crack [9]. When plastic yielding of a ductile adhesive layer occurs, another asymptotic problem applies when σ is sufficiently small compared with τ. Then, the asymptotic problem is that shown in Fig. 1(b) for a semi-infinite crack loaded remotely by the same K-field. In this case also, the effect of yielding in the thin adhesive layer on the stress distribution ahead of the crack tip in the uncracked layer is emphasized.

2. Effect of plastic yielding on stress redistribution

As discussed above, the thin ductile adhesive layers in Fig. 1(a) are assumed to be elastic–perfectly plastic with a yield stress in shear of τ, and are modeled as having zero thickness. The plane strain problem is considered where the central cracked layer has the same elastic properties (E, ν) as the semi-infinite blocks adjoining across the interfaces. Under monotonic increase of the applied remote stress σ, the zones of yielding of half-height d spread allowing slip in the form of a tangential displacement discontinuity across the interface in the yielded region. The condition $\sigma_{xy} = \pm\tau$ is enforced within the yielded zones of the interface. The Dugdale-like condition $K_2 = 0$ at the ends of the yielded zones ensures that the shear stress on the interface falls off continuously just outside the yielded zone, and it determines the relation of d/w to σ/τ under the monotonic loading considered. Integral equation methods are employed to solve this problem as well as the others posed below; the methods used are outlined briefly in Appendix A.

The two most important functional relations needed to solve the three-dimensional tunneling crack problem discussed below are shown in Figs. 3 and 4. In Fig. 4, $\bar{\delta}$ is the average crack opening displacement defined by

$$\bar{\delta} = \frac{1}{2w}\int_{-w}^{w} \delta(\xi)\,d\xi \tag{1}$$

The elastic value of $\bar{\delta}$, valid when there is no yielding $(\tau \to \infty)$, is $\bar{\delta}_0 = \pi(1-\nu^2)\sigma w/E$. Yielding of the adhesive layers begins to make a significant contribution to the

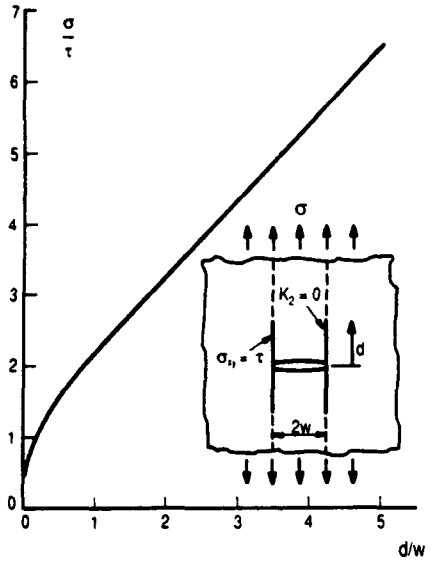

Fig. 3. Relation between applied stress and height of the yielding zone in a thin ductile adhesive layer.

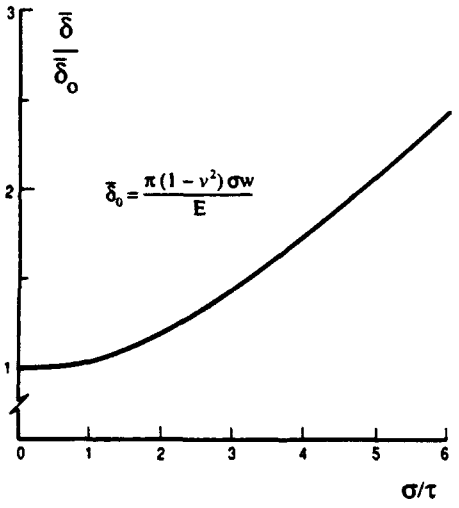

Fig. 4. Average crack opening displacement as a function of the ratio of applied stress to shear yield stress of the thin ductile adhesive layer.

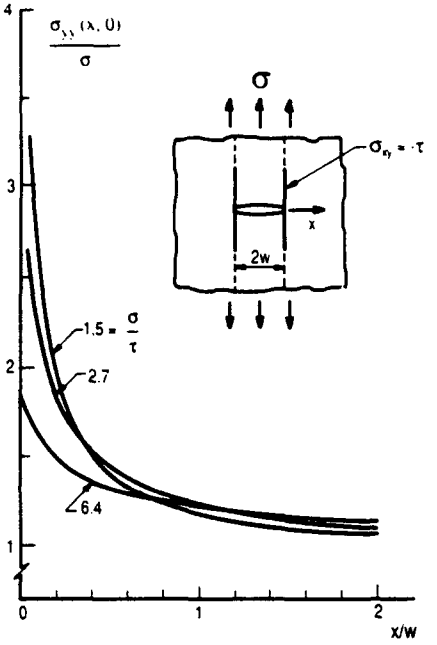

Fig. 5. Stress distribution ahead of the crack tip in the uncracked layer at several levels of applied stress to shear yield stress of the thin adhesive layer.

average crack opening displacement when σ/τ exceeds unity. The redistribution of normal stress $\sigma_{yy}(x, 0)$ in the block of material across the interface is shown in Fig. 5 for three levels of σ/τ. The curve shown for $\sigma/\tau = 1.5$ is only very slightly below the elastic distribution

$$(\sigma_{yy}(x, 0) = (\bar{x} + 1)/(\bar{x}^2 + 2\bar{x})^{1/2}$$

for $\bar{x} \equiv x/w > 0.05$. Reduction of stress ahead of the crack tip begins to be appreciable when $\sigma/\tau = 2.7$, and is quite significant when $\sigma/\tau = 6.4$. The drop in stress just across the interface is offset by a slight increase in stress relative to the elastic distribution further from the interface. This feature is seen in all the stress redistribution results.

Stress redistribution can be presented in another way when d/w is sufficiently small, by use of the asymptotic problem shown in Fig. 1(b). Provided d/w is sufficiently small, the yielding behavior is small-scale yielding with the elastic stress intensity factor K as the controlling load parameter. The remote field imposed on the semi-infinite crack is the elastic K-field. This asymptotic problem has also been solved with integral equation techniques. The extent of the yield zone in the asymptotic problem is

$$d = 0.052 \left(\frac{K}{\tau}\right)^2 \tag{2}$$

Figure 6 displays the normal stress directly ahead of the crack tip in the adjoining block normalized by the elastic stress field for the limit $\tau = \infty$. The stress ratio in Fig. 6 depends on x/d but is otherwise independent of K in the asymptotic problem. Yielding reduces the stress below the elastic level over a region ahead of the crack tip which is slightly larger than $d/10$. Beyond that region the stresses are slightly elevated above the elastic levels and approach the elastic distribution as x/d becomes large. The stress redistribution due to debonding (Fig. 6) is more dramatic: this is discussed below.

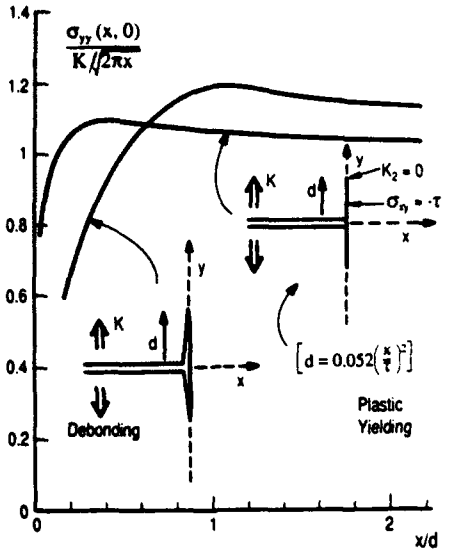

Fig. 6. Stress redistribution ahead of the crack tip in the layer across the interface for the two asymptotic problems ($d \ll w$).

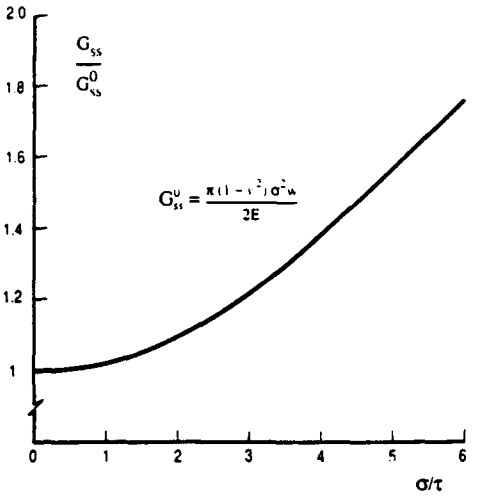

Fig. 7. Normalized steady-state energy release rate for the tunneling crack in the case of thin ductile adhesive layers with shear yield stress τ.

3. Effect of plastic yielding on tunnel cracking

As stated above, the steady-state energy release rate for a three-dimensional tunneling crack can be computed by use of the plane strain solution. For the geometry and loading shown in Figs. 1(a) and 2, the leading edge of the tunneling crack propagating in the z direction experiences mode 1 conditions. Let G_{ss} denote the energy release rate averaged over the propagating crack front. An energy balance accounting for the release of energy per unit advance of the tunnel crack under steady-state conditions gives $2wG_{ss}$ as the work done by the tractions acting across the plane of the layer crack in the plane strain problem as those tractions are reduced to zero from σ. For the present problems, this is the same as

$$G_{ss} = \int_0^{\sigma} \bar{\delta}(\sigma')\, d\sigma' \tag{3}$$

where $\bar{\delta}$ is the average crack opening displacement for the traction-free plane strain crack under monotonically increased remote σ. The elastic result for $d=0$ (*i.e.* $\tau=\infty$) is

$$G_{ss}^0 = \frac{\pi(1-\nu^2)\sigma^2 w}{2E} \tag{4}$$

The ratio of G_{ss} to G_{ss}^0 can be computed from the data in Fig. 4 by use of simple numerical integration. The result is plotted in Fig. 7. Increases of the steady-state release rate above the elastic value become important when σ/τ exceeds unity.

4. Effect of debonding and frictionless slipping on stress redistribution

The plane strain interface debonding problem for the geometry of Fig. 1(a) is as follows for the case where no frictional resistance is exerted across the debonded interfaces (*i.e.* $\tau=0$). According to ref. 7, the debonded interface will be fully open when $d/w<0.24$, and the interface crack tip at the end of the debond is subject to mixed mode conditions, as discussed for the asymptotic problem below. For $0.24<d/w<0.71$, the debond crack tip is closed and therefore in a state of pure mode 2, but a portion of the interface near the main layer crack is still open. For $d/w>0.71$, the interface is fully closed and the interface crack tip is in mode 2. The top curve for the normalized mode 2 stress intensity factor in Fig. 8 applies to the frictionless case. It was computed using the integral equation methods outlined in Appendix A under the constraint that the interface remains closed. The results are strictly correct only for $d/w>0.71$ (and agree with the results of ref. 7), but are only slightly in error for smaller d/w. The average crack opening displacement $\bar{\delta}$ needed for the tunnel crack calculations is shown in Fig. 9, where the top curve again applies to the frictionless case.

The role of debonding on stress redistribution is seen in Fig. 10, where curves of the stress ahead of the right-hand layer crack tip (normalized by the remote applied stress σ) are plotted for various levels of debonding, all for the closed interface with $\tau=0$. Debonding clearly has a significant effect on lowering of the stress on the adjoining material just across the interface; more so than for plastic yielding of a thin

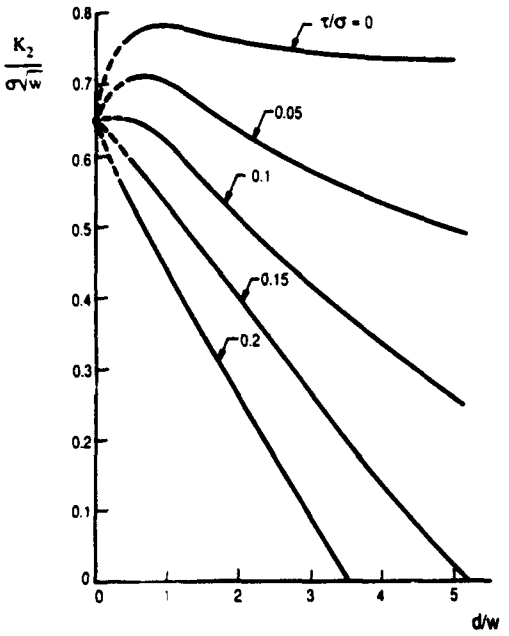

Fig. 8. Normalized mode 2 stress intensity factor for the debonding interface crack at several levels of interface friction stress to applied stress.

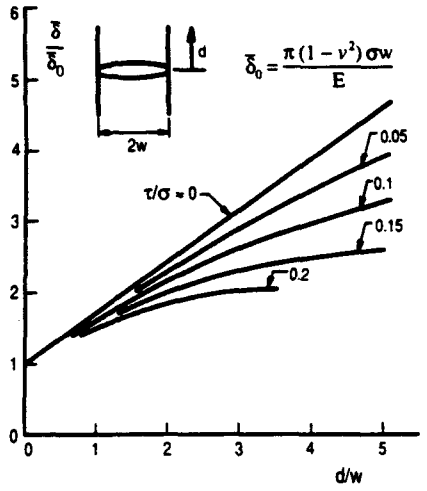

Fig. 9. Average crack opening displacement as a function of debond length at several levels of interface friction stress to applied stress.

ductile layer discussed in connection with Fig. 5. For sufficiently small d/w, the debonded interface is fully open and the asymptotic problem for a semi-infinite crack impinging on the interface applies, as shown in the insert in Fig. 6. The stress redistribution is plotted in Fig. 6, which shows that the stress ahead of the layer crack tip is reduced below the level in the absence of debonding over a distance from the interface equal to half the debond length d. Figure 6 also shows that debonding appears to be more effective in protecting

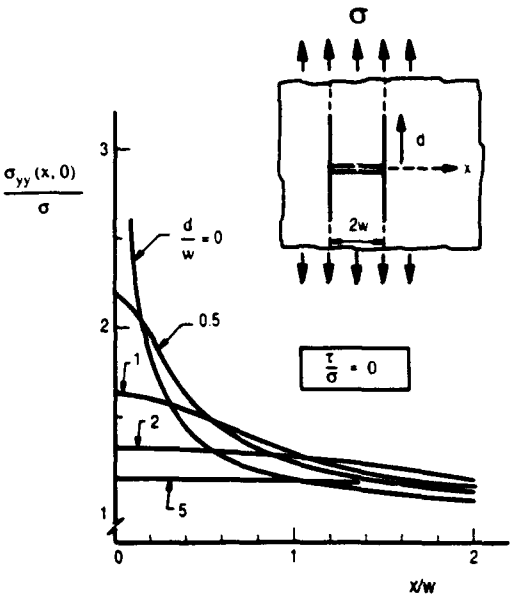

Fig. 10. Stress distribution ahead of the crack tip in the uncracked layer across the interface for the case of no interface friction.

the uncracked layer across the interface than plastic yielding of a thin ductile adhesive layer.

As a digression, the mode 1 and 2 stress intensity factors are recorded for the open interface crack tip for the asymptotic problem of Fig. 6

$$\frac{K_1}{K} = 0.399$$

and (5)

$$\frac{K_2}{K} = 0.322$$

The associated ratio of the energy release rate of the interface crack tip to that of a mode 1 crack penetrating straight through the interface without debonding is 0.263 when both the deflected tips and the penetrating tip emerge from the main crack tip at the same applied K. These results correct results given in ref. 9 that were in error for the case of the doubly-deflected interface crack. A complete set of corrections of this energy release rate ratio for this case over the full range of elastic mismatch across the interface is given in ref. 10.

5. The effect of frictional slipping on debonding and tunnel cracking

Figures 8 and 9 show curves for the normalized mode 2 stress intensity factor and the average crack

opening displacement respectively in the plane strain problem for several levels of a constant friction stress τ relative to σ acting over the bonded interface. A constant friction stress, as opposed for example to a Coulomb friction stress, has been used by some workers to represent the frictional forces exerted across slipping interfaces in composites. The purpose of the present limited study is to illustrate the effect of friction in establishing the extent of debonding and its associated influence on the three-dimensional tunneling energy release rate. Almost certainly, additional studies will be required before understanding is good, including studies with other friction laws. Some results for the effect of Coulomb friction on the mode 2 interface stress intensity factor are given in ref. 11.

Let K_c denote the mode 2 toughness of the interface. Attention will be concentrated on the behavior following initiation of interface debonding when the debond length d is sufficiently large (*i.e.* greater than $\sim w/4$) such that the debond interface crack tip is in mode 2. Impose the debonding condition $K_2 = K_c$ on the solution presented in Figs. 8 and 9. The relationships of the applied stress with the debonding length and the average crack opening displacement that result are plotted in Figs. 11 and 12. The two nondimensional stress parameters in these figures are the applied stress parameter $\sigma(w)^{1/2}/K_c$ and the constant friction stress parameter $\tau(w)^{1/2}/K_c$. (It is necessary to interpolate values between the curves of Figs. 8 and 9 to arrive at the plots in Figs. 11 and 12, since a constant value of $\tau(w)^{1/2}/K_c$ does not correspond to a constant value of τ/σ.) In the range of d less than $\sim w/4$, the predictions are not expected to be correct since the interface undergoes mixed mode debonding and not mode 2 debonding. Thus, the details in the vicinity of the initiation of debonding are not correct. In particular, the value of $\sigma(w)^{1/2}/K_c$ at which $\bar{\delta}$ begins to depart from $\bar{\delta}_0$ (see Fig. 12) would depend on the mixed mode condition for debond initiation. But once debonding has progressed to the point that the interface crack tip is closed, the mode 2 criterion is appropriate and the curves are accurate.

In the absence of friction the debonding process is unstable, since for a fixed σ, K_2 has a maximum when $d \approx w$ and then drops slightly to an asymptote as d increases further. Under a prescribed σ, the mode 2 debond would advance dynamically after it was initiated. In this sense, the curves shown in Figs. 11 and 12 for $\tau = 0$ represent unstable debonding behavior. Friction stabilizes the debonding process, giving rise to a monotonically increasing debond length and average crack opening displacement as the applied stress increases A nondimensional friction stress of the order of $\tau(w)^{1/2}/K_c = 1/8$ or more is required if friction is to be important.

The steady-state energy release rate for tunnel cracking can be computed from the curves in Fig. 12 using eqn. (3). The results of this calculation are plotted in Fig. 13. As before, G_{ss} is normalized by the value for a layer crack with no debonding given in eqn. (4). The above remarks on accuracy in the vicinity of debond initiation also apply to these curves. It can be seen from Fig. 13 that debonding can significantly promote tun-

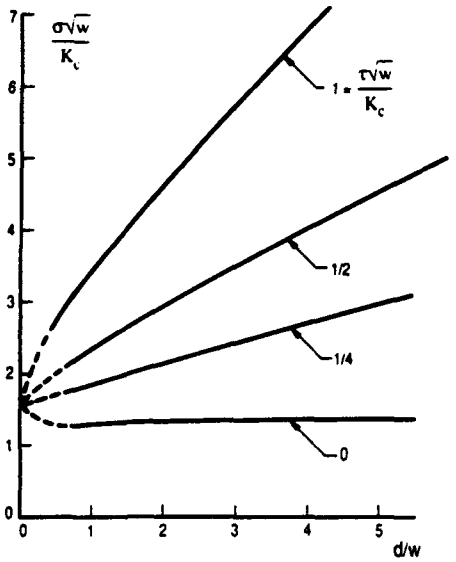

Fig. 11. Relation of normalized applied stress and debond height at several levels of the non-dimensional interface friction stress: the condition $K_2 = K_c$ is imposed, where K_c is the mode 2 interface toughness.

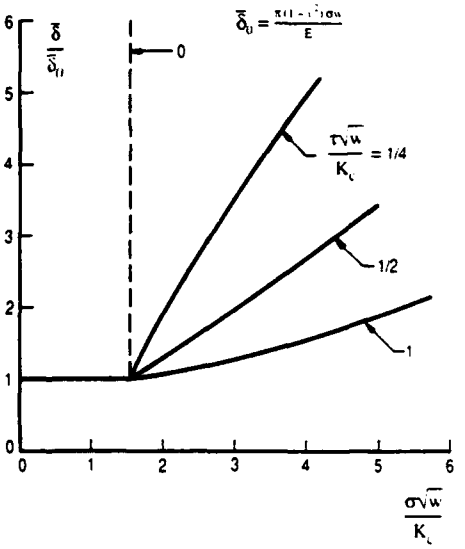

Fig. 12. Relation of the average crack opening displacement and normalized applied stress at several levels of the nondimensional interface friction stress: the condition $K_2 = K_c$ is imposed, where K_c is the mode 2 interface toughness.

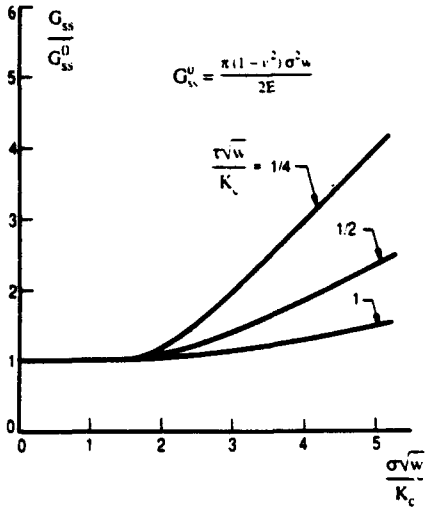

Fig. 13. Steady-state energy release rate for the tunneling crack: the condition $K_2 = K_c$ is imposed, where K is the mode 2 interface toughness.

neling cracking when the nondimensional friction stress is less than about $\tau(w)^{1/2}/K_c = 1/2$.

6. Accounting for residual stress in the cracked layer

The role of a uniform residual tension $\sigma_{yy} = \sigma_R$ preexisting in the layer that undergoes tunnel cracking can readily be taken into account in the various results presented above. For the purpose of discussion, let $\sigma_{yy} = \sigma_A$ be the applied stress, replacing the notation for σ given above. The results in Figs. 3, 4, 7–9 and 11–13 apply as they stand if σ is identified with $\sigma_A + \sigma_R$. The results for stress redistribution shown in Figs. 5 and 10 can also be used, with the following modifications. With σ identified with $\sigma_A + \sigma_R$, the results in Figs. 5 and 10 are correct for the *change* in σ_{yy} in the layer ahead of the tip due to cracking if the numerical value of the ordinate is reduced by 1. To obtain the total stress σ_{yy} in the layer in question, one must then add the *change* and the stress σ_{yy} existing in the layer prior to the cracking event.

Acknowledgments

The work of K. S. Chan was supported by the Internal Research Program, Southwest Research Institute, San Antonio, Texas. The work of M. Y. He was supported by the DARPA URI at the University of California, Santa Barbara (ONR Contract N00014-86-K-0753). The work of J. W. Hutchinson was supported in part by the DARPA URI (Subagreement P.O. # VB38639-0 with the University of California, Santa Barbara, ONR Prime Contract N00014-86-K-0753) and by the Division of Applied Sciences, Harvard University.

References

1 D. B. Marshall and J. J. Ratto, *J. Am. Ceram. Soc.*, *74* (1991) 2979–2987.
2 H. C. Cao and A. G. Evans, *Acta Metall. Mater.*, *39* (1991) 2997.
3 C. A. Folsom, F. W. Zok, F. F. Lange and D. B. Marshall, *J. Am. Ceram. Soc.*, *75* (1992) 2969–2975.
4 B. J. Dalgleish, K. P. Trumble and A. G. Evans, *Acta Metall. Mater.*, *37* (1989) 1923–1931.
5 M. C. Shaw, D. B. Marshall, M. S. Dadkhah and A. G. Evans, Cracking and damage mechanisms in ceramic/metal multilayers, *Acta Metall. Mater.*, in press.
6 M. Y. He, F. E. Heredia, D. J. Wissuchek, M. C. Shaw and A. G. Evans, *Acta Metall. Mater.*, *41* (1993) 1223–1228.
7 A. Dollar and P. S. Steif, *J. Appl. Mech.*, *58* (1991) 584–586.
8 J. W. Hutchinson and Z. Suo, Mixed mode cracking in layered materials, *Adv. Appl. Mech.*, *29* (1991) 63–191.
9 M. Y. He and J. W. Hutchinson, *Int. J. Solids Struct.*, *25* (1989) 1053–1067.
10 M. Y. He and J. W. Hutchinson, The effect of residual stress on the competition between crack deflection and penetration at an interface, to be published.
11 A. Dollar and P. S. Steif, *J. Appl. Mech.*, *56* (1989) 291–298.

Appendix A: Numerical approaches

Two integral equation formulations were used in the solution of the problems discussed. As these have been used by various authors to solve related plane strain problems, details of the methods are not given here. In some cases, results were generated by use of both schemes as a check. The methods used for the problems for the closed interface cracks at the ends of the finite length layer crack (see Fig. 1(a)) are discussed first.

The integral equations in method 1 are formed by representation of both the layer crack and the mode 2 interface cracks in terms of distributions of dislocations. With reference to Fig. 1(a), let $b_0(x) = -\mathrm{d}\delta_y/\mathrm{d}x$ denote the amplitude of the dislocation opening distribution extending from 0 to w along $y = 0$, and let $b_2(y) = -\mathrm{d}\delta_x/\mathrm{d}y$ denote the amplitude of the dislocation shearing distribution along $x = w$ extending from 0 to d. The condition that $\sigma_{yy} = 0$ along $y = 0$ for $-w < x < w$ can be written as

$$\int_0^w H_1(x, x')b_0(x')\,\mathrm{d}x' + \int_0^d H_2(x, y)b_2(y)\,\mathrm{d}y = -\sigma \qquad (6)$$

where $H_1(x, x')$ denotes the stress $\sigma_{yy}(x)$ along $y = 0$ due to $b_0(x')$, with due regard for the symmetry of this distribution with respect to $x = 0$, and $H_2(x, y)$ denotes $\sigma_{yy}(x)$ due to $b_2(y)$, with the appropriate four-fold

symmetry on this distribution imposed. Similarly, the condition that $\sigma_{xy} = -\tau$ along $x = w$ between 0 and d (with the corresponding shear conditions met along the other three legs of the H-crack) is

$$\int_0^w H_3(y, x')b_0(x')\,dx' + \int_0^d H_4(y, y')b_s(y')\,dy' = -\tau \qquad (7)$$

where $H_3(y, x')$ is $\sigma_{xy}(y)$ along $x = w$ due to $b_0(x')$ and $H_4(y, y')$ is $\sigma_{xy}(y)$ due to $b_s(y')$.

Method 2 uses the solution for the problem of four symmetrically placed dislocations interacting with a traction-free crack extending along the x-axis from $-w$ to w. With $H(y, y')$ denoting the shear stress $\sigma_{xy}(y)$ along $x = w$ between 0 and d due to $b_s(y')$, with due regard for the other three symmetrically placed dislocations, the single integral equation for b_s is

$$\int_0^d H(y, y')b_s(y')\,dy' = -\sigma_{xy}^0(y) - \tau \qquad (8)$$

where $\sigma_{xy}^0(y)$ is the shear stress along $x = w$ due to the remote stress acting on the layer crack in the absence of the interface cracks.

The kernels of the above integrals have Cauchy singularities. The dislocation distributions can be techniques. Once the distributions are known in either obtained by use of several well known numerical method, they can be used with other integral expressions to compute the stress components at any point in the plane and the mode 2 stress intensity factor at the end of the interface crack. For the cases in which K_2 is nonzero, the distribution $b_s(y)$ has an inverse square root singularity at $y = d$, while it diminishes with the square root of the distance from $y = d$ for the plastic yielding problems with $K_2 = 0$. The solutions do not rely on a precise incorporation of the correct behavior of the dislocation distributions at the corner point at $x = w$ on $y = 0$. A number of choices were made, including representations that built in the correct lowest order functional behavior near this point.

The asymptotic problem for the semi-infinite layer crack and the mode 2 interface cracks (see Fig. 1(b)) was solved using method 2. Now, $H(y, y')$ is the shear stress along $x = 0$ between 0 and d due to just two symmetrically placed dislocations on $x = 0$ at $\pm y'$ interacting with a traction-free semi-infinite crack, and $\sigma_{xy}^0(y)$ is the shear stress on $x = 0$ due to the K-field in the absence of the interface cracks. The second asymptotic problem discussed in connection with Fig. 6, in which the interface crack opens, is also solved using method 2, but here both shear dislocations and opening dislocations must be used and the problem becomes a set of dual integral equations. In all the cases involving method 2, the kernel functions H can be obtained in closed form by use of complex variable methods of elasticity.

MATERIALS

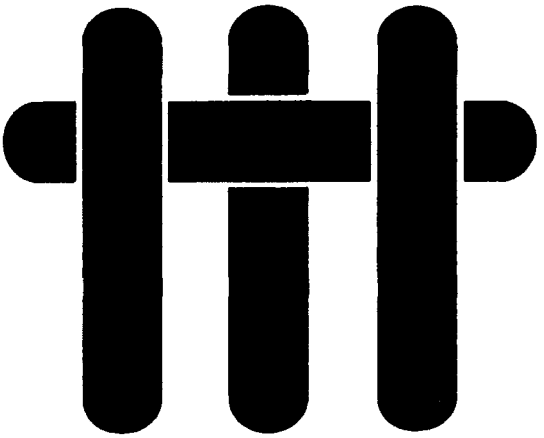

Notch Sensitivity and Stress Redistribution in CMCs

Thomas J. Mackin,* Thomas E. Purcell,† Ming Y. He* and Anthony G. Evans*

*High Performance Composites Center
Materials Department
College of Engineering
The University of California at Santa Barbara
Santa Barbara, CA 93106-5050

†Pratt and Whitney
United Technologies
17900 Beeline Highway
Jupiter, Fl 33478

ABSTRACT

Fiber reinforced ceramic matrix composites depend upon inelastic mechanisms to diffuse stress concentrations associated with holes, notches and cracks. These mechanisms consist of fiber debonding and pullout, multiple matrix cracking and shear band formation. In order to understand these effects, experiments have been conducted on several double-edge-notched CMC's that exhibit different stress redistribution mechanisms. Stresses have been measured and mechanisms identified by using a combination of methods including: x-ray imaging, edge-replication and thermoelastic analysis. Multiple matrix cracking was found to be the most effective stress redistribution mechanism.

1. INTRODUCTION

One of the major attributes of fiber reinforced ceramic matrix composites (CMC's) is the existence of inelastic mechanisms that allow stress redistribution around strain concentration sites such as notches, holes, attachments, etc.[1-4] These mechanisms, analogous to plasticity in metals, involve combinations of matrix cracking and fiber pull-out.[1,6-10] Recent research has identified three principal damage phenomena that occur in the vicinity of holes and notches (Fig 1): Class I, the propagation of a single matrix crack accompanied by fiber fracture and pullout; Class II, the formation of multiple matrix cracks in the absence of fiber failure; and Class III, the formation of shear bands. Other damage mechanisms may, of course, exist. The operative damage class depends upon the magnitudes of non-dimensional parameters which combine interface, fiber, and matrix properties.[1,7,8,10] The intent of the present article is to provide an experimental assessment of stress redistribution effects around notches in CMC's that exhibit both Class II and Class III damage behaviors.

CMC's exhibit a variety of tensile (Fig 2a) and shear (Fig 2b) stress/strain curves,[1,10,14] with varying amounts of inelastic strain prior to failure. One purpose of the present study is to attempt to relate features of the inelastic strain measured in tensile and shear tests to the stress redistribution behavior. This would be achieved through an understanding of the operative inelastic mechanisms and their role in governing the dominant mode of damage (Fig 1).

The importance of stress redistribution is manifest in the notch sensitivity, which is a key factor affecting the practical utility of a structural material. [11,12] Notches and holes are a source of strain concentration. The corresponding stress concentration depends upon the material response. One limit obtains for elastic materials, where the stress concentrations are severe and result in extreme notch sensitivity. When inelastic mechanisms operate, the stresses redistribute in regions of large strain concentration and reduce the notch sensitivity. In some cases, the stress concentration can be completely eliminated, resulting in a notch insensitive material.[3,13] More generally, the behaviors can be presented on a notch sensitivity diagram[11,12] (Fig. 3). In this diagram, the ordinate is a measure of the tensile strength normalized by the un-notched strength, while the abscissa is the notch/hole size ($2a_0$) relative to the plate width (2b). Each line represents a measure of the inelastic displacement permitted by the material near the notch

tip, prior to failure. This measure is given by the ratio of the notch length to the length of the inelastic zone.[11]

Related stress redistribution mechanisms are known to occur in polymer matrix composites (PMC's), particularly upon cyclic loading. [13-21] Studies on PMCs have established a precedent for a test methodology[15-21] that can be used to monitor damage in CMCs and thereby measure its effects on the stress distribution. The methods include the use of Moiré interferometry to measure strain distributions, thermoelastic measurements to assess stress distributions,[15-19] x-ray imaging with dye penetration to highlight damage,[2, 13] and replication methods to examine matrix cracking.[15-21] All of these methods may be augmented by conventional optical and scanning electron microscopy. In the present study, a combination of these methods is used to study stress redistribution in three CMCs: SiC/CAS,[3,22] C/C[2] and SiC/SiC.[10] The materials and their properties are described elsewhere.[2,3,10,22]

The experimental procedure given principal emphasis is the thermoelastic emission method, which provides a measure of the stress distribution.[15-19,23-26] A brief synopsis of this method is given in the next section, prior to a description of the experiments and their analysis.

2. STRESS ANALYSIS BY THERMOELASTIC EMISSION

Stress Pattern Analysis from Thermoelastic Emission (SPATE) is a technique that relates instantaneous changes in the hydrostatic stress at any location in a material to instantaneous changes in local temperature.[23-26] The method has been used extensively to evaluate stress distributions in monolithic metals and polymer matrix composites.[15-19] The underlying phenomenon concerns the temperature change that occurs when an elastic body is subjected to hydrostatic deformation under adiabatic conditions. The fundamental thermodynamic relation for the temperature change $\dot{T}$ and its dependence on the hydrostatic stress rate $\dot{\sigma}_{kk}$, is given by (see Appendix):[23-30]

$$\dot{T} = -\left[\frac{T_0\beta}{K_m\beta^2 T_0+\rho_0 C_v}\right]\dot{\sigma}_{kk} \qquad (1)$$

where K_m is the isothermal bulk modulus, C_v is the specific heat at constant volume, β is the bulk thermal expansion coefficient, ρ_0 is the density, and T_0 is the mean temperature. The denominator in Eqn (1) is dominated by the term in density and specific heat, resulting in a useful approximation,

$$\dot{T} \approx -\left[\frac{T_0\beta}{\rho_0 C_v}\right]\dot{\sigma}_{kk} \qquad (2)$$

Typically, the material constants are combined to define a thermoelastic 'constant,' κ given by,

$$\kappa = \frac{\beta}{\rho_0 C_v} \qquad (3)$$

In the SPATE method a sinusoidal stress input is used, which creates a thermal response at both the first and second harmonics. The temperature change, ΔT, at the first harmonic, is given by,[20-25]

$$\Delta T = \kappa T_0 \Delta\sigma_{kk} \sin(\omega t) \qquad (4)$$

where ω is the frequency, $\Delta\sigma_{kk}$ is the hydrostatic stress amplitude, and t is time. A key feature of thermoelastic emission is that the spatial variation in temperature, $\Delta T(x,y)$, is related to the hydrostatic stress distribution, $\Delta\sigma_{kk}(x,y)$.[††] Moreover, when matrix damage occurs, such as microcracks, the properties which influence κ, (namely ρ_0, C_v, and β) are unchanged and eqn (4) still applies.

For typical values of the imposed stress range, $\Delta\sigma_{kk}$, the expected temperature changes for CMC's are between ≈ 0.1°C and 0.01°C. Very sensitive measurements are thus required. Furthermore, to satisfy the adiabatic assumption, the thermometry must be in thermal equilibrium with the test specimen. To satisfy these requirements, recent experimental techniques use

---

[††] For a composite, the material constants that relate stress and temperature involve combinations of the properties of the fiber and the matrix, leading to anisotropy in the thermoelastic 'constant', κ. The magnitude can be obtained either by calibration or calculation. [22,23]

the principle of black body radiation and infrared thermometry, wherein the radiant photon flux from a specimen is measured by a detector sensitive to infrared radiation.*[23,24] In practice, the detector response is the sum of the photon radiance due to the thermoelastic effect, that due to equilibrium radiance, and the background. Improvements in signal to noise are made by averaging the sample many times at a given location. This is accomplished by locking the detector data acquisition onto the frequency of the applied cyclic stress. A commercial system which embodies these concepts† has been used to measure thermoelastic emission from the test specimens. The system consists of a mercury doped CdTe detector affixed to a liquid nitrogen cooled dewar. The detector is housed within a camera body to reduce the effect of spurious radiation. A collimator and lenses at the inlet to the camera body focus the emitted IR onto the detector. The IR emitted from the sample is measured over a spot size of 400μm diameter at a working distance of 25cm and 0.001°C temperature sensitivity. Before testing, specimens are coated with a thin layer of commercial flat black paint to provide uniform emission from the sample surface. Background IR is reduced by placing a flat black card behind the specimen.

The experiments are conducted by applying a 10Hz, uniaxial cyclic load, creating a 10Hz fluctuation in the thermoelastic response. The frequency is chosen to minimize the effects of thermal conduction from the measurement zone during the measurement time, approximating adiabatic conditions.[23,24] The maximum load is usually chosen to correspond to a stress less than the elastic limit, while the minimum is chosen to retain specimen alignment. A lock-in amplifier controls the data acquisition system by locking the detector output to the frequency of the applied load. The phase lag is automatically adjusted by locking into the peak signal difference at the test frequency. Locking into the applied cyclic load performs two basic functions: It correlates the thermal signal to the applied stress, and it eliminates the effect of absolute temperature changes that may be occurring in the specimen.

---

* Typical IR detectors have a band gap of ~ 0.1eV, corresponding to photon wavelengths <14 microns.

† SPATE 9000 IR imaging system by Ometron

3. EXPERIMENTAL PROCEDURES

Test coupons were fabricated from panels of 0/90 composites of C/C, SiC/SiC and SiC/CAS. These materials and their properties are described in detail elsewhere.[2,3,10,22] Representative tensile and shear stress-strain curves are shown in Fig 2. The chosen composites exhibit a broad range of behavior. In tension, the C/C is nearly linear whereas the SiC/CAS has substantial non-linearity. Moreover, in shear this trend is reversed.

Double edge-notches were cut into the sides of the test coupons using a diamond blade, resulting in a nominal notch root radius of 250μm, and having relative notch depths, $0.33 \leq a_0/b \leq 0.5$. Aluminum tabs were bonded onto the ends of the test coupons for gripping purposes. The specimens were aligned and clamped using hydraulic grips in an Instron universal test machine with a 50,000lb load cell.. A strain gage was attached at a location remote from the reduced section to allow monitoring of the far field strain. The strain gage was connected to a dynamic strain amplifier, the output of which was used to calibrate the thermal emission.

Each test was interrupted at various points along the stress-strain curve in order to assess the stress distribution, as well as the development of damage around the notches. The stress was obtained using the thermoelastic emission procedure, described above, whereby the temperature distribution provides a map of the hydrostatic stress at the surface of the specimen (Eqn 4). Stress changes elicited by damage appear as changes in the temperature distribution. A 'stress concentration factor' (SCF) associated with the notches was computed from the thermoelastic images by taking the ratio of the local to far field temperatures. The 'stress concentration factor' is defined as (Eqn 4)

$$SCF = \frac{\Delta\sigma_{kk,local}}{\Delta\sigma_{kk,far\ field}} = \frac{\Delta T_{local}}{\Delta T_{far\ field}} \qquad (5)$$

As damage is introduced into the specimen, the SCF changes, and serves as a measure of stress redistribution.

Damage was characterized using both radiographic procedures and acetate tape replicas. The radiographs were obtained as follows: While under

load, a zinc iodide penetrant was dispersed onto the specimen.[2,13] The specimens were then unloaded, removed from the grips, and placed into an x-ray system. The penetrant enters into the damaged region and provides absorption contrast for an x-ray image of the damaged region.[2] Acetate replicas were obtained while the load was maintained in order to hold the matrix cracks open. Sections of replication tape were cut and held over the notch root region, and a small amount of acetone applied above the tape. The replicas were dried, removed and examined using optical microscopy.†† Combinations of damage imaging and thermoelastic emission provide a pictorial view of damage evolution and its effect on stress redistribution.

4. RESULTS

4.1 SPATE Calibration

Before proceeding with thermoelastic measurements, a SPATE calibration experiment was conducted on an edge notched steel specimen. The notches were milled into the sides of the sample for precise control over the notch root radius. Loads were used that ensure an elastic response everywhere in the specimen. A low resolution full field SPATE scan (Fig 4), combined with line scans, demonstrate the thermal response. In these images, the highest temperature difference is at the notch root, with a continuous decrease in temperature with distance away from the notch. †† For purposes of analysis, the temperature field is calibrated to the strain gage response in the far field by comparing thermoelastic and strain gage signals and adjusting the SPATE output accordingly. Several items are notable: (i) The specimen was not perfectly aligned, resulting in bending stresses. This is evident from the slope of the line scans both through the far field and the notches. (ii) There are fluctuations in the far field signal (10% of the signal). These arise from polishing scratches, variations in surface emissivity, and thermal fluctuations in the background. (iii) Edge effects appear on scans made in the vicinity of the notch and at the sample edges. The consequence is that a finite edge region, approximately 400μm in width, cannot be analyzed. The edge effect arises for two reasons: First, when

---

†† Assistance in replication was provided by D. Brodnicky at Pratt and Whitney.

†† The resolution of the grey scale images is an artifact of photographic reproduction, and is not indicative of the system resolution.

scanning near an edge, the detector spot is partially off the specimen. Second, as the specimen is cyclically loaded, the edges of the specimen move relative to the detector, adding unacceptable noise levels to the signal.

Stress concentration factors are derived from the temperature measurements by comparing the temperatures at the notch root with the temperature in the far-field (Eqn 5). Finite element (FEM) solutions (Fig 5) reveal that σ_{xx} near the notch root is about equal to the applied stress, while σ_{yy} is between 3 to 4 times larger The thermoelastic signal, which depends upon the sum, σ_{xx} and σ_{yy}, isthus dominated by σ_{yy} near the notch. The experimental SCF is superposed onto the finite element results (Fig 5). Upon noting that the spot size is 400μm, the SPATE measurement correlates satisfactorily with the stress concentration calculated by FEM.

4.2 CMC Measurements

Measurements made on the notched C/C material provide SPATE images obtained at two peak load levels (Fig 6a). These are accompanied by a radiographic image of the same specimens[2] (Fig 6b). The C/C material develops shear bands perpendicular to the notch which are comprised of multiple matrix cracks, characteristic of a Class III system[2] (Fig 1). Both SPATE and radiographic images illustrate this effect. The SPATE scan (Fig 6b) reveals a dramatic elongation in the notch root field, coincident with the development of the shear bands. Such bands form in this composite because of its relatively low shear strength (Fig 2b). Line scans connecting the notches (Fig 7) establish that there is a reduction in the magnitude of the notch root stress concentration as the shear bands extend. The line scans are overlayed with a net-section stress line to better illustrate changes in stress concentration. The results are quantified by plotting a measure of the stress concentration factor (SCF), eqn 5, as a function of shear band length, ℓ (Fig 8). The σ_{xx} stress at this location near the notch should be approximately equal to the applied stress (Fig 5). Consequently, this ratio of temperatures is primarily a measure of the σ_{yy} stress concentration ahead of the notch. The initial SCF is quite low compared with that measured on the steel specimen. This difference is attributed to machining damage that has already changed the local consititutive properties. Anisotropy effects may also be involved. Nevertheless, it is evident that the stress concentration factor

diminishes as the shear band length increases, consistent with finite element calculations [2] (fig 9).

A similar series of experiments conducted on the SiC/CAS material revealed different characteristics (figs 10-11). The SPATE images (fig 10) indicate that the zone of highest temperature *moves away from the notch root toward the specimen center* as the peak load increases. At the highest load, the temperature is essentially uniform across the net section (fig 11), implying that the stresses are also uniform and about equal to the net section stress. Such observations are consistent with the notch insensitive behavior found for this material (fig 2). Surface replicas revealed a multiplicity of matrix cracks emanating from the notch (fig 10), with no evidence of shear bands in this material. These observations classify the SiC/CAS material as a class II composite. Stress redistribution is achieved through the inelastic tensile deformation provided by multiple matrix cracks.[1,10]

SPATE images and line scans obtained for the SiC/SiC material (Figs 12 and 13) show some stress redistribution. However, stress concentration persists throughout. The damage mechanism operating in this material is presently unknown. Whichever mechanism operates, it is clearly less effective in stress redistribution than either the shear band or the multiple matrix cracking mechanisms that occur in the C/C and SiC/CAS composites, respectively.

5. ANALYSIS AND INTERPRETATION

The combination of SPATE measurements with x-ray and surface replicated images indicate that matrix cracking damage, occurring as either shear bands or multiple matrix cracks, modify the stress around notches. To further understand the implications of the SPATE results, it is recalled that the measurements are made at small stress levels, following the introduction of damage at larger stresses. Consequently, the damage must influence the stress/strain laws applicable at small strains. Unloading/reloading measurements conducted in both tension and shear have indicated that the unloading modulus diminishes as a consequence of matrix crack damage [1,10,22] (Fig 14). The damaged material would be located primarily ahead of the notch in the SiC/CAS composite, but normal to the notch, within the shear bands, in the C/C composite. The diminished modulus is regarded as the phenomenon that

causes the stresses inferred from the SPATE measurements to differ from the elastic solution . It is proposed that the damage creates a gradient in the elastic modulus, such that the stresses near the notch are reduced, as sketched in Fig 15. Moreover, results for stress redistribution in materials subject to shear bands[2] (Fig 9) indicate features comparable to the measurements performed on the C/C composite. A more detailed understanding of stress redistribution would require that SPATE measurements be made over a range of superposed mean stresses, thereby illuminating the non-linear stress-strain behavior in the damaged regions. Such measurements would provide constitutive relations that could be used in stress redistribution calculations.

SUMMARY

SPATE measurements, in conjunction with x-ray and replica observations, indicate the existence of damage mechanisms that result in local gradients in elastic modulus. These gradients in modulus cause stress redistribution. The magnitudes of these effects at small strains have been established from SPATE measurements. These measurements have also revealed differing stress redistribution behavior for each of the three composite systems, associated with different damage mechanisms. The damage mechanisms themselves, have been described elsewhere.[1-5] While the present study affirms that damage mechanisms occur, which change the local properties of the composite, [31-33] quantitative assessment of stress redistribution requires further research. Most importantly, the stress redistribution which arises at peak loads will be more extensive than that found at small strain by the SPATE measurement, because of the additional contributions to the inelastic strain caused by sliding at the fiber/matrix interface.[1,6,10,22]

APPENDIX

The Thermoelastic Phenomenon

Thermoelasticity describes the relationship between applied stress and temperature in an elastic body. For completeness, a derivation of the thermoelastic effect is given, based on formulae presented by Budiansky,[28] and similar to that proposed by Wong et al.[25] The change in internal energy in a body is given by the first law of thermodynamics[29]

$$dU = dQ + PdV \tag{A1}$$

where the change in internal energy, dU, is related to the heat conduction, dQ, and the work performed on the body, PdV. Upon combining with the second law,[29] the rate of change of internal energy becomes

$$\dot{U} = T\dot{S} + V\sigma_{ij}\dot{\varepsilon}_{ij} \tag{A2}$$

The dilatational† and deviatoric strain-rates are related, respectively, to the corresponding stress rates by[27-29]

$$\dot{e} = \frac{\dot{\sigma}}{K_m} + \beta\dot{T} \tag{A3}$$

and

$$\dot{e}_{ij} = \frac{\dot{s}_{ij}}{2G_m} \tag{A4}$$

where K_m is the adiabatic bulk modulus, G_m is the adiabatic shear modulus, and β is the coefficient of thermal expansion,. The derivative of the Helmholtz free energy is given by

$$\dot{F} = \dot{U} - T\dot{S} - S\dot{T} \tag{A5}$$

---

† For convenience the subscript kk is omitted on both the dilatational stress and strain.

which, with eqns (A2) to (A4), gives

$$\dot{F} = V(\sigma\dot{e} + s_{ij}\dot{e}_{ij}) - S\dot{T} \tag{A6}$$

or

$$dF = V(\sigma de + s_{ij}de_{ij}) - SdT \tag{A7}$$

Since the strain and temperature are independent variables, both the free energy and entropy may be expressed as functions of these variables,

$$F = F(e,e_{ij},T) \tag{A8}$$
$$S = S(e,e_{ij},T)$$

From elasticity,

$$\sigma = K_m e - K_m \beta T \tag{A9a}$$

and

$$e_{ij} = \frac{s_{ij}}{2G_m} \tag{A9b}$$

Equations (A7) and (A9), in conjunction with (A8) can be used to derive a functional relationship between changes in stress and changes in temperature. The total differential of the Helmholtz free energy and the entropy become,

$$dF = \frac{\partial F}{\partial e}de + \frac{\partial F}{\partial e_{ij}}de_{ij} + \frac{\partial F}{\partial T}dT \tag{A10}$$

and

$$dS = \frac{\partial S}{\partial e}de + \frac{\partial S}{\partial e_{ij}}de_{ij} + \frac{\partial S}{\partial T}dT \tag{A11}$$

Comparing (A10) and (A7), the partial derivatives of the Helmholtz free energy are

$$\frac{\partial F}{\partial e} = V\sigma \qquad \frac{\partial F}{\partial e_{ij}} = Vs_{ij} \qquad \text{and} \quad \frac{\partial F}{\partial T} = -S \tag{A12}$$

These relationships can be used to determine the partial derivatives of the entropy. Noting that F is a perfect differential[27-30] and

$$S = -\frac{\partial F}{\partial T}$$

the partials of S can be determined as follows:

$$\frac{\partial S}{\partial e} = -\frac{\partial}{\partial e}\frac{\partial F}{\partial T} = -\frac{\partial}{\partial T}\frac{\partial F}{\partial e} \tag{A13}$$

Moreover, from relations (A12), by assuming constant volume (small strain), and elastic constants independent of temperature,

$$\frac{\partial F}{\partial e} = V\sigma \tag{A14}$$

such that,

$$\frac{\partial S}{\partial e} = -V\frac{\partial \sigma}{\partial T} \tag{A15}$$

Using (A9a) as the functional form of σ, the partial with respect to temperature is

$$\frac{\partial \sigma}{\partial T} = -K_m\beta \tag{A16}$$

leading to

$$\frac{\partial S}{\partial e} = K_m\beta V \tag{A17}$$

In a similar manner,

$$\frac{\partial S}{\partial e_{ij}} = -V\frac{\partial s_{ij}}{\partial T} = 0 \qquad \text{(A18)}$$

The differential of heat is related to the specific heat at constant volume, and temperature through[28]

$$dQ = \rho_0 V C_v dT \qquad \text{(A19)}$$

and with entropy defined as[29]

$$TdS = dQ \qquad \text{(A20)}$$

then,

$$\frac{\partial S}{\partial T} = \frac{\rho_0 V C_v}{T} \qquad \text{(A21)}$$

Using (A17, A18 and A21) in (A11) gives an expression for the total differential of the entropy in terms of the independent variables

$$dS = \frac{\rho_0 V C_v}{T} dT + K_m \beta V de \qquad \text{(A22)}$$

Multiplying by T, and taking the rate of change of the differentials gives

$$T\dot{S} = \rho_0 V C_v \dot{T} + K_m \beta V T \dot{e} \qquad \text{(A23)}$$

Under adiabatic conditions,

$$T\dot{S} = \dot{Q} = 0.$$

Then, equation (A23) reduces to an expression for the dilatational strain rate as a function of temperature,

$$\dot{e} = -\frac{\rho_0 C_v}{K_m \beta T}\dot{T} \qquad \text{(A24)}$$

Using (A3) in (A24) gives an expression for the hydrostatic stress rate (eqn 1)

$$\dot{\sigma} = -K_m\beta\left(1 + \frac{\rho_0 C_v}{K_m \beta^2 T}\right)\dot{T}$$

This equation relates temperature changes in an elastic body to changes in the hydrostatic stress. The second term in brackets is much larger than the first, resulting in a simpler approximation that, typically, differs in value by less than 0.6%, (eqn 2)

$$\dot{\sigma} \approx -\frac{\rho_0 C_v}{\beta T}\dot{T}$$

The important assumptions that lead to this equation are: (i) a reversible process, (ii) adiabatic conditions, (iii) e, e_{ij} and T are independent variables, (iv) constant volume (small strains), and (v) the elastic constants do not change with temperature.

ACKNOWLEDGEMENTS

This research was sponsored by DARPA through the University Research Initiative program under ONR contract N-00014086-K-0753. Special thanks to the technical support staff at Pratt and Whitney, West Palm Beach, including Scott Stevens, Gene Leiske and DuWayne Brodnicky; the engineering staff: Jennifer Heine and Barrie Peters; and the management: Brad Cowles and Doug Nethaway.

LIST OF FIGURES

Figure 10. SPATE images of the SiC/CAS composite following loading to (a) 30MPa, (b) 50 MPa and (c) 90 MPa. Corresponding images with contour lines are shown in (d), (e) and (f). These images show stress redistribution due to multiple matrix cracking.

Figure 11. SPATE line scans extracted from the full field scans shown in Figure 10 graphically illustrate stress redistribution across the net section.

Figure 12. SPATE images obtained for the SiC/SiC material.

Figure 13. Overlay of line scans connecting the notches (a) as-received specimen, (b) after loading to 160MPa.

Figure 14. The unloading modulus decreases with increasing stress.[10]

Figure 15. A gradient in modulus E(x) results in stress redistribution ahead of a notch.

REFERENCES

1. A. G. Evans, F. W. Zok and T. J. Mackin, " The Mechanical Performance of Ceramic-Matrix Composites," to be published.

2. F. E. Heredia, S. M. Spearing, M. Y. He, T. J. Mackin, A. G. Evans, P. Mosher, and P. Bronsted, "Notch Effects in Carbon Matrix Composites," J. Amer Cer Soc, in press.

3. C. Cady, T. J. Mackin and A. G. Evans, "Stress Redistribution and Notch Insensitivity in a Ceramic Matrix Composite," J. Amer Cer Soc, to be published.

4. S. Mall, D. E. Bullock and J. J. Pernot, "Tensile Fracture Behavior of Fiber Reinforced Ceramic Matrix Composites with Holes," to be published.

5. A. G. Evans, "The Mechanical Performance of Reinforced Ceramic, Metal and Intermetallic Matrix Composites," Mat Sci and Eng., A 143, pp. 63-76, 1991.

6. J. W. Hutchinson and H. M. Jensen, "Models of Fiber Debonding and Pullout in Brittle Composites with Friction," Mechs of Materials, 9, 139-63, 1990.

7. D. B. Marshall, "Analysis of Fiber Debonding and Sliding Experiments in Brittle Matrix Composites," Acta Metall. Mater. Vol 40, No. 3, pp. 427-441, 1992.

8. M. D. Thouless, O. Szaibero, L. S. Sigl, and A. G. Evans, J Amer Cer Soc, 72, pp. 525-532, 1989.

9. W. A. Curtin, "Theory of Mechanical Properties of Ceramic Matrix Composites," J Am. Ceram Soc., 74, pp. 2837-45, 1991.

10. A. G. Evans, J. M Domerque and E. Vagaggini, "A Methodology for Relating Macroscopic Behavior of Ceramic Matrix Composites to Constitutive Properties," J Amer Cer Soc, to be published.

11. G. Bao and Z. Suo, "Remarks on Crack-Bridging Concepts," in Micromechanical Modelling of Quasi-Brittle Materials Behavior, edited by V. V. Li, Appl Mech. Rev., Vol 45, No. 8., pp. 355-365, August, 1992.

12. Z. Suo, S. Ho and X. Gong, "Notch Ductile-to Brittle Transition Due to Localized Inelastic Band," J. Mat. Engr. Tech., in press.

13. S. M. Spearing, P. W. R. Beaumont, and M. F. Ashby, "Fatigue Damage Mechanics of Notched Graphite-Epoxy Laminates," in Composite Materials: Fatigue and Fracture, ASTM STP 1110, edited by T. K. O'Brien, pp. 596-616, 1991.

14. P Bronsted, F. E. Heredia and A. G. Evans, "The In-Plane Shear Properties of 2-D Ceramic Matrix Composites," J. Amer Cer Soc, in press

15. W. W. Stinchcomb and C. E. Bakis, "Fatigue Behavior of Composite Laminates," Fatigue of Composite Materials, Edited by K. L. Reifsnider, Elsevier Science Publishers B.V., pp. 105-180, 1990.

16. K. L. Reifsnider and C. E. Bakis, "Adiabatic Thermography of Composite Materials," Characterization of Advanced Materials, Edited by W. Altergott and E. Henneke, Plenum Press, New York, pp. 65-76, 1991.

17. K. L. Reifsnider, W. W. Stinchcomb, C. E. Bakis, and R. Y. Yih, " The Mechanics of Micro-Damage in Notched Composite Laminates," Damage Mechanics in Composites - AD-Vol. 12, Edited by A. S. D. Wang and G. K. Haritos, ASM, New York, pp. 65-72, 1987.

18. C. E. Bakis, R. A. Simonds, L. W. Vick, and W. W. Stinchcomb, "Matrix Toughness, Long-Term Behavior, and Damage Tolerance of Notched Graphite Fiber-Reinforced Composite Materials, " ASTM STP 1059, pp. 349-370, 1990.

19. C. E. Bakis and K. L. Reifsnider, "Nondestructive Evaluation of Fiber Composite Laminates by Thermoelastic Emission," Review of Progress in Quantitative Nondestructive Evaluation, Vol. 7B, Edited by D. O. Thompson and D. E. Chimend, Plenum Publishing Corp., pp. 1109-1116, 1988.

20. C. E. Bakis, H. R. Yih, W. W. Stinchcomb, and K. L. Reifsnider, "Damage Initiation and Growth in Notched Laminates Under Reversed Cyclic Loading," ASTM STP 1012, pp. 66-83, 1989.

21. R. A. Simonds, C. E. Bakis, and W. W. Stinchcomb, "Effects of Matrix Toughness on Fatigue Response of Graphite Fiber Composite Laminates, ASTM STP 1012, pp. 5-18, 1989.

22. D. S. Beyerle, S. M. Spearing, F. W. Zok, and A. G. Evans, "Damage and Failure in Unidirectional Ceramic-Matrix Composites," J. Am. Ceram. Soc. 75[10] 2719-25 (1992).

23. N. F. Enke, "Thermographic Stress Analysis of Isotropic Materials," Ph. D. Thesis, Department of Engineering Mechanics, The University of Wisconsin-Madison, 1989.

24. Thermoelastic Stress Analysis, N. Harwood and W. M. Cummings, Adam Hilger, IOP publishing, 1991.

25. A. K. Wong, J. G. Sparrow, and S. A. Dunn, "On The Revised Theory of the Thermoelastic Effect," J. Phys. Chem. Solids Vol. 49, No. 4, pp. 395-400, 1988.

26. A. K. Wong, R. Jones and J. G. Sparrow, "Thermoelastic Constant of Thermoelastic Parameter?" Phys. Chem. Solids Vol. 48, No. 8, pp. 749-753, 1987.

27. B. Budiansky and R. J. O'Connell, "Bulk Thermoelastic Attenuation of Composite Materials," J. Geophysical Research, Vol. 88, No. B12, pp. 10,343-10,348, December 10, 1983.

28. B. Budiansky, "Thermal and Thermoelastic Properties of Isotropic Composites," J. Comp. Materials, Vol. 4, pp. 286-295, July 1970.

29. Heat and Thermodynamics, M. W. Zymansky, 5th Edition, McGraw-Hill, 1968.

30. Equilibrium Statistical Mechanics, E. A. Jackson, Prentice-Hall International Series in Engineering of the Physical Sciences, 1968.

31. D. Zhang and B. I. Sandor, "Thermographic Analysis of Stress Concentrations in a Composite," Experimental Mechanics, pp. 121-125, June 1989.

32. D. Zhang, N. F. Enke, and B. I. Sandor, "Thermographic Stress Analysis of Composite Materials," accepted for publication in Experimental Mechanics, June 1989.

33. R. Jones, M. Heller, D. Lombardo, S. Dunn, J. Paul and D. Saunders, "Thermoelastic Assessment of Damage Growth in Composites," Composite Structures, 12, pp. 291-314, 1989.

Class I

Matrix Cracking + Fiber Failure

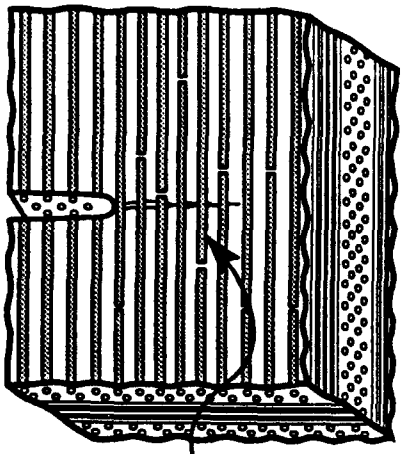

Pull-Out Tractions
Redistribute Stress

Class II

Matrix Cracking: No Fiber Failure

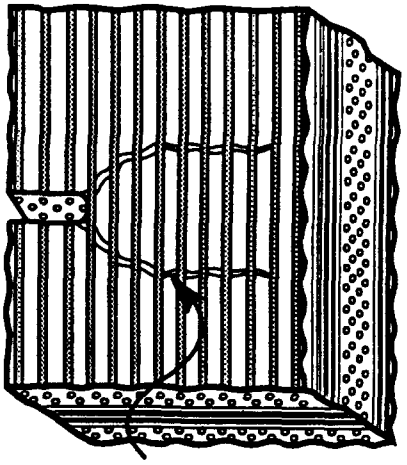

Matrix Cracks
Redistribute Stress

Class III

Shear Damage By Matrix Cracking

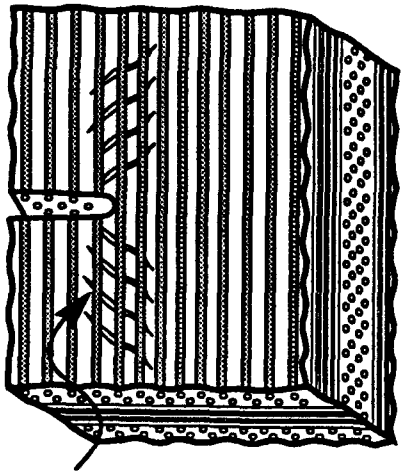

Shear Damage Zone
Redistributes Stress

Figure 1

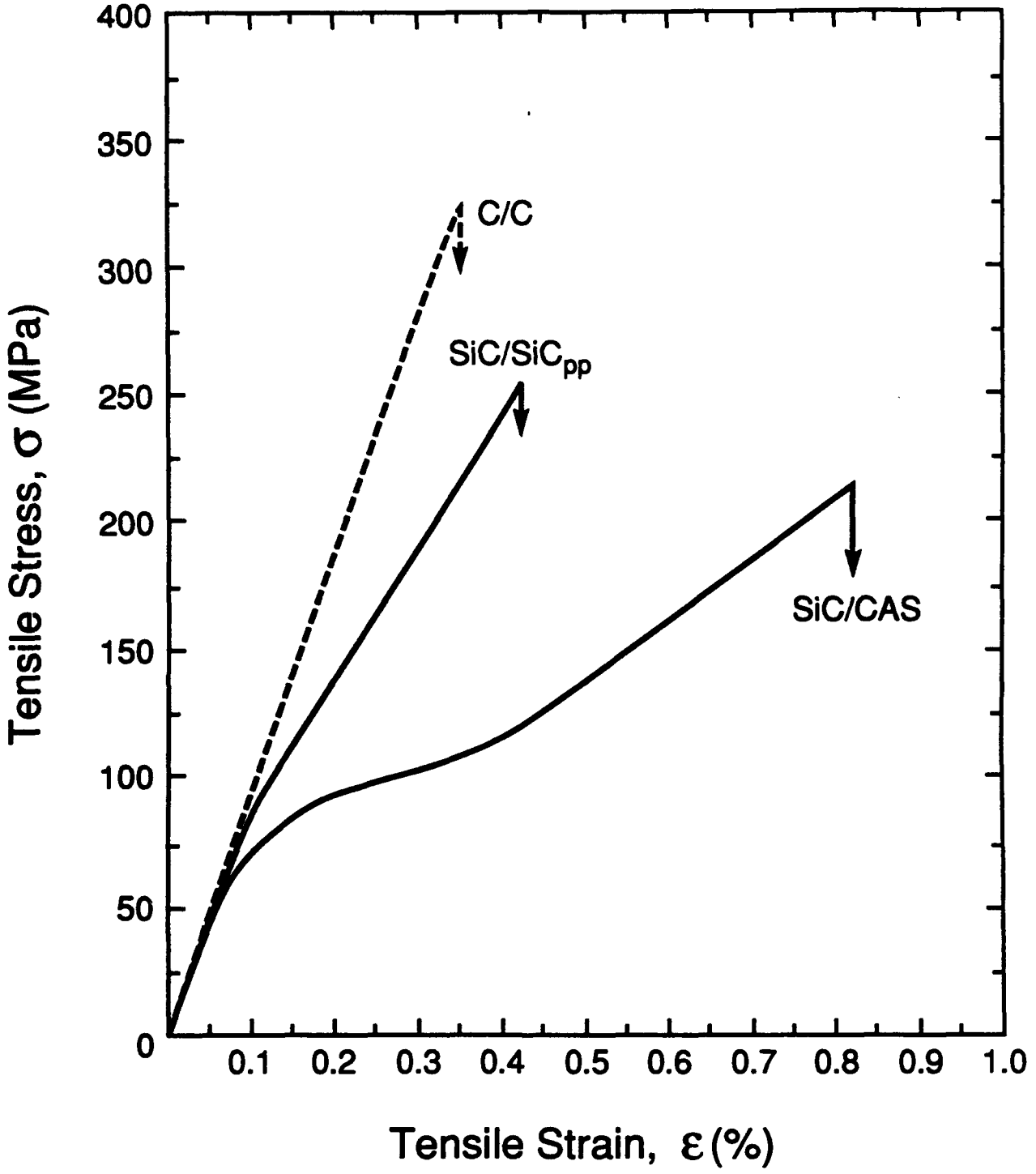
400
350
300
250
200
150
100
50
0
Tensile Stress, σ (MPa)
C/C
SiC/SiCpp
SiC/CAS
0.1
0.2
0.3
0.4
0.5
0.6
0.7
0.8
0.9
1.0
Tensile Strain, ε (%)

Figure 2a

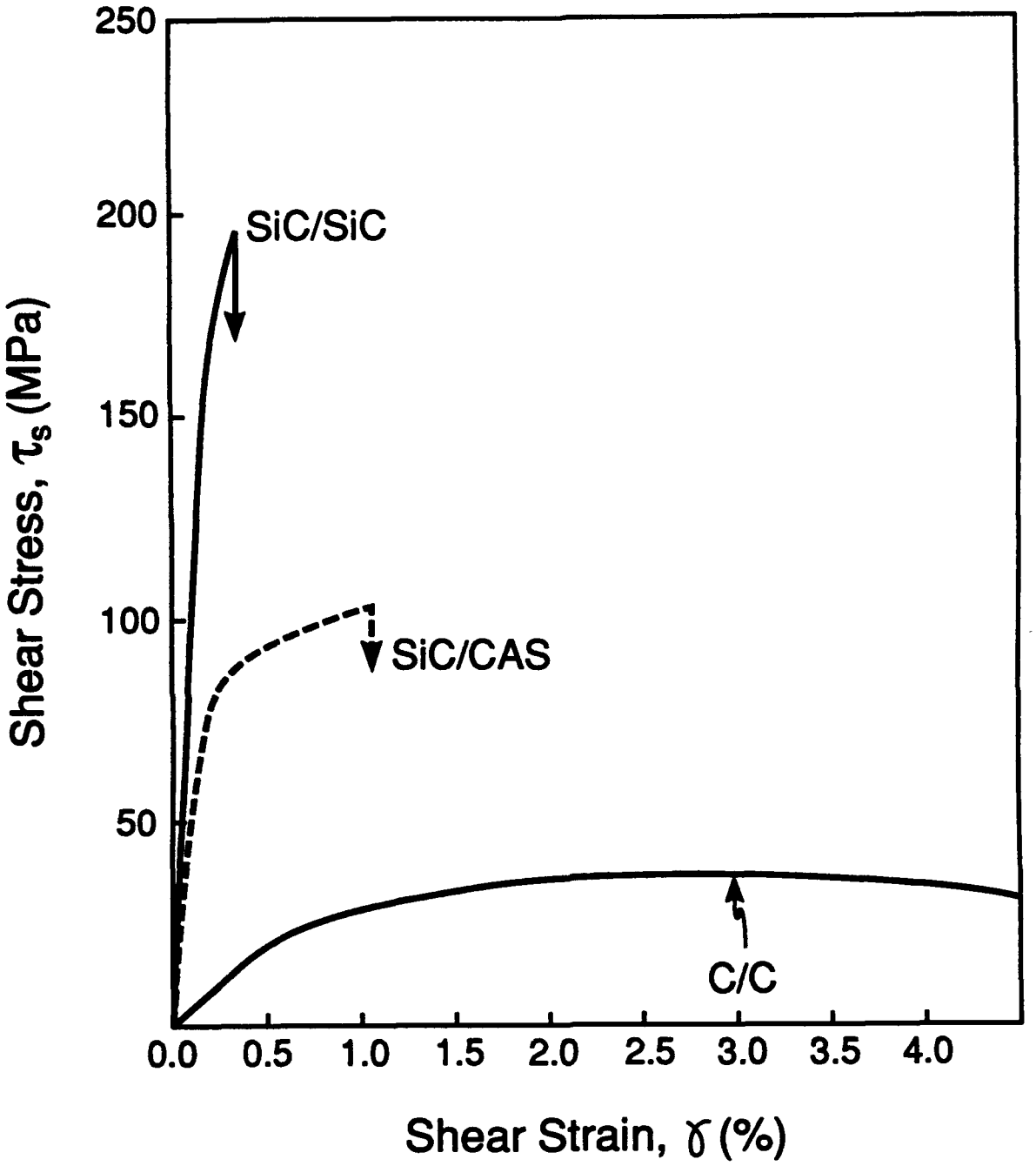
250
200
150
100
50
SiC/SiC
SiC/CAS
C/C
Shear Stress, τ_s (MPa)
0.0
0.5
1.0
1.5
2.0
2.5
3.0
3.5
4.0
Shear Strain, γ (%)

Figure 2b

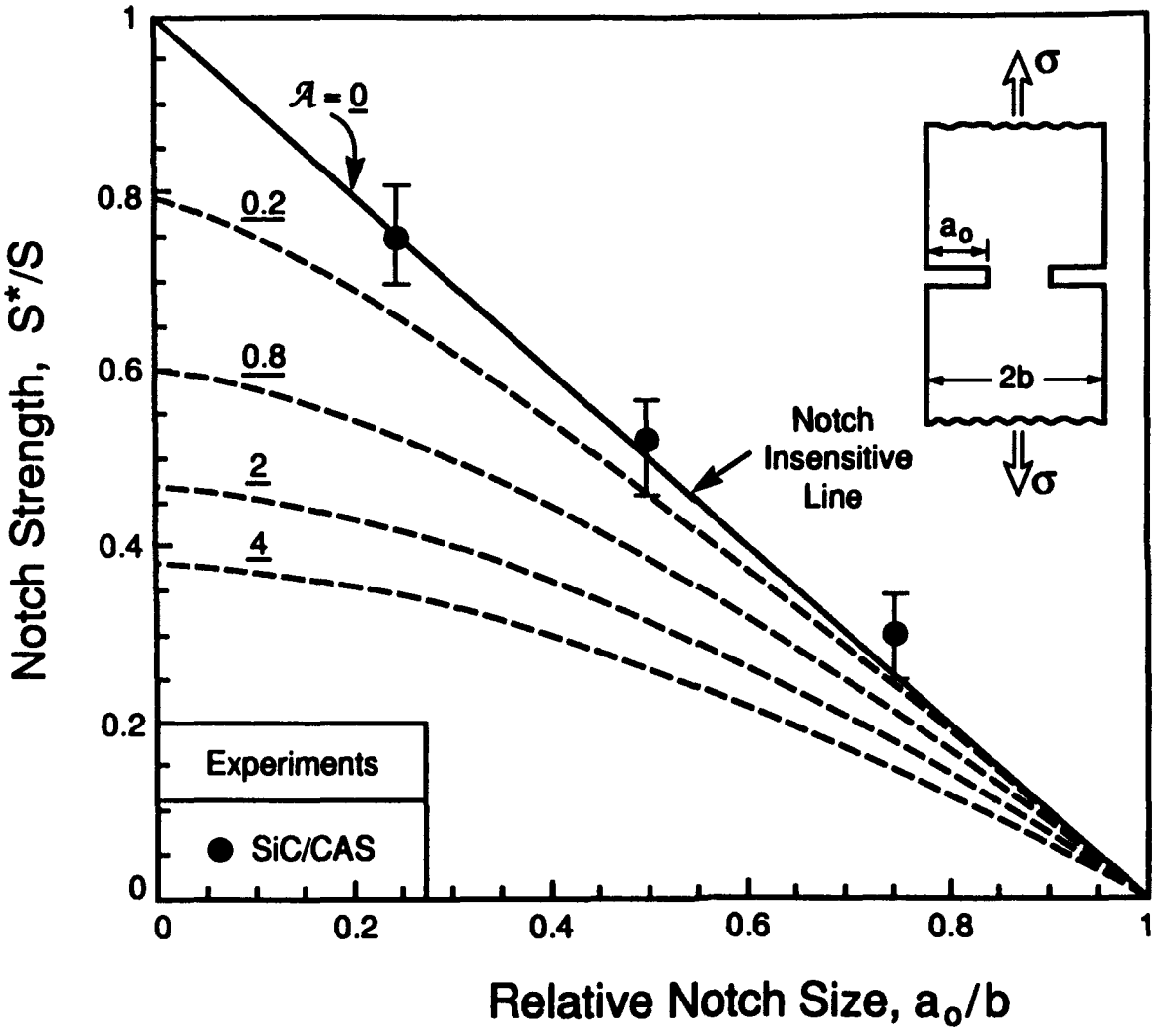
Notch Strength, S*/S
Relative Notch Size, a_o/b
$\mathcal{A} = 0$
0.2
0.8
2
4
Notch Insensitive Line
Experiments
SiC/CAS
a_o
2b
σ
σ
0
0.2
0.4
0.6
0.8
1

Figure 3

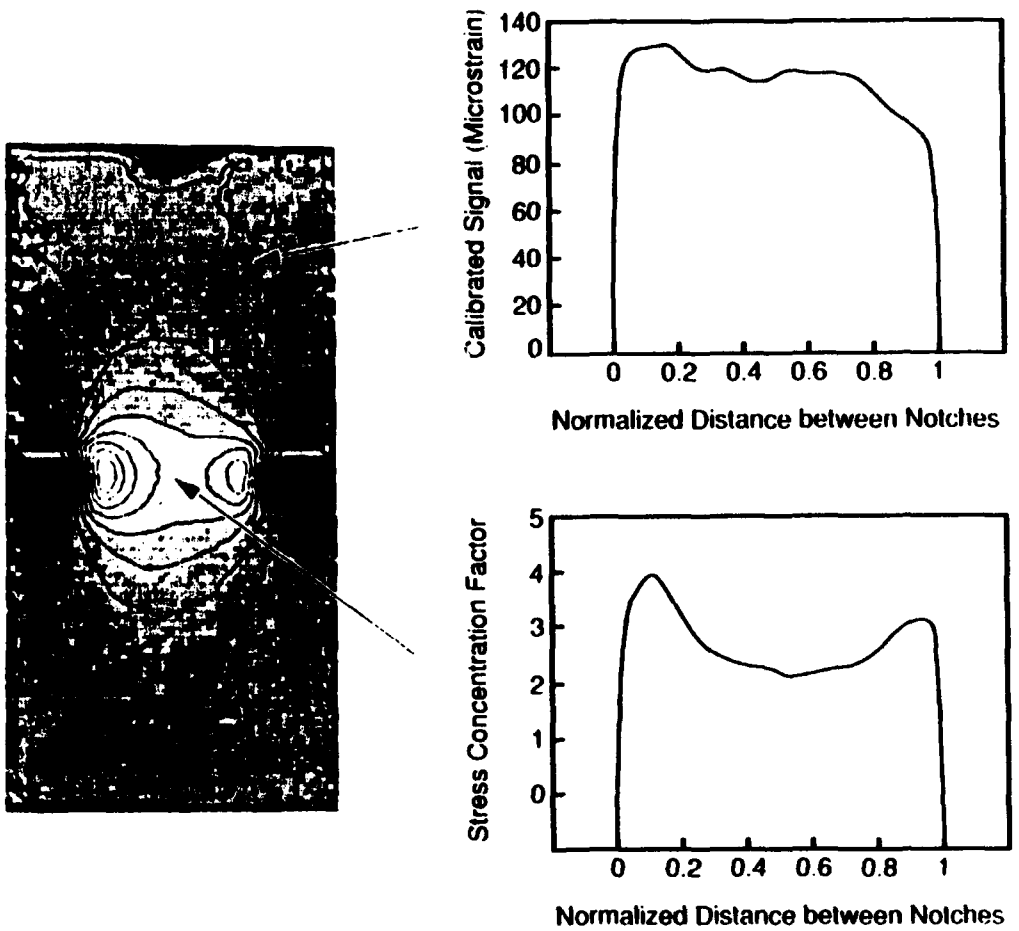
Calibrated Signal (Microstrain)
140
120
100
80
60
40
20
0
0 0.2 0.4 0.6 0.8 1
Normalized Distance between Notches
Stress Concentration Factor
5
4
3
2
1
0
0 0.2 0.4 0.6 0.8 1
Normalized Distance between Notches

Figure 4

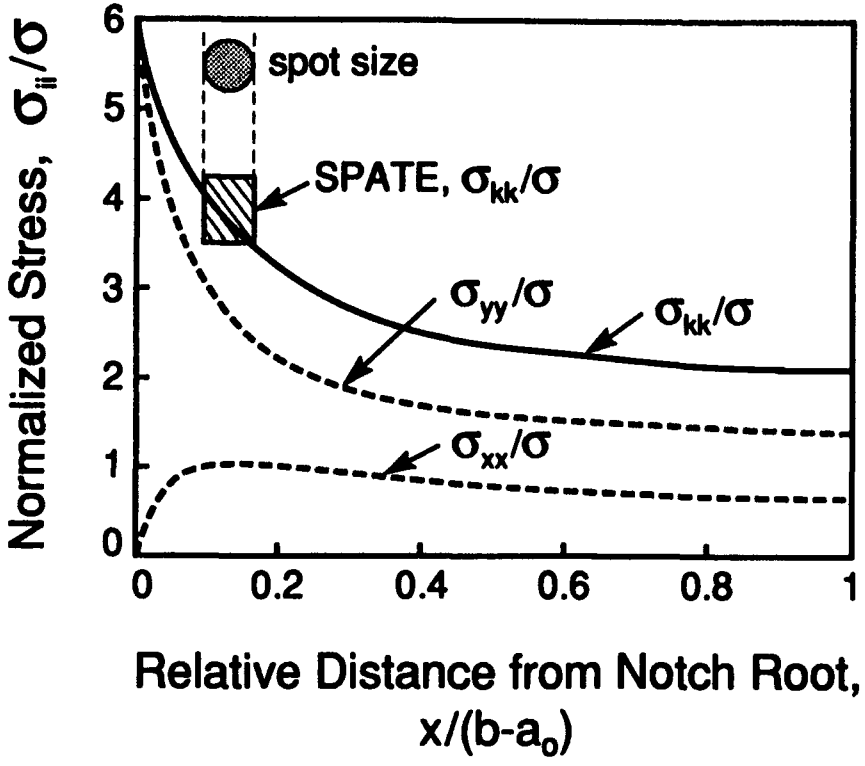
Normalized Stress, σ_{ii}/σ
6
5
4
3
2
1
0
spot size
SPATE, σ_{kk}/σ
σ_{yy}/σ
σ_{kk}/σ
σ_{xx}/σ
0
0.2
0.4
0.6
0.8
1
Relative Distance from Notch Root,
$x/(b-a_o)$

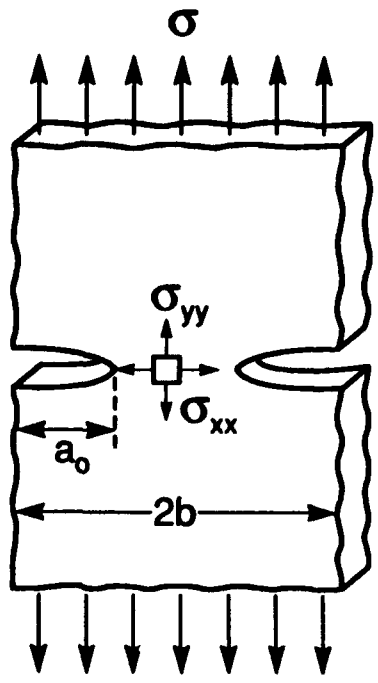
σ
σ_{yy}
σ_{xx}
a_o
2b

Figure 5

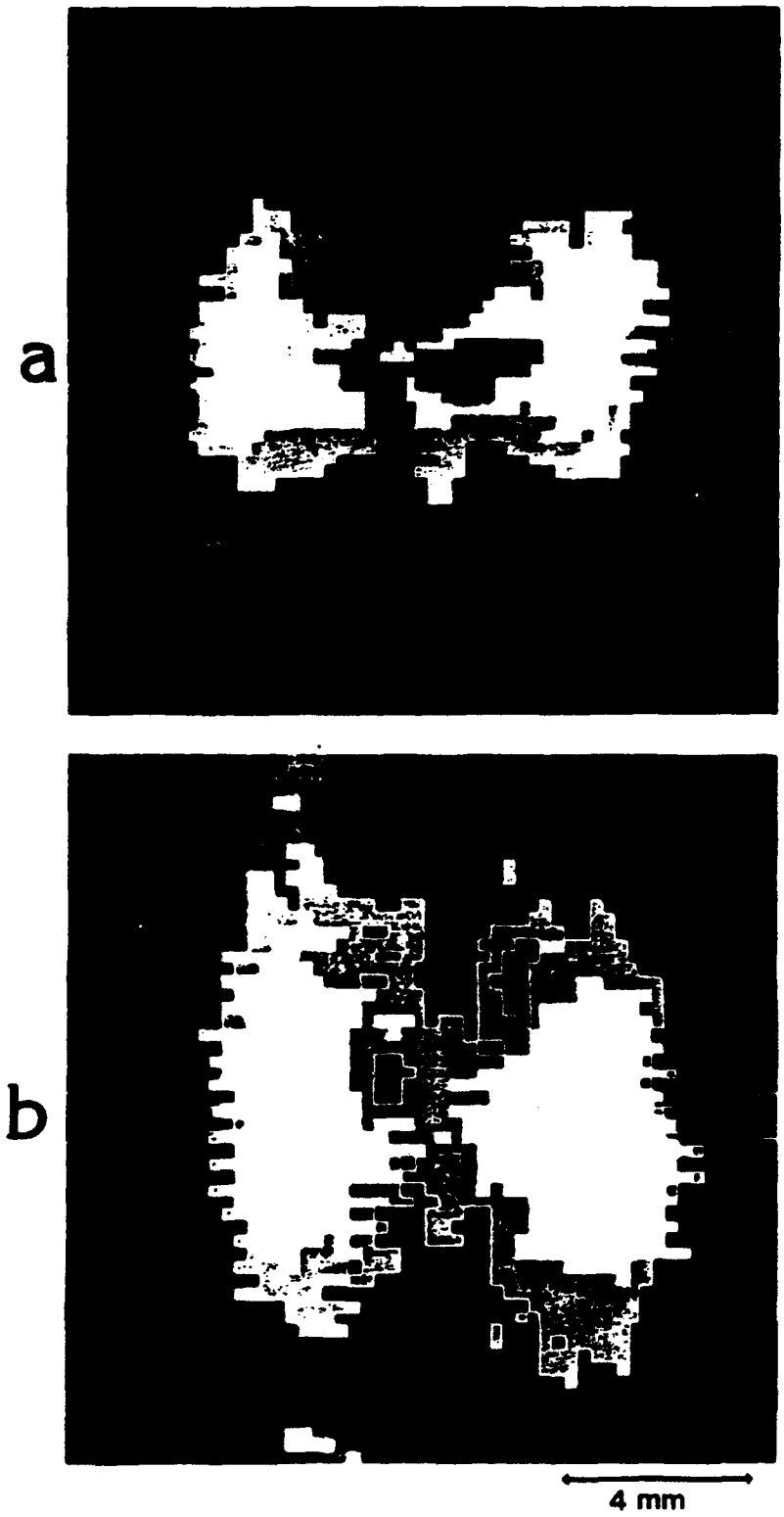

Figure 6

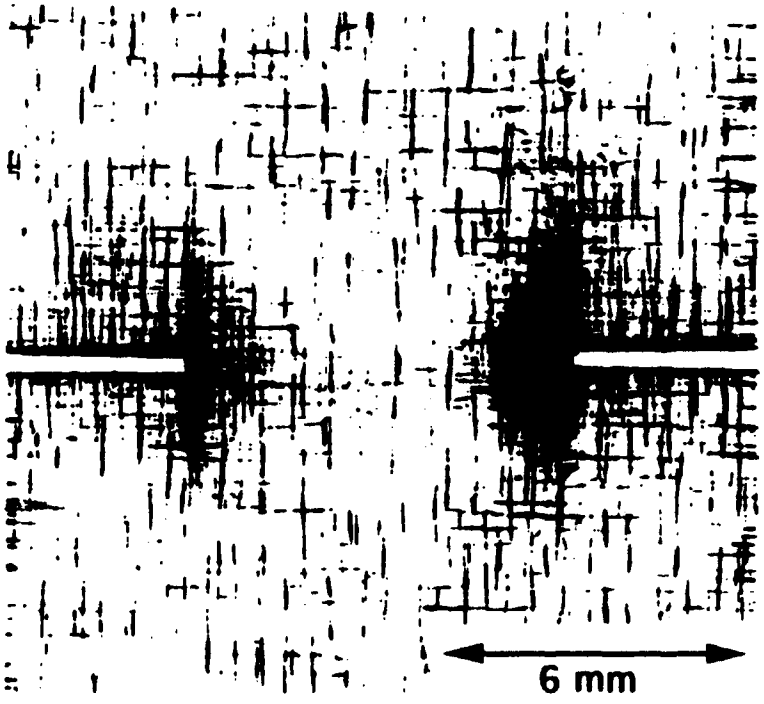

Figure 6c

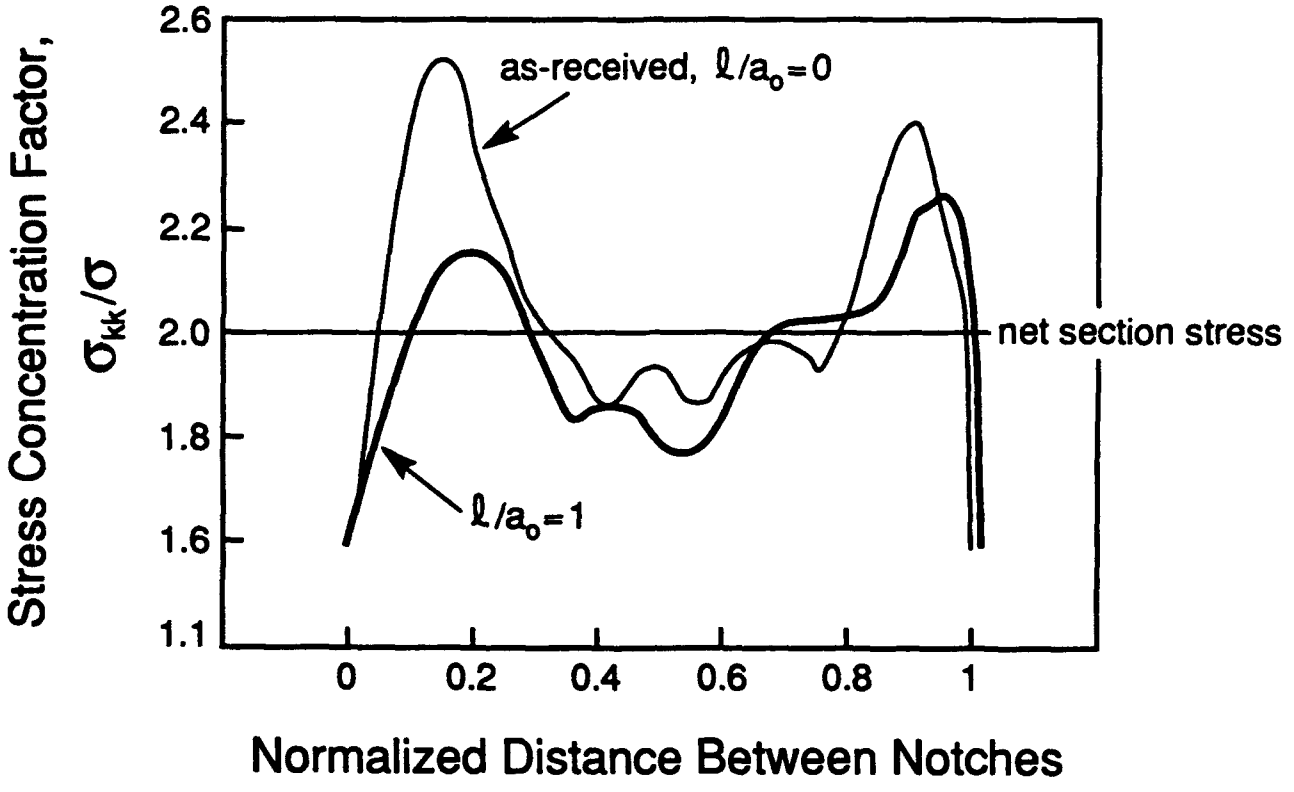
Stress Concentration Factor, σ_{kk}/σ
2.6
2.4
2.2
2.0
1.8
1.6
1.1
as-received, $\ell/a_o=0$
net section stress
$\ell/a_o=1$
0
0.2
0.4
0.6
0.8
1
Normalized Distance Between Notches

Figure 7

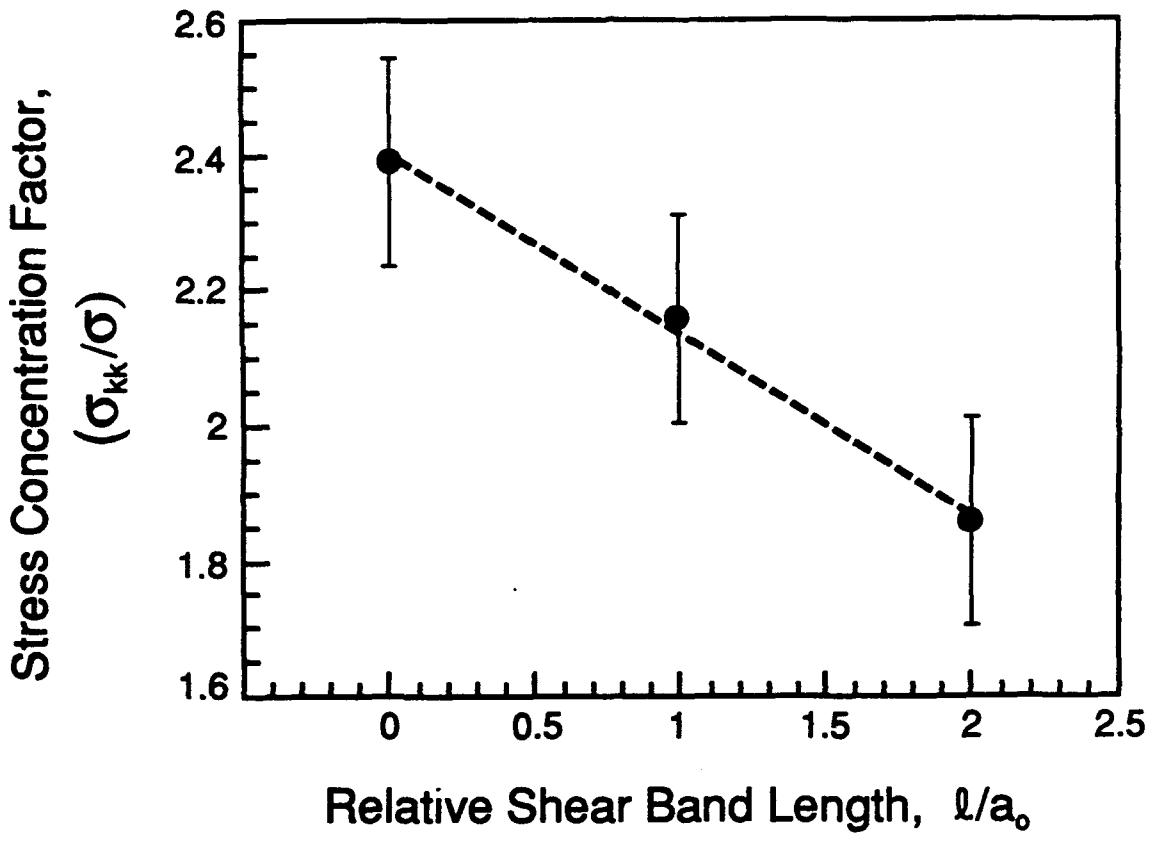
Stress Concentration Factor,
(σ_{kk}/σ)
2.6
2.4
2.2
2
1.8
1.6
0
0.5
1
1.5
2
2.5
Relative Shear Band Length, ℓ/a_o

Figure 8

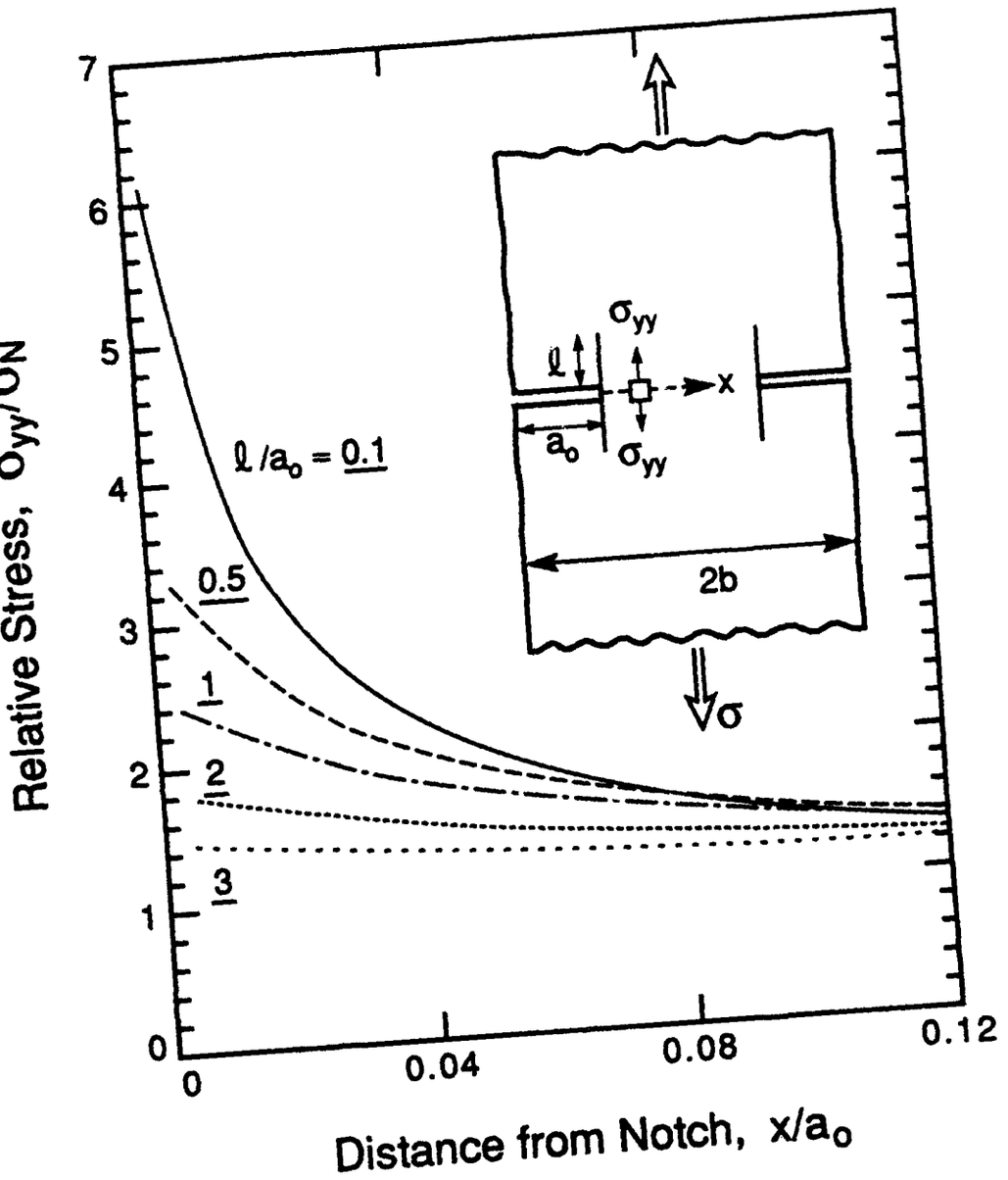
Relative Stress, σ_{yy}/σ_N
Distance from Notch, x/a_o
$\ell/a_o = 0.1$
0.5
1
2
3
σ_{yy}
ℓ
x
a_o
σ_{yy}
2b
σ
0
1
2
3
4
5
6
7
0
0.04
0.08
0.12

Figure 9

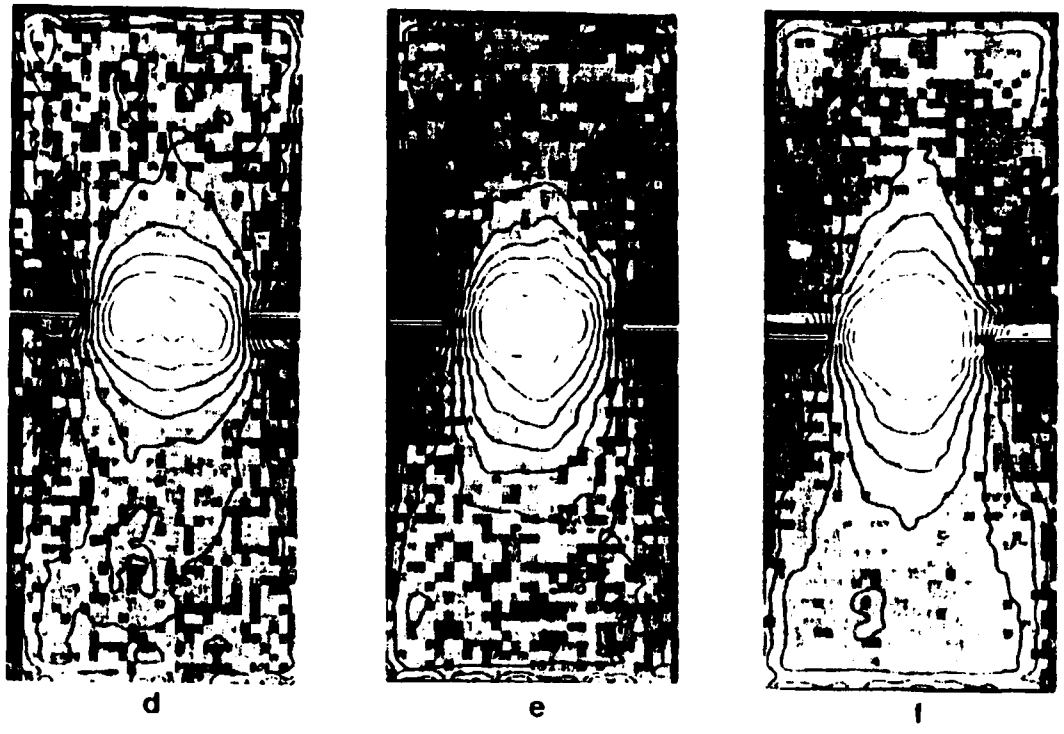

Figure 10

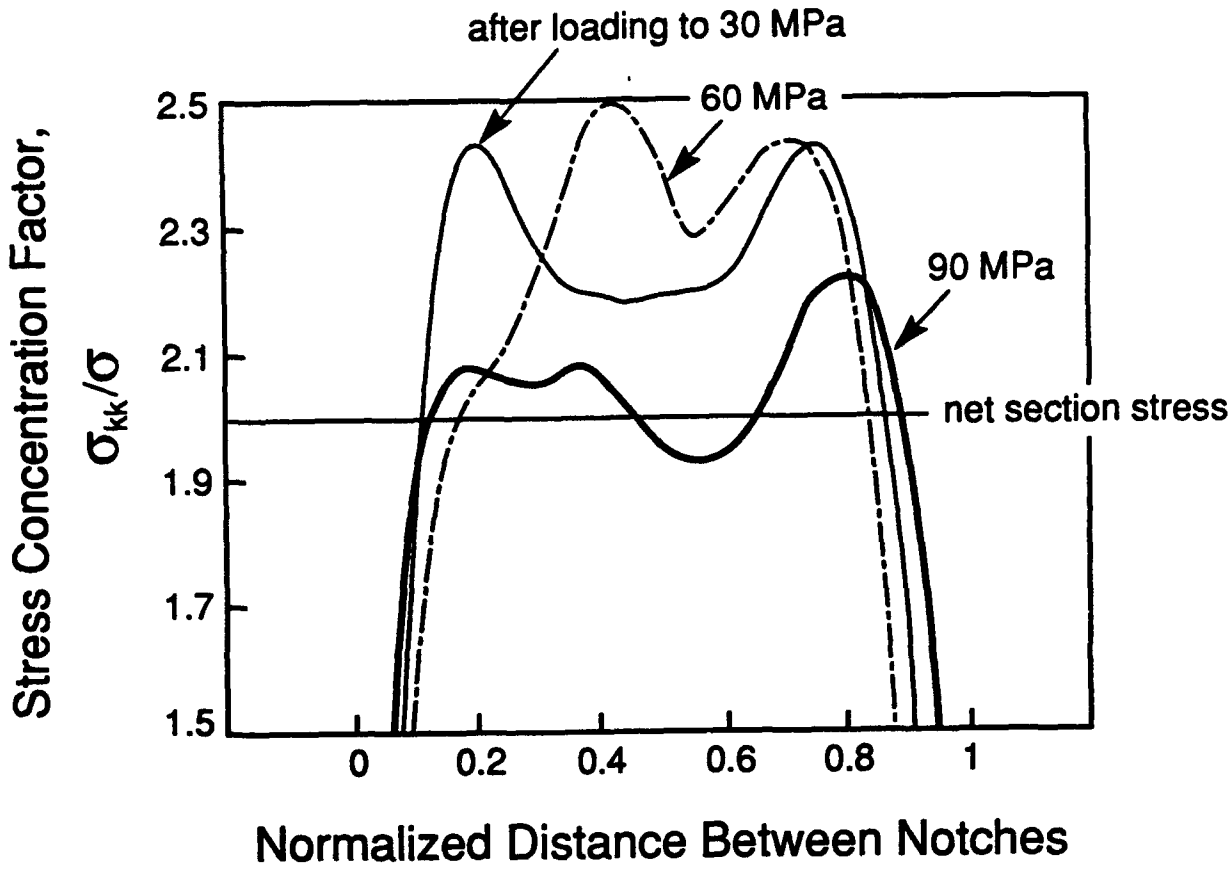
after loading to 30 MPa
60 MPa
90 MPa
net section stress
Stress Concentration Factor, σ_{kk}/σ
2.5
2.3
2.1
1.9
1.7
1.5
0
0.2
0.4
0.6
0.8
1
Normalized Distance Between Notches

Figure 11

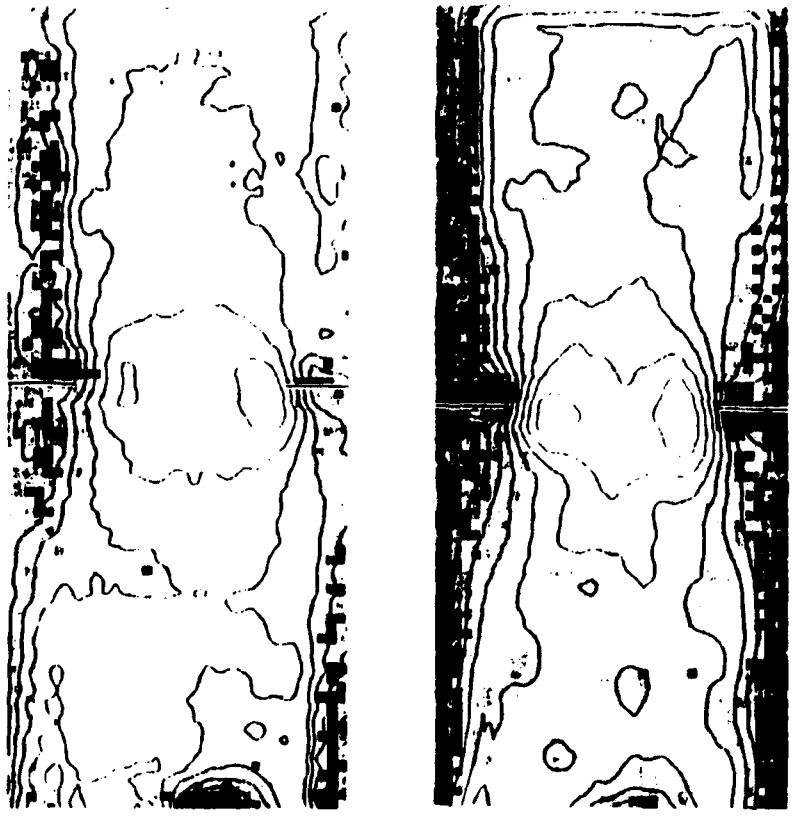

Figure 12

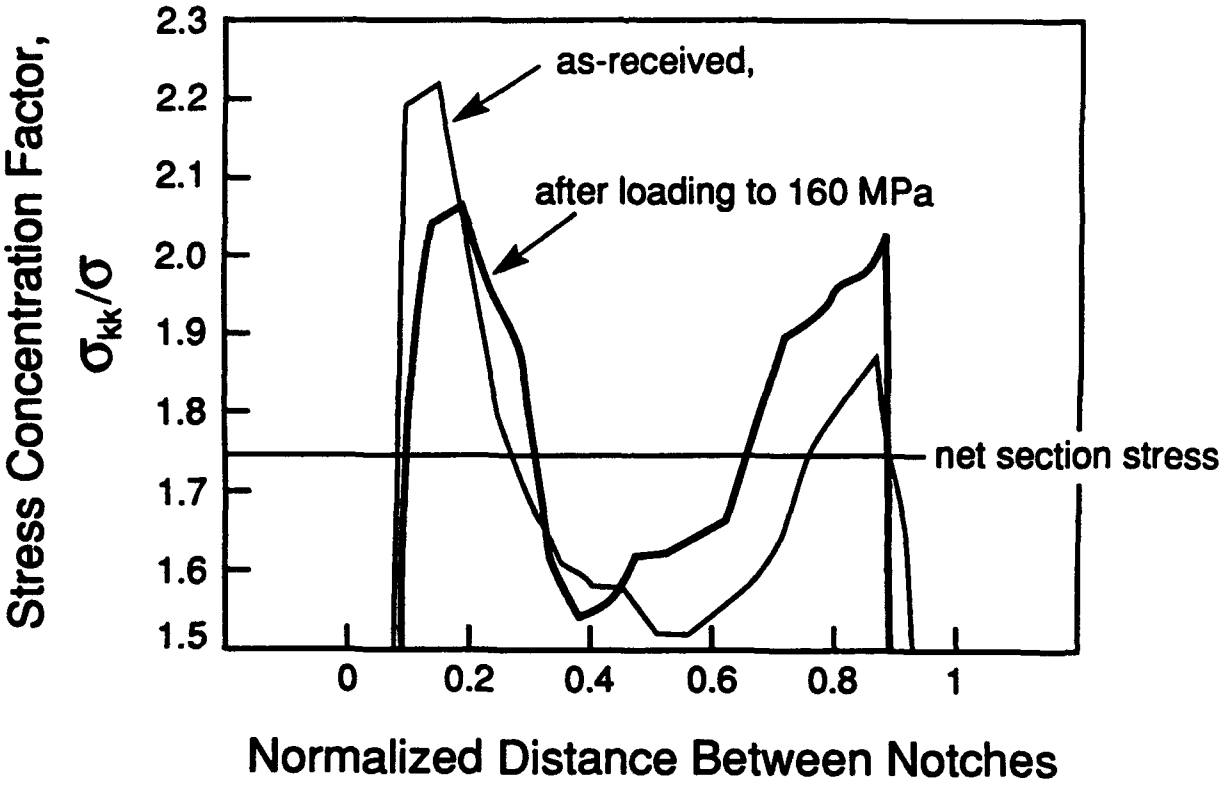
Stress Concentration Factor, σ_{kk}/σ
2.3
2.2
2.1
2.0
1.9
1.8
1.7
1.6
1.5
as-received,
after loading to 160 MPa
net section stress
0
0.2
0.4
0.6
0.8
1
Normalized Distance Between Notches

Figure 13

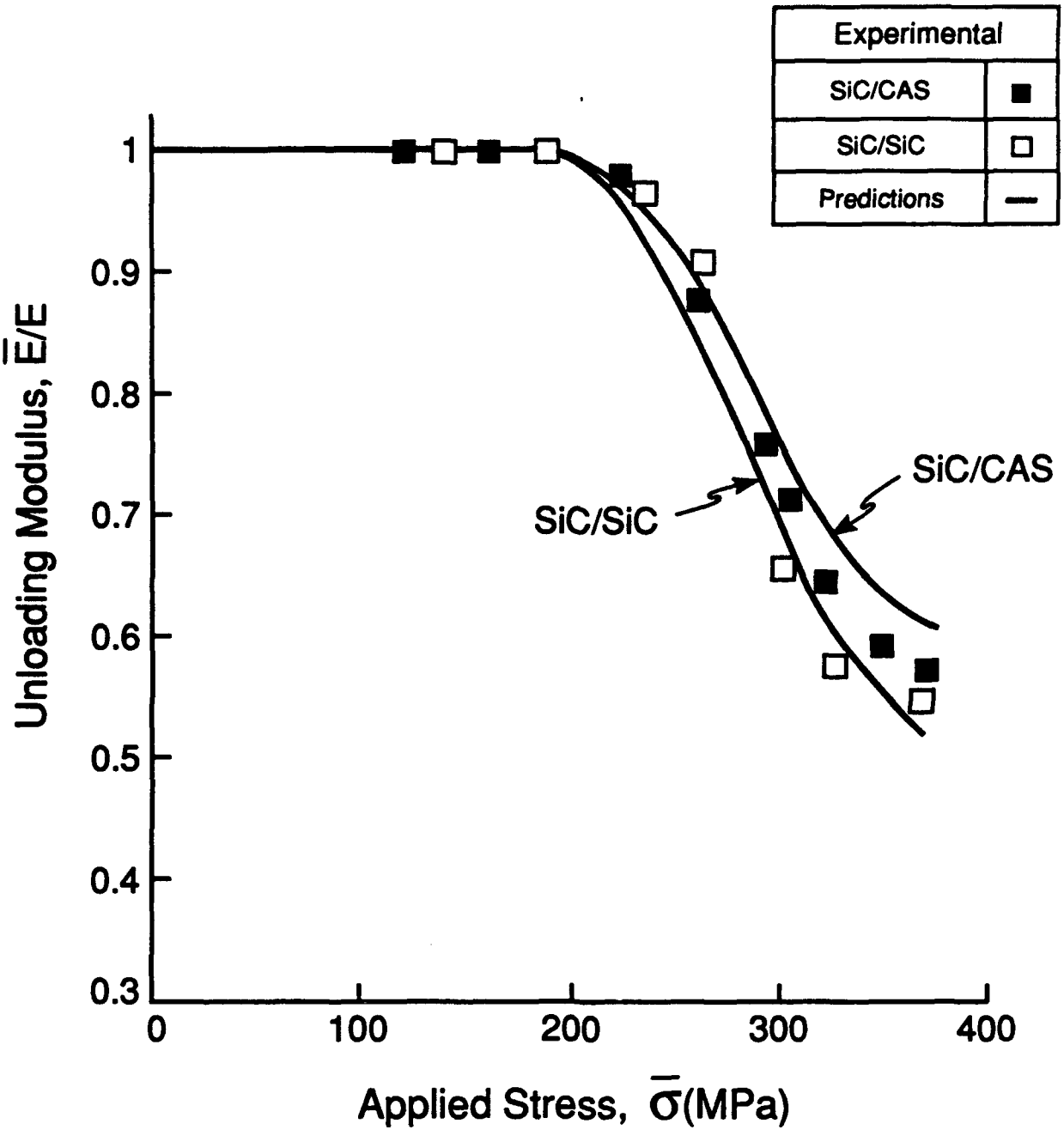
Experimental
SiC/CAS
SiC/SiC
Predictions
Unloading Modulus, $\bar{E}/E$
1
0.9
0.8
0.7
0.6
0.5
0.4
0.3
0
100
200
300
400
SiC/SiC
SiC/CAS
Applied Stress, $\bar{\sigma}$(MPa)

Figure 14

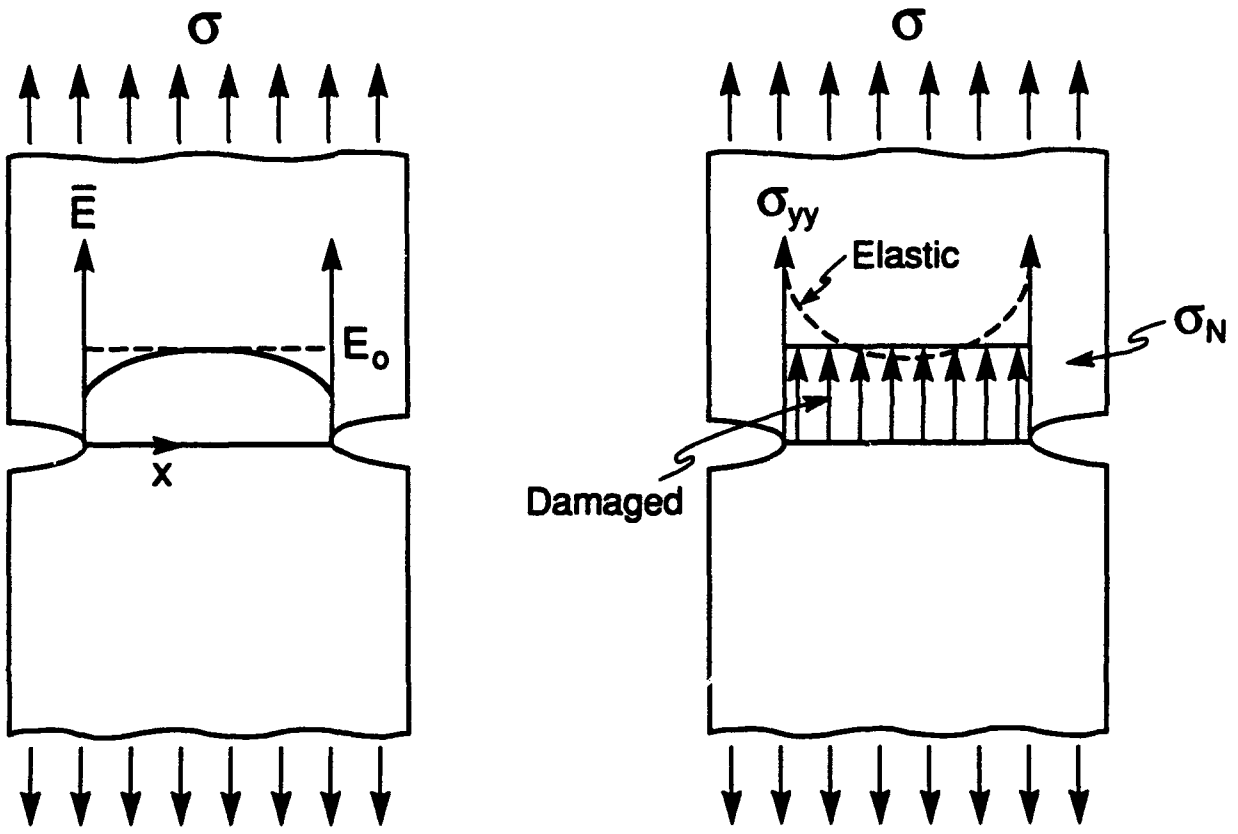

a) Modulus Distribution, $\bar{E}(x)$

b) Stress Distribution, $\sigma_{yy}(x)$

Figure 15

NOTCH-SENSITIVITY AND SHEAR BANDS IN BRITTLE MATRIX COMPOSITES

M.-Y. HE, B. WU AND Z. SUO

Mechanical and Environmental Engineering Department

University of California

Santa Barbara, CA 93106-5070

Submitted to *Acta Met. Mater.* June 1993

Revised January 1994

Abstract—Matrix cracking, fiber breaking and interface sliding cause nonlinear deformation in fiber-reinforced brittle matrix composites. When a notched sample is loaded in tension, the nonlinear deformation usually localizes around the notch, spreads the stress in the ligament more evenly, and thereby leads to a higher fracture load. We simulate the interplay of two deformation mechanisms: a tensile band ahead of, and shear bands perpendicular to, a notch. The shear deformation evens out the stress distribution in the tensile band, and the strength of the tensile band sets the extent of the shear deformation. Each band is simulated by a traction-deformation law. The work of fracture is computed from a small-scale inelastic problem, and the fracture loads of notched samples from a large-scale inelastic problem. Several important conclusions emerge from the simulation. First, weak shear bands can substantially increase the work of fracture. Second, the fracture loads of notched samples are well correlated with the unnotched strength, work of fracture and notch size, by a formula independent of the shear band description. The results of the simulation are used to explain the available experimental data, and to suggest an evaluation procedure for notch-sensitivity.

1. INTRODUCTION

Compared to ductile alloys, fiber-reinforced brittle matrix composites fracture at small strains, being limited by fiber breaking strains. Yet stresses around notches in such composites can be reduced by *localized deformation*. Three deformation mechanisms have been identified [1-4]: i) multiple matrix cracks with no fiber breaking, ii) a tensile band consisting of broken fibers pulling out from the matrix against friction, and iii) shear bands consisting of matrix microcracking and fiber bending. In this paper, we simulate the interplay of the tensile and the shear bands, and explore features in the results that simplify mechanical evaluation of these composites.

The simulation is motivated by recent experiments on carbon matrix composites [3,4] Figure 1 illustrates a notched sample loaded in tension, with shear bands extending perpendicular

to the notch prior to fracture. The bands consist of microcracks in the matrix and bending of the fiber bundles. General fracture breaks the ligament ahead of the notch. Visible on a fracture surface are broken fibers and damaged matrix. For a given composite with a range of notched sample geometry and size, fracture loads are found to be well correlated by a toughness value K_c (about 15 MPa $m^{1/2}$ for a carbon matrix composite tested in [3]).

The conclusion of these experiments is better appreciated as follows. Consider a specimen containing a notch of length $2a$, which is small compared to the specimen width, subjected to remote stress $\bar{\sigma}$. Denote $\bar{\sigma}_{max}$ as the stress that causes the specimen to fracture, and evaluate the "toughness" according to $K_c = \bar{\sigma}_{max}\sqrt{\pi a}$. Repeat the experiment for several specimens of different notch sizes. Although the fracture load $\bar{\sigma}_{max}$ decreases as the notch size increases, K_c is found to be nearly independent of the notch size. The applicability of Linear Elastic Fracture Mechanics is puzzling in this case because the specimens at the onset of fracture have large inelastic zones. In particular, the height of the shear bands often exceeds the notch size. Our simulation will resolve this paradox.

Shear bands in polymer and metal matrix composites have been modeled by various authors [5-7]. In this paper, the tensile fracture process is modeled by a traction-deformation law, Fig. 1, which is more appropriate when fiber pullout significantly contributes to fracture resistance. The near-notch shear bands do not cause fracture, but increase the tensile fracture load. The shear bands redistribute the stress in the tensile band, but do not change the bridging law.

2. THE MECHANICS MODEL

General conditions under which composites develop near-notch shear bands remain unclear. Shear bands are usually observed in a composite having higher failure strain in the matrix than in the fibers, e.g. in certain carbon, polymer and metal matrix composites. Presumably multiple matrix cracks ahead the notches are suppressed, and the shear bands set in

as an alternative deformation mechanism. Depending on matrix material, either microcracking or plastic flow facilitates the shear deformation. Shear bands have been observed in unidirectional, woven and cross-ply composites.

The crack-bridging model has been applied to any composite in which the matrix fractures before the fibers. However, in composites having larger matrix failure-strains the matrix fails after the fibers. In many such materials, the complicated deformation process—fiber breaking and matrix tearing—is still localized in the vicinity of the fracture plane, and the material a small distance away from the fracture plane remains undamaged and deforms elastically. Consequently, the deformation process can still be simulated by a nonlinear traction-deformation law. In the following, the relevant results of the tensile bands without shear bands are summarized.

2.1 *Previous Results on a Tensile Band*

A tensile band is represented by a continuous array of nonlinear springs obeying a relation between the tensile stress σ and the deformation δ:

$$\sigma / \sigma_0 = \chi(\delta / \delta_0). \tag{1}$$

Here σ_0 is the bridging strength, and δ_0 the limiting deformation beyond which stress vanishes. The sample is elastic outside the band; δ is defined as the *excess deformation* in addition to the elastic deformation of the composite. The dimensionless function χ describes the shape of the curve, rising when δ is small, reaching the peak and then softening (inset of Fig. 1). The stress is assumed to be bounded everywhere in the sample, i.e. the fracture toughness at the tip of the tensile band is ignored. The simplification is justified if the crack tip toughness is small compared to the fracture resistance due to the bridging, which is usually the case for ceramic matrix composites.

The bridging law has been deduced from the properties of the fiber, matrix and interface for composites where matrix fractures before fibers [8,9]. Composites having higher matrix

failure-strains are less studied, but important features can be inferred. The bridging strength σ_0 must be the volume-fraction average of the matrix and fiber strengths. The fiber strength dispersion and the interface sliding resistance [10,11] remains to be important, because they govern the thickness of the deformation band, which in turn governs the limiting deformation δ_0. In this paper, relation (1) is prescribed as a part of the constitutive description of the material.

Consider an unnotched sample subjected to a deformation-controlled load. The sample is simulated by two blocks connected by an array of springs that represent the tensile band. The two blocks deform elastically, and the springs deform uniformly according to (1). The peak load is reached at σ_0. After the peak load, the band continues to deform as the two blocks elastically unload. The sample fractures when δ reaches δ_0, and the stress vanishes everywhere. During such a stress history, the two elastic blocks return to their original states, so that the work by the external load up to fracture is solely consumed by the tensile band. Thus, the work per unit area of the tensile band is

$$\Gamma_0 = \int_0^{\delta_0} \sigma \mathrm{d}\delta = \sigma_0 \delta_0 \int_0^1 \chi(\xi) \mathrm{d}\xi \,. \tag{2}$$

This *work of fracture* of the springs scales with both the bridging strength and the limiting separation.

Next consider an infinite sample containing a semi-infinite notch. The two blocks are now connected by the nonlinear springs ahead the notch, but the notch faces are free of traction. Remote from the notch tip and the tensile band, the stress field is unaffected by the nonlinear springs, and is therefore identical to the stress field around a sharp crack tip in a purely elastic block. That is, the remote stress field scales as $r^{-1/2}$, with r being the distance from the notch tip. The amplitude of the remote stress field is given by the stress intensity factor K. Of course, the stress field near the notch tip is nonsingular. The energy released when the notch extends a unit distance is given by Γ_0 [12], and the critical K_c for fracture is related to Γ_0 by $\Gamma_0 = K_c^2 / E$. Here E is Young's modulus of the elastic blocks, assuming, for simplicity, that the blocks are isotropic.

Now consider an infinite sample containing a finite notch of length $2a$, subjected to remote stress $\bar{\sigma}$; see Fig. 2, the inset at the upper right corner. If the notch size is sufficiently large, an annulus exists around the notch tip, inside which the stress field is still approximately the same as the K-field. In this case, the stress intensity factor can be computed from the applied stress by the classical formula $K = \bar{\sigma}\sqrt{\pi a}$. The fracture load, $\bar{\sigma}_{max}$, is reached when $K = K_c$. Consequently, for a sufficiently large notch, the fracture load is given by $\bar{\sigma}_{max} = (\Gamma_0 E / \pi a)^{1/2}$. This is the Griffith condition plotted in Fig. 2.

When the notch is small, nowhere in the two blocks can the stress field be the same as the K-field. As such, the stress intensity factor cannot be defined for two blocks connected by springs with a small notch. Yet the fracture load can be computed as follows. When subjected to the stress $\bar{\sigma}$, the two blocks separate more at the tip of the notch than at a position ahead the notch tip. This nonuniformity causes the notched sample to fracture at a stress $\bar{\sigma}$ below the bridging strength σ_0. Analyzing the problem coupling the elastic blocks and the nonlinear springs, one determines the applied stress $\bar{\sigma}$ as a function of the separation at the notch tip δ_t. For the generic bridging law shape in Fig. 2, the applied stress $\bar{\sigma}$ first increases with the notch tip separation δ_t, reaches a peak $\bar{\sigma}_{max}$, and then drops. This peak stress is the fracture load.

Figure 2, referred to as a *notch-sensitivity diagram*, summarizes the calculated fracture loads for several bridging law shapes [13,14]. For each bridging law shape, the peak stress is σ_0, the limiting displacement is δ_0, and the work of fracture Γ_0 is the area under the bridging law as given by (1). Each bridging law defines a basic *material length* $\Gamma_0 E / \sigma_0^2$ which, roughly speaking, scales the size of the zone where the nonlinearity is important. The notch size a is measured in units of this material length in Fig. 2. As evident from the diagram, the results do not vary significantly with the bridging law shapes. As discussed before, the Griffith condition is the exact asymptote for large notches, but incorrect for small notches. Independent of the bridging law shape χ, the same limit is approached at each end of the diagram: the fracture load approaches the unnotched strength $\bar{\sigma}_{max} = \sigma_0$ when the notch size is small, and is given by the

Griffith formula when the notch is large. Accordingly, it is not surprising that different bridging laws give similar results.

The following formula interpolated from the two limits gives the approximate fracture loads for any finite notch size

$$\bar{\sigma}_{max} / \sigma_0 = \left[1 + \pi a / \left(\Gamma_0 E / \sigma_0^2\right)\right]^{-1/2}. \tag{3}$$

This equation is also included in Fig. 2. Given a composite with a fixed material length $\Gamma_0 E / \sigma_0^2$, the fracture load will not be significantly reduced by the presence of a notch provided the notch size is small, say $a / \left(\Gamma_0 E / \sigma_0^2\right) < 0.1$. On the other hand, the Griffith formula is approximately valid when $a / \left(\Gamma_0 E / \sigma_0^2\right) > 2$.

2.2 *Simultaneous Tensile and Shear Bands*

In what follows we investigate the interaction between the tensile and the shear bands. Since the shape of the bridging law is of secondary importance, we will study this interaction by assuming that the tensile band deforms like an array of linear springs:

$$\sigma = k\delta. \tag{4}$$

Here k is the spring stiffness and, as before, the spring breaks at stress σ_0. The work of fracture of an unnotched sample with a uniformly deforming tensile band is

$$\Gamma_0 = \sigma_0^2 / 2k. \tag{5}$$

We will assume that the stress is bounded everywhere; that is, the stress intensity factor vanishes at the tip tensile band. For the linear spring model, this implies that the tensile band spreads over the entire ligament ahead of the notch.

The interaction between the tensile and the shear bands can be understood as follows. The separation of the tensile band is nonuniform near a notch. With the linear law used in this simulation, the sample fractures when the stress at the tail of the tensile band reaches σ_0. At this point, the stress at the other positions in the tensile band is below σ_0, so that the failure load is less than the net cross-section times σ_0. The shear bands will make the separation of the

tensile band less nonuniform, and thereby give rise to higher fracture loads. On the other hand, the extent of the shear bands is governed by the strength of the tensile band. For example, in the limiting case when the tensile band is vanishingly weak, the shear band will not form before the composite breaks.

To assess the general validity of certain conclusions, two descriptions of the shear bands will be used in this paper. In the first description, Fig. 3a, the shear stress σ_s and the sliding displacement δ_s are connected by

$$\sigma_s = k_s \delta_s. \tag{6}$$

The spring stiffness k_s is a material constant. The stress intensity is assumed to vanish at the tips of the shear bands. For the linear spring model, this requires that the shear bands extend to the sample boundary, Fig. 3a.

Shear experiments with a carbon matrix composite show that a constant resistance prevails over almost the entire shear deformation process [4]. This will be used as a second description in the simulation, i.e. a constant shear resistance T is prescribed in the shear bands, Fig. 3b. It is assumed that T is a material property invariant with sample size and geometry. For this description, the vanishing stress intensity at the tips of the shear bands will determine a finite hight of the bands, H, Fig. 3b.

As before, the elastic response of the composites is taken to be isotropic. The shear bands are assumed to remain closed, so that the normal displacements are continuous across the shear bands. All numerical calculations were done with the ABAQUS finite element code, under plane stress conditions, with Poisson's ratio $\nu = 0.3$. The solution is also applicable to plane strain conditions if Young's modulus E everywhere is replaced by $E/(1 - \nu^2)$.

3. RESULTS

3.1 Work of Fracture

Figure 3 shows a semi-infinite notch in an infinite sample. The stress field remote from

the notch tip is prescribed by the square-root singular solution, scaled with the intensity factor K. The fracture toughness K_c is attained when the stress at the tail of the tensile band σ_t reaches the spring strength σ_0. Once K_c is computed, the work of fracture of the composite (as opposed to that of the springs) is computed from

$$\Gamma = K_c^2 / E. \tag{7}$$

The ratio Γ/Γ_0 indicates the role of the shear bands in toughening the composites.

First use the description that the shear bands behave like linear springs. Linearity and dimensional considerations dictate that

$$\sigma_t = \alpha K (k / E)^{1/2}. \tag{8}$$

The dimensionless number α depends only on k_s/k, which is computed using finite elements. In the above, $K = K_c$ when $\sigma_t = \sigma_0$. A combination of (5), (7) and (8) gives

$$\Gamma / \Gamma_0 = 2 / \alpha^2. \tag{9}$$

Figure 3a plots the calculated results. As anticipated, stiff shear bands add little to the work of fracture, but weak shear bands add substantially.

Next use the description that the shear deformation is resisted by a constant stress T. The system is linear in both K and T so that

$$\sigma_t = f_1 K H^{-1/2} + f_2 T, \tag{10}$$

$$K_{II} = f_3 K - f_4 T H^{1/2}. \tag{11}$$

Here K_{II} is the mode II stress intensity factor at the tip of the shear band, and fs are dimensionless numbers depending on Hk/E. With $K_{II} = 0$ and $\sigma_t = \sigma_0$, one rearranges (10) and (11) as

$$T / \sigma_0 = 1 / (f_2 + f_1 f_4 / f_3), \tag{12}$$

$$\Gamma / \Gamma_0 = 2(Hk / E) / (f_1 + f_2 f_3 / f_4)^2. \tag{13}$$

Once the coefficients f_i are computed by using finite elements, the above defines a relation between Γ/Γ_0 and T/σ_0 via the parameter Hk/E. This relation is plotted in Fig. 3b. Again, the shear bands contribute little to the work of fracture if the shear resistance T is large.

That the curves in Figs. 3a and 3b turn sharply may be an artifact due to the model used

in the paper. In reality, the inelastic deformation is not localized to the mathematical planes. In some composites, the shear bands may involve more intricate micro-mechanisms, which cannot be described by a simple traction law [5]. These uncertainties will persist in any model that predicts work of fracture. However, the situation becomes much better when one tries to correlate the fracture loads of notched samples with an *experimentally measured* work of fracture, as demonstrated in the following.

3.2 Notch-Sensitivity

Consider a sample containing a finite notch loaded in tension by stress $\bar{\sigma}$, Fig. 4a. The notch size $2a$ is small compared to the sample width, so that the sample is assumed to be infinite. The fracture loads in the absence of the shear bands are given in Fig. 2; the enhancement due to the shear bands is studied in this section. For composites with the linear stress-deformation laws (4) and (6), both tensile and shear bands extend to the sample boundary. The stress in the tail of the tensile band varies linearly with the applied stress:

$$\sigma_t = \beta\bar{\sigma}. \tag{14}$$

Here β depends on both k_s/k and ak/E, which is computed using finite elements. Note that $ak/E = a/\left(2\Gamma_0 E/\sigma_0^2\right)$ for the linear spring. For the linear spring, the applied stress $\bar{\sigma}$ reaches the fracture load, $\bar{\sigma}_{max}$, when σ_t reaches the bridging strength σ_0. Consequently, $\bar{\sigma}_{max}/\sigma_0 = 1/\beta$, which is plotted in Fig. 4a. The fracture loads depend on shear property k_s/k. Weak shear bands relieve stress concentration and thereby lead to high fracture loads. The diagram conveys the essentials of the role of the shear bands, but is difficult to use in practice because of the uncertainties in the shear band characterization discussed previously.

Figure 4b plots the same results, but using the total work of fracture Γ of semi-infinite notches calculated previously to replace Γ_0. The new diagram shows that curves for different values of k_s/k collapse onto one curve. That is, the fracture loads are insensitive to the constitutive details of the shear bands, so long as the total work of fracture Γ is used to scale the

diagram. The outcome is not unexpected because, again, the curves for different values of k_s/k have the same asymptote for either small or large notches. For small notches, the fracture load is close to the strength of the unnotched composite, $\bar{\sigma}_{max} = \sigma_0$. For large notches, the fracture load is given by Griffith formula, $\bar{\sigma}_{max} = (\Gamma E / \pi a)^{1/2}$. Indeed, the fracture load curve in Fig. 4b is identical to that in Fig. 2 computed using the linear springs.

Encouraged by this finding, we then use constant T for the shear bands to confirm the general validity (Fig. 5a). The tensile stress at the notch tip and K_{II} at the shear band tip are linear in $\bar{\sigma}$ and T:

$$\sigma_t = g_1 \bar{\sigma} + g_2 T, \tag{15}$$

$$K_{II} H^{-1/2} = g_3 \bar{\sigma} - g_4 T. \tag{16}$$

The dimensionless coefficients g_i depend on ak/E and Hk/E, and were calculated by using finite elements. With $K_{II} = 0$ and $\sigma_t = \sigma_0$, one finds from (15) and (16) that

$$T / \sigma_0 = 1 / (g_2 + g_1 g_4 / g_3), \tag{17}$$

$$\bar{\sigma}_{max} / \sigma_0 = 1 / (g_1 + g_2 g_3 / g_4). \tag{18}$$

For a given notched composite, ak/E and T/σ_0 are fixed, the shear band height H at the onset of fracture is determined from (17). Using this height, one can plot (18) in the form of Fig. 5a. The fracture loads vary with shear resistance T, as anticipated. The same results are plotted in Fig. 5b, replacing Γ_0 by Γ computed previously. Once again, the notch-sensitivity diagram is almost independent of the shear band property T/σ_0. For small T/σ_0, our calculation have shown that the height of the shear bands H can be several times the notch size a at the onset of fracture.

Note that the fracture load curves in Fig. 4b and 5b are identical, even though the shear properties are different. Given the uncertainties in characterizing nonlinear deformation near the notches, a pragmatic approach to determine fracture loads in notched samples should be valuable. As suggested by the present simulation, two measurements are required for a given composite: the bridging-strength σ_0 from an unnotched sample, and the work of fracture Γ

from a sample containing a "large" notch. The latter may be readily accomplished in practice because the Griffith formula $\bar{\sigma}_{max} = (\Gamma E / \pi a)^{1/2}$ is valid so long as $a / (\Gamma E / \sigma_0^2) > 2$. This condition applies even when the height of the shear bands is larger than the notch size. The fracture loads for a sample containing a finite notch can then be obtained from Fig. 2 or Eqn. (3), with Γ_0 replaced by the measured Γ.

An example using the experimental data in [3] will illustrate the procedure. For a carbon-carbon composite, the unnotched strength is measured to be σ_0 = 300 MPa, the fracture load is $\bar{\sigma}_{max}$ = 100 MPa for a sample with notch size a = 6 mm. Upon fracture, the height of the shear band is slightly larger than the notch size. Using the standard calibration for a crack in an infinite sample, one finds that the fracture toughness is $K_c = \bar{\sigma}_{max}\sqrt{\pi a}$ = 14 MPa $m^{1/2}$. (The finite sample width only gives a small correction.) Also note that $a / (\Gamma E / \sigma_0^2) = a / (K_c / \sigma_0)^2 =$ 2.4, so that the notch is large enough for the Linear Fracture Mechanics to apply. The fracture loads measured from samples containing notches of a = 1, 2, 4, 6 mm indeed are well represented by the notch sensitivity diagram; see Fig. 5a in Ref [3].

4. CONCLUDING REMARKS

Three important conclusions are drawn from this simulation. First, shear bands in brittle-matrix composites can substantially increase work of fracture, which in turn reduces notch-sensitivity. Second, regardless of the relative height of the shear bands H/a, Linear Fracture Mechanics is valid if the notch size is sufficiently large, $a / (K_c / \sigma_0)^2 > 2$. Third, for samples containing small notches, the fracture loads are well correlated with the work of fracture, the unnotched strength and the notch size by

$$\bar{\sigma}_{max} / \sigma_0 = \left[1 + \pi a (\sigma_0 / K_c)^2\right]^{-1/2}.$$

Note that the formula is independent of the shear band properties and the relative height H/a, but is restricted to samples having small notches compared to the width. The conclusions are reached by two shear band descriptions with wide range parameter variations, and are expected

to have much more general validity. For example, finite samples with either crack-like notches or holes may be similarly treated. That is, the notch sensitivity diagrams presented in [13] can be used with materials with shear bands, with Γ reinterpreted as the total work of fracture.

Acknoledgements—The authors wish to thank Professor B. Budiansky for reviewing the manuscript and suggesting improvements. The work was supported by the Defense Advanced Research Projects Agency through the University Research Initiative under the Office of Naval Research contract N-0014-92-J-1808. ZS was in addition supported by the National Science Foundation through a Young Investigator Award MSS-9258115.

REFERENCES

1. C. Cady and A.G. Evans, *J. Am. Ceram. Soc.* In press.
2. J.M. Domergue, H.C. Cao, A.G. Evans and D. Petrak, *J. Am. Ceram. Soc.* In press.
3. F.E. Heredia, S. M. Spearing, T.J. Mackin, M.Y. He, A.G. Evans, P. Mosher and P. Brondsted, submitted to *J. Am. Ceram. Soc.*
4. P. Brondsted, F.E. Heredia and A.G. Evans, submitted to *J. Am. Ceram. Soc.*
5. M. Spearing, P.W.R. Beaumont and M.F. Ashby, in *Composite Materials: Fatigue and Fracture*, ASTM STP 1110, edited by T.K. O'Brien, p. 596 (1991).
6. Y.A. Bahei-El-Din, G.J. Dvorak and J.-F. Wu, *Engng. Fracture Mech.* **34**, 105 (1989).
7. J. Tirosh, *J. Appl. Mech.* **40**, 785 (1973).
8. D.B. Marshall, B.N. Cox and A.G. Evans, *Acta Metall. Mater.* **35**, 2607 (1985).
9. D.B. Marshall, M.C. Shaw and W.L. Morris, *Acta Metal. Mater.*, **40**, 443 (1992).
10. M.D. Thouless, A.G. Evans, *Acta Metall.* **36**, 517 (1988).
11. W.A. Curtin, *J. Mech. Phys. Solids.* **41**, 217 (1993).
12. J.R. Rice, *ASME J. Appl. Mech.* **35**, 379 (1968).
13. Z. Suo, S. Ho and X. Gong, *ASME J. Engng. Mater. Tech.* **115**, 319 (1993).
14. B. Budiansky and Y.L. Cui, *J. Mech. Phys. Solids* (1994). In Press.

FIGURE CAPTIONS

Fig. 1 A drawing of a notched sample, loaded in tension, damaged with a tensile band and two shear bands.

Fig. 2 Notch-sensitivity diagram.

Fig. 3 Fracture energy ratios showing the contribution of the shear bands: a) shear band is an array of linear springs, and b) shear band has a constant resistance T.

Fig. 4 Notch-sensitivity diagram including shear bands with linear stress-sliding law. a) The notch size is normalized by the work of fracture of the tensile band, Γ_0. b) The crack size is normalized by the total work of fracture, Γ.

Fig. 5 Notch-sensitivity diagram including shear bands with constant resistance. a) The notch size is normalized by the work of fracture of the tensile band, Γ_0. b) The crack size is normalized by the total work of fracture, Γ.

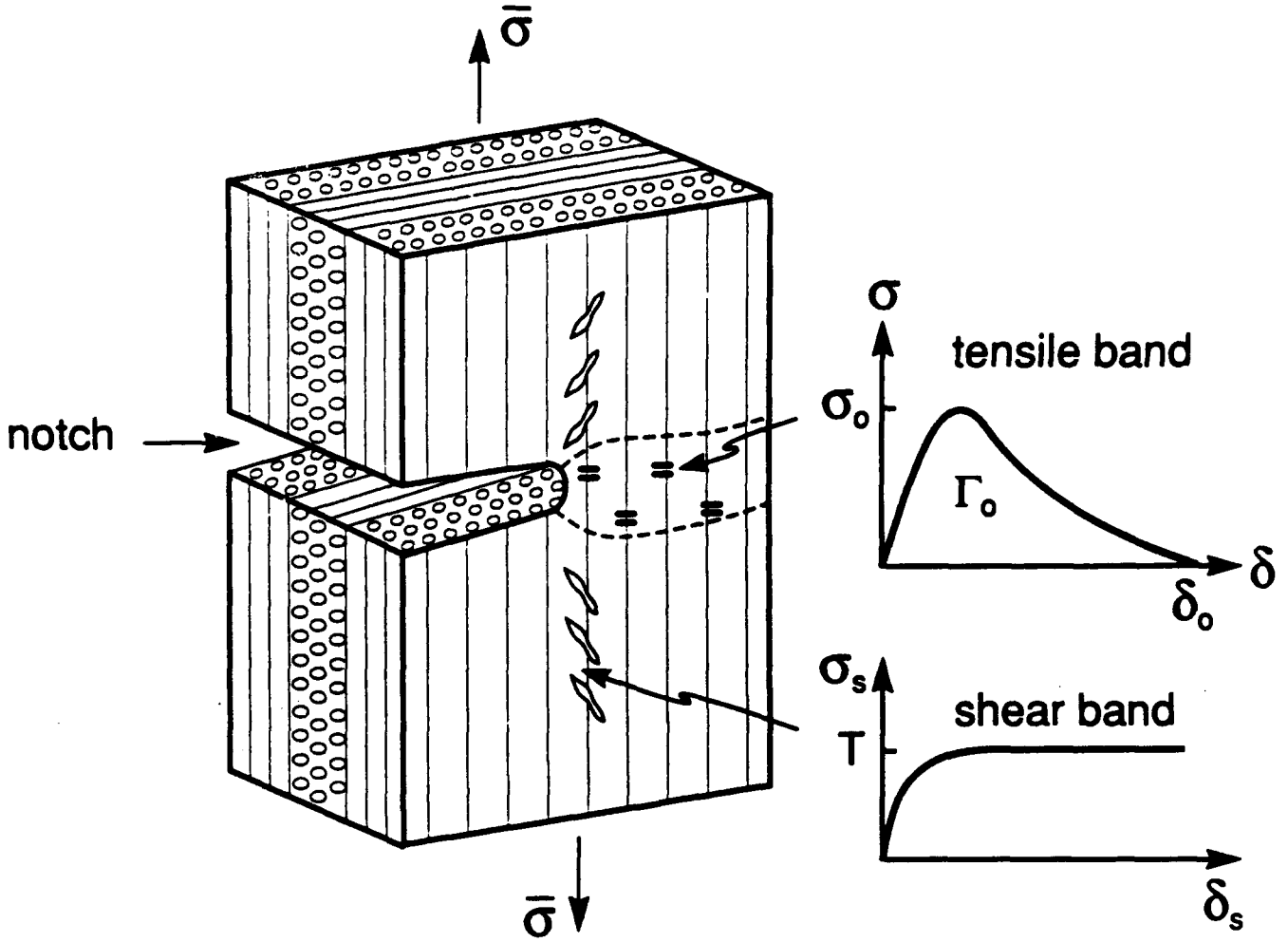
$\bar{\sigma}$
notch
σ
tensile band
σ_o
Γ_o
δ
δ_o
σ_s
shear band
T
δ_s
$\bar{\sigma}$

Figure 1

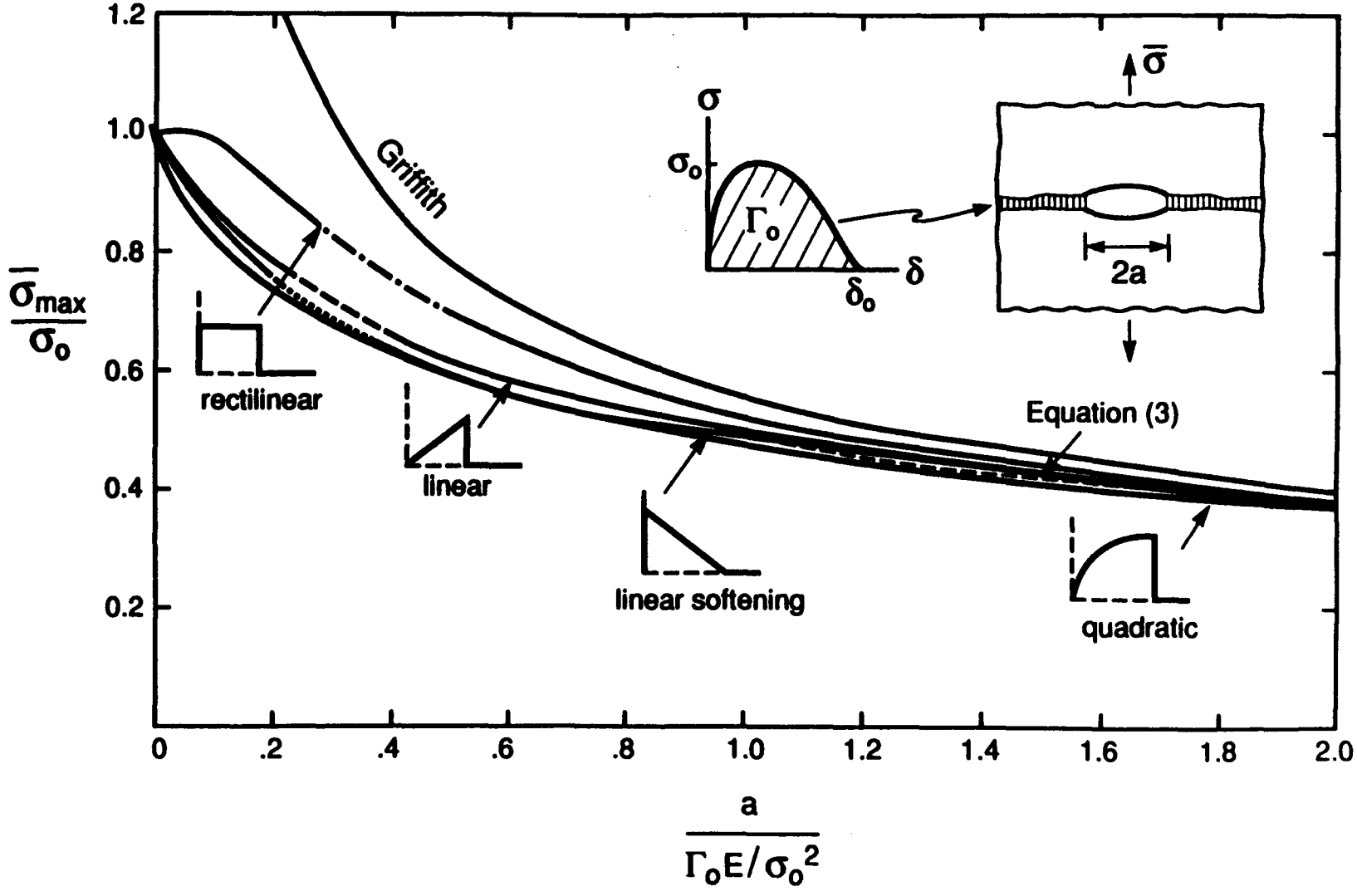
1.2
1.0
0.8
0.6
0.4
0.2
0
.2
.4
.6
.8
1.0
1.2
1.4
1.6
1.8
2.0
$\frac{\bar{\sigma}_{max}}{\sigma_o}$
$\frac{a}{\Gamma_o E/\sigma_o^2}$
Griffith
rectilinear
linear
linear softening
quadratic
Equation (3)
σ
σ_o
Γ_o
δ
δ_o
$\bar{\sigma}$
2a

Fig. 2

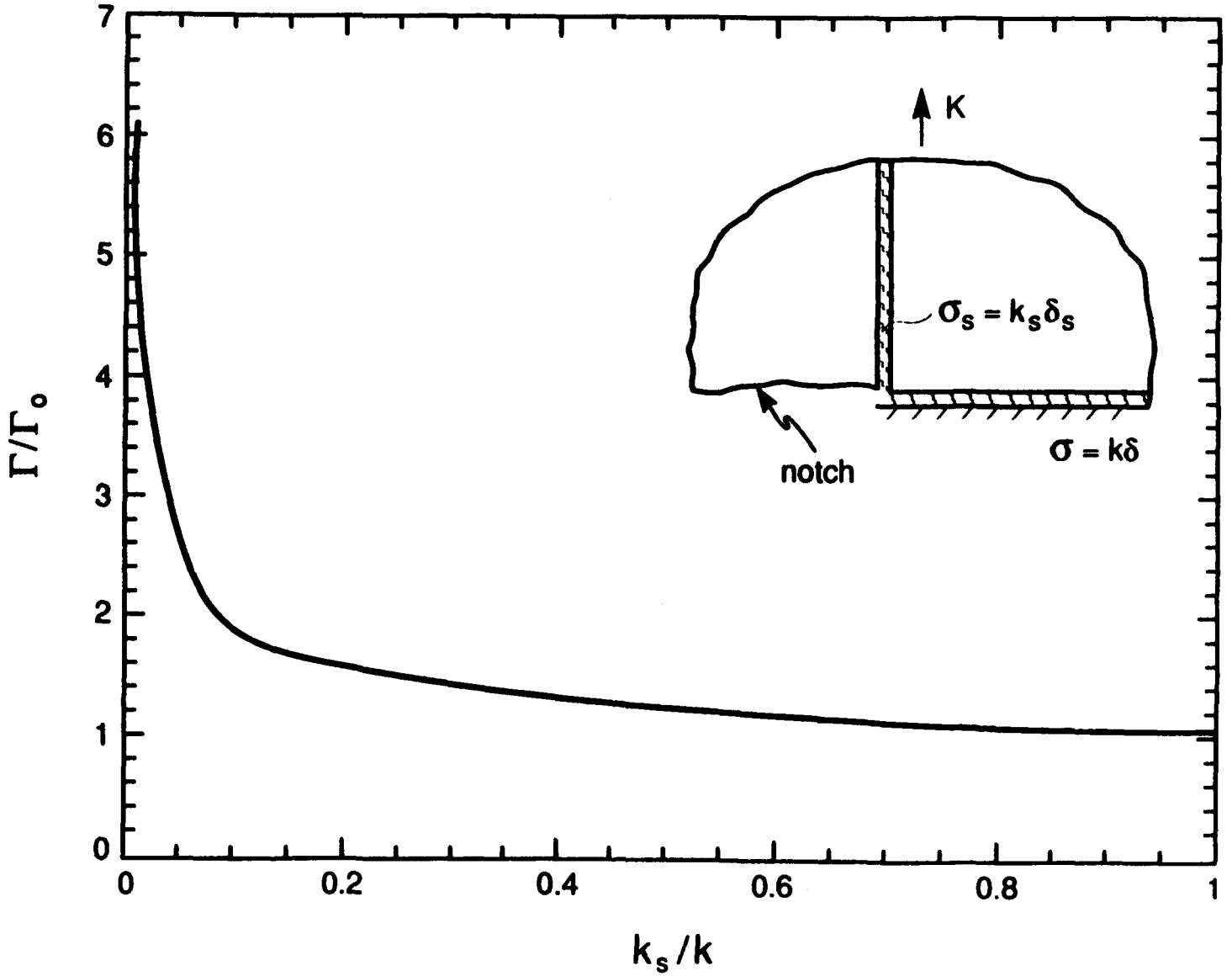

Figure 3a

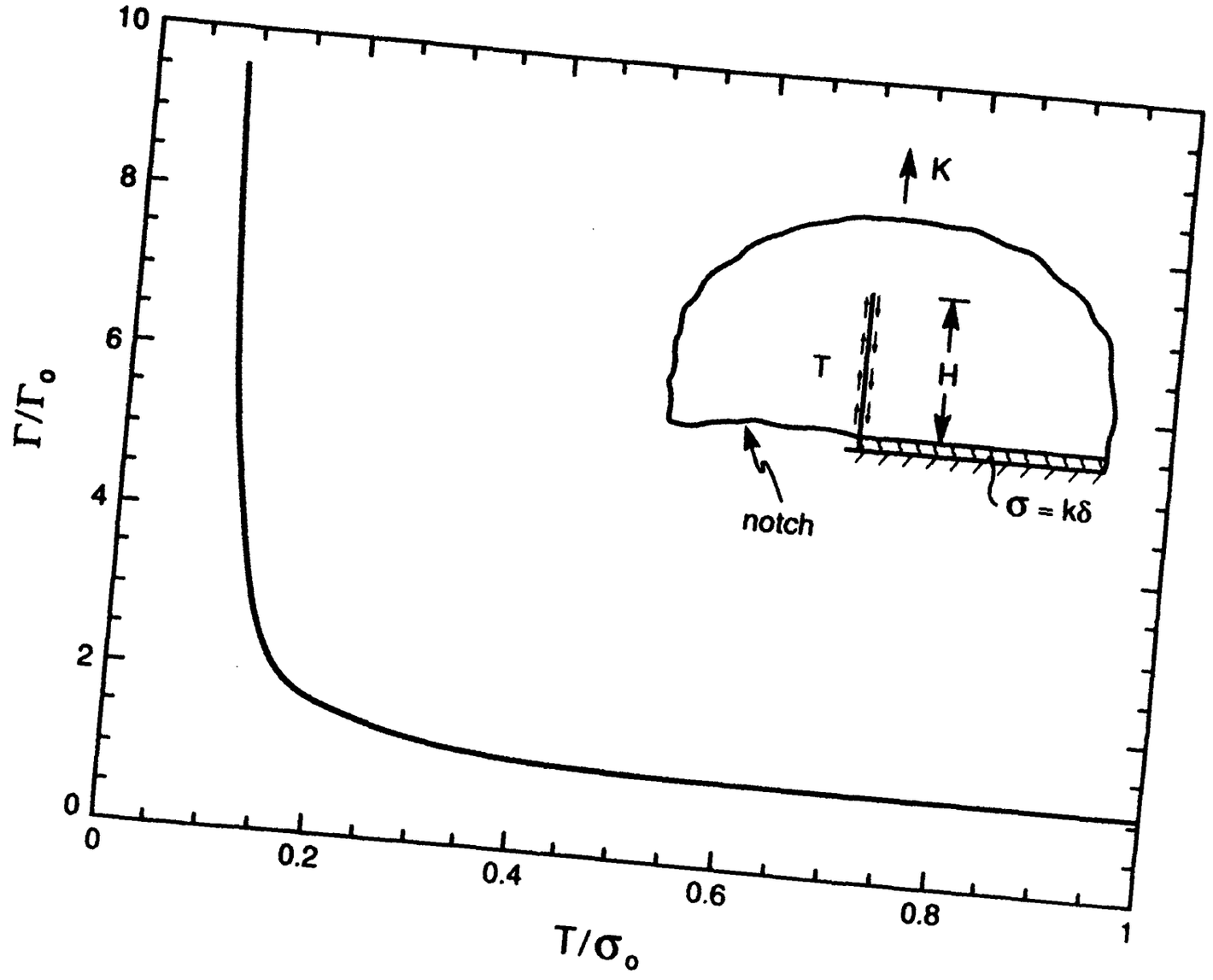

Figure 3b

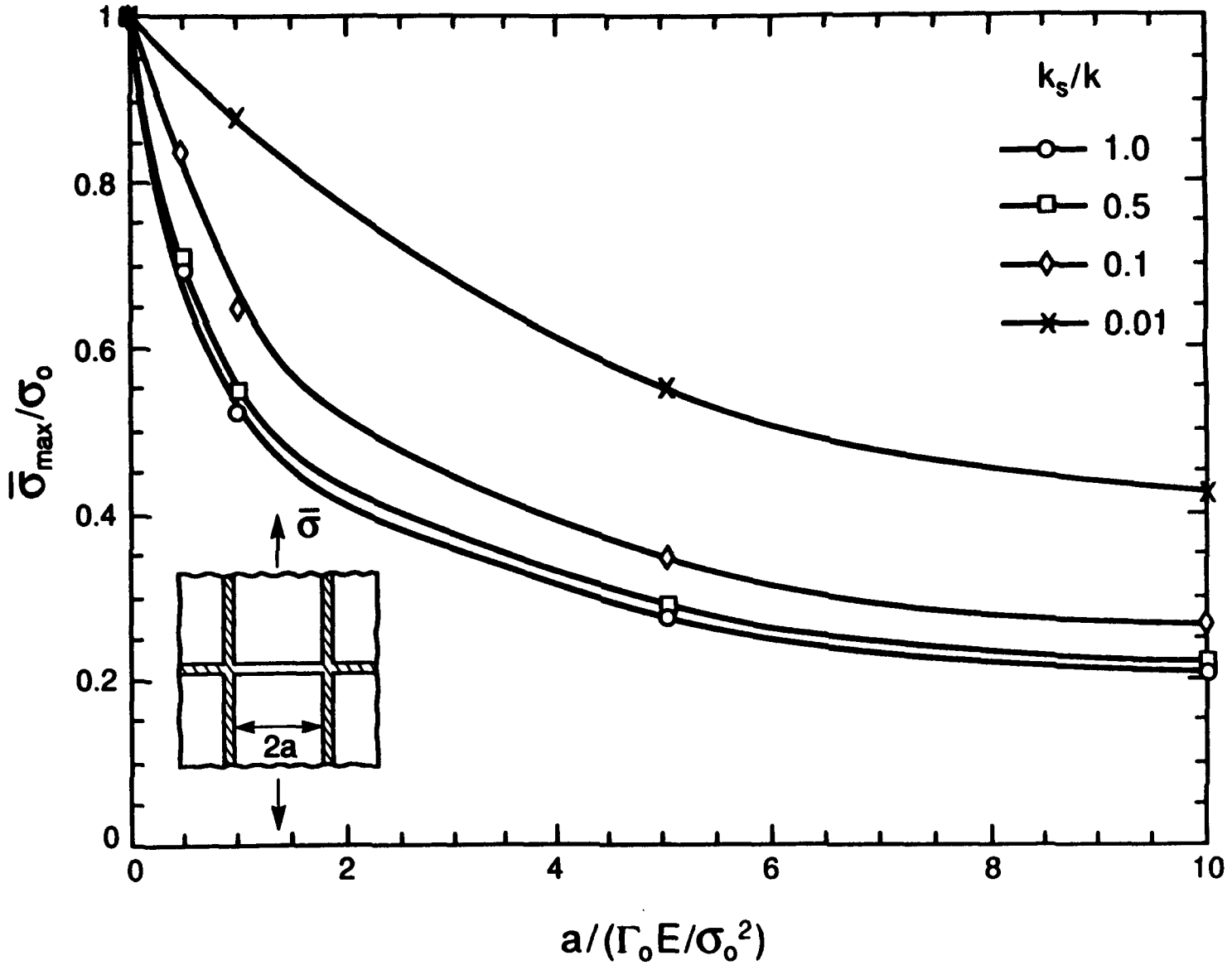

Figure 4a

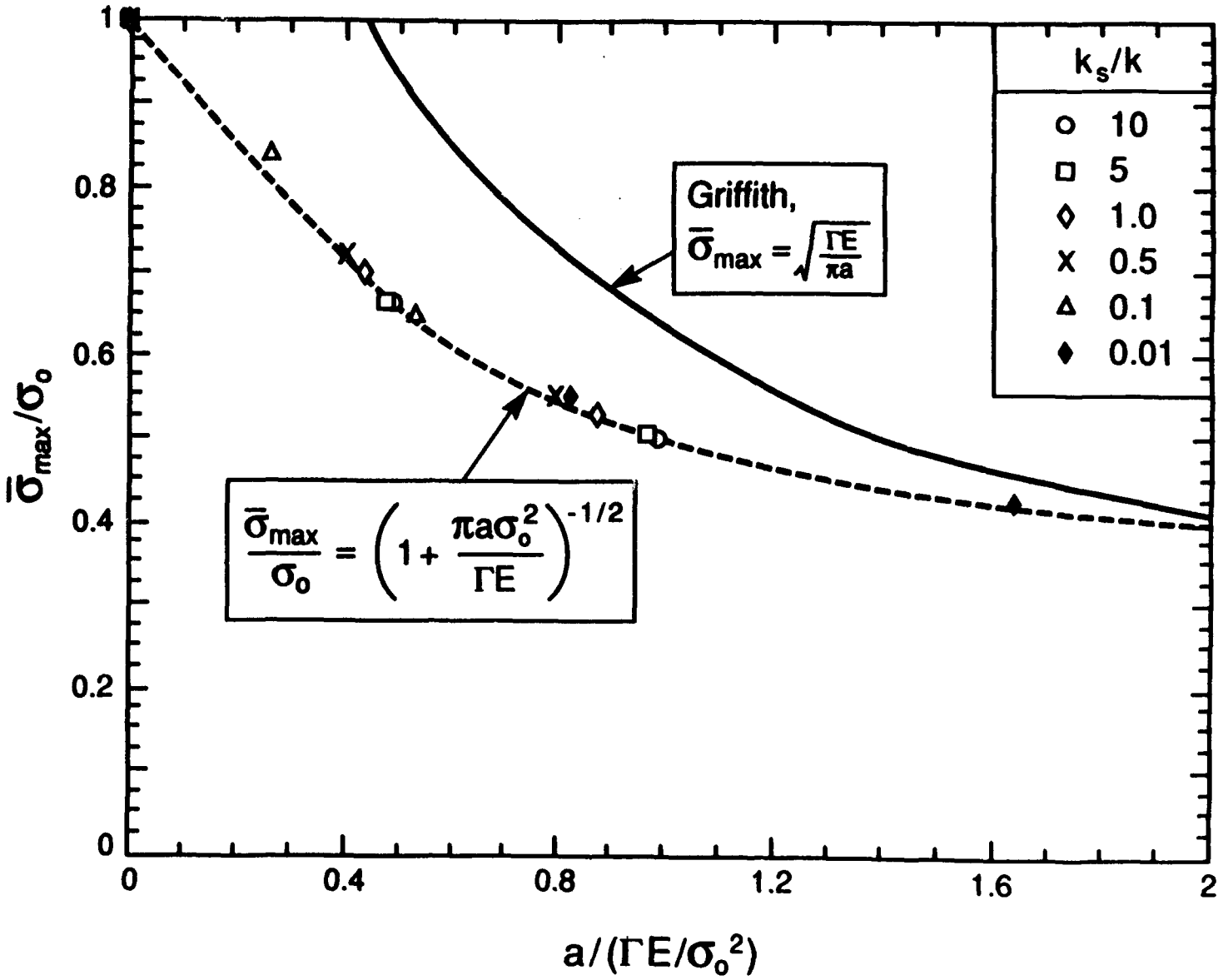

Figure 4b

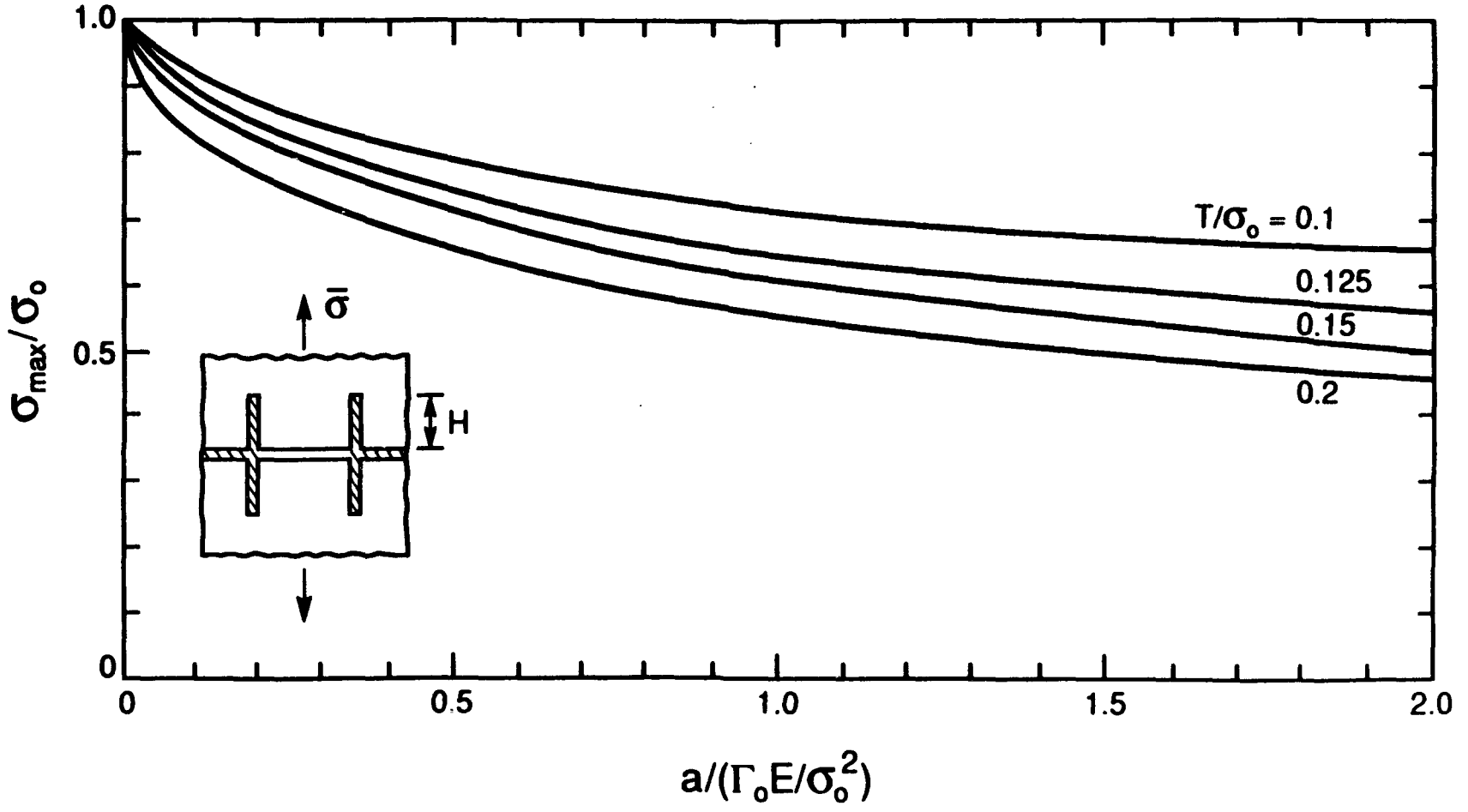
1.0
0.5
0
0
0.5
1.0
1.5
2.0
σ_{max}/σ_o
$a/(\Gamma_o E/\sigma_o^2)$
$T/\sigma_o = 0.1$
0.125
0.15
0.2
$\bar{\sigma}$
H

Figure 5a

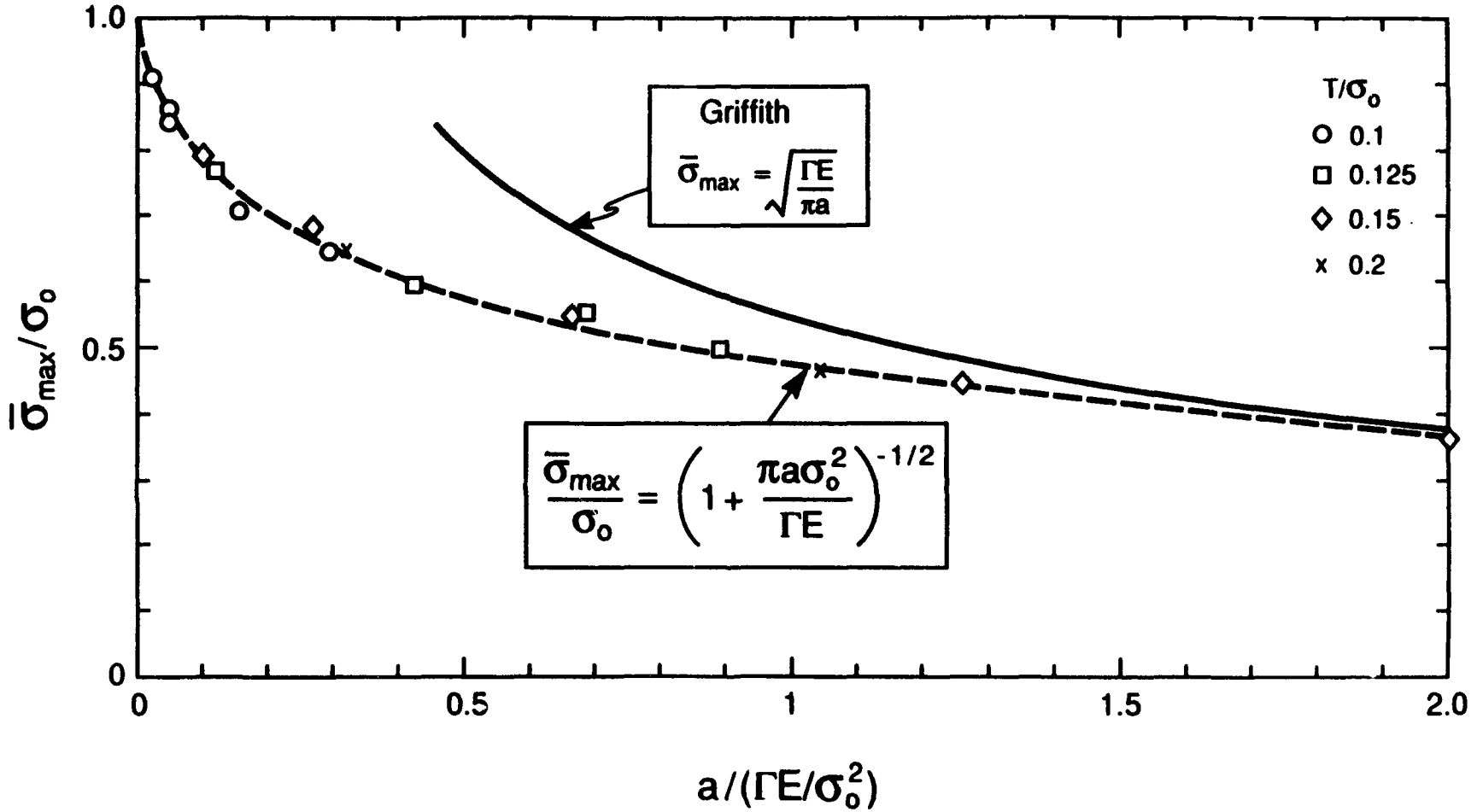
1.0
0.5
0
0
0.5
1
1.5
2.0
$\bar{\sigma}_{max}/\sigma_o$
$a/(\Gamma E/\sigma_o^2)$
Griffith
$\bar{\sigma}_{max} = \sqrt{\frac{\Gamma E}{\pi a}}$
$\frac{\bar{\sigma}_{max}}{\sigma_o} = \left(1 + \frac{\pi a \sigma_o^2}{\Gamma E}\right)^{-1/2}$
T/σ_o
O 0.1
□ 0.125
◇ 0.15
x 0.2

Figure 5b

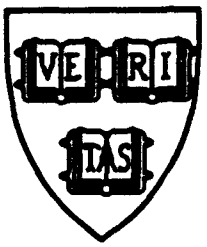

MECH-224

ON LARGE SCALE SLIDING IN FIBER-REINFORCED COMPOSITES

Z. Cedric Xia, John W. Hutchinson, Anthony G. Evans* and Bernard Budiansky
Division of Applied Sciences, Harvard University, Cambridge, MA 02138, U.S.A.
and *Materials Department, University of California, Santa Barbara, CA 93106, U.S.A.

Division of Applied Sciences
HARVARD UNIVERSITY
Cambridge, Massachusetts 02138

November 1993

ON LARGE SCALE SLIDING IN FIBER-REINFORCED COMPOSITES

Z. Cedric Xia, John W. Hutchinson, Anthony G. Evans* and Bernard Budiansky
Division of Applied Sciences, Harvard University, Cambridge, MA 02138, U.S.A.
and *Materials Department, University of California, Santa Barbara, CA 93106, U.S.A.

ABSTRACT

A critical examination is made of the use of the line-spring model to represent fiber bridging of matrix cracks in the analysis of failure phenomena in fiber reinforced brittle matrix composites. Attention is focused on composite systems designed to undergo fiber debonding and sliding when matrix cracking occurs. For most composites of this class, it is found that the distance along the fiber within which sliding occurs is often too large to justify use of the line-spring representation. A model which allows for large scale sliding (the LSS model) is proposed and applied to three problems: a matrix crack emerging from a semi-infinite unbridged through-crack in a uni-directional fiber reinforced composite, the same problem for the finite length unbridged through-crack, and matrix cracking of a cross-ply composite. Primary emphasis is placed on the stress concentration in the bridging fibers. Predictions from the LSS model are compared with those from the line-spring model. In general, the line-spring model is found to overestimate the stress concentration in critically located fibers. A discussion of the significance of the lower estimates of the stress concentration factors is given for several composite systems.

NOMENCLATURE (partial listing)

c_f, c_m	fiber, matrix volume fractions ($c_f + c_m = 1$)
E	longitudinal Young's modulus, $= c_f E_f + c_m E_m$
E_f, E_m	fiber, matrix Young's moduli
ℓ	length of the sliding zone
R_f	fiber radius
σ_f	tensile stress in the bridging fibers
$p = c_f \sigma_f$	smeared-out bridging stress in the bridging fibers
τ	interface sliding shear stress

1. INTRODUCTION

High strength ceramic fibers are employed to enhance the fracture performance of ceramic matrices. A well designed composite can sustain matrix cracks traversing the composite. Unbroken, debonded fibers then provide bridging restraint across the matrix crack faces. After the matrix is fully cracked, the intact fibers continue to carry additional load. Eventually the fibers fail and the composite ruptures, but the load-bearing capacity may substantially exceed the stress for matrix cracking.

An approach to studying matrix cracking and fiber stress concentrations in fiber-reinforced composites has emerged, wherein a line-spring model is used to represent the effect of intact fibers bridging matrix cracks. If the radius and spacing of the fibers are small compared to other length scales characterizing the deformation of the composite, the bridging-fiber forces can be smeared-out and treated as stresses provided by springs connecting crack faces. A bridging law is then used to relate the spring stress to the crack opening displacement. If the fiber-matrix interface has negligible debonding energy, if initial stresses are ignored, and if a constant frictional sliding stress τ is assumed, the following nonlinear bridging law results from an elementary shear lag analysis:

$$p(x) = \beta\sqrt{\delta(x)/2} \tag{1}$$

where $p(x)$ is the smeared-out fiber bridging stress and $\delta(x)$ is the effective opening displacement along the bridged region. The nonlinear spring constant β is given by

$$\beta = \left\{\frac{4c_f^{\,2}E_f E^2 \tau}{R_f c_m^{\,2} E_m^{\,2}}\right\}^{\frac{1}{2}} \tag{2}$$

where the notation is defined in the Nomenclature. The distance along the fiber ℓ within which sliding occurs on each side of the crack surface is related to the smeared-out fiber bridging stress by

$$\ell(x) = \frac{c_m E_m R_f}{2c_f E \tau} p(x) \tag{3}$$

The bridging law is consistent with ℓ greater than several fiber radii.[1]

---

[1] Readers should be aware that the bridging law (1,2) is not exactly the same as some in the earliest papers on the subject. The formula for β given by Marshall, Cox and Evans (1985) and Marshall and Cox (1987) is missing a factor $[c_m E_m/E]^{-1/2}$. Marshall and Cox (1988) give a formula identical to that given here. McCartney's (1987) formula is also the same as the present one, apart from a factor $1-\nu^2$. The transverse interaction between the fiber

The bridging law can be used together with integral equation methods to formulate and solve various problems for stresses in bridging fibers and stress intensity factors of matrix cracks. Thus, for example, it was in this way that Marshall *et al* (1985) and McCartney (1987) obtained conditions for the spread of a matrix crack from an initial, finite length bridged matrix crack. The critical stress required to propagate the matrix crack approaches the steady-state cracking stress for a semi-infinite bridged matrix crack, originally obtained by energy-based analyses by Aveston, Cooper and Kelly (1971) and Budiansky, Hutchinson and Evans (1986). Marshall and Cox (1987) and Budiansky and Cui (1993) have used the line spring approach based on (1) to study the effect of an unbridged through-crack in a uni-directional composite on the subsequent propagation of a matrix crack extending from the through-crack. These authors also determine the maximum stress experienced by the bridging fibers as the matrix crack spreads. Given the strength of the fibers, they estimate the ultimate strength of the composite as a function of initial through-crack flaw size. With much the same aim, Xia and Hutchinson (1993) have used the line-spring approach to investigate matrix cracking and fiber stress concentration in cross-ply composites.

Line-spring models have become valuable tools in the micromechanics analysis of various toughening mechanisms (see Bao and Suo (1992) for a review). These models replace bridging elements by an equivalent traction-displacement law applied as a boundary condition along the crack line. For the fiber bridging model, the constituent properties of the composite and the interface are nicely incorporated into one single spring parameter, β. In addition, the spring model allows use of well established analytical techniques to solve crack bridging problems. As convenient and powerful as the line-spring model appears to be, suspicions have arisen that results obtained from this model for fiber stress concentration in the presence of through-cracks may be unduly high. Specific experimental evidence giving rise to these suspicions is cited in Section 6 of this paper, where it is noted that the ultimate strength of some cross-ply composites should not be as high as experimentally measured, given the stress concentration levels predicted in the fibers by the line-spring model. It was this apparent discrepancy between theory and

---

and the matrix due to Poisson contraction can be approximated in various ways leading to such minor variations in the law (see discussion in the Appendix of He *et al* (1993)). More recently, Meda and Steif (1993) proposed a modification of the bridging law with a nonzero bridging stress as δ becomes zero.

experiment which motivated a critical examination of the line-spring model for this application, and which led to the identification of large scale sliding (LSS) as one possible source of the discrepancy.

The large scale sliding model is proposed in the next section, and a solution procedure using this model is outlined. It is then applied to three representative problems in subsequent sections: (i) the asymptotic problem for a semi-infinite through-crack collinear with a semi-infinite bridged matrix crack (Fig. 1), (ii) a finite length through-crack with fully extended collinear matrix cracks (see ahead to Fig. 5a), and (iii) a multiply cracked cross-ply laminate (see ahead to Fig. 5b). For each problem, key parameters of the problem are identified and solutions based on the line-spring model are obtained. The new LSS model is then applied to the problem, and the results are compared with those from the line-spring model. For composite constituent properties chosen within practical ranges, substantial reductions of stress concentration in the most highly stressed fibers just ahead of the through-crack tip are predicted by the LSS model relative to the line-spring model. At the same time, it is demonstrated that line-spring results are applicable when the constituent properties are such that small scale sliding does occur. Summary discussion is given in the last section, along with the appraisal of the experimental observations alluded to above.

2. THE LARGE SCALE SLIDING MODEL

The uni-directional fiber-reinforced composite containing a semi-infinite through-crack with a fully extended matrix crack will be used to introduce the LSS model. As shown in Fig. 1, the crack is loaded by a remote, mode I field specified by the monotonically increasing stress intensity factor K_I. Plane strain conditions are assumed for the composite blocks, and the mode I field is that for a crack in an elastically orthotropic solid. The primary quantity of interest is the stress in the leading fibers just ahead of the through-crack tip, at $x=0$.

The line-spring model is indicated in the lower left-hand corner of Fig. 1. The traction-separation law (1) and (2) is applied as a boundary condition along the x-axis, for $x>0$. In region A, outside the sliding zone, the solid is characterized by the orthotropic elastic behavior of the composite, i.e. the matrix material reinforced by perfectly bonded, uni-directional fibers. A

nonlinear integral equation for the distribution of the opening displacement $\delta(x)$ is formulated. Solution of this equation provides both the opening displacement and the distribution of the stress in the fibers where they cross the x-axis, ahead of the through-crack tip. Details of this solution will be given in the next section.

The rationale for a line-spring approximation requires that the extent of sliding be small compared to all relevant in-plane lengths. Only then can a sliding zone of finite width be confidently replaced by an equivalent traction-displacement condition applied along a line. In the present problem of Fig. 1, there is only a single characteristic length parameter, described in the next section. In the other problems, additional relevant lengths may be pertinent, such as the length of a through-crack or, in the case of the cross-ply composite, the ply thickness.

The LSS model distinguishes between region B in which fiber sliding has occurred and region A in which it has not. Denote the boundary between regions A and B by Γ, characterized by the extent of fiber sliding $\ell(x)$. This boundary is not known in advance but must be determined as part of the solution process. If it is assumed that sliding is one-signed, consistent with K_I being monotonically increased, the load transfer from the fibers to the matrix, within B, is known precisely. For a theory based on smeared-out fibers, the load transfer is equivalent to a body force per unit volume given by

$$f = \frac{2c_f\tau}{R_f} \tag{4}$$

It acts in the sense shown in Fig. 1, required by symmetry with respect to the x-axis. Denote the stress in a fiber at the line of the matrix crack on y=0 by σ_f^0, and denote its value at the top of the slipped region at $y=\ell$ by σ_f^Γ. A simple shear lag analysis based on equilibrium of the fiber (see Fig. 1) and compatibility of strain at the top of the sliding zone requires

$$\sigma_f^\Gamma = \sigma_f^0 - \frac{2\tau}{R_f}\ell \tag{5a}$$

$$\frac{\sigma_f^\Gamma}{E_f} = \frac{c_f\sigma_f^0}{E} \tag{5b}$$

These combine to give

$$\ell = \frac{c_m E_m R_f}{2E\tau}\sigma_f^0 \tag{6}$$

In addition to the body force f in region B, the sliding fibers exert a line load (load per unit thickness per unit length in the x-direction) along Γ equal to $c_f\sigma_f^\Gamma$. The one remaining quantity needed to fully describe the behavior of the slipped segment of a fiber is its vertical displacement v^Γ at the top of the slipped region. It is related to the other quantities by

$$v^\Gamma = \frac{1}{E_f}\left(\sigma_f^0 \ell - \frac{\tau}{R_f}\ell^2\right) \tag{7}$$

where, by symmetry, the vertical displacement of the fibers is zero along y=0 for x>0.

The LSS model is posed as follows. Assuming that the location of Γ is known (it must be determined by iteration), the sliding fibers in B may be regarded as separate entities from the rest of the solid. Represent the remnant material in region B by a linear elastic material whose properties are those of the matrix with cylindrical holes rather than fibers. These are constrained only in the transverse direction, because the fiber and matrix remain in frictionless contact. This replacement will be specified more precisely below. The material in A is assigned the orthotropic moduli of the composite with bonded fibers. The loads on the planar body comprising regions A and B are the remote K_I -field, the vertical body force f in B, and the vertical line load $c_f\sigma_f^\Gamma$ acting along Γ. The remnant matrix in B has zero tractions acting along the matrix crack line (y=0, x>0). The sliding fibers in B are governed by the *three* equations (5a), (6) and (7) and are described by *four* unknowns, σ_f^Γ, σ_f^0, ℓ and v^Γ. The deformation of the sliding segments of the fibers is coupled to that of the remaining body by requiring that v^Γ coincide with the vertical displacement of the body on Γ, i.e. $v^\Gamma(x) = v(x\ell(x))$.

In a given iteration with $\ell(x)$ regarded as known, the system of equations for the body in regions A and B, together with Eqs. (5a) and (7) for the sliding fiber segments and the coupling condition on Γ, specifies a solution for all field quantities, including the stresses in the fibers. In general, however, this solution will not be consistent with Equation (6) specifying the vertical extent of the zone of sliding. Given σ_f^0 from the current iteration, Eq. (6) can be used to generate $\ell(x)$ for the next iteration. However performed, an *iteration process must be used to determine the location of* Γ.

Like the composite material in region A, the remnant elastic material in region B is orthotropic with one axis of orthotropy aligned with the y-axis; transverse isotropy with respect to the y-axis would be assumed for both materials in most instances. The moduli of the remnant material in B are those of the matrix material alone, but containing cylindrical holes with freely sliding fibers. Since the composites being considered in this paper are assumed to have a residual compression acting across the fiber-matrix interface, the sliding fibers in region B continue to constrain the behavior of the remnant matrix by frictionless contact. Various methods are available for estimating the moduli of the remnant material. The one employed for the present problems will be mentioned in the next section. For the problems investigated in this paper, the main quantities of interest are rather insensitive to details of the elastic properties in B. In fact, it was found that the moduli of the material in A could be substituted for those in B with little consequence. The significance of this substitution is that the problem for the combined regions A and B becomes elastically homogeneous, opening up such LSS problems to solution by analytical methods which could not otherwise be used.

In this paper the LSS problems have been analyzed by accounting for the different elastic properties in regions A and B. A finite element method has been used for this purpose. Most aspects of the implementation of the model in a finite element code are standard. It is convenient to regard the sliding fibers in region B as a "fiber sheet" which has a Young's modulus $c_f E_f$ in the y-direction and all other moduli (including shear moduli) taken to be zero. The sliding stress τ acts on the fiber sheet as the body force f but in the direction opposite to that on the remnant matrix. The fiber sheet has zero vertical displacement along the x-axis and is connected to the planar body along Γ. The fiber sheet representation is completely equivalent to equations (5a) and (7). As already mentioned, (6) is used to update the location of Γ for the next iteration when σ_f^0 has been determined.

3. A MATRIX CRACK EMERGING FROM A SEMI-INFINITE THROUGH-CRACK

The problem addressed in this section is an asymptotic problem in which a matrix crack has extended from the tip of a semi-infinite through-crack which is loaded by a remote mode I field with stress intensity K_I. Two sub-problems are considered: the problem mentioned in connection

with Fig.1 where the bridged matrix crack extends to infinity, and a version of the same problem where the matrix crack has finite length a_m. The emphasis in the first problem will be on determination of the stress distribution in the fibers where they bridge the matrix crack. The bridging stress of the leading fibers will also be of concern in the second problem, along with the stress intensity factor at the tip of the matrix crack. These quantities will be computed using both the line-spring model and the LSS model. The problem of Fig. 1 for the fully extended matrix crack is considered first.

A closed form expression can be readily obtained for the bridging stress of the leading fibers, $p_0=p(0)$, as predicted by the line-spring model based on the bridging law (1). Application of the J-integral to connect the remote field to the opening along the crack faces gives

$$J = \frac{K_I^2}{A\bar{E}} = \int_0^{\delta(0)} p(\delta)d\delta \tag{8}$$

Here $\bar{E}=E/(1-\nu^2)$ where E is the Young's modulus of the composite for stressing parallel to the fibers , ν is the Poisson strain ratio of transverse contraction to axial elongation, and A is an orthotropy factor. This factor, which depends on c_f and on non-dimensional moduli combinations specifying the properties of the uni-directionally reinforced composite (such as E_f/E_m) has been presented by Budiansky and Cui (1993). Substitution of the bridging law (1) into (8) yields

$$p_0 = \left(\frac{3\beta^2 K_I^2}{4A\bar{E}}\right)^{\frac{1}{3}} \tag{9}$$

Determination of the distribution of the bridging stress, p(x), for the line-spring model requires the formulation and solution of an integral equation. These procedures are now well established; therefore, the equation and the numerical analysis used in its solution will not be recorded here. The analysis employed has been used by Xia and Hutchinson (1993) to study similar equations. The integral equation for p(x) can be put in non-dimensional form using two quantities: the bridging stress at the tip, p_0, and a quantity with the dimensions of length,

$$d = \left(\frac{3A\bar{E}K_I}{\beta^2}\right)^{\frac{2}{3}} \tag{10}$$

This is the only length parameter in the problem. Numerical results for the bridging stress p(x) normalized by p_0 are plotted as a function of x/d in Fig. 2 as a solid line; note that the bridging stress p is $c_f\sigma_f$. The curve in Fig. 2 is universal in the sense that there is no additional parametric dependence. Included in Fig. 2 is the classical inverse square root stress distribution, $K_I/(2\pi x)^{1/2}$, specifying the remote field, which takes the form $p/p_0 = (2/3)^{2/3}/\sqrt{2\pi(x/d)}$. Note that the length quantity d characterizes the transition to the classical field, with any significant difference from it disappearing for x greater than about 1.5d. The length of the sliding zone at the tip will be compared to d in the assessment of whether LSS conditions pertain.

Now consider the large scale sliding model of this problem. It is convenient to use the two quantities p_0 and d defined above. The formula (6) relating the slip length to the stress in the fibers along the line of the matrix crack (y=0) can be rewritten as

$$\frac{\ell(x)}{d} = \left(\frac{2}{3}\right)^{\frac{1}{3}} \frac{c_f E_f E}{c_m E_m A\bar{E}} \frac{p(x)}{p_0} \tag{11}$$

where now $p(x) = c_f\sigma_f^0(x)$. The body force f is given by

$$f = \frac{p_0}{d}\left(\frac{3}{2}\right)^{\frac{1}{3}} \frac{c_m^2 E_m^2 A\bar{E}}{c_f E_f E^2} \tag{12}$$

and the remotely applied stress intensity factor is linked to σ_0 and d by

$$K_I = \left(\frac{2}{3}\right)^{\frac{2}{3}} p_0\sqrt{d} \tag{13}$$

It follows from (11)-(13) that, according to the LSS model, the stress distribution in the bridging fibers, normalized by p_0, will depend only on x/d, in addition to the non-dimensional moduli parameters characterizing the composite, such as E_f/E_m, and the fiber volume fraction c_f. In all the numerical examples presented in this paper the Poisson's ratios of the fiber and the matrix are taken to be the same and equal to 0.2. In the four problems studied in this paper, we have used Hill's (1965) self-consistent results for the transversely isotropic elastic properties of the composite in region A. The moduli in region B have also been represented as transversely isotropic and have been determined using the same self-consistent equations, but replacing fibers by cylindrical holes for the purpose of estimating the axial modulus, the Poisson's ratio relating the transverse and axial strains, and the longitudinal shear modulus. The transverse modulus and

Poisson's ratio relating the two transverse strains were taken to be the same as those of the composite with bonded fibers. This approximately accounts for the constraint afforded by contact across the fiber/matrix interface. The transversely isotropic properties were used to generate the plane strain moduli quantities needed in each of the problems studied here. The LSS model is now fully specified.

Numerical calculations were carried out for a wide range of E_f/E_m and c_f (with $\nu_f=\nu_m=0.2$). To appreciate the numerical results, consider the ratio of the extent of sliding of the fibers at the through-crack tip to d as predicted by the line-spring model, i.e. (11) with $p(0)=p_0$,

$$\frac{\ell(0)}{d}=\left(\frac{2}{3}\right)^{\frac{1}{3}}\frac{c_f E_f E}{c_m E_m \bar{A}\bar{E}}\equiv\left(\frac{2}{3}\right)^{\frac{1}{3}}\xi \tag{14}$$

For typical values of the parameters appearing on the right hand side of (14) the ratio of sliding length to d will not be small compared to unity. Only materials with small ξ will give rise to a small values of this ratio. It will be seen that if ξ is not small the LSS predictions will differ appreciably from those of the line-spring model. This is illustrated by the LSS stress distributions for $E_f/E_m=1$ and various c_f, covering a range of ξ, in Fig. 2. The LSS distributions progressively approach the distribution of the line-spring model for decreasing ξ. But of the examples shown, agreement arises only for $\xi=0.05$ corresponding to the unrealistically small fiber volume fraction $c_f = 0.05$. Fig. 3a presents LSS results for the stress in the fibers just ahead of the through-crack tip. The results are presented as the ratio $(c_f\sigma_f)_{LSS}/(c_f\sigma_f)_{lsm}$, where $(c_f\sigma_f)_{lsm}=p_0$ is the line-spring model prediction. This ratio reflects the extent to which the LSS prediction is lower than the line-spring prediction for the most severely stressed fibers. For all practical values of E_f/E_m and c_f, the line-spring model overestimates the fiber stress concentration substantially. Fig. 3b reveals a remarkable near-collapse to a single relationship of all the numerical results in Fig. 3a when they are plotted as $(c_f\sigma_f)_{LSS}/(c_f\sigma_f)_{lsm}$ versus ξ. The solid line in Fig. 3b is an empirical curve fit to the numerical data. For this problem, Fig. 3b clearly shows that the parameter ξ provides a measure of the degree to which LSS predictions differ from the line-spring predictions. In turn, by (14), this confirms that the necessity of invoking an LSS approach is tied to the magnitude of the ratio of the sliding length at the through-crack tip to d.

A selected set of the above numerical computations with the LSS model were repeated with only a change in the elastic moduli in region B. We found very little sensitivity in the predictions for the fiber stresses to the details of the moduli in B. An excellent approximation to the results presented above were obtained by taking the moduli in B to be the same as those in A. Evidently, the essential difference between the LSS and line-spring models lies in the modeling of the spatial aspects of the load transfer from the fibers and not in complications of the modified moduli in region B. The finite height of the sliding zone at the tip of the through-crack tends to diffuse the stress concentration in the most highly stressed fibers.

Next consider a matrix crack of finite length a_m ahead the through-crack tip as shown in the insert in Fig. 4. Now the emphasis will be on the stress intensity factor K_t at the matrix crack tip, as well as the stress concentration in the fiber at the through-crack tip. The line-spring model version of this problem was first solved for all values of a_m/d, and the results are presented in Fig. 4. Fig. 4a displays K_t/K_I as a function of normalized matrix crack length, a_m/d, while Fig. 4b displays the companion plot of $c_f\sigma_f/p_0$ for the fibers just ahead of the through-crack tip. Also shown in Fig. 4 are numerical results obtained from the LSS model for $E_f/E_m=1$ and several values of c_f, again chosen to illustrate the approach to the line-spring predictions when c_f (and thus ξ) becomes small. Differences between the predictions of the two models for the matrix crack stress intensity factor are relatively small. The substantial reductions in stress concentration in the lead fibers predicted by the LSS model compared to the line-spring model are seen to be only weakly dependent on a_m/d.

4. UNI-DIRECTIONAL COMPOSITE CONTAINING A FINITE THROUGH-CRACK AND FULLY EXTENDED MATRIX CRACKS

The second problem to be investigated using the LSS model is that of a uni-directional fiber-reinforced composite containing a finite through-crack of length 2a with fully extended matrix cracks emerging from each tip, as depicted in Fig. 5a. A remote stress σ acts on the composite. This problem was previously studied by Budiansky and Cui (1993) by means of the line-spring model in an effort to determine the tensile strength of the composite in the presence of crack-like flaws. Determination of the stress concentration in the leading fiber ahead of the through-crack

tip has special interest, because failure of the leading fibers will precipitate failure of the composite.

Define the stress concentration factor (SCF) for the leading fibers at the through-crack tip as

$$\lambda = \frac{c_f \sigma_f}{\sigma} \tag{15}$$

where $c_f\sigma_f$ is again the smeared-out bridging stress of the leading fibers. Since the through-crack is not bridged by fibers, λ will exceed unity. The line-spring version of the problem is again obtained by formulating and solving an integral equation. In accordance with the analysis of Budiansky and Cui, the solution for λ is fully characterized by a single non-dimensional parameter, η, defined as

$$\eta = \frac{3\pi c_f^{\,2} E_f E^2}{c_m^{\,2} E_m^{\,2} A\bar{E}} \frac{a\tau}{R_f \sigma} \tag{16}$$

The relation between λ and η obtained from the numerical solution of the integral equation is plotted in Fig. 6a as the solid line. A remarkably accurate approximation to this result is given by

$$\lambda = \sqrt{1+\eta^{2/3}} \tag{17}$$

shown as the dashed curve in Fig. 6a (obtained from Eq. (12) of Budiansky and Cui).

The LSS model is similar to that developed for the previous problem. The slip length in (3) is now normalized by the half-length of the unbridged through-crack and written as

$$\frac{\ell(x)}{a} = \frac{3\pi c_f E_f E}{2 c_m E_m A\bar{E}} \frac{1}{\eta} \frac{p(x)}{\sigma} \tag{18}$$

and the body force f is expressed as

$$f = \frac{\sigma}{a} \frac{2 c_m^{\,2} E_m^{\,2} A\bar{E}}{3\pi c_f E_f E^2} \eta \tag{19}$$

It can now be shown from a non-dimensionalization of the governing equations for the LSS model that the SCF, λ, depends on η and on the non-dimensional parameters such as E_f/E_m and c_f specifying the composite.

There are two length quantities in this problem: the half-crack length a and the measure d which may still be defined as in (10), but now with $K_I = \sigma\sqrt{\pi a}$. To place the need for an LSS

approach into perspective, the height of the sliding zone at the tip of the through-crack, $\ell(a)$, as predicted by the line-spring model will be compared to both a and d. By (15), the approximation (17), and (18),

$$\frac{\ell(a)}{a} = \frac{c_f E_f E}{c_m E_m A\bar{E}} \frac{3\sqrt{1+\eta^{2/3}}}{2\eta} = \xi \frac{3\sqrt{1+\eta^{2/3}}}{2\eta} \tag{20}$$

A plot of $\ell(a)/(\xi a)$ versus η is given in Fig. 7a. Similarly, the line-spring estimate of the other length ratio is

$$\frac{\ell(a)}{d} = \frac{c_f E_f E}{c_m E_m A\bar{E}} \frac{\sqrt{1+\eta^{2/3}}}{(3\eta/2)^{1/3}} = \xi \frac{\sqrt{1+\eta^{2/3}}}{(3\eta/2)^{1/3}} \tag{21}$$

and $\ell(a)/(\xi d)$ is also plotted in Fig. 7a. For a given value of the parameter ξ, the ratio $\ell(a)/d$ is nearly constant over most of the range of η, while $\ell(a)/a$ is largest for small η and falls off gradually for large η. Based on experience with the previous problem, LSS conditions are again expected to depend on the magnitude of ξ as well as η.

Results obtained from the LSS model for three values of c_f with $E_f/E_m = 1$ ($\nu_f = \nu_m = 0.2$) are included in Fig. 6a. The appreciable deviation between the two models with increasing c_f is clearly evident. The influence of a change in E_f/E_m is displayed in Fig. 6b. It is apparent that the discrepancy between the two models is considerable over essentially the entire practical range of parameter space, with the LSS model predicting lower values of stress concentration. The numerical data points from the two plots of Fig. 6 for η=1, 5 and 30 are used to plot the ratio $(c_f\sigma_f)_{LSS}/(c_f\sigma_f)_{lsm}$ as a function of ξ in Fig. 7b. The lowest curve in this figure is the empirical fit to the numerical results for the semi-infinite through-crack problem in Fig. 3b, which corresponds to the limit $\eta=\infty$. It can be noted that for η ranging from about 5 to ∞ the reduction in the LSS prediction for the stress in the leading fibers relative to the line-spring model depends primarily on ξ.

5. A MULTIPLY CRACKED CROSS-PLY LAMINATE

The last of the problems to be studied is a fiber-reinforced cross-ply laminate with unbridged through-cracks across the 90^o plies connected by bridged matrix cracks in the 0^o plies, as illustrated in Fig. 5b. The plies are equally spaced with ply thickness 2t, and the applied stress carried by the composite is σ. The pattern is doubly periodic with the spacing between cracks taken as 2L. The sequence of events leading to an idealized pattern such as that envisioned in Fig. 5b is as follows. For the properties of a typical brittle-matrix cross-ply composite, the first cracks to form as the applied stress is increased are those in the 90^o plies which spread from flaws and tunnel in the direction perpendicular to the plane of Fig. 5b. They extend all the way across the 90^o plies. At higher applied stresses, these cracks serve as flaws from which plane strain matrix cracks spread across the 0^o plies. The fibers in the 0^o plies of a well designed composite must survive this process if the composite is to display any appreciable "ductility". The process just described has been analyzed in some detail by Xia and Hutchinson (1993), who used a line-spring model to represent fiber bridging in the 0^o plies. Their emphasis was on the applied stress associated with matrix cracking and the stress concentration in the most highly stressed fibers located at the ply interfaces. The doubly periodic cracking pattern shown in Fig. 5b is one of two patterns considered by Xia and Hutchinson to model crack interaction effects. The issue to be addressed here is whether the stresses predicted by the line-spring model for the most highly stressed fibers are unduly high, with clear implications for survivability of cross-plies with fully developed matrix cracks.

The fibers at the interfaces between the 90^o and 0^o plies will experience the highest stress. Again, define the stress concentration factor, λ, for these most highly stressed fibers by (15). The parametric dependence of this stress concentration factor has the general form

$$\lambda = \lambda\left(\frac{E_f}{E_m}, c_f, \eta, \frac{t}{L}\right) \tag{22}$$

where t/L is the crack density and η is now defined using t rather than a as

$$\eta = \frac{3\pi c_f^{\,2} E_f E^2}{c_m^{\,2} E_m^{\,2} A\bar{E}} \frac{t\tau}{R_f \sigma} \tag{23}$$

The dependence of λ on ν_f and ν_m is left implicit; $\nu_f=\nu_m=0.2$ is used in the calculations.

In the case that the fibers and the matrix have identical elastic properties, the cross-ply is homogeneous and isotropic prior to any cracking. Solutions to the line-spring model version of the problem can be obtained by the integral equation techniques used by Xia and Hutchinson (1993). The results of the line-spring model for the SCF for the case $t/L=0$ are shown in Fig. 8. Because all the load is carried by the bridging fibers in the 0^o plies, λ is never less than 2. The stress concentration factors for the same problem obtained from the LSS model are also plotted in Fig. 8 for three values of c_f. The conclusion is that the line-spring model again overestimates the SCF in the range of practical values, sometimes significantly so.

Consider next the effect of the crack density, t/L, on the stress concentrations in the bridging fibers. An important consequence of multiple matrix cracking and sliding is the alleviation and ultimate elimination of the stress concentration in the fibers in the 0^o plies. Elimination arises when the fibers are fully sliding (i.e., $\ell = L$ across the entire ply), as shown by elementary considerations of fiber equilibrium and stretching for the geometry in Fig. 5b. An accurate estimate of the critical density of matrix cracks at which λ drops to 2 is obtained by setting $\ell = L$ and $p=2\sigma$ in (3) giving

$$\left(\frac{t}{L}\right)_{crit} = \frac{c_f E t \tau}{c_m E_m R_f \sigma} = \frac{c_m E_m A \bar{E}}{3\pi c_f E_f E}\eta \qquad (24)$$

Stated differently, as the applied stress σ increases, the matrix crack density increases until the fibers become fully sliding. In this state, the stress in each fiber where it bridges a matrix crack is given by $\sigma_f=2\sigma/c_f$.

Numerical calculations based on the LSS model have been performed for a representative case of $E_f/E_m=1$ and $c_f=0.4$. Results for $\lambda=c_f\sigma_f/\sigma$ are plotted as a function of the crack density t/L for different values of η in Fig. 9. The numerical results are connected by dashed lines to the intercepts corresponding to first attainment of $\lambda=2$ given by the formula (24). The accuracy of the simple formula is evident. Indeed, the numerical solutions revealed that the sliding zone approached the condition $\ell = L$ fairly uniformly across the 0^o plies, as assumed in the derivation of (24).

In summary, as the applied stress on the cross-ply is increased, leading first to tunnel cracking in the 90^o plies and then matrix cracking in the 0^o plies, the stresses in the fibers at the ply interfaces will be the greatest. However, as the applied stress and the matrix crack density increase, the stress concentration *factor* for the fibers at the ply interfaces drops until matrix cracking is saturated with full sliding. In this state, the fibers uniformly share the load and the stress in the fibers at the matrix crack line becomes $\sigma_f=2\sigma/c_f$.

6. THE EXPERIMENTAL SITUATION

The ultimate tensile strengths (S_u) of many unidirectional and cross-ply CMCs have been reported to conform with predictions based on global load sharing (GLS) (Curtin, 1991). The GLS model considers that the load is distributed uniformly among all intact fibers. The CMC materials that give good agreement with the GLS model include various SiC/C composites (Heredia *et al*, 1992), SiC/CAS (Prewo, 1986) and SiC/CAS (Beyerle *et al*, 1992). Each of these materials has the common characteristic that the interface sliding stress τ is relatively small ($2<\tau<40$ MPa). The situation has been comprehensively summarized by Curtin (1993). The implication of this agreement for the present discussion is that the stress concentration in the fibers is minimal at the failure loads, despite the presence of manufacturing flaws and matrix cracks. Otherwise, the stress concentration would lead to premature fiber failure and ultimate tensile strength values appreciably below the GLS predictions.

To further explore the situation, the preceding LSS model is used to evaluate the fiber stress concentration for various of the experimental conditions wherein GLS predictions have been found to apply. The most stringent test of the LSS model arises for cross ply laminates. For this case, the unbridged crack dimension is the largest (the ply dimension 2t), resulting in correspondingly large values of η (Eq. 23). Experimental information for several CMCs is summarized in Table I. These experimental characteristics can be most readily compared with the LSS model by using (24), with $\sigma=S_u$, to predict the crack spacing at which the stress concentration in the fibers is eliminated. For all three composites, $(t/L)_{crit}$ is about unity or less (Table I). Crack spacings in CMCs almost invariably satisfy $t/L>1$ prior to composite rupture (Beyerle *et al*, 1992; Guillaumat, 1993). The applicability of the GLS criterion for the ultimate

tensile strength is thus consistent with the predictions of the LSS model. One other factor is relevant for the SiC/C composite, which gives the largest $(t/L)_{crit}$ (Table I). Processing flaws tend to induce inter-ply shear cracks (Turner *et al*, 1993) which suppress matrix cracks in the 0^o plies, while also eliminating stress concentrations in the fibers.

The comparison with experiments has emphasized the importance of large scale sliding in governing the stresses in fibers within cross-ply composites, resulting in the applicability of global load sharing concepts for predicting the ultimate tensile stress. Related arguments would apply regarding the role of manufacturing flaws within the plies. Such flaws result in unbridged cracks, which would be expected to introduce stress concentrations into the fibers. The line-spring model and the LSS results taken together show that, where these stress concentrations exist, they can be relatively small provided that η is less than about 3 (cf. Fig. 6), especially when E_f/E_m is large. The clear implication from (16) is that the material becomes more tolerant to manufacturing flaws when the interface sliding resistance is low.

ACKNOWLEDGMENTS

This work was partially supported by the DARPA University Research Initiative ONR Prime Contract N00014-92-J-1808, by the NSF through grant DMR-89-20490, and by the Division of Applied Sciences, Harvard University.

REFERENCES

Aveston, J., Cooper, G.A. and Kelly, A. (1971) Single and multiple fracture, in *The Properties of Fiber Composites*, Proc. National Physical Laboratory, Guildford, IPC Science and Technology, U.K., 15-26.

Bao, G. and Suo, Z. (1992) Remarks on crack-bridging concepts. *Appl. Mech. Rev.* **24**, 355-366.

Beyerle, D.S., Spearing, S.M. and Evans, A.G. (1992) Damage mechanisms and the mechanical properties of a laminated 0/90 ceramic/matrix composite, *J. Am. Ceram. Soc.*, **75**, 3321-3330.

Budiansky, B. and Cui, Y.L. (1993) On the tensile strength of a fiber-reinforced ceramic composite containing a crack-like flaw. *J. Mech. Phys. Solids*, in press.

Budiansky, B., Hutchinson, J.W. and Evans, A.G. (1986) Matrix fracture in fiber-reinforced ceramics. *J. Mech. Phys. Solids*, **34**, 167-189.

Curtin, W. A. (1993) The tough to brittle transition in brittle matrix composites. *J. Mech. Phys. Solids*, **41**, 217-221.

Curtin, W. A. (1991) The ultimate strength of ceramic matrix composites. *J. Am. Ceram. Soc.*, **74**, 2037-2041.

Guillaumat, L. (1993) Ph.D. Thesis, Laboratoire des Composites Thermostructuraux, Domaine Universitaire, Bordeaux, France.

He, M. Y., Wu, B. X., Evans, A. G. and Hutchinson, J. W. (1993) Inelastic strains due to matrix cracking in unidirectional fiber-reinforced composites. Submitted for publication.

Heredia, F. E., Spearing, S. M., Evans, A. G., Mosher, P. and Curtin, W. A. (1992) The mechanical properties of continuous fiber reinforced ceramic composites. *J. Am. Ceram. Soc.*, **75**, 3321-3327.

Hill, R. (1965) Theory of mechanical properties of fiber-strengthened materials: III. Self consistent model. *J. Mech. Phys. Solids*, **13**, 189-198.

Marshall, D.B. and Cox, B.N. (1987) Tensile fracture of brittle matrix composites: influence of fiber strength. *Acta. Met.*, **35**, 2607-2619.

Marshall, D.B. and Cox, B.N. (1988) A J-integral method for calculating steady-state matrix cracking stress in composites. *Mech. Mater.*, **7**, 127-133.

Marshall, D.B., Cox, B.N. and Evans, A.G. (1985) The mechanics of matrix cracking in brittle-matrix fiber composites. *Acta. Met.*, **33**, 2013-2021.

McCartney, L.N. (1987) Mechanics of matrix cracking in brittle -matrix fibre-reinforced composites. *Pro. R. Soc. Lond.*, **A409**, 329-350.

Meda, G. and Steif, P.S. (1993) A detailed analysis of cracks bridged by fibers, Part II: cracks of intermediate size, to be published.

Prewo, K. (1986) Tension and flexural strength of silicon carbide fiber reinforced glass ceramics. *J. Mat. Sci.*, **21**, 3590-3597.

Turner, K. S., Speck, J. S. and Evans, A. G. (1993) The tensile and shear properties of carbon matrix composites, submitted to *J. Am. Ceram. Soc.*

Xia, Z.C. and Hutchinson, J.W. (1993) Matrix cracking of cross-ply ceramic composites. *Acta. Met. Mater.*, in press.

TABLE 1

Properties of cross-ply CMCs

Material	E_m (GPA)	τ (MPa)	S_u (MPa)	η	$c_f\sigma_f/\sigma$	$(t/L)_{crit}$
SiC/C	20	10	340	90	≈2	1.03
SiC/CAS	100	15	220	10	2	0.81
SiC/LAS	100	3	300	1	2	0.08

E_f=200GPa

R_f=7μm

c_f=0.4, c_m=0.6

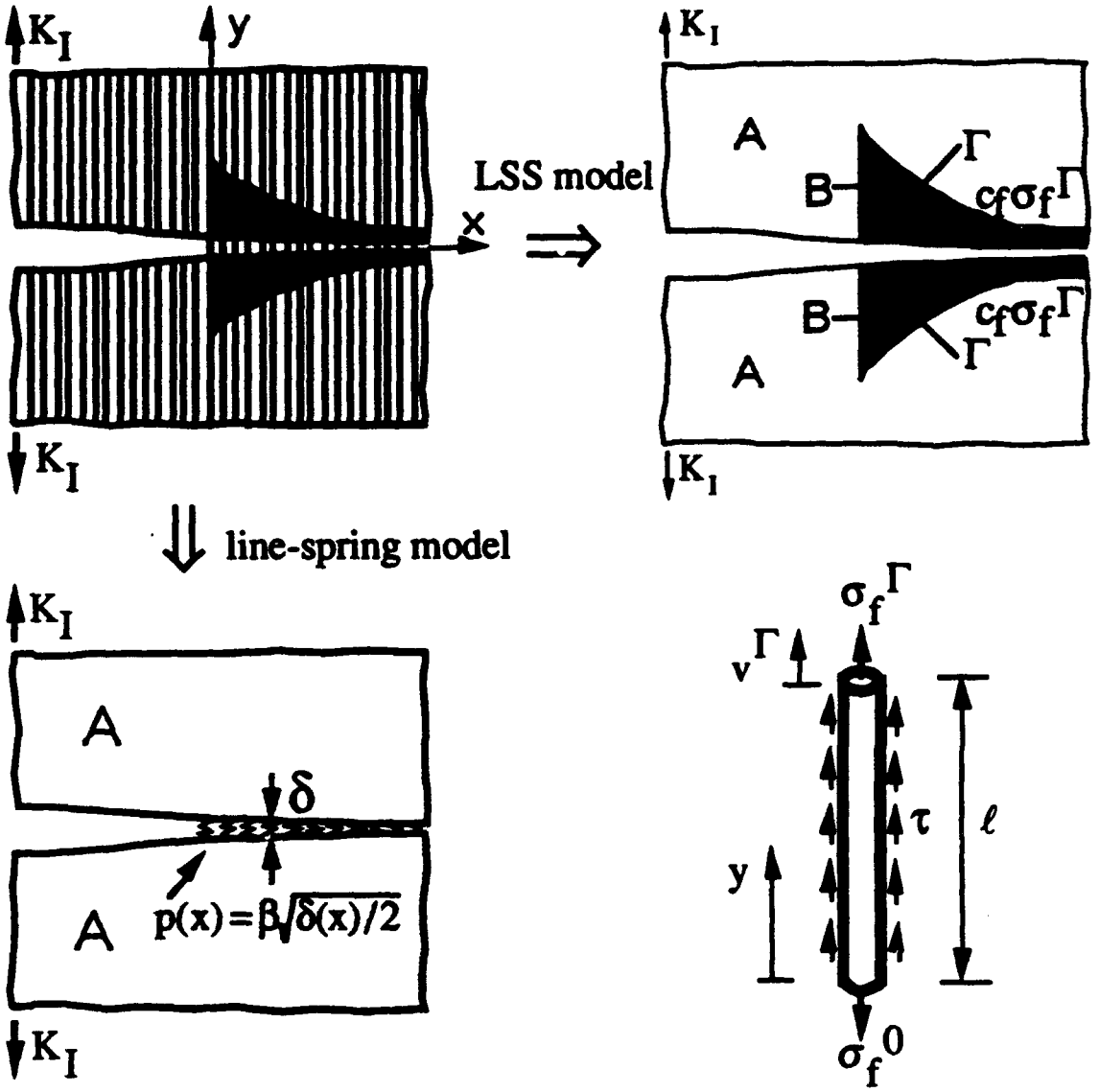

Fig. 1. A semi-infinite, unbridged through-crack with a semi-infinite, collinear bridged matrix crack. Conventions for the line-spring model and the large scale sliding model

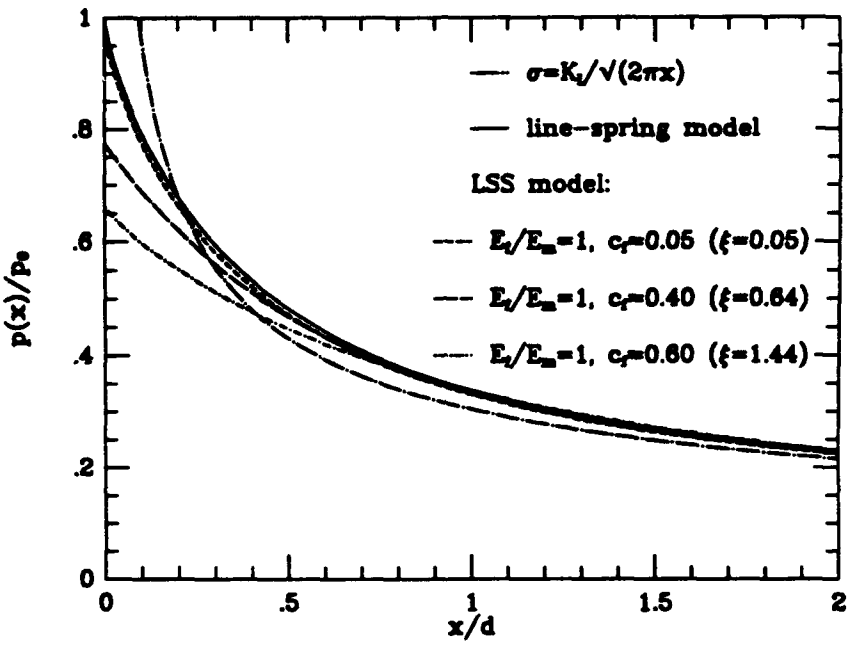

Fig.2. Bridging stress distributions ahead of the through-crack tip.

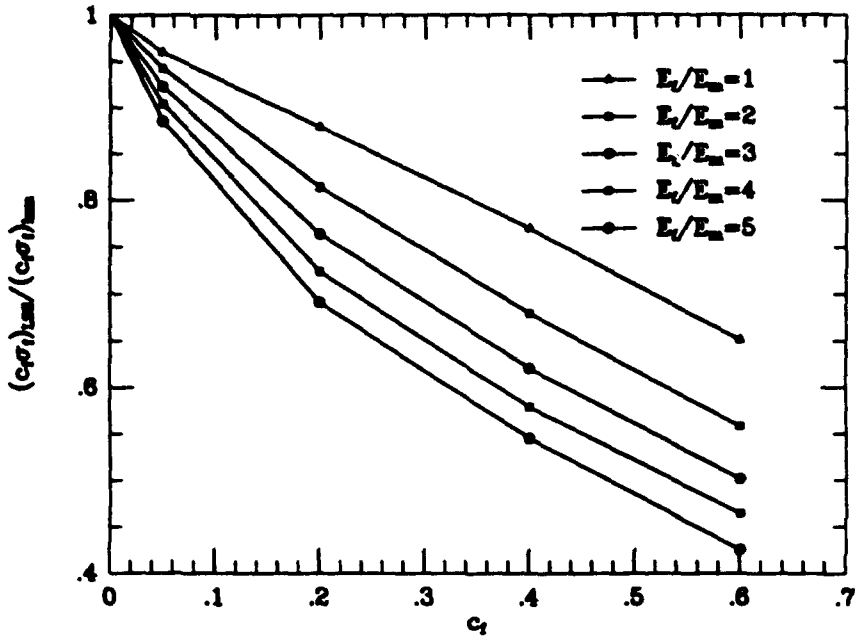

Fig. 3a. Ratio of the bridging stress directly ahead of the through-crack tip as predicted by the LSS model to that by the line-spring model (*i.e.*, p_0 given in (9)).

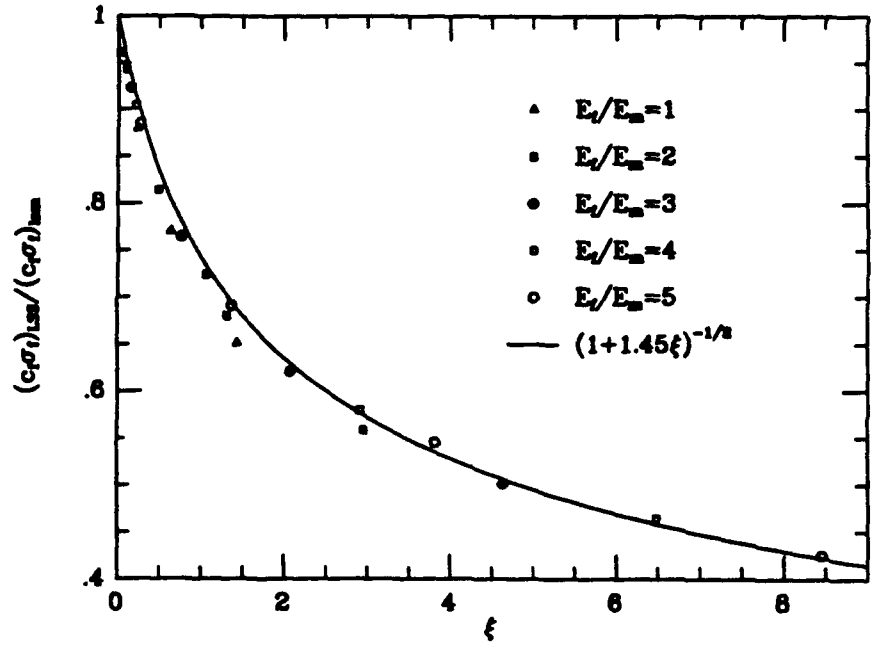

Fig. 3b. The ratio in a) plotted against ξ defined in (14). The solid line curve is an empirical fit to the computed values.

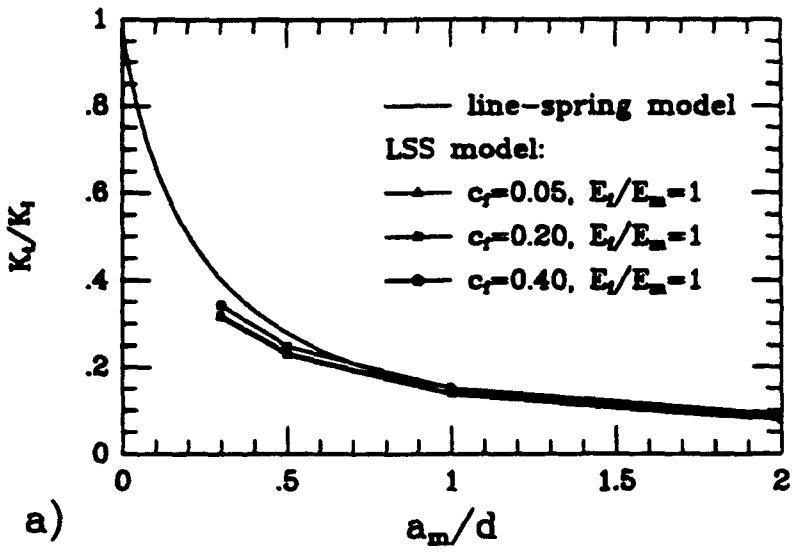

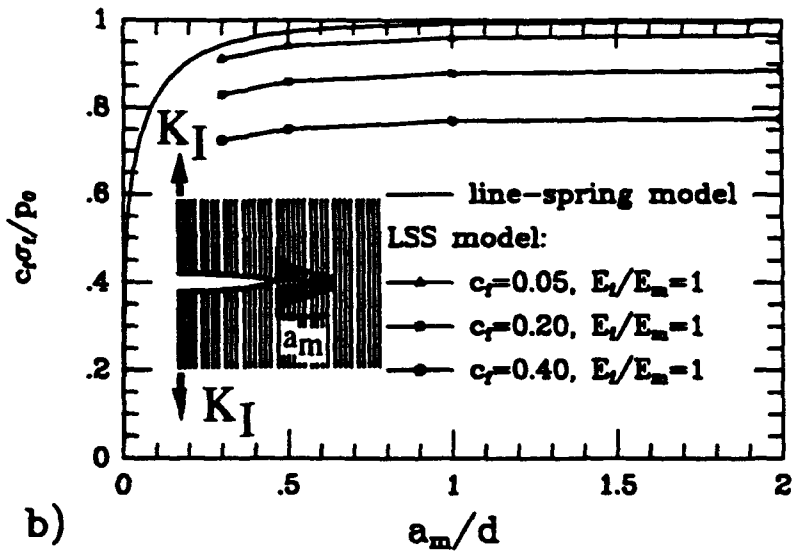

Fig. 4 a). Ratio of the stress intensity factor of the bridged matrix crack to remote stress intensity factor as a function of the normalized matrix crack length.

b). Ratio of the bridging stresses just ahead of the unbridged through-crack as a function of the normalized matrix crack length as predicted by the two models.

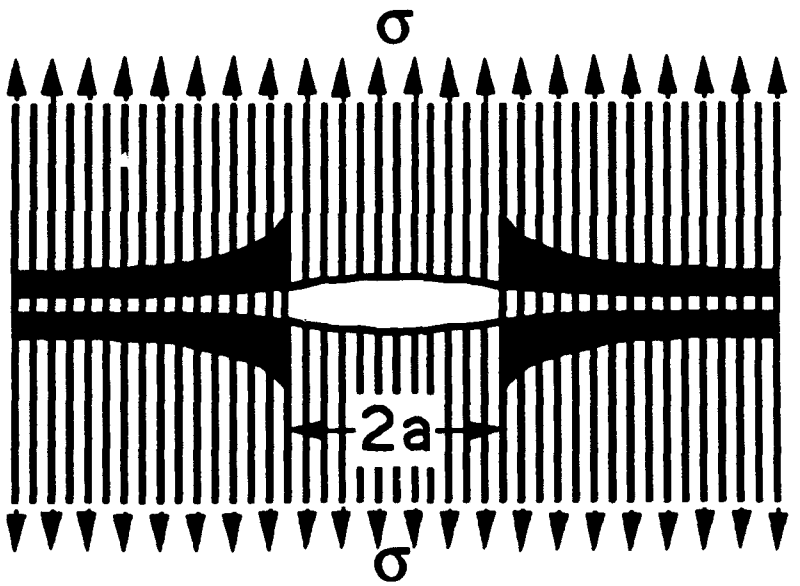

a). Finite length unbridged through-crack with collinear semi-infinite bridged matrix cracks.

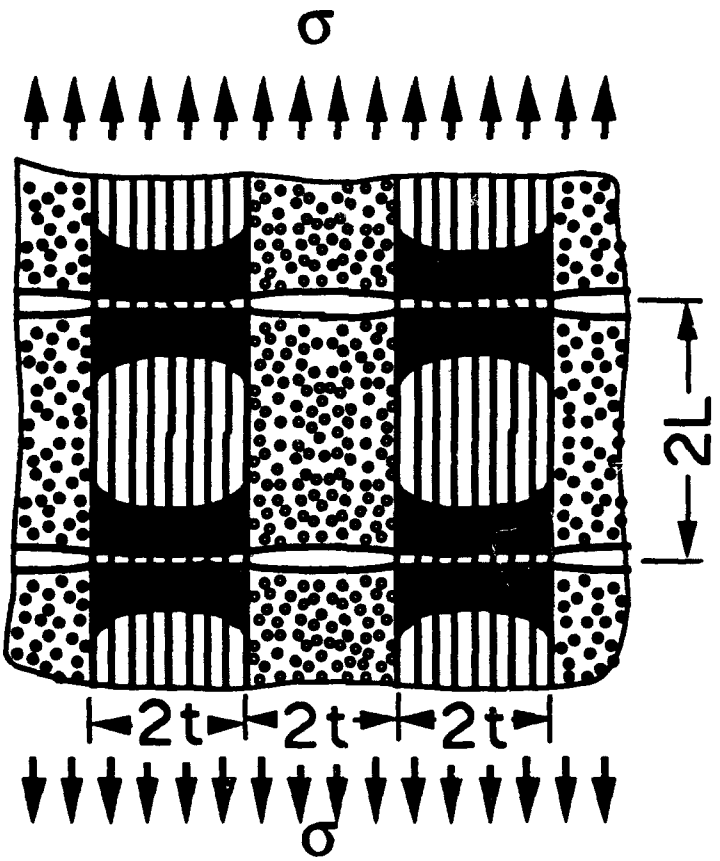

b). Transverse section of a cross-ply matrix with a uniform distribution of unbridged through-cracks in the 90° plies and bridged matrix cracks in the 0° plies.

Fig.5. Conventions

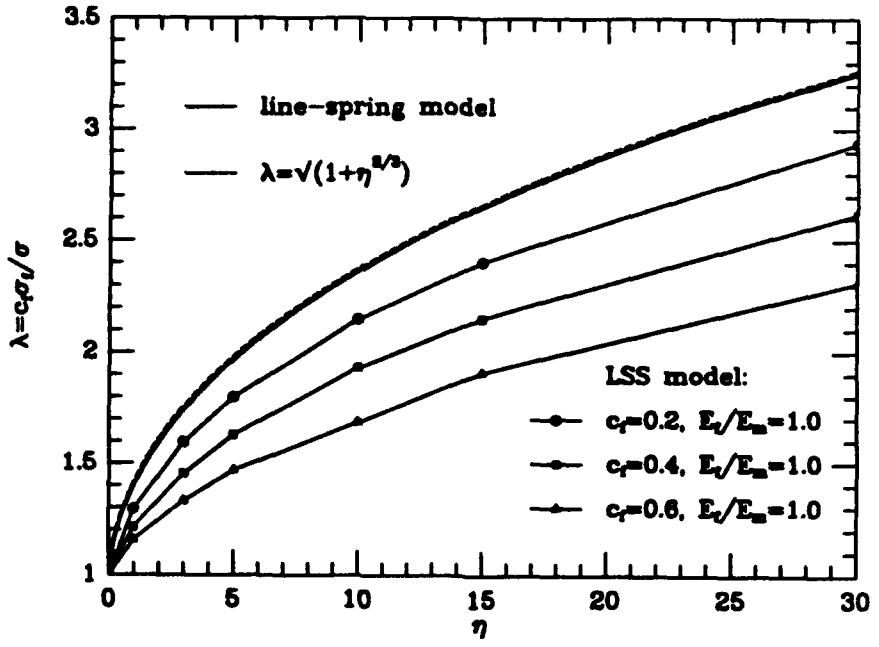

a). The effect of varying fiber volume fraction in the LSS model.

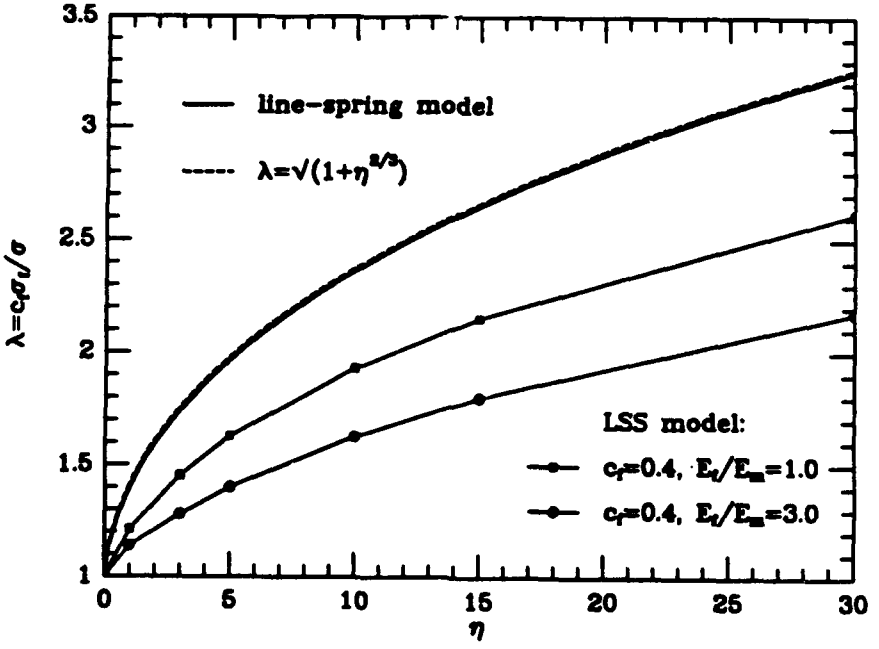

b). The effect of varying E_f/E_m in the LSS model.

Fig. 6. Stress concentration factor for the bridging stress just ahead of a finite length through-crack as a function of η defined in (16) as predicted by the two models.

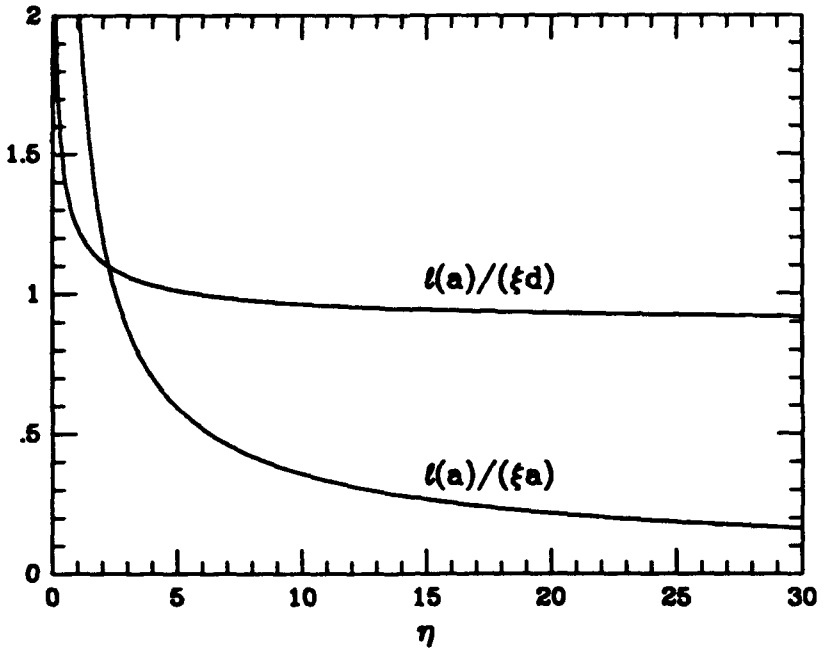

Fig. 7a. Normalized variation of the ratios of the height of the sliding zone at the tip of the through crack, $\ell(a)$, to the crack half-length, a, and the length quantity, d, defined in (10), as predicted by the line-spring model.

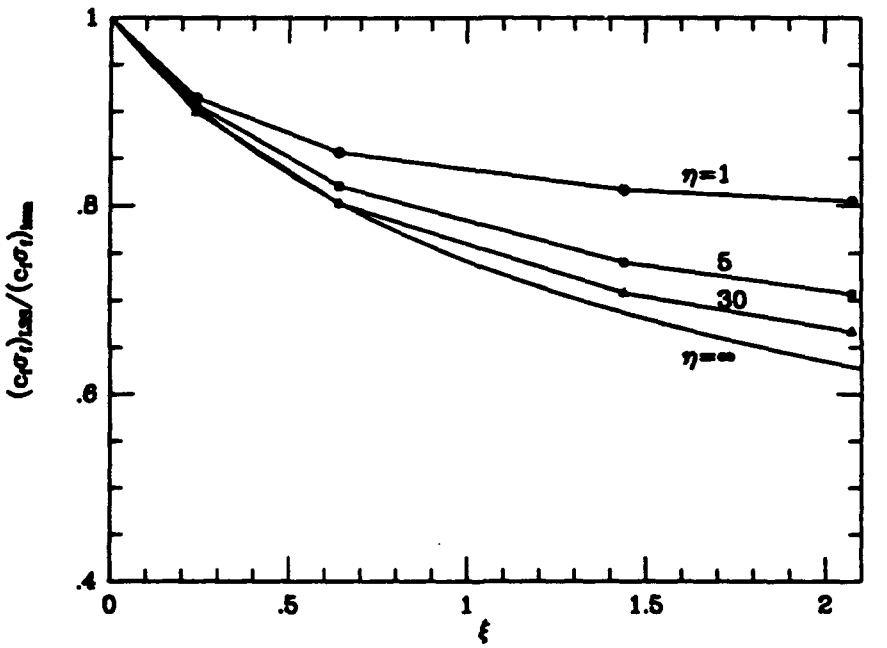

Fig. 7b. Ratio of the bridging stresses just ahead of the through-crack tip from the two models cross-plotted against ξ for several values of η.

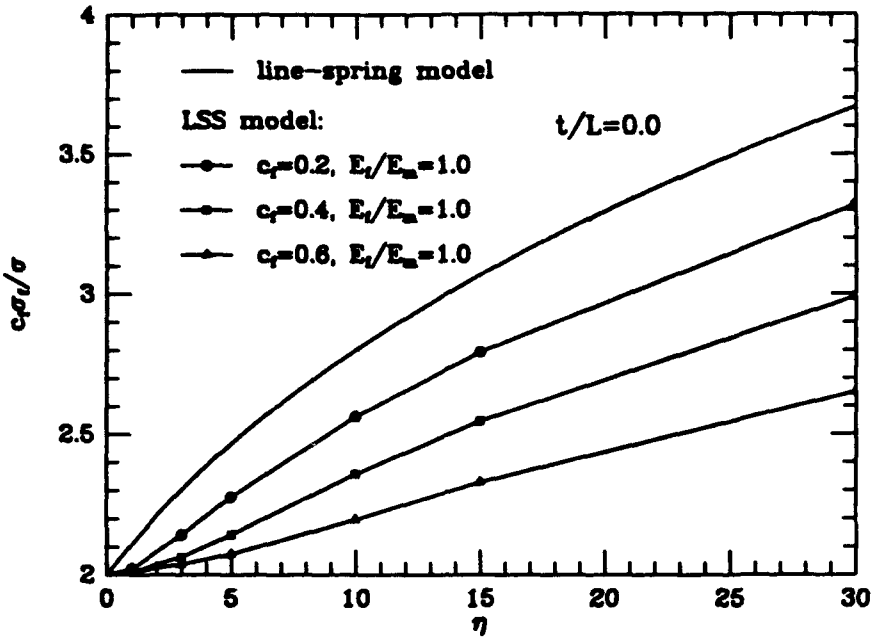

Fig. 8. Stress concentration factor for the bridging stresses at the interface between the 0° and 90° plies of a cross-ply composite as predicted by the two models for the case t/L=0. The line-spring prediction depends only on η, defined in (23); the LSS prediction depends on η and on constituent parameters such as c_f and E_f/E_m.

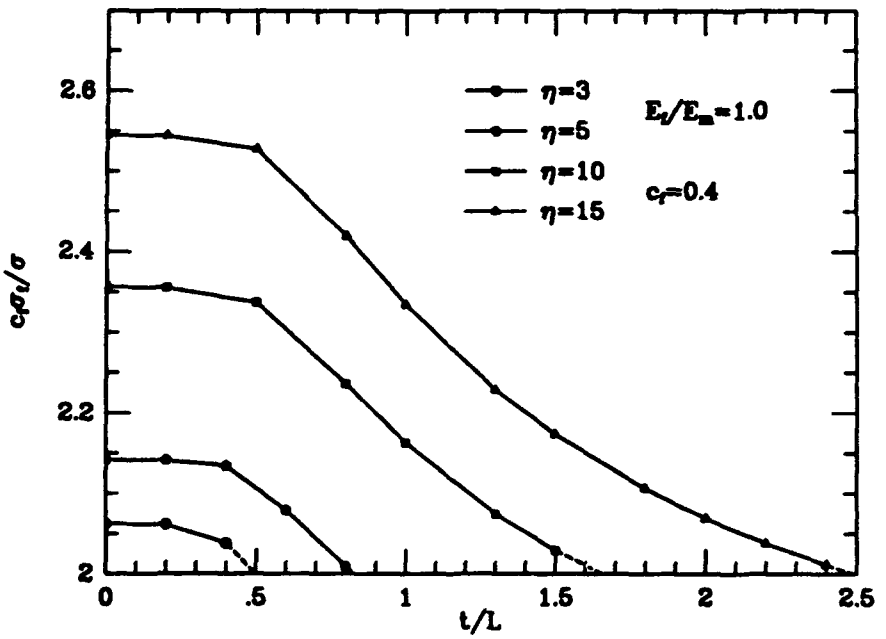

Fig. 9. Stress concentration factor for the bridging stress at the interface between the 0° plies and the 90° plies in a cross-ply composite as a function of crack density, t/L, as predicted by the LSS model. The intercept with the horizontal axis is given by (24).

J. Mech. Phys. Solids Vol. 42, No. 1, pp. 1-19, 1994.
Printed in Great Britain.

0022-5096/94 $6.00 + 0.00

ON THE TENSILE STRENGTH OF A FIBER-REINFORCED CERAMIC COMPOSITE CONTAINING A CRACK-LIKE FLAW

BERNARD BUDIANSKY and YINGQING LAWRENCE CUI
Division of Applied Sciences, Harvard University, Cambridge, MA 02138, U.S.A.

(*Received* 4 *May* 1993; *in revised form* 29 *August* 1993)

ABSTRACT

THE TENSILE STRENGTH of a fiber-reinforced ceramic composite containing a through-the-fiber flaw in the form of a sharp crack is studied. The strength of a brittle unreinforced ceramic containing a sharp crack of length $2a_0$, subjected to uniaxial load in the direction normal to the crack plane, is given by linear elastic fracture mechanics as $\sigma_s = K_m/\sqrt{\pi a_0}$, where K_m is the fracture toughness of the material. However, for a fiber-reinforced ceramic, the strength can only be determined on the basis of a full analysis of crack growth in the matrix and the failure of crack-bridging fibers. The tensile strength of a flawed ceramic material that is reinforced by fibers aligned in the direction perpendicular to the flaw surfaces is studied in this paper. Crack-bridging fibers are assumed to slip relative to the matrix when a critical interface shear stress is reached. The orthotropy of the composite produced by the presence of aligned fibers is rigorously accounted for in the analysis. The dependence of the composite tensile strength on fiber tensile strength, matrix toughness, flaw-size and frictional shear stress at the fiber–matrix interface is determined and described in terms of a universal set of non-dimensional parameters.

INTRODUCTION

THIS PAPER IS CONCERNED with the tensile strength of flawed, fiber-reinforced ceramics. On the basis of linear elastic fracture mechanics, an unreinforced brittle ceramic containing a sharp, two-dimensional flaw of length $2a_0$, loaded in the direction perpendicular to the faces of the flaw, has a tensile strength given by $\sigma_s = K_m/\sqrt{\pi a_0}$, where K_m is the fracture toughness of the material. However, the tensile strength of a fiber-reinforced ceramic can only be determined by a full analysis of a process involving matrix crack growth, frictional sliding along the fiber–matrix interfaces and failure of crack-bridging fibers. We shall study the configuration shown in Fig. 1, in which a large, aligned-fiber reinforced ceramic body containing an isolated center flaw of length $2a_0$ that cuts through the fibers is subjected to uniform remote tension in the fiber direction. We define the tensile strength as the maximum applied stress the composite can carry, and seek to determine this stress theoretically.

As in most previous studies the fibers are assumed to be held in the matrix by friction; that is, sliding between the fibers and the matrix is suppressed only if the interface frictional shear is less than some limiting stress τ. The brittle ceramic matrix is assumed to have a fracture toughness K_m, and, except near the tip of the matrix

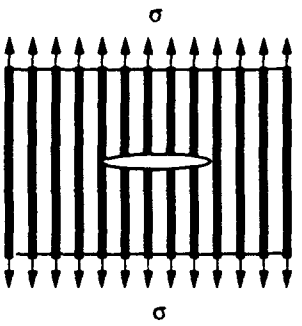

FIG. 1. Initial through-the-fibers crack-like flaw.

crack, the composite is treated as a homogeneous orthotropic elastic medium. The effects of crack-bridging fibers are taken into account by means of a spring model that embodies the additional assumption that the frictional resistance is low enough to permit long slip lengths relative to the fiber diameter. Failure of the composite is assumed to be associated with the fracture of crack-bridging fibers in the matrix crack plane and we assume that there is no statistical variation in fiber strength. It is further assumed that during the course of matrix crack extension leading to the final failure of the composite, no longitudinal splitting or shear banding takes place in the vicinity of the flaw tip. Both splitting and statistical variation in fiber strength may often be important, but we neglect them in the present study.

The mechanical behavior of both flawed and unflawed unidirectional fibrous composites has been a subject of research efforts for the past two decades. Matrix cracking without associated fiber failure is a distinctive tensile damage mechanism often observed in unidirectional fibrous ceramic composites. The tensile stress required for the steady-state propagation of a single, long matrix crack, known as the matrix cracking stress, was first evaluated by AVESTON *et al.* (1971) for the limits of large and small frictional shear resistance at the fiber–matrix interfaces. More recently, BUDIANSKY *et al.* (1986) extended these results to intermediate friction values. For the limiting case of very long initial flaws, the solution for tensile strength has been obtained by BUDIANSKY and AMAZIGO (1989) on the basis of the *small scale bridging* condition, wherein (see Fig. 2) the bridge length Δa prior to fiber failure is very small relative to the original flaw length $2a_0$. Although MARSHALL and COX (1987) have done extensive calculations for a composite with a flaw of arbitrary length, their presentation is quite complicated and it is difficult to extract the desired general, comprehensive results for the composite tensile strength from their paper.

There are many parameters governing the tensile failure of unidirectional composites, such as fiber tensile strength, matrix toughness, flaw-size, fiber and matrix elastic properties and fiber–matrix frictional shear stress. We shall, however, be able to determine the composite strength σ_c in terms of just the following three basic stress quantities that suffice to characterize the flawed composite:

- σ_0, the critical applied stress for the initiation of matrix cracking;
- σ_{mc}, the steady-state matrix-cracking stress; and

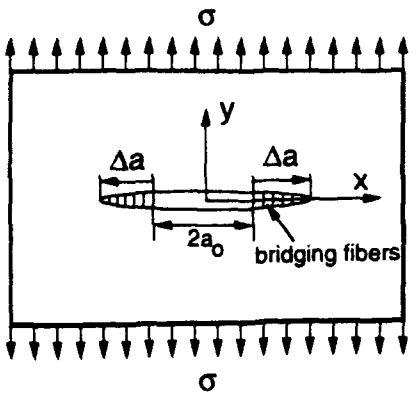

FIG. 2. Matrix cracking initiated from flaw tips.

- $\sigma_{fs} = c_f S$, the base fibers-only strength,

where S is the fiber fracture stress and c_f is the fiber volume concentration. More precisely, the ratio of σ_c to any one of these stresses depends on only *two* ratios of the three parameters. We start with a qualitative description of the matrix crack growth process that leads to failure of a flawed, unidirectional fiber composite.

DESCRIPTION OF FAILURE PROCESS

When a tensile stress σ is applied to the composite in the fiber direction (Fig. 1), failure due to a pre-existing, through-the-fibers flaw that is normal to the fibers always begins with growth of the crack in the matrix (Fig. 2), and ends with the fracture of bridging fibers. Consider a typical curve of applied stress σ vs matrix crack growth Δa, shown schematically in Fig. 3. Such a curve would be governed by the requirement that the average energy release rate along the matrix crack front must remain equal to the critical value for matrix crack extension. In the absence of fiber failure, a typical

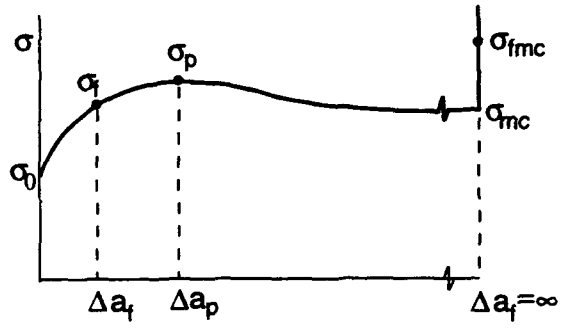

FIG. 3. Applied stress vs matrix crack growth.

$\sigma - \Delta a$ curve has the following qualitative features. Crack growth starts when the applied stress σ reaches the initiation stress σ_0, which is essentially a crack-size parameter. Due to the constraining effects of crack-bridging fibers, matrix crack growth requires increasing applied stress σ until a peak value σ_p is reached at $\Delta a = \Delta a_p$. Then the crack growth continues under decreasing applied σ, which approaches the steady-state matrix cracking stress σ_{mc} asymptotically for $\Delta a \to \infty$. (It is also conceivable that for sufficiently small values of the initiation stress σ_0, the applied stress σ may never reach a peak value at a finite Δa, but simply increases monotonically as it approaches the steady-state matrix-cracking stress σ_{mc} asymptotically.) After the matrix crack extends to infinity, the applied loading is supported entirely by the crack-bridging fibers, and the vertical line at $\Delta a = \infty$ indicates that further increase in σ is then possible.

Now consider fiber failure. Corresponding to each point on the $\sigma - \Delta a$ curve, there is a smeared-out bridging stress distribution $p(x)$ that has its maximum value $p(a_0)$ at the *original* flaw tip. Let Δa_f denote the amount of matrix crack growth corresponding to the first-fiber-failure criterion $p(a_0) = c_f S$, and if $\Delta a_f < \infty$, let σ_f be the value of the associated applied load. Similarly, for the composite containing a matrix crack that has grown to infinity from each edge of the original flaw (Fig. 4), let σ_{fmc} denote the value of the applied stress σ that gives $p(a_0) = c_f S$. In both cases, we find that maintaining the applied load σ at the value that produces the first fiber failure results in the failure on the matrix crack plane of all the fibers. Accordingly, the strength σ_s of the composite is set by one of the following three conditions:

(i) the flaw-tip fibers fail during *increasing* applied stress at a value of applied stress $\sigma_f < \sigma_p$ and $\Delta a_f < \Delta a_p$; then $\sigma_s = \sigma_f$;

(ii) the applied stress reaches the peak value σ_p without the occurrence of fiber failure, and σ_p exceeds the value of the stress σ_{fmc} needed to produce flaw-tip fiber failure when the crack is infinitely long; then $\sigma_s = \sigma_p$;

(iii) the matrix crack extends to infinity without fiber failure, and σ_p is less than σ_{fmc}; then $\sigma_s = \sigma_{fmc}$.

A complete determination of the strength of flawed composites will therefore require

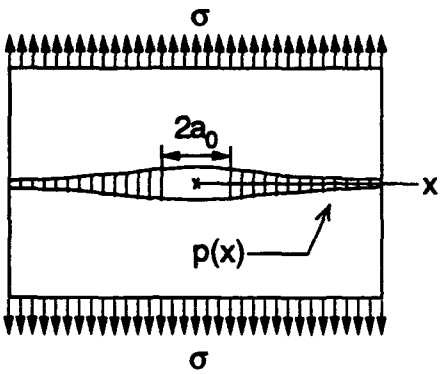

FIG. 4. Auxiliary problem: fully cracked matrix.

consideration of both the transient crack-growth problem of Fig. 2 and the auxiliary problem of the fully cracked composite shown in Fig. 4.

Matrix Cracking: Initiation, Growth and Steady-state

Crack growth criterion

We shall now discuss an appropriate criterion for matrix crack growth in an aligned-fiber composite (Fig. 1). What we seek is a criterion based on the stress-intensity factor of a crack, bridged or unbridged, in an equivalent, uniform, orthotropic (but transversely isotropic) material (Fig. 2). Consider the plane-strain energy release rate $\mathcal{G}$ for a Mode-I crack lying in the plane of transverse isotropy. We can write

$$\mathcal{G} = \frac{1-\nu^2}{AE} K_I^2 \tag{1}$$

where K_I is the conventional stress-intensity factor, E is the Young's modulus for longitudinal tension normal to the crack plane, ν is the associated Poisson's ratio (for the ratio of transverse contraction to longitudinal extension), and A is a dimensionless factor that characterizes the orthotropy. We will assume that matrix crack growth occurs when the orthotropic energy release rate $\mathcal{G}$, given by (1), satisfies the condition

$$\mathcal{G} = (1-c_f)\mathcal{G}_m \tag{2}$$

where $\mathcal{G}_m$ is the critical energy release rate for fracture in the *matrix*, given by

$$\mathcal{G}_m = \frac{1-\nu_m^2}{E_m} K_m^2 \tag{3}$$

in terms of the elastic constants of the matrix and its fracture toughness K_m. The factor $(1-c_f)$ accounts for the reduction in length of the edge of the matrix crack due to the presence of the aligned fibers. It follows that the critical orthotropic stress intensity factor K_{IC} for matrix cracking in the direction perpendicular to the direction of fibers in unidirectional fibrous ceramic composites is

$$K_{IC} = K_m \sqrt{\frac{AE(1-\nu_m^2)}{E_m(1-\nu^2)}(1-c_f)}. \tag{4}$$

The magnitude of A as a function of the plane-strain compliances of an orthotropic material follows from the formula given by Tada *et al.* (1985) for the energy release rate (see Appendix A). If we let E, E_f and E_m be the Young's moduli of the composite, fiber and matrix, respectively, and if we assume, for the sake of simplicity, that fibers and matrices have the same Poisson's ratio $\nu_f = \nu_m = \nu$, then E is given by the rule of mixtures formula $E = c_f E_f + (1-c_f)E_m$. The dependence of A on E_f/E_m and c_f for $\nu_f = \nu_m = 1/4$ has been calculated on the basis of the Hill (1965) self-consistent estimates for the effective compliances of an aligned-fiber composite having isotropic

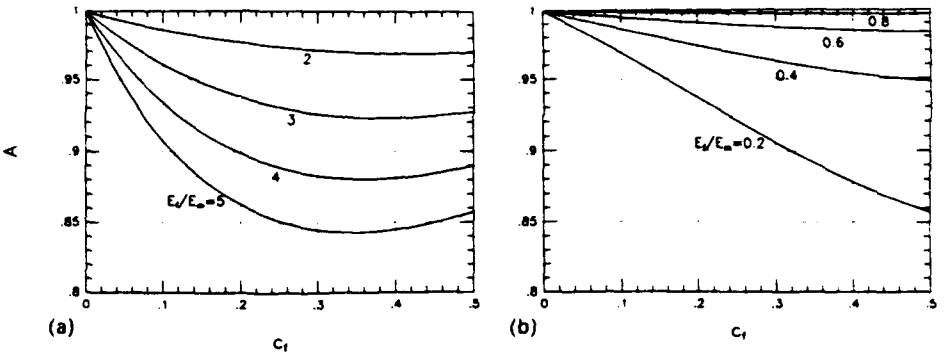

FIG. 5. Orthotropy factor A vs fiber concentration c_f: (a) $E_f/E_m \geq 1$; (b) $E_f/E_m \leq 1$.

constituents, and the results for A vs c_f are plotted in Fig. 5(a) for various values of $E_f/E_m > 1$. [These curves, and the associated formulas shown in Appendix A, correct errors in the earlier work by BUDIANSKY and AMAZIGO (1989).] Figure 5(b) shows A for several values of $E_f/E_m < 1$.

It is important to note that the parameter K_{IC} is a material property of the composite which encompasses information about matrix toughness, fiber volume concentration, the orthotropy induced by unidirectional fiber reinforcement and the moduli of the matrix and composites. In order to analyse the matrix cracking problem illustrated in Fig. 2, we will be calculating the orthotropic stress intensity factor K_I in the presence of both external loading and crack bridging fibers, and then using $K_I = K_{IC}$ as the criterion for matrix crack growth.

Matrix cracking initiation

For the special case of matrix cracking *initiation* in the configuration of Fig. 1, we can use the familiar formula $K_I = \sigma\sqrt{\pi a_0}$, which is valid for any anisotropic as well as isotropic 2D elastic body (SIH *et al.*, 1965). Setting $K_I = K_{IC}$ gives the matrix crack-growth initiation stress of the composite—one of our three basic stress parameters—as

$$\sigma_0 = K_{IC}/\sqrt{\pi a_0}. \tag{5}$$

Thus σ_0 may be regarded as a crack-length parameter, decreasing like $a_0^{-1/2}$. Note too, that for $\nu_f = \nu_m = \nu$, the initiation stress σ_0 is related to the corresponding strength σ_{c0} of an unreinforced, cracked monolithic ceramic of the same crack geometry by

$$\sigma_0 = \sqrt{\frac{A(1-c_f)E}{E_m}}\,\sigma_{c0}. \tag{6}$$

Matrix crack growth

Equations connecting the applied stress, the bridging-fiber stress distribution, and the matrix crack extension in the absence of fiber failure (Fig. 2) are presented in

Appendix B. In this formulation the orthotropic stress-intensity factor is kept equal to K_{IC}, and the smeared-out bridging fiber stress $p(x)$ is related to the displacement $v(x)$ of the upper crack face (Fig. 2) by

$$p(x) = \beta_{\searrow} v(x) \tag{7}$$

where the equivalent spring constant β is given by

$$\beta = \left\{ \frac{4c_f^2 E_f E^2 \tau}{R(1-c_f)^2 E_m^2} \right\}^{1/2} \tag{8}$$

where R is the fiber radius and τ is the interface slipping shear resistance stress. This relation follows from the assumption of "large" slip lengths adjacent to the crack faces and neglect of initial stresses (AVESTON *et al.*, 1971; BUDIANSKY *et al.*, 1986; BUDIANSKY and AMAZIGO, 1989). Various non-dimensional forms of the governing equations and their numerical solution are discussed in detail in Appendix B.

Steady-state matrix cracking

As already mentioned, when the matrix crack extension becomes large, the applied stress σ approaches the steady-state matrix cracking stress of AVESTON *et al.* (1971). Under the assumptions adopted, the steady-state matrix cracking stress σ_{mc} is given by

$$\sigma_{mc} = \left[\frac{6c_f^2(1-\nu_m^2)K_m^2 \tau E_f}{(1-c_f)RE} \right]^{1/3} \frac{E}{E_m}. \tag{9}$$

This is the second of the three basic stress parameters that define the composite; the third one, we remind the reader, is just $\sigma_{fs} = c_f S$.

MATRIX CRACK GROWTH AND PEAK STRESS

The analysis and calculations described in Appendix B provide the connections between the applied stress σ and the matrix crack extension Δa (Figs 2–3) shown non-dimensionally in Fig. 6. (These relations assume no fiber fracture, and so the basic stress parameter $c_f S$ is not involved.) The abscissa σ_0/σ_{mc} is a measure of the original flaw size. Note that for $\Delta a/a_0 > 0.5$ the curves giving σ/σ_{mc} vs σ_0/σ_{mc} cross each other in the vicinity of $\sigma_0/\sigma_{mc} = 0.95$. It follows that the peak stress σ_p during crack growth (see Fig. 3) must occur for $\Delta a_p/a_0 > 5$ whenever the flaw size corresponds to $\sigma/\sigma_{mc} < 0.94$; but for $\sigma_0/\sigma_{mc} > 1$, $\Delta a_p/a_0$ must be less than 0.5!

As discussed earlier, the strength σ_c of the flawed composite will, for some parametric ranges, be equal to the peak stress σ_p attained during matrix crack growth (Fig. 3). The results for σ_p obtained from the solution of the crack-growth equations are completely described by the curve in Fig. 7, which shows σ_p/σ_{mc} as a function of σ_0/σ_{mc}. (This curve is actually the upper envelope of the family of curves in Fig. 6.) Note that σ_p is almost always very close to either σ_0 or σ_{mc}. The accuracy to which

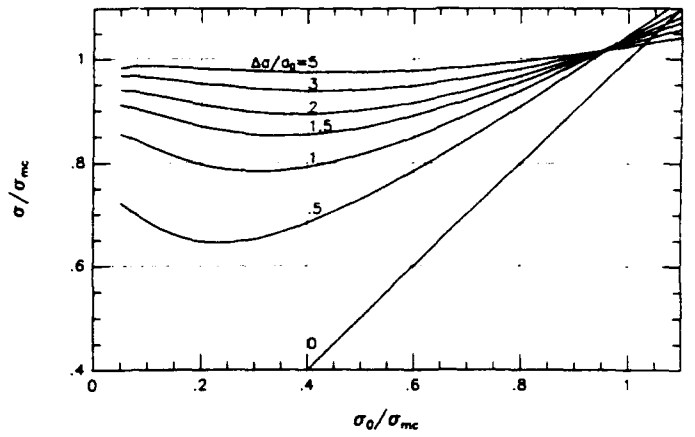

FIG. 6. Applied stress for various amounts of matrix crack growth.

we could calculate σ_p was much better than that of the associated values of Δa_p. It may be that σ_p becomes equal to σ_{mc} beyond a sufficiently large value of σ_0/σ_{mc}, corresponding to a monotonic increase in the value of the applied stress as the matrix crack grows to infinity, but the numerical calculations do not resolve this point. In any case, this is not important, and, as we shall see, parametric ranges for which the strength σ_c is given by σ_p turn out to be small.

FULLY CRACKED MATRIX: AN AUXILIARY PROBLEM FOR σ_{fmc}

We will find that there are significant ranges of the ratios of the three basic stress parameters for which failure of the flawed composite occurs only after the matrix

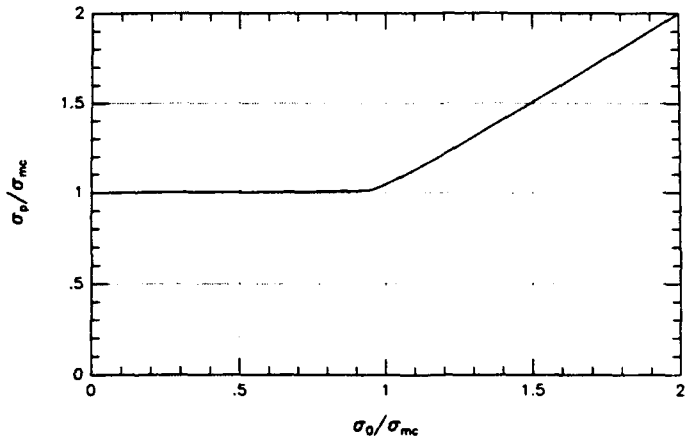

FIG. 7. Peak stress during matrix crack growth.

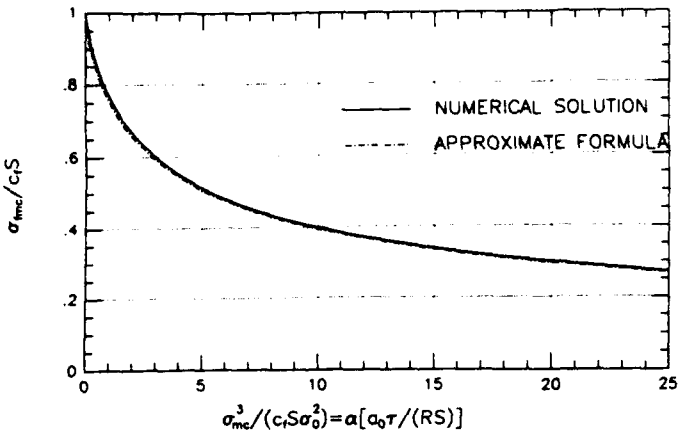

FIG. 8. Results for σ_{fmc} fully cracked matrix.

crack has become infinite, and then σ_c equals the strength σ_{fmc} of the fully cracked configuration sketched in Fig. 4. Clearly, σ_{fmc} is independent of the fracture toughness K_m of the matrix, but because of the bridging-fiber stress concentration induced at the edge of the original through-the-fibers crack, σ_{fmc} suffers a reduction from the base fibers-only strength c_fS it would have if the flaw were absent. An integral-equation formulation for the calculation of σ_{fmc} is given in Appendix C in terms of the non-dimensional combination

$$\tilde{a}_0 \equiv \frac{\sigma_{mc}^3}{c_f S\sigma_0^2} = \alpha\left[\frac{a_0\tau}{RS}\right] \tag{10}$$

of the basic stress parameters, where

$$\alpha = \left[\frac{6\pi(1-\nu^2)c_f EE_1}{A(1-c_f)^2E_m^2}\right]. \tag{11}$$

The parameter $\tilde{a}_0$, independent of K_m, may be regarded as a measure of the original flaw size. The solution found numerically for $\sigma_{fmc}/(c_fS)$ as a function of this parameter is shown by the solid curve in Fig. 8.† A remarkably accurate approximation to this result is given by

$$\tilde{a}_0 \equiv \frac{\sigma_{mc}^3}{c_f S\sigma_0^2} = 2\left[\left(\frac{\sigma_{fmc}}{c_fS}\right)^{-4/3} - \left(\frac{\sigma_{fmc}}{c_fS}\right)^{2/3}\right]^{3/2} \tag{12}$$

which provides the dot–dash curve in Fig. 8. This formula was discovered fortuitously, and we have not found a persuasive way to derive it.

†See SUO *et al.* (1992) as well as BAO and SUO (1992) for the results of similar calculations based on other bridging laws, and suggestions concerning the possibility of unifying these results over a wide range of bridging laws via energy concepts.

STRENGTH σ_c: RESULTS AND DISCUSSION

We can now put together the final results for the strength σ_c of the composite in terms of the basic stress parameters σ_0, σ_{mc} and $c_f S$, and we will display these results in several different forms to bring out various trends. By monitoring the magnitude of the bridging-fiber stress at the original flaw tip during the matrix crack growth, as calculated from the analysis of Appendix B, the magnitude of the load σ_c corresponding to fiber failure during this growth has been determined, and, on the basis of the discussion given in the earlier description of the failure process, the appropriate choices have been made for the assignment of σ_f, σ_p, or σ_{fmc} to the strength σ_c. This has been done on the basis of various non-dimensional forms of the governing equations, described in detail in Appendix B.

One non-dimensional form of the results for σ_c is

$$\frac{\sigma_c}{\sigma_0} = F_1\left(\frac{c_f S}{\sigma_{mc}}, \frac{\sigma_0}{\sigma_{mc}}\right) \tag{13}$$

where σ_c/σ_0 may be regarded as a *modified strengthening ratio* provided to a flawed ceramic by aligned-fiber reinforcement. {The *actual* strengthening ratio is σ_c/σ_{c0}, to which σ_c/σ_0 [see (6)] is a fair approximation.} We prefer, however, to introduce the parameter

$$\Lambda = \sqrt{1+2\left(\frac{c_f S}{\sigma_{mc}}\right)^3} \tag{14}$$

in lieu of $c_f S/\sigma_{mc}$ in exhibiting the results for the strength of the composite, and we have done so in Fig. 9, where we show curves of σ_c/σ_0 vs Λ for various values of σ_0/σ_{mc}. The quantity Λ is the *modified toughening ratio* K/K_{IC} found by BUDIANSKY

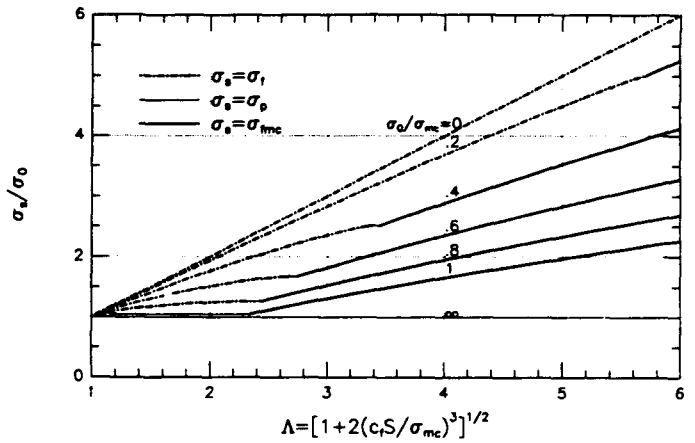

FIG. 9. Modified strengthening ratio σ_c/σ_0 for various values of σ_0/σ_{mc}. The parameter Λ is the modified toughening ratio for small-scale bridging.

and AMAZIGO (1989) for the case of *small-scale bridging*. The significance of Λ is that it provides the modified strengthening ratio of a composite containing a very long initial crack, which corresponds to a very small value of σ_0/σ_{mc}. Thus, $\sigma_c/\sigma_0 = \Lambda$ for $\sigma_0/\sigma_{mc} = 0$, and this is an upper bound to σ_c/σ_0 for all finite values of σ_0/σ_{mc}. In effect, the sequence of curves in Fig. 9 shows quantitatively how much the small-scale-bridging strengthening due to aligned-fiber reinforcement is reduced for flaws of decreasing size.

As indicated by the key to the line types in Fig. 9, the strength σ_c, at each fixed value of σ_0/σ_{mc}, always starts out equal to σ_1 at low values of Λ; for a sufficiently large value of Λ, this first range, associated with fiber failure during matrix crack growth (Fig. 3), merges into a generally small interval in Λ for which σ_c is given by the "peak" stress σ_p; and then, beyond another critical value of Λ, failure at $\sigma_c = \sigma_{tmc}$ in the fully cracked matrix becomes the rule. Note that because σ_0/σ_{mc} does not depend on S, each of the curves of Fig. 9 can be interpreted as showing the influence of fiber strength on the composite strength.

The results for σ_c have also been computed in the form

$$\frac{\sigma_c}{\sigma_0} = F_2\left(\frac{c_f S}{\sigma_{mc}}, \frac{c_f S}{\sigma_0}\right) \tag{15}$$

and Fig. 10 shows σ_c/σ_0 vs Λ for various fixed values of $c_f S/\sigma_0$, which may be regarded as a crack length parameter that is an increasing function of the initial flaw size. Since $c_f S/\sigma_0$ is independent of the shear stress τ, each curve in Fig. 10 shows how the fiber-matrix interface friction affects the strength. The matrix cracking stress σ_{mc} is an increasing function of τ [equation (9)], and therefore the small-scale-bridging toughening ratio Λ gets larger as τ goes down. The curves in Fig. 10 show that for flaws of finite size the strengthening generally remains an increasing function of $1/\tau$, except for some insignificant isolated parametric ranges.

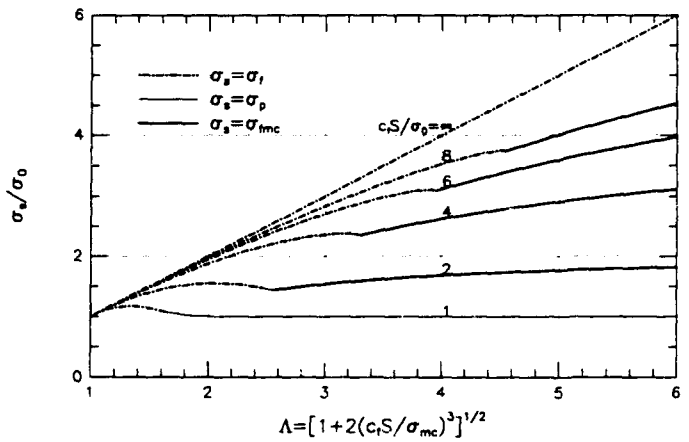

FIG. 10. Modified strengthening ratio σ_c/σ_0 for various values of $c_f S/\sigma_0$. The parameter Λ is the modified toughening ratio for small-scale bridging.

In both Figs 9 and 10, displaying the ratio σ_s/σ_0 as the dependent variable provides the answer to the question: how much has the flawed matrix been strengthened by aligned fibers? An alternative viewpoint is to contemplate the base fibers-only strength $\sigma_{fs} = c_f S$ as a starting point of reference, and study what happens to the ratio $\sigma_s/c_f S$ under the degrading influence of a flaw *and* the reinforcing presence of the matrix. A useful representation of the results is in the form

$$\frac{\sigma_s}{c_f S} = F_3\left(\frac{\sigma_{mc}^3}{c_f S \sigma_0^2}; \frac{\sigma_{mc}}{c_f S}\right) \tag{16}$$

as shown in Fig. 11. The abscissa $\bar{a}_0$ is a flaw-size parameter that is independent of the matrix toughness K_m, and the increasing values of $\sigma_{mc}/c_f S$ labelling each curve reflect increasing values of K_m. The curve for $\sigma_{mc}/c_f S = 0$ reproduces the one in Fig. 7; for $K_m = 0$, the matrix will crack out to infinity as soon as a load is applied, and then the strength will be given by σ_{fmc}. The curves in Fig. 11 show that σ_{fmc} constitutes a lower bound to the strength, and that for reasonable finite values of $\sigma_{mc}/(c_f S)$ only modest increases above this value are obtained. In terms of the parameters of (16) and Fig. 11, the identity of the failure mode can exhibit a curious progression. Thus, for $\sigma_{mc}/c_f S = 0.75$, σ_s is given by σ_f for large flaw size; then, as a_0 decreases, $\sigma_s = \sigma_p$ over for a tiny interval of the abscissa; this is followed by $\sigma_s = \sigma_{fmc}$ along the bottom curve; and finally, below a critical value of flaw size, $\sigma_s = \sigma_p$ again. Actually, values of the abscissa much below unity are unlikely to be in a range of practical interest.

The formula (12) suggests that the results of Fig. 11 might usefully be replotted as shown in Fig. 12, wherein $\sigma_s/(c_f S)$ is shown over the full practical range of $(\bar{a}_0)^{-1/2}$. Note that for $\sigma_{mc}/c_f S$ greater than some critical value between 0.75 and 0.85, failure always occurs during finite extension of the matrix crack.

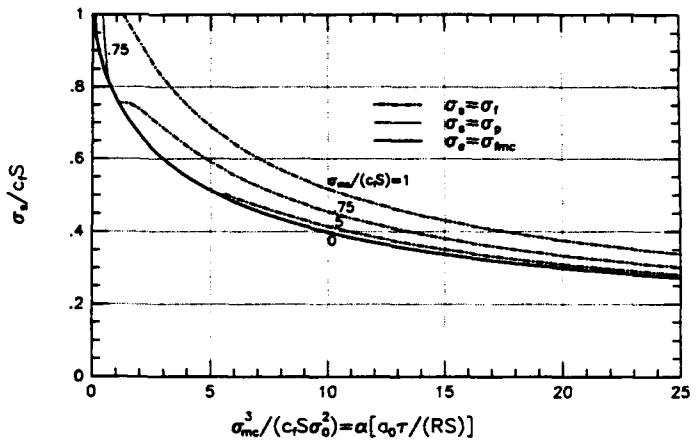

FIG. 11. Strength ratio $\sigma_s/(c_f S)$ vs $\bar{a}_0 \equiv \sigma_{mc}^3/c_f S\sigma_0^2$ for various values of $\sigma_{mc}/(c_f S)$. The constant α is defined in (11).

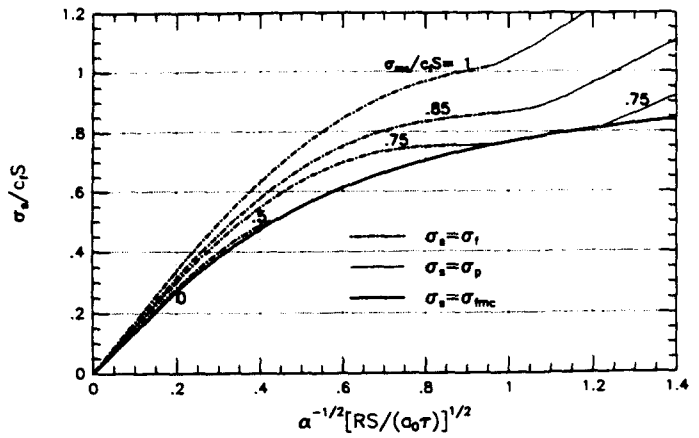

FIG. 12. Strength ratio $\sigma_\infty/(c_fS)$ vs $(\bar{a}_0)^{-1/2} \equiv (\sigma_{mc}^2/c_fS\sigma_0^2)^{-1/2}$ for various values of $\sigma_{mc}/(c_fS)$. The constant α is defined in (11).

NUMERICAL EXAMPLES

To provide some quantitative feel for the theoretical results of Figs 9–12, we present a set of numerical examples for a well-documented ceramic composite system that was used in matrix cracking experiments by MARSHALL *et al.* (1985), consisting of silicon-carbide fibers in a lithium-alumino-silicate glass matrix. The nominal values of pertinent parameters were

$$\left.\begin{aligned} c_f &= 0.5 \\ \nu_m = \nu_f &= 0.25 \\ E_m &= 85\,\text{GPa} \\ E_f &= 200\,GPa \end{aligned}\right\} \Rightarrow E = 142.5\,\text{GPa} \qquad \begin{aligned} R &= 8\,\mu\text{m} \\ K_m &= 2\,\text{MPa m}^{1/2} \\ S &= 1\,\text{GPa} \\ \tau &= 2\,\text{MPa}. \end{aligned}$$

On the basis of this data, we get

$$A = 0.95, \quad \sigma_{mc} = 265\,\text{MPa}, \quad \Lambda = 3.8.$$

Table 1 shows the strength predictions of the present analysis, for several values of flaw length $2a_0$ and the corresponding values of σ_0, c_fS/σ_0 and $\bar{a}_0$. Numerical results

TABLE 1

$2a_0$ (μm)	σ_0 (MPa)	c_fS/σ_0	$\bar{a}_0$	σ_∞ (MPa)	σ_s/σ_0	$\sigma_\infty/(c_fS)$	Type
32.5	250	2	0.60	415	1.7	0.83	σ_{fmc}
130	125	4	2.38	319	2.6	0.64	σ_{fmc}
290	83.3	6	5.36	257	3.1	0.51	σ_f
520	62.5	8	9.53	213	3.4	0.43	σ_f

for σ_c are given, as well as the ratios σ_c/σ_0 and $\sigma_c/(c_f S)$; the failure type (i.e. σ_f, σ_p or σ_{tmc}) is listed.

In these examples the strength σ_{s0} of the unreinforced ceramic is about 10% higher than σ_0 [equation (6)]. Thus, the composite containing a flaw (or sharp notch) about 1.2 mm in length is strengthened considerably (by about a factor of three) by the presence of aligned fibers that do not bridge the initial flaw. But the failure mode, of the σ_f type, remains catastrophic, occurring before the onset of widespread matrix cracking at σ_{mc}. In contrast, the strength of the matrix with the smallest of the flaws considered above is increased by only about 50%, but this is enough to raise σ_c above σ_{mc}.

Concluding Remarks

Our study has produced theoretical results for the tensile strength of a flawed, aligned-fiber ceramic composite in succinct non-dimensional forms that encompass the effects of a large number of geometrical and physical variables. The results for the strength σ_c, displayed in terms of three basic characterizing reference stresses σ_0, σ_{mc} and $c_f S$ in Figs 9–12, may provide a basis for the micromechanical design and analysis of such materials, as well as for the formulation of design criteria. A useful lower bound to the strength σ_c is given by the post-matrix-cracking failure stress σ_{tmc} provided by Fig. 8.

The present study provides a sound foundation from which to proceed to elaborations that include the effects of initial stress and statistical variations in the fiber strength. The latter, in particular, can lead to intra-matrix fiber failures at locations off the crack faces, and the consequent higher fiber-pullout lengths during failure can produce substantial increases in predicted composite strengths (Thouless and Evans, 1988). However, the extent to which design should rely on beneficial effects of statistical dispersions in fiber strength remains an open question. Finally, it should be emphasized that the possible intervention of failure modes not considered here, such as longitudinal splitting or shear localization, requires investigation.

Acknowledgements

We are grateful to Professor A. G. Evans for his comments on this work and to Professor Z. Suo for an illuminating discussion. This work was partially supported by the DARPA University Research Initiative (Subagreement P.O. # VB38639-0 with the University of California, Santa Barbara, ONR Prime Contract N00014-86-K-0753 and Subagreement P.O. # KK3007 with the University of California, Santa Barbara, ONR Prime Contract N00014-92-J-1808), the Office of Naval Research (Contract N00014-90-J-1377), and by the Division of Applied Sciences, Harvard University.

References

Aveston, J., Cooper, G. A. and Kelly, A. (1971) Single and multiple fracture. Proc. National Physical Laboratory, Guildford, *The Properties of Fiber Composites*, pp. 15-26. IPC Science and Technology, U.K.

Bao, G. and Suo, Z. (1992) Remarks on crack-bridging concepts. *Appl. Mech. Rev.* **45**, 355–366.

Budiansky, B. and Amazigo, J. C. (1989) Toughening by aligned, frictionally constrained fibers. *J. Mech. Phys. Solids* **37**, 93–109.

Budiansky, B., Hutchinson, J. W. and Evans, A. G. (1986) Matrix fracture in fiber-reinforced ceramics. *J. Mech. Phys. Solids* **34**, 167–189.

Erdogan, F. and Gupta, G. D. (1972) On the numerical solution of singular integral equations. *Q. Appl. Math.* **29**, 525–534.

Hill, R. (1965). Theory of mechanical properties of fiber-strengthened materials—III. Self consistent model. *J. Mech. Phys. Solids* **13**, 189–198.

Marshall, D. B., Cox, B. N. and Evans, A. G. (1985) The mechanics of matrix cracking in brittle-matrix fiber composite. *Acta Metall.* **33**, 2013–2021.

Marshall, D. B. and Cox, B. N. (1987) Tensile fracture of brittle matrix composites: influence of fiber strength. *Acta Metall.* **35**, 2607–2619.

Sih, G. C., Paris, P. C. and Irwin, G. R. (1965) On cracks in rectilinearly anisotropic bodies. *Int. J. Fracture Mech.* **1**, 189–203.

Suo, Z., Ho, S. and Gong, X. (1992) Notch ductile-to-brittle transition due to localized inelastic band. *ASME J. Engng Mater. Technol.* **115**, 319–326.

Tada, H., Paris, P. and Irwin, G. R. (1985) *The Stress Analysis of Cracks Handbook*. Del Research, St Louis.

Thouless, M. D. and Evans, A. G. (1988) Effects of pull-out on the mechanical properties of ceramic–matrix composites. *Acta Metall.* **36**, 517–522.

Appendix A: Orthotropic Factor A

This Appendix corrects the one with the same title in the paper by Budiansky and Amazigo (1989), in which several blunders occur.

We consider a transversely isotropic, orthotropic elastic material satisfying the stress–strain relations

$$\begin{cases} \varepsilon_x = \sigma_x/\bar{E} - \nu\sigma_y/E - \tilde{\nu}\sigma_z/\bar{E} \\ \varepsilon_y = -\nu\sigma_x/\bar{E} + \sigma_y/E - \nu\sigma_z/E \\ \varepsilon_z = -\tilde{\nu}\sigma_x/\bar{E} - \nu\sigma_y/E + \sigma_z/\bar{E} \\ \gamma_{xy} = \tau_{xy}/G. \end{cases} \tag{A1}$$

According to Tada *et al.* (1985), quoting results of Sih *et al.* (1965), the plane-strain energy release rate at the edge of a mode-I crack lying in the transversely isotropic x–z plane is

$$\mathcal{G} = CK_I^2 \tag{A2}$$

where

$$C = \sqrt{\frac{A_{11}A_{22}}{2}}\left[\sqrt{\frac{A_{22}}{A_{11}}} + \frac{2A_{12}+A_{66}}{2A_{11}}\right] \tag{A3}$$

and the A_{ij} are defined by the plane-strain constitutive relations

$$\begin{cases} \varepsilon_x = A_{11}\sigma_x + A_{12}\sigma_y \\ \varepsilon_y = A_{12}\sigma_x + A_{22}\sigma_y \\ \gamma_{xy} = A_{66}\tau_{xy}. \end{cases} \tag{A4}$$

The A_{ij} are given by

$$A_{11} = \frac{1-\bar{\nu}^2}{\bar{E}}, \quad A_{12} = -\frac{\nu(1+\bar{\nu})}{E}, \quad A_{22} = \frac{1-\nu^2\bar{E}/E}{E}, \quad A_{66} = \frac{1}{G}. \tag{A5}$$

Hence, in the representation

$$\mathcal{G} = \frac{(1-\nu^2)K_I^2}{AE} \tag{A6}$$

we have

$$A = \frac{1-\nu^2}{CE}. \tag{A7}$$

For the aligned fiber composite, the elastic constants E, $\bar{E}$, G, $\bar{\nu}$ have been calculated for the case $\nu = \nu_f = \nu_m$ in terms of c_f, E_m and E_f, and the resulting dependence of A on c_f is plotted in Figs 5(a) and (b) for various values of E_f/E_m.

APPENDIX B: FORMULATION AND NUMERICAL SOLUTION FOR MATRIX CRACKING INITIATED FROM A CRACK-LIKE FLAW

Formulation

This section details the formulation of an integral equation and an associated scalar equation for matrix cracking that is initiated from a pre-existing flaw. The matrix crack together with the original flaw is modeled as a crack of length $2(a_0+\Delta a)$ (see Fig. 2) with a cohesive, bridged zone of length Δa at both ends. The upper crack face displacement is

$$v(x) = \frac{2(1-\nu^2)}{AE}\sigma\sqrt{(a_0+\Delta a)^2-x^2} - \frac{2(1-\nu^2)}{\pi AE}\int_{a_0}^{a_0+\Delta a} p(\xi) \times \log\left|\frac{\sqrt{(a_0+\Delta a)^2-x^2}+\sqrt{(a_0+\Delta a)^2-\xi^2}}{\sqrt{(a_0+\Delta a)^2-x^2}-\sqrt{(a_0+\Delta a)^2-\xi^2}}\right| d\xi. \tag{B1}$$

Except for the factor A, the first term is the standard crack face displacement due to remote uniform loading of an isotropic material. The second term is the crack face closure displacement due to the bridging stresses, and, again except for A, is obtained by superposition of the crack face displacements due to concentrated loading on crack surfaces given by TADA *et al.* (1985). The orthotropy factor A, defined by (1) in terms of energy release rate, correctly takes orthotropy into account in this expression for displacement. (This can most easily be shown by weight-function considerations.) An integral equation for $p(x)$ may be obtained by equating $v(x)$ in (B1) to $[p(x)/\beta]^2$ in accordance with the bridging law (7), and then differentiation with respect to x gives

$$p(x)\frac{dp(x)}{dx} = -\frac{2\beta^2(1-\nu^2)x}{\pi AE\sqrt{(a_0+\Delta a)^2-x^2}} \times \left[\int_{a_0}^{a_0+\Delta a}\frac{\sqrt{(a_0+\Delta a)^2-\xi^2}}{\xi^2-x^2}p(\xi)\,d\xi + \frac{\pi\sigma}{2}\right] \quad \text{for} \quad a_0 \leqslant x \leqslant a_0+a. \tag{B2}$$

A scalar equation that must be satisfied simultaneously with (B2) is obtained by asserting that the orthotropic stress intensity factor K_I [which depends on σ and $p(x)$ in the same way as for isotropy] must remain equal to K_{IC}. Hence (TADA *et al.*, 1985)

$$K_I = \sigma_\infty \sqrt{\pi(a_0+\Delta a)} - 2\sqrt{\frac{a_0+\Delta a}{\pi}} \int_{a_0}^{a_0+\Delta a} \frac{p(x)}{\sqrt{(a_0+\Delta a)^2 - x^2}}\,dx = K_{IC}. \tag{B3}$$

By making the substitutions

$$\begin{cases} x = (a_0+\Delta a)s & p(x) = \sigma_{mc} q(s) \\ \alpha = \dfrac{1}{1+\Delta a/a_0} & \sigma = \Sigma \sigma_{mc} \quad \sigma_0 = \Sigma_0 \sigma_{mc} \end{cases} \tag{B4}$$

one may express the governing equations (B2) and (B3) in the normalized forms

$$\sqrt{1-s}\, q(s) \frac{dq(s)}{ds} = -\frac{4 f_1(s)}{3\pi^2 \alpha \Sigma_0^2} \left[\int_\alpha^1 f_2(t,s) q(t)\,dt + \frac{\pi}{2}\Sigma \right] \quad \text{for} \quad \alpha \leqslant s \leqslant 1 \tag{B5}$$

$$\Sigma - \frac{2}{\pi} \int_\alpha^1 f_3(s) q(s)\,ds = \sqrt{\alpha}\,\Sigma_0 \tag{B6}$$

where

$$f_1(y) = \frac{y}{\sqrt{1+y}}, \quad f_2(t,s) = \frac{\sqrt{1-t^2}}{t^2-s^2} \quad \text{and} \quad f_3(s) = \frac{1}{\sqrt{1-s^2}}. \tag{B7}$$

For assigned values of α, (B5) and (B6) can be solved for Σ and $q(s)$ vs Σ_0, and thereby provide the results of Fig. 6, and the curve for σ_p/σ_{mc} in Fig. 7. The condition of fiber fracture at $x = a_0$ is $q(1) = c_f S/\sigma_{mc}$. Hence, for given values of Σ_0 and $c_f S/\sigma_{mc}$, (B5) and (B6) can be solved (by a Newton–Raphson technique) for the corresponding distributions $p(s)$ and magnitudes of α and $\Sigma_f = \sigma_f/\sigma_{mc}$ at fracture, and then the points for $\sigma_\infty/\sigma_0 = \sigma_f/\sigma_0 = \Sigma_f/\Sigma_0$ on the dot–dash curves of Fig. 9 can be plotted.

To get points on the dot–dash curves of Fig. 10, we assign values of $c_f S/\sigma_0$ as well as $c_f S/\sigma_{mc}$, replace Σ_0 in (B5) and (B6) by the ratio of these quantities, and similarly solve for Σ_f.

Finally, to plot the curves for $\sigma_\infty = \sigma_f$ in Figs 11 and 12, it is convenient to renormalize the governing equations by letting

$$\bar{a}_0 = \frac{\sigma_{mc}^3}{c_f S \sigma_0^2}, \quad \bar{q}(s) = \frac{p(s)}{c_f S}, \quad \bar{\Sigma} = \frac{\sigma}{c_f S} \tag{B8}$$

to get

$$\sqrt{1-s}\,\bar{q}(s) \frac{dq(s)}{ds} = -\frac{4 f_1(s) \bar{a}_0}{3\pi^2 \alpha} \left[\int_\alpha^1 f_2(t,s) q(t)\,dt + \frac{\pi}{2}\bar{\Sigma} \right] \quad \text{for} \quad \alpha \leqslant s \leqslant 1 \tag{B9}$$

$$\bar{\Sigma} - \frac{2}{\pi} \int_\alpha^1 f_3(s) \bar{q}(s)\,ds = \sqrt{\alpha} \left(\frac{\sigma_{mc}}{c_f S} \right)^{3/2} \sqrt{\alpha/\bar{a}_0}. \tag{B10}$$

The fracture criterion is now $\bar{q}(1) = 1$, and so, for assigned values of $\bar{a}_0$ and $\sigma_{mc}/(c_f S)$ the magnitude of $\bar{\Sigma}_\infty = \bar{\Sigma}_f$ corresponding to this condition can be found from (B9) and (B10).

We omit a detailed description of the fairly straightforward procedures used to plot the curves in Figs 9–12 corresponding to the results in Figs 7 and 8 for σ_p and σ_{imc}.

Numerical procedure

This section describes the numerical procedure used to solve (B5) and (B6) for $q(s)$ and Σ; the method is equally applicable to (B9) and (B10). Make the substitutions

$$s = \tfrac{1}{2}[(1+\alpha)+(1-\alpha)z], \quad t = \tfrac{1}{2}[(1+\alpha)+(1-\alpha)\zeta], \quad q(s(z)) \equiv Q(z) \tag{B11}$$

in (B9)–(B10) to get

$$\sqrt{1-z}\,q(z)\frac{dQ(z)}{dz} = -\frac{4f_1[M(z)]}{3\pi^2\alpha\Sigma_0}\sqrt{\frac{1-\alpha}{2}}\left\{\frac{1-\alpha}{2}\int_{-1}^{1} f_3[t(\zeta),M(z)]Q(\zeta)\,d\zeta + \frac{\pi}{2}\Sigma\right\} \quad \text{(B12)}$$

for $-1 \leqslant z \leqslant 1$, and

$$\Sigma - \frac{1-\alpha}{\pi}\int_{-1}^{1} f_3[M(z)]Q(z)\,dz = \sqrt{\alpha}\Sigma_0. \quad \text{(B13)}$$

Note that the displacement $v \propto \sqrt{1-z}$ near $z = 1$, and since $Q \propto \sqrt{v}$ it is appropriate to write

$$Q(z) = (1-z)^{1/4}\sum_{k=1}^{M} a_k T_{k-1}(z) \quad \text{(B14)}$$

where $T_k(z)$ is the Chebyshev polynomial of the first kind of degree k. For given values of α, and Σ_0, the M coefficients a_k, together with the additional unknown Σ, were determined by collocation of (B12) at the M points

$$z_r = \cos\left(\frac{\pi r}{M+1}\right) \quad (r = 1, 2, \ldots, M) \quad \text{(B15)}$$

and enforcement of (B13). The definite integrals with respect to z in (B12) and (B13) were evaluated by means of the general Cauchy–Chebyshev formula (ERDOGAN and GUPTA, 1972)

$$\int_{-1}^{1}\frac{F(\zeta)\,d\zeta}{(z_r-\zeta)\sqrt{1-\zeta^2}} = \frac{\pi}{M+1}\sum_{p=1}^{M+1}\frac{F(\zeta_p)}{z_r-\zeta_p} \quad (r = 1, 2, \ldots, M) \quad \text{(B16)}$$

and the standard Gaussian integration formula

$$\int_{-1}^{1}\frac{F(z)\,dz}{\sqrt{1-z^2}} = \frac{\pi}{M+1}\sum_{p=1}^{M+1}F(z_p) \quad \text{(B17)}$$

where

$$z_p = \zeta_p = \cos\left[\frac{(2p-1)\pi}{2(M+1)}\right] \quad (p = 1, 2, \ldots, M+1). \quad \text{(B18)}$$

A Newton–Raphson iterative scheme was used to find solutions for the a_ns and Σ, with convergence specified by a relative change of less than 0.01% in the values of each of the unknowns in successive iterations. The physical argument that for a long matrix crack the applied stress σ should approach the steady-state matrix cracking stress σ_{mc} provides a consistency check on the accuracy of the numerical solution. It was found that with M between 40 and 60, the consistency check was always satisfied to within about 0.1%.

APPENDIX C: AUXILIARY PROBLEM FOR σ_{fmc}

We obtain an integral equation for the auxiliary problem of Fig. 4 by letting $\Delta a \to \infty$ in (B2). The result is

$$p(x)\frac{dp(x)}{dx} = -\frac{2\beta^2(1-\nu^2)}{\pi AE}\int_{a_0}^{\infty}\frac{x}{\xi^2-x^2}p(\xi)\,d\xi \quad \text{for} \quad a_0 \leqslant x < \infty. \quad \text{(C1)}$$

By making the substitutions shown in (B4), together with

$$x = a_0 y \quad \text{(C2)}$$

we obtain

$$\bar{q}(y)\frac{d\bar{q}(y)}{dy} = -\frac{2\bar{a}_0}{3\pi^2}\int_1^{\infty}\frac{y}{\eta^2-y^2}\bar{q}(\eta)\,d\eta \quad \text{for} \quad 1 \leqslant y < \infty. \tag{C3}$$

Note (Fig. 4) that under the applied stress σ, $\bar{q}(\infty) = \sigma/(c_f S) = \bar{\Sigma}$, and the condition for fiber fracture at the original flaw tip is given by

$$\bar{q}(1) = 1. \tag{C4}$$

Accordingly, for assigned values of $\bar{a}_0 \equiv \sigma_{fmc}^2 c_f S\sigma_0^2$, the solutions $\bar{q}(y)$ of (C3) that satisfy (C4) provide the associated values of $\bar{q}(\infty) = \bar{\Sigma}_f \equiv \sigma_{fmc}/(c_f S)$ needed to plot the solid curve of Fig. 8. In the numerical solution of (C3) the transformation

$$y = 1 + \frac{1+\omega}{1-\omega} \tag{C5}$$

was introduced to map the infinite domain into the interval $(-1, 1)$, and, except for the need to impose the condition $\bar{q} = 1$ at $\omega = -1$, the subsequent procedure used was similar to that outlined in Appendix B.

MATERIALS

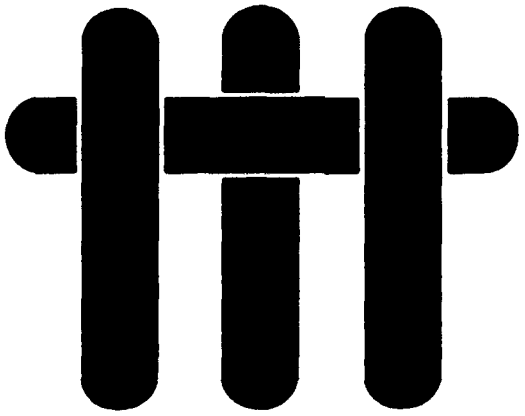

SiC/CAS: A NOTCH INSENSITIVE CERAMIC MATRIX COMPOSITE

by

Carl M. Cady, Thomas J. Mackin, and Anthony G. Evans*

*High Performance Composites Center
Materials Department
College of Engineering
University of California, Santa Barbara
Santa Barbara, California 93106–5050

KJS-Evans-11•TA-Ntch Sns CMC 93/05/05•4:42 PM-5/19/93

ABSTRACT

Tension experiments performed on a 0/90 laminated SiC/CAS composite at room temperature establish that this material is notch insensitive. Multiple matrix cracking is determined to be the stress redistribution mechanism. This mechanism is found to provide a particularly efficient means for creating local inelastic strains, which eliminate stress concentrations.

1. INTRODUCTION

One of the most important attributes of ceramic matrix composites (CMCs) is the existence of mechanisms that redistribute stress at strain concentration sites, such as notches and holes.[1-5] These mechanisms involve matrix cracking as well as fiber pull-out and bridging. The basic stress redistribution phenomena are manifest as three classes of behavior (Fig. 1), each associated with different contributions of matrix cracking and fiber pull-out.[2,6] Class I behavior, dominated by fiber bridging and pull-out, has been extensively documented and characterized through the development of large scale bridging models[1,5,7,8] (LSBM). Class III systems redistribute stress by shear band formation. This phenomenon has also been analyzed[9,10] and related to the in-plane shear strength of the material. Class II behavior has received least attention, and yet, appears to be the most effective means of stress redistribution.[4] The underlying phenomenon is the occurrence of multiple matrix cracks, with minimal accompanying fiber failure. The intent of the present article is to study matrix cracking and stress redistribution around strain concentration sites in a class II system. Moreover, it has been proposed that continuum damage mechanics (CDM) may be useful for characterizing stress redistribution in such materials.[2,12] The present results may provide perspective on the potential for CDM as an analysis procedure.

The material of choice is a Nicalon™ silicon carbide fiber in a calcium alumino silicate glass ceramic matrix (SiC/CAS) material.[13] The material is in the form of a 0/90 laminate. The tensile characteristics and the constituent properties are described elsewhere[11,14,15] (Fig 2). In this material, the matrix crack spacing in the 0° plies changes with stress[11,14] (Fig. 3) in a manner that fundamentally governs stress redistribution.

2. EXPERIMENTAL APPROACH

2.1 Material

Plates of the SiC/CAS composite were provided by Corning.[13] The material was laid up in a 0/90 laminate structure with a nominal fiber volume fraction, $f \approx 0.36$, and a fiber fraction aligned in each of the two principle axes, $f_1 \approx 0.18$. The laminate structure consisted of 16 alternating 0°, 90° layers with a double 90° center layer. The structure was densified by a hot pressing technique. After densification, the total thickness of the composite was ~ 3 mm. Optical microscopy established that the average thickness of each ply to be ≈ 180 μm.

2.2. Test Procedures

Tensile specimens with a variety of holes and notches, located at both the center and the edges (Fig. 4), were cut from the plates by diamond machining. The ratio of the notch length to the sample width (a_o/b) was varied between 0.25 and 0.75. The specimens were then polished to remove surface irregularities and to reveal the first underlying fiber layer in the composite. Tensile tests were performed on these specimens, by using gripping and alignment procedures described in other articles.[10,11]

The tensile tests were carried out on a servohydraulic load frame. Strain gages were used to measure localized strains at the notch tip and in the far field. In some cases, the specimens were monotonically loaded to failure, in order to document the influence of the notch on the ultimate tensile strength (UTS), designated S*. In other cases, the tests were interrupted at various fractions of the UTS, whereupon several measurements and observations

were made concerning matrix crack accumulation, as well as stress redistribution.

Matrix crack measurements were accomplished by using a surface replica technique that duplicated the topography of the specimen surface. Stress redistribution was assessed using thermoelastic measurements, by means of a technique involving stress pattern analysis through thermal emission (SPATE).[4] In this technique, temperature gradients produced by cycling the stress between 1.5 and 40 MPa at 10 Hz are measured and related to the first stress invariant, σ_{kk}.

Some tensile experiments were performed with sequential, repeated load cycling, subject to full unloading and reloading. The properties of the interface and the misfit strain were obtained from the associated hysteresis loops and the permanent strain.[15-19] Finally, measurements of fiber pull-out were made using scanning electron microscopy (SEM) on the failure plane.

3. RESULTS

3.1 Monotonic Loading

Stress/strain curves obtained from edge-notched specimens revealed appreciable non-linearity before failure (Fig. 2b). This non-linearity also coincided with an increase in compliance. The ultimate tensile strength (UTS) data are presented in terms of the ratio of the notched UTS, designated S*, to the unnotched UTS, designated S. This ratio is plotted as a function of the relative notch width, a_o/b. The results are summarized in Fig. 4. It is evident from these results that the 0/90 SiC/CAS material exhibits *notch insensitive behavior*.[1] In fact, there is evidence that some notch *strengthening* may be occurring.

3.2 Damage Observations

Measurements of matrix cracks (Fig. 5) taken from samples tested to failure, as well as from the replicas, indicate a relatively high crack density close to the notch root. Generally, cracks first appear at the notch root (Fig. 6). Then, as the load increases, the density of cracks increases. Thereafter, some of the cracks extend throughout the cross section. Eventually, the saturation crack spacing is approached near the notch root. The final average crack spacing decreased as the ratio a_o/b increased, such that the crack density in the specimen with $a_o/b = 0.75$ most closely resembled that found in an unnotched tensile specimen after testing.

SPATE measurements revealed an initial stress concentration at the notch root (Fig. 7), which diminished as matrix cracks appeared. These measurements relate to the matrix cracks, which generate a compliance gradient,[4] that lowers the stress concentration, as well as redistributing the stress across the remaining section. A comparison of SPATE line scans with acetate replicas taken at the same damage level (Fig. 8) provides striking evidence of the effect of multiple matrix cracking.

The fiber pull-out measurements and the hysteresis loop data (Figs. 9 and 10) can be used to provide information about the interface sliding stress, τ, and the residual stress, q.[11,14,16-19] The sliding stress obtained from these measurements ($\tau \approx 20$ MPa) is in reasonably good agreement with the values previously reported for this material.[11,14] However, the permanent strains suggest a residual stress, q = 30 MPa, somewhat lower than that found previously.[11,14] This difference reflects changes in processing conditions.

4. DISCUSSION

All of the above results indicate that the 0/90, SiC/CAS behaves as a *notch insensitive* material in tension at room temperature. The most direct evidence is given by the trend in the UTS with notch size (Fig. 4). Confirmatory evidence is provided by the crack density distribution, as well as the SPATE results.

The crack density within the 0° plies may be approximately related to the σ_{yy} stress in those plies, in accordance with the curve shown in Fig. 3. Notably, the crack density measured around the notch (Fig. 6) may be used with Fig. 3 to estimate the σ_{yy} stress distribution. The results (Fig. 11) confirm that the stress concentration is small prior to failure.

The SPATE measurements (Fig. 7) reflect the influence of the matrix cracks on the elastic stiffness of the material around the notch.[4] The gradient in stiffness caused by these cracks allows the σ_{kk} stress to redistribute and eventually become uniform across the net section. Thus, the change in the SPATE line scans with peak load provide an excellent qualitative picture of how the tensile stresses are being redistributed across the net section. However, as yet, they cannot be used to accurately measure the magnitude of those stresses.

5. CONCLUSION

Some simple experiments have been performed which vividly demonstrate that a 0/90 SiC/CAS composite is notch insensitive in tension at room temperature. The behavior is related to the inelastic strains (Fig. 2) that arise from matrix cracking (Fig. 3), which redistribute stress around notches.

The matrix cracking mechanism appears to be particularly efficient for this purpose, because stress concentrations can be completely eliminated, even though the ductility is small, < 1% (Fig. 2). Since the matrix crack density is relatively high at strain concentration sites, it should be possible to develop a mechanism-based CDM approach[12] which could be used to predict redistribution effects. The available matrix cracking models,[17-20] combined with the constituent properties should be suitable for this purpose.

ACKNOWLEDGEMENTS

This work was supported by the Defense Advanced Research Projects Agency through the University Research Initiative under Office of Naval Research Contract No. N-00014-86-K-0753. Thanks go to Corning Glass Works, especially Kenneth Chyung, for providing the material. Special thanks to Jean-Marc Domergue for useful discussions. Thanks to Pratt and Whitney for sharing their SPATE equipment and Tom Purcell for assistance with the SPATE experiments.

REFERENCES

[1] G. Bao and Z. Suo, "Remarks on Crack Bridging Concepts," *Applied Mech. Rev.*, **45[8]**, 355–66, 1992.

[2] A.G. Evans, F. Zok and T.J. Mackin, "The Mechanical Performance of Ceramic Matrix Composites," *Solid State Physics*, to be published.

[3] S. Mall, D.E. Bullock and J.J. Pernot, "Tensile Fracture Behavior of Fiber Reinforced Ceramic Matrix Composite with Hole," to be published.

[4] T.J. Mackin, T.E. Purcell, M.Y. He and A.G. Evans, "Notch Sensitivity and Stress Redistribution in CMCs," to be published.

[5] Z. Suo, S. Ho and X. Gong, "Notch Brittle to Ductile Transition Due to Localized Inelastic Band," *J. Matl. Eng. Tech.*, in press.

[6] A.G. Evans, "The Mechanical Properties of Reinforced Ceramics, Metal and Intermetallic Matrix Composites," *Mat. Sci. Eng.* **A143**, 63, 1991.

[7] B.N. Cox and C.S. Lo, "Load Ratio, Notch and Scale Effects for Bridged Cracks in Fiberous Composites," *Acta Metall. Mater.*, **40**, 69, 1992.

[8] B.N. Cox and D.B. Marshall, "Crack Bridging in the Fatigue of Fibrous Composites," *Fatigue and Fracture of Engineering Materials*, **14**, 847, 1991.

[9] H.S. Chan, M.Y. He, and J.W. Hutchinson, "Cracking and Stress Redistribution in Ceramic Layered Composites," *Mater. Sci. Eng.*, in press.

[10] F.E. Heredia, S.M. Spearing, M.Y. He, T.J. Mackin and A.G. Evans, "Notch Effects in Carbon Matrix Composites," *J. Amer. Ceram. Soc.*, in press.

[11] D. Beyerle, S.M. Spearing and A.G. Evans, "Damage Mechanisms and the Mechanical Properties of a Laminated 0/90 Ceramic/Matrix Composite," *J. Amer. Ceram. Soc.*, **12**, 3321, 1992.

[12] D. Hayhurst, F.A. Leckie and A.G. Evans, "Component Design-Based Model for Deformation and Rupture of Tough Fibre-Reinforced Ceramic Matrix Composites," *Proc. Roy. Soc.*, London, **A434**, 369, 1991.

[13] K. Chyung, U. S. Patent 4, 615, 987 (7 October, 1986).

[14] D. Beyerle, S.M. Spearing, F.W. Zok and A.G. Evans, "Damage and Failure in Unidirectional Ceramic-Matrix Composites," *J. Amer. Ceram. Soc.*, **[10]** 2719, 1992.

[15] T.J. Kotil, J.W. Holmes and M. Comninou, "Origin of Hysteresis Observed During Fatigue of Ceramic-Matrix Composites," *J. Am Ceram. Soc.*, **73**[7], 1879–83, 1990.

[16] A.W. Pryce and P. Smith, "Modelling the Stress/Strain Behaviour of Unidirectional Ceramic Matrix Composite Luminates," *J. Mater. Sci.*, **27**, 2695–2704, 1992.

[17] A.G. Evans, J-M. Domergue and E. Vagaggini, "Methodology for Relating the Tensile Constitutive Behavior of Ceramic Matrix Composites to Constituent Properties," *J. Amer. Ceram. Soc.*, in press.

[18] E. Vagaggini, J-M. Domergue and A.G. Evans, "Relationships Between Macroscopic Performance of Ceramic Matrix Composites and Constituent Properties: I: Theory and Methodology," *J. Amer. Ceram. Soc.*, in press.

[19] J-M. Domergue, E. Vagaggini and A.G. Evans, "Relationships Between Macroscopic Performance of Ceramic Matrix Composites and Constituent Properties: III: Application to 2-D CMCs," *J. Amer. Ceram. Soc.*, in press.

[20] J.W. Hutchinson and H. Jensen, "Models of Fiber Debonding and Pullout in a Brittle Composite with Friction," *Mech. Mtls.*, **9**, 139–63, 1990.

FIGURE CAPTIONS

Fig. 1. The mechanisms of fiber pull-out and matrix cracking that lead to stress redistribution in CMCs are identified with 3 classes of behavior.

Fig. 2. Tensile stress-strain curve for 0/90 laminated SiC/CAS composite indicating unload-reload hysteresis loops, (a) schematic, (b) experimental results.

Fig. 3. The trend in crack density with stress for the 0° plies with applied stress for 0/90 SiC/CAS.

Fig. 4. Effect of notch size on relative UTS, indicating that SiC/CAS is notch insensitive in tension at room temperature. The inset shows a schematic of the test specimen. The parameter $\mathcal{A}$ is a measure of the notch size to the damage zone size [1,5]. For SiC/CAS the calculated value of $\mathcal{A}$ is approximately 0.02.

Fig. 5. A replica showing the matrix cracks that occur between two edge notches .

Fig. 6. The crack density as a function of distance from the notch at differing levels of net section stress, σ_N, for a specimen with edge notches, $a_o/b = 0.5$.

Fig. 7. Typical results of SPATE measurements: (a) full-field temperature distributions before and after matrix cracking. (The low resolution of these images is an artifact of the gray scale imaging). Regions of greatest temperature change are shown in black near the notch roots, with a continuous decrease in temperature change with distance from these locations. (b) Line scans after exposure to various peak loads show the distribution of σ_{kk} between the notches. The differences in shape depict the role of damage in stress redistribution. The stress concentrations are artificially low near the notch root due to a smoothing program that filters out the notch-root edge effect.

Nevertheless, the average stress between the notches is, in all cases, consistent with the net section stress indicated in the figure.

Fig. 8. A comparison of SPATE images at several loads with the replicas taken at the same loads. The replicas record the crack density at each damage level, while SPATE images reveal the hydrostatic stress distribution.

Fig. 9. Fiber pull-out distribution measured from the failure plane

Fig. 10. Hysteresis loop data presented as a function of the peak stress with the predicted line for τ = 20 MPa indicated.

Fig. 11. Estimate of the distribution of σ_{yy} stresses between the notches based upon crack density measurements (Fig. 3). Results shown for two levels of net section stress, σ_N.

Class I

Matrix Cracking + Fiber Failure

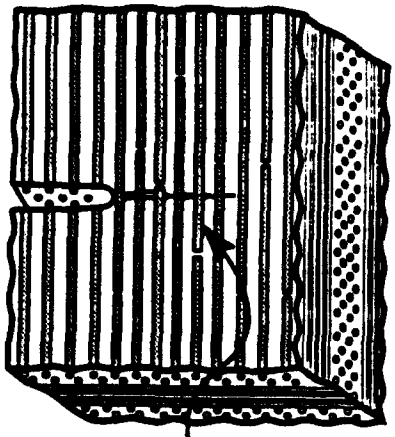

Pull-Out Tractions
Redistribute Stress

Class II

Matrix Cracking: No Fiber Failure

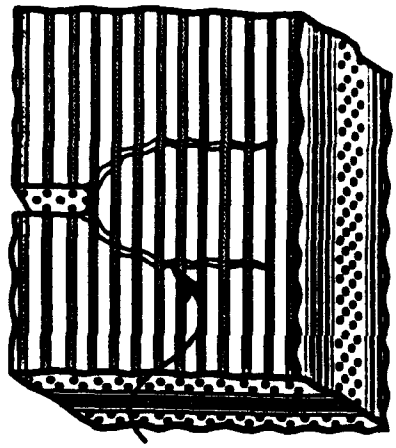

Matrix Cracks
Redistribute Stress

Class III

Shear Damage By Matrix Cracking

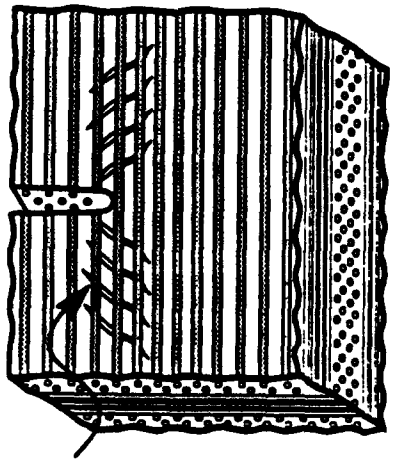

Shear Damage Zone
Redistributes Stress

Figure 1

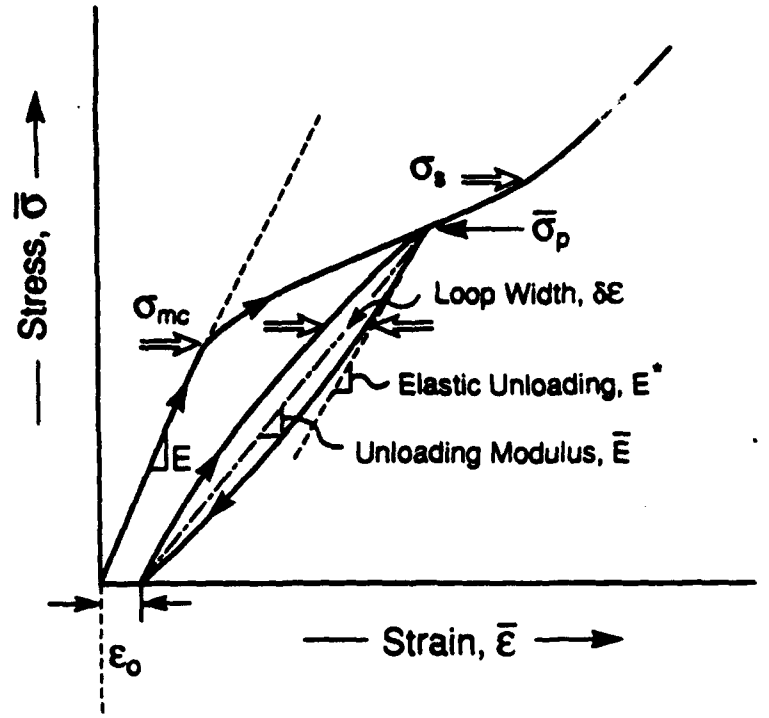

a) Schematic

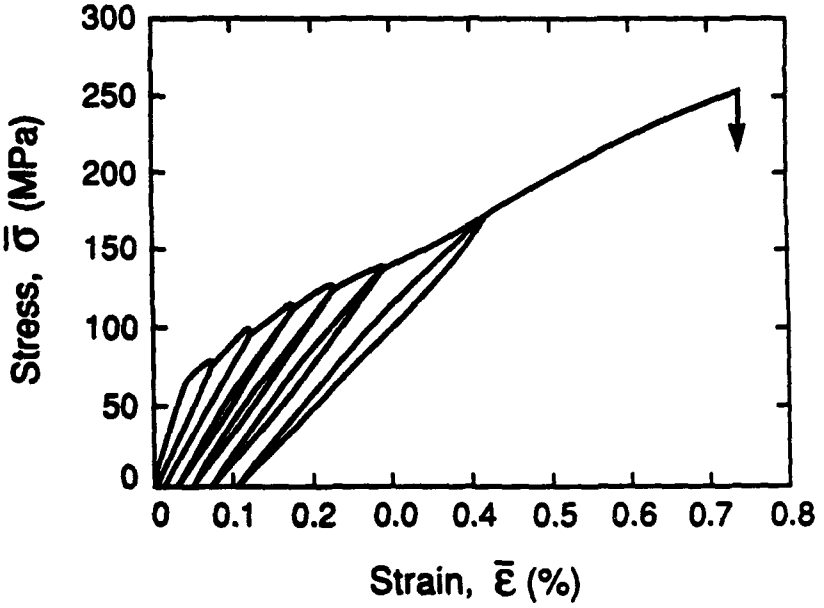

b) Experimental Results, 0/90 SiC/CAS

Cady.Evans.URI-4/89-amb-D161081-8

Figure 2

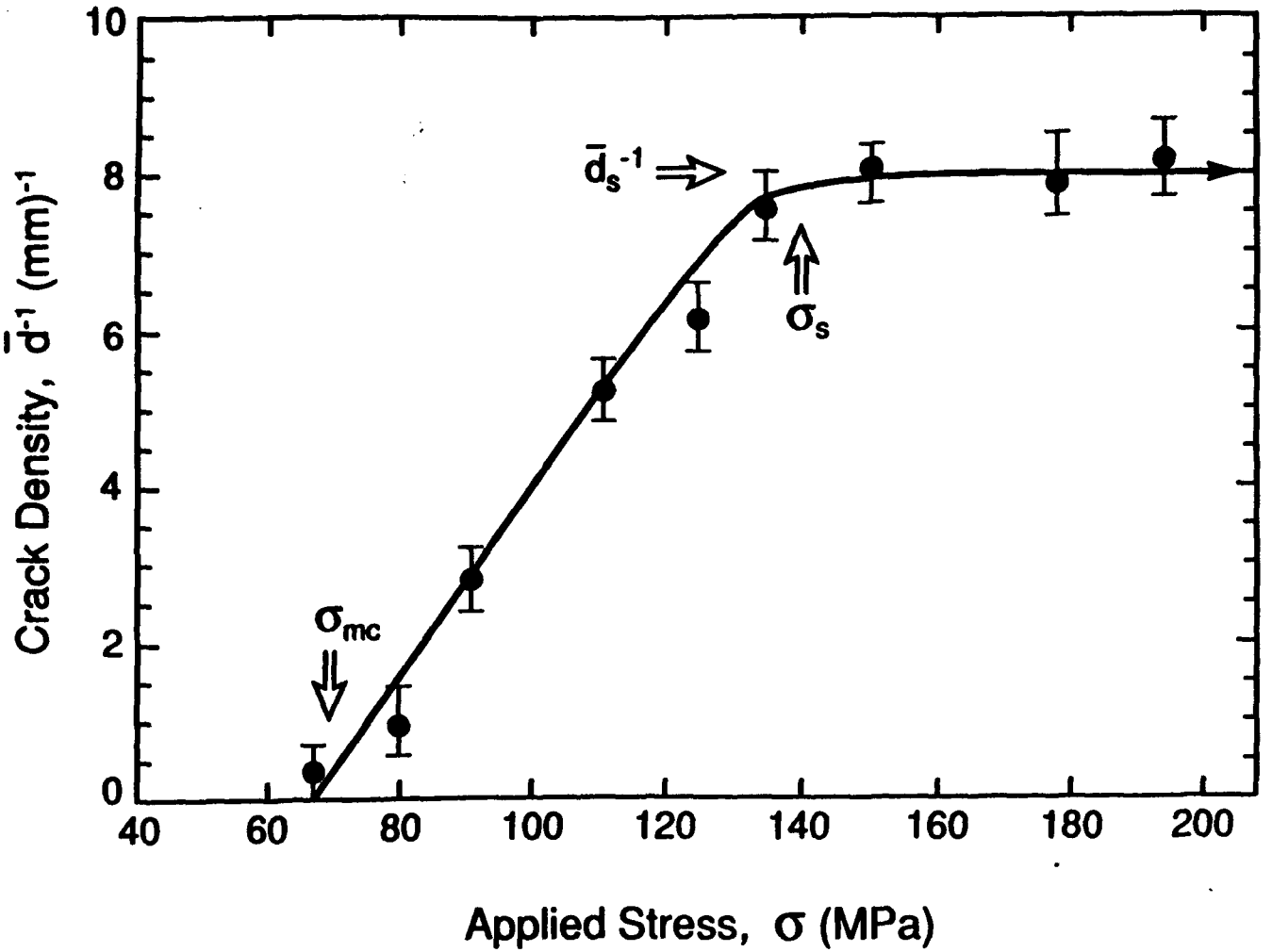
Crack Density, $\bar{d}^{-1}$ (mm)$^{-1}$
Applied Stress, σ (MPa)
$\bar{d}_s^{-1}$
σ_{mc}
σ_s
0
2
4
6
8
10
40
60
80
100
120
140
160
180
200

Fig. 3

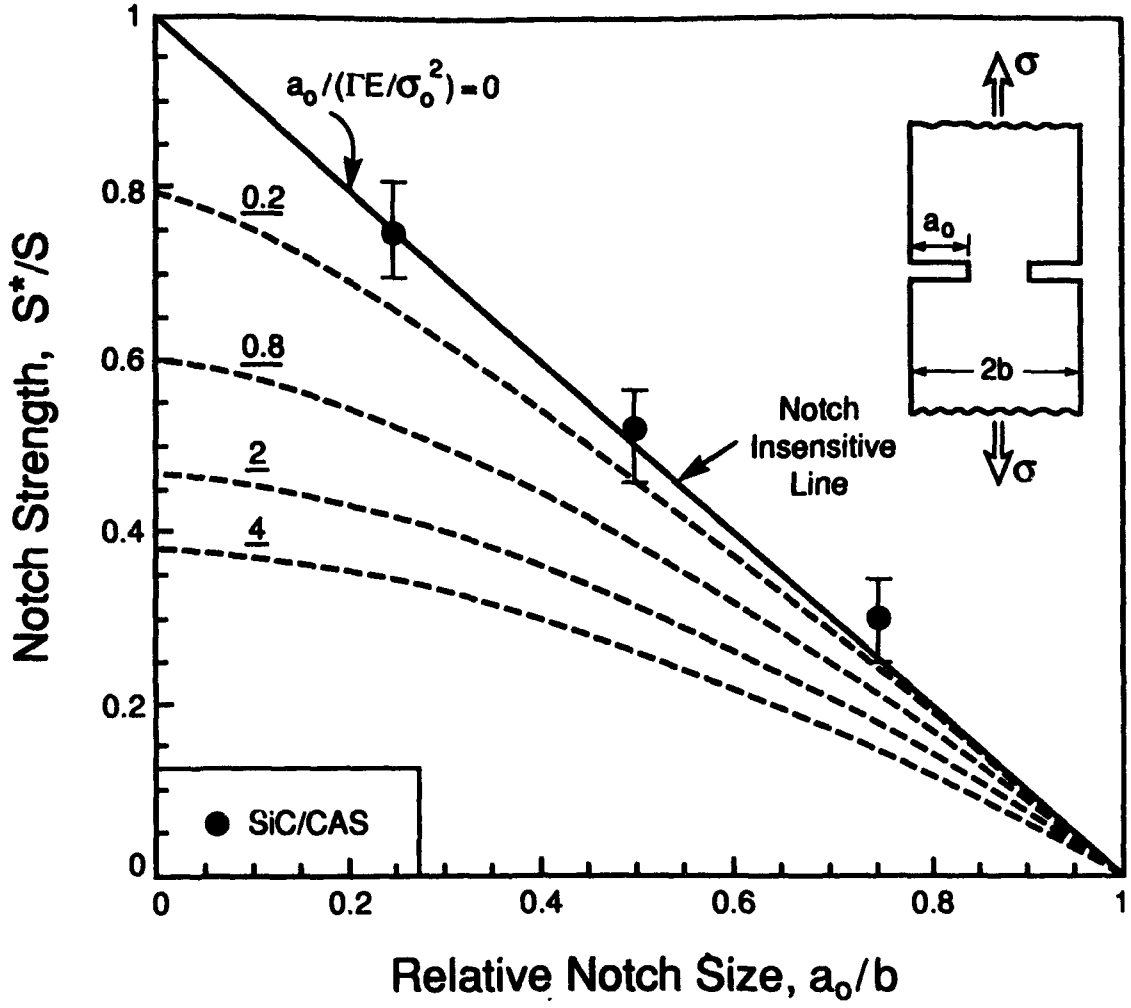

Figure 4

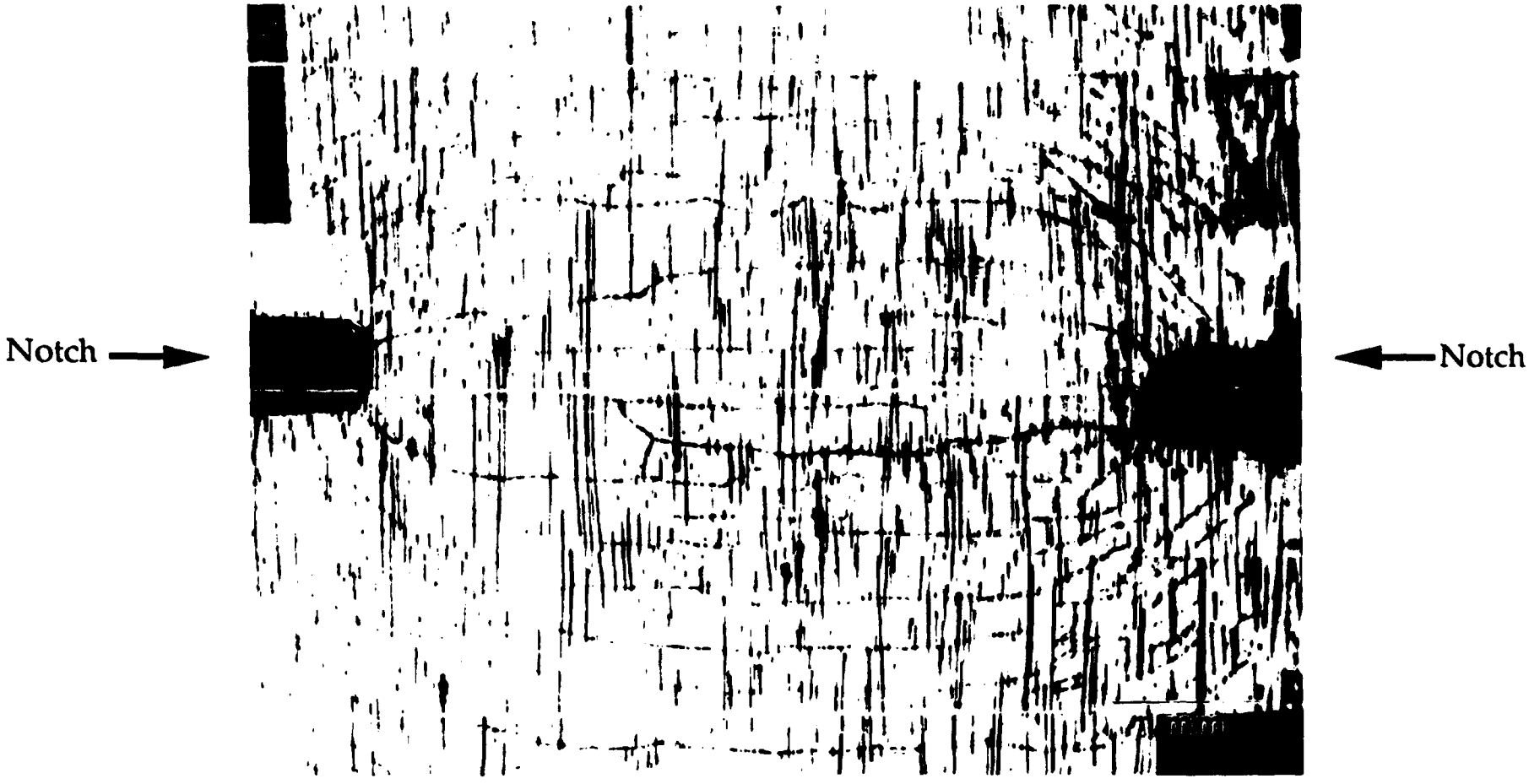

Figure 5

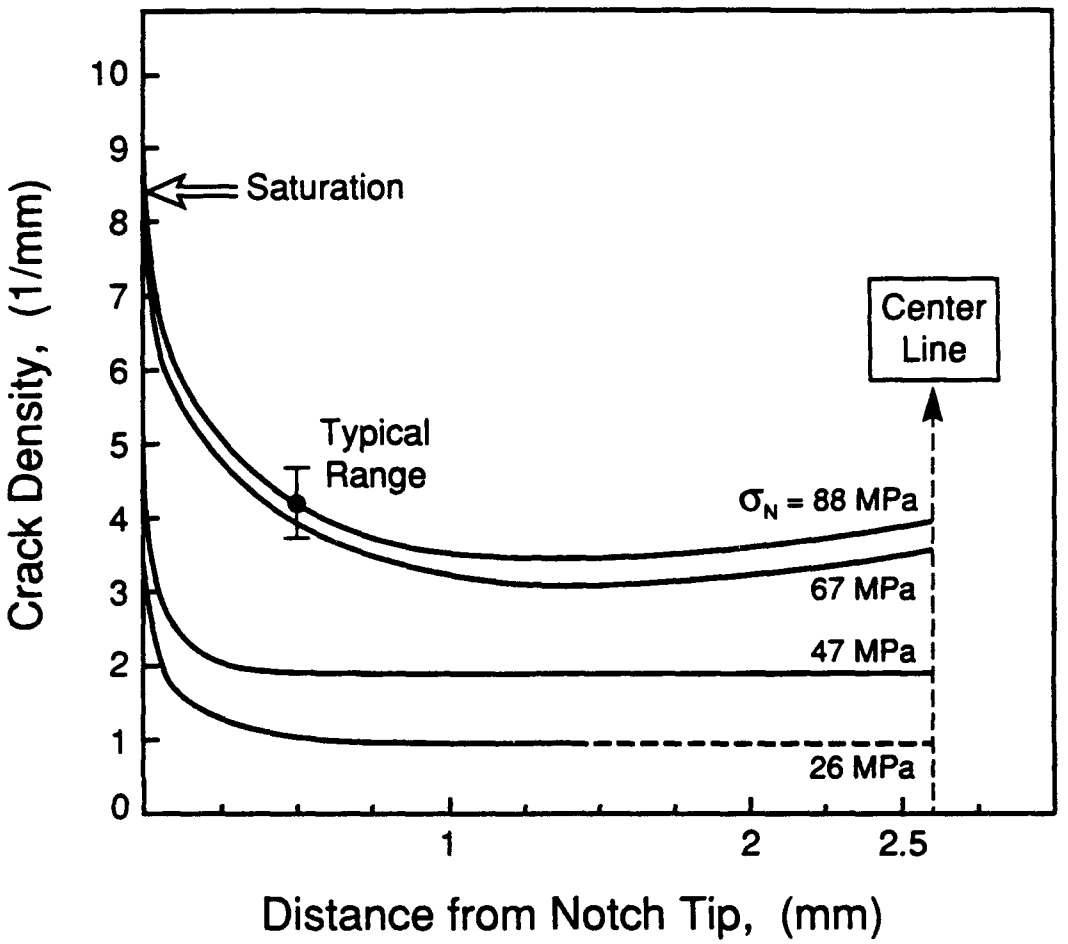
Crack Density, (1/mm)
10
9
8
7
6
5
4
3
2
1
0
Saturation
Center Line
Typical Range
σ_N = 88 MPa
67 MPa
47 MPa
26 MPa
1
2
2.5
Distance from Notch Tip, (mm)

Fig. 6

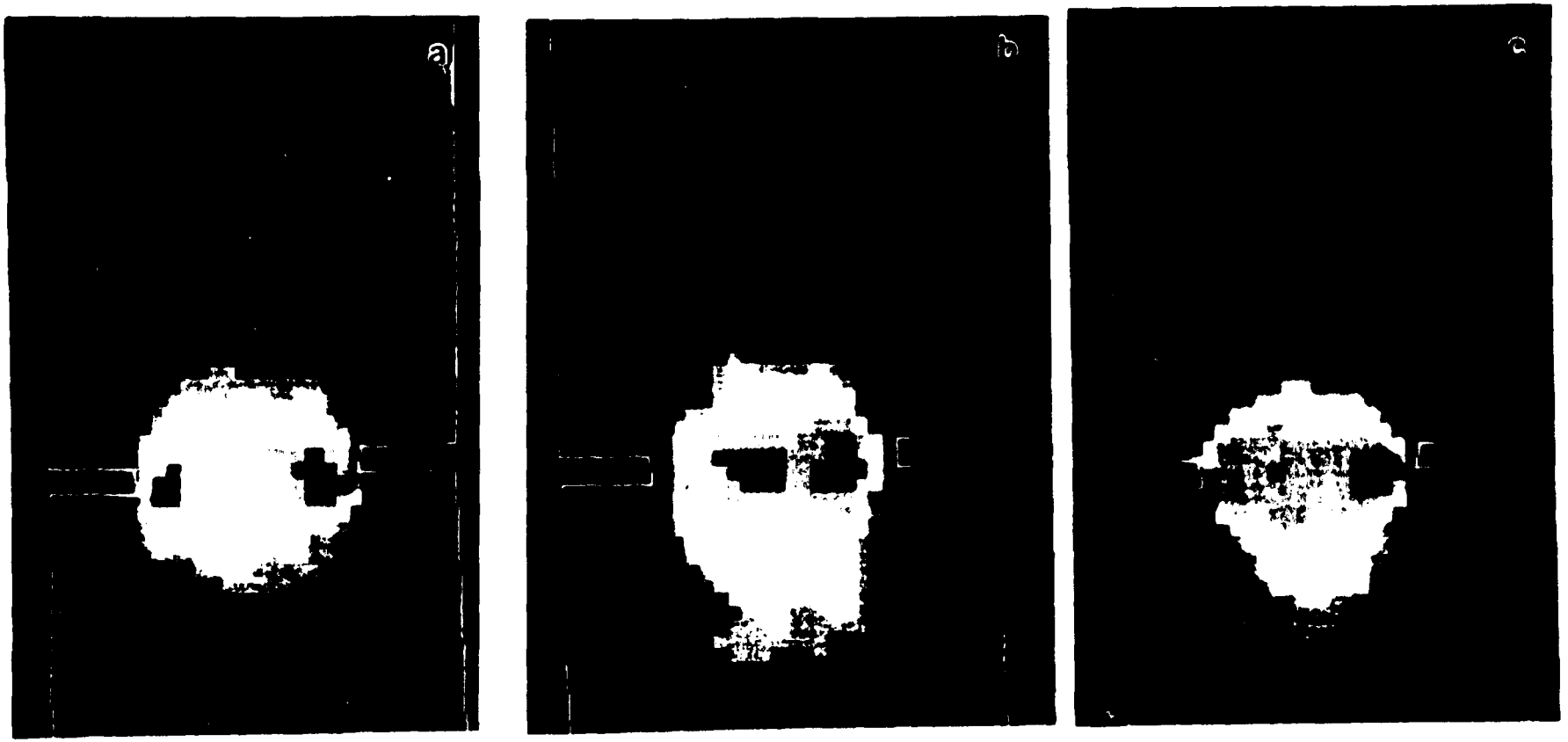

30 MPa

60 MPa

90 MPa

Figure 7a

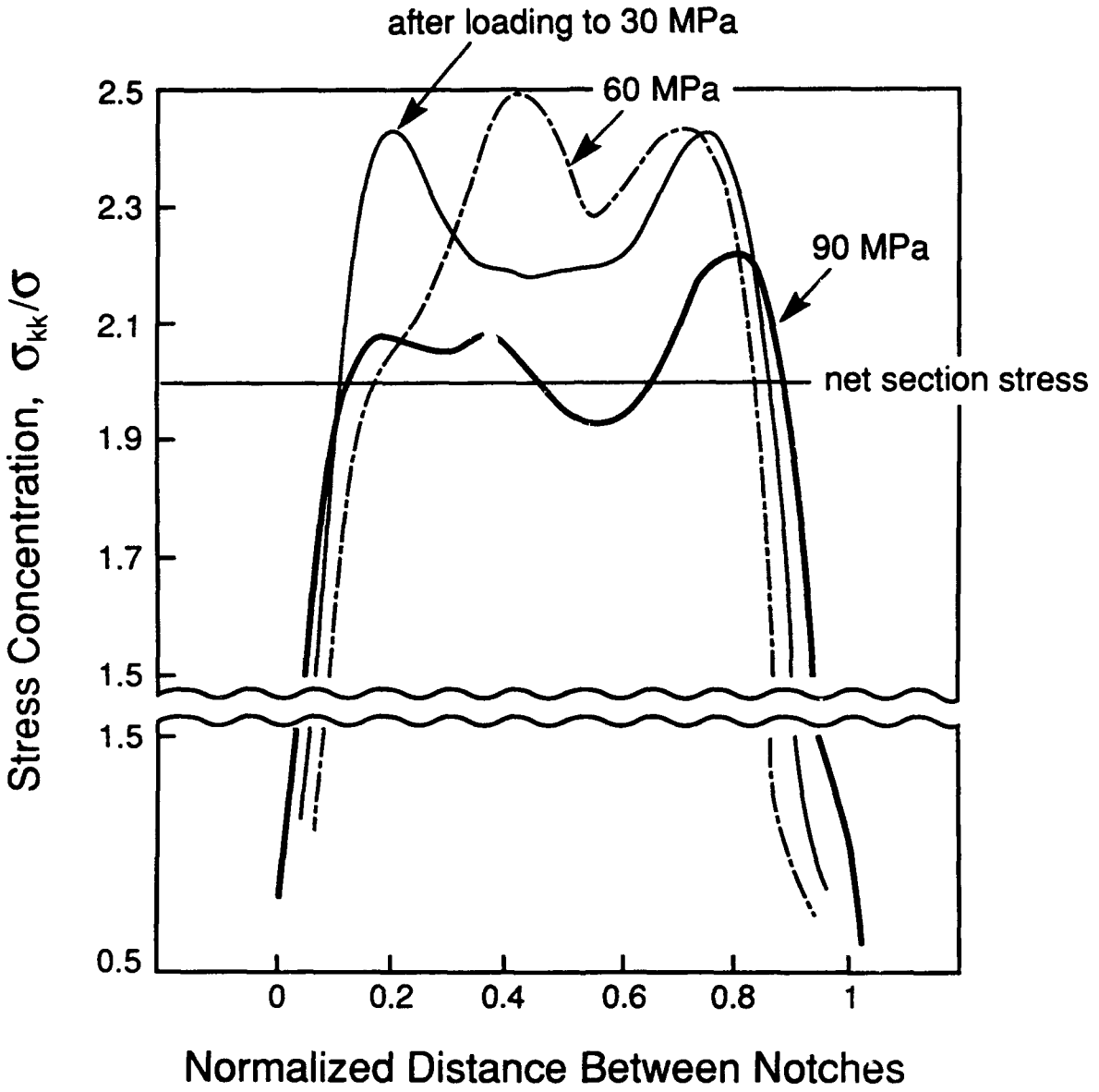
after loading to 30 MPa
60 MPa
90 MPa
net section stress
Stress Concentration, σ_{kk}/σ
2.5
2.3
2.1
1.9
1.7
1.5
1.5
0.5
0
0.2
0.4
0.6
0.8
1
Normalized Distance Between Notches

Figure 7b

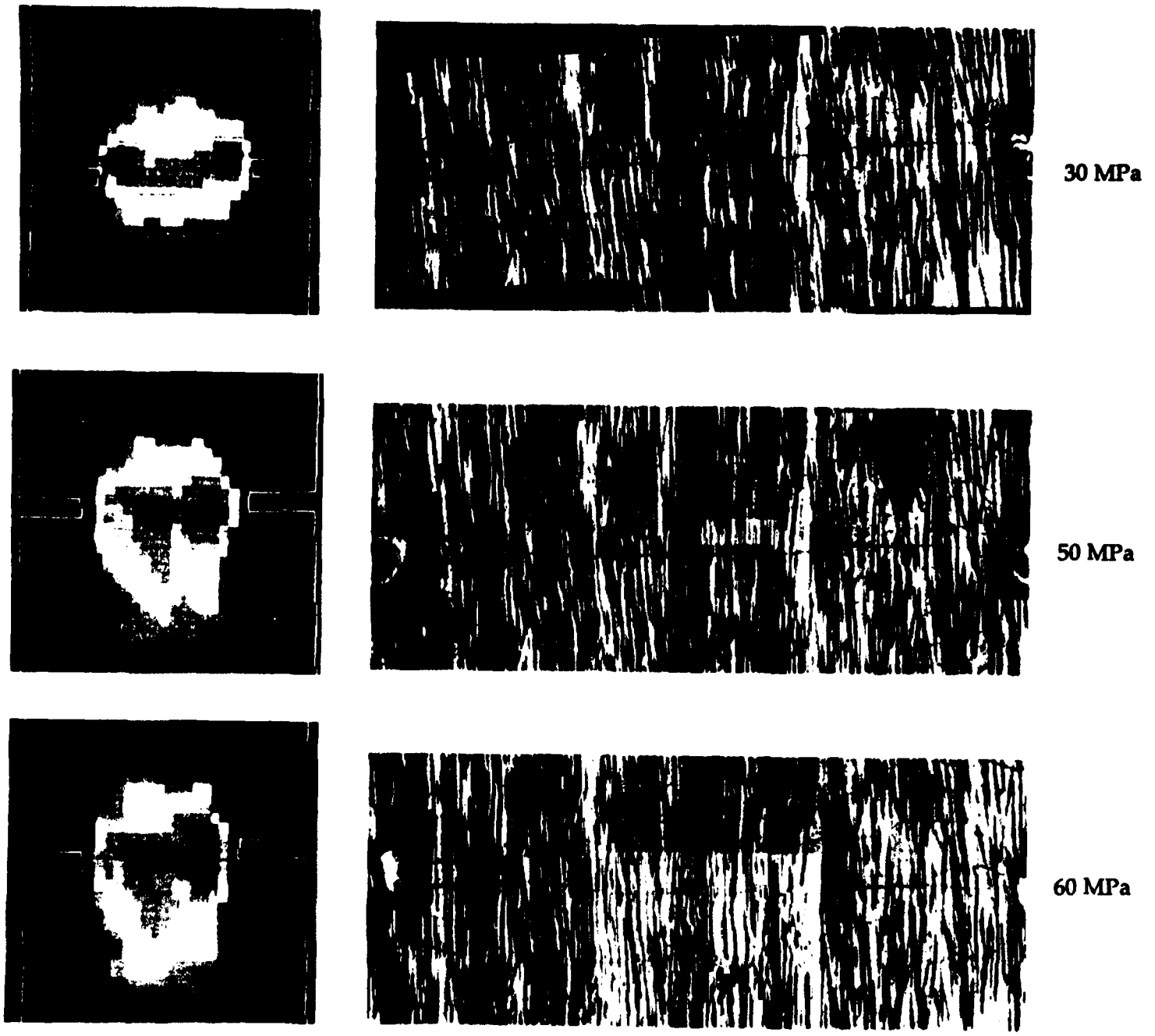

Figure 8

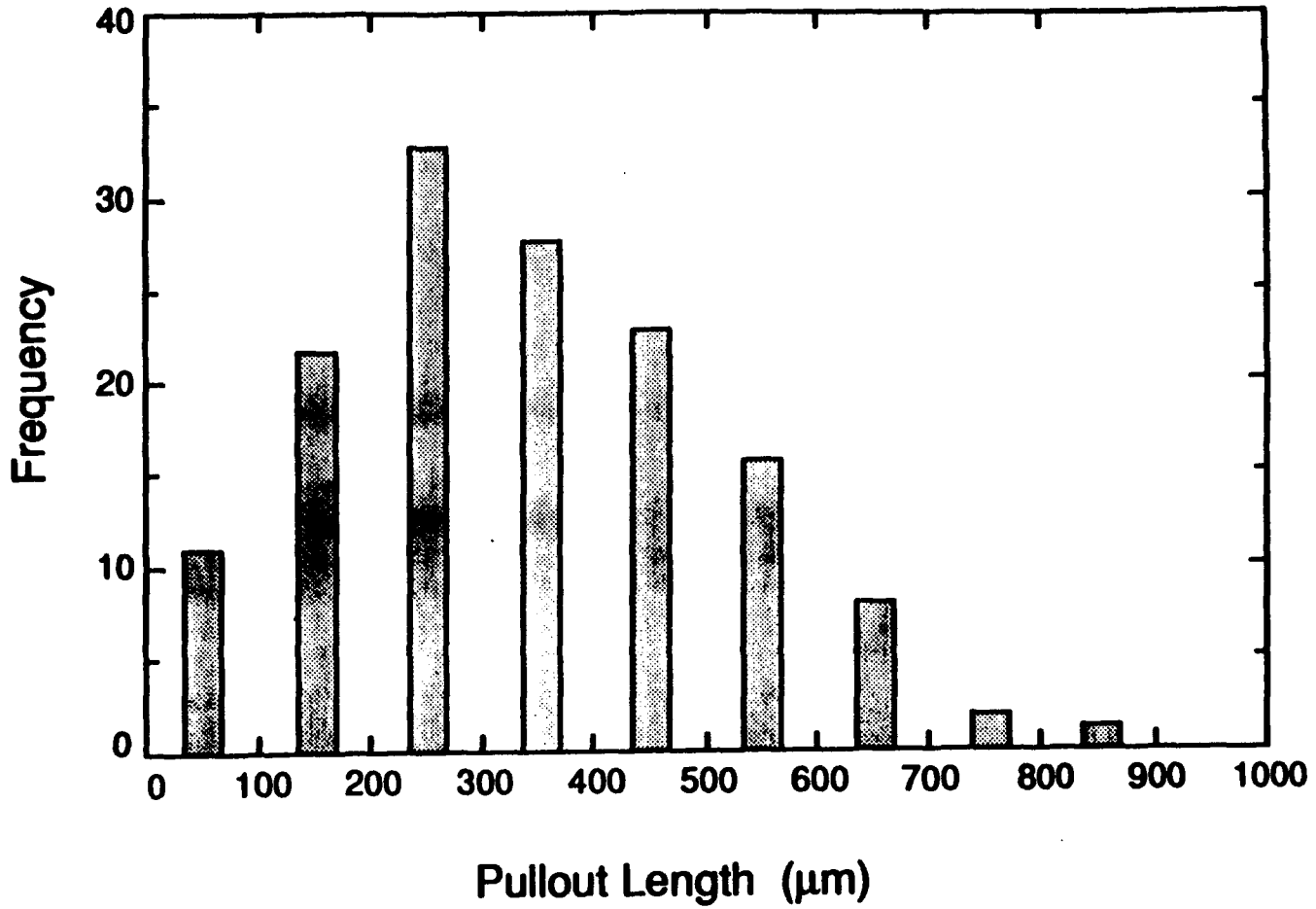
40
30
20
10
0
Frequency
0
100
200
300
400
500
600
700
800
900
1000
Pullout Length (μm)

Fig. 9

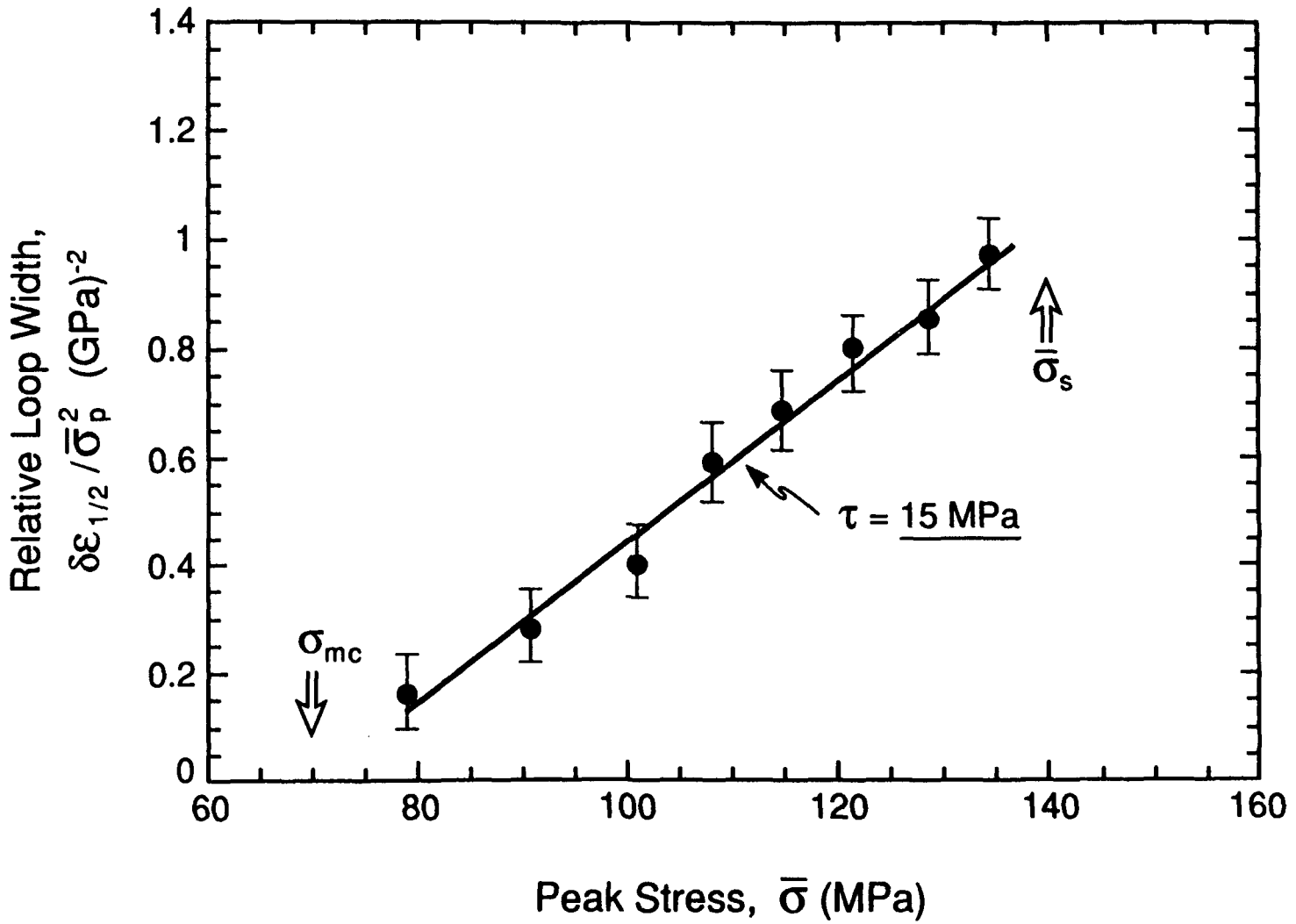

Fig. 10

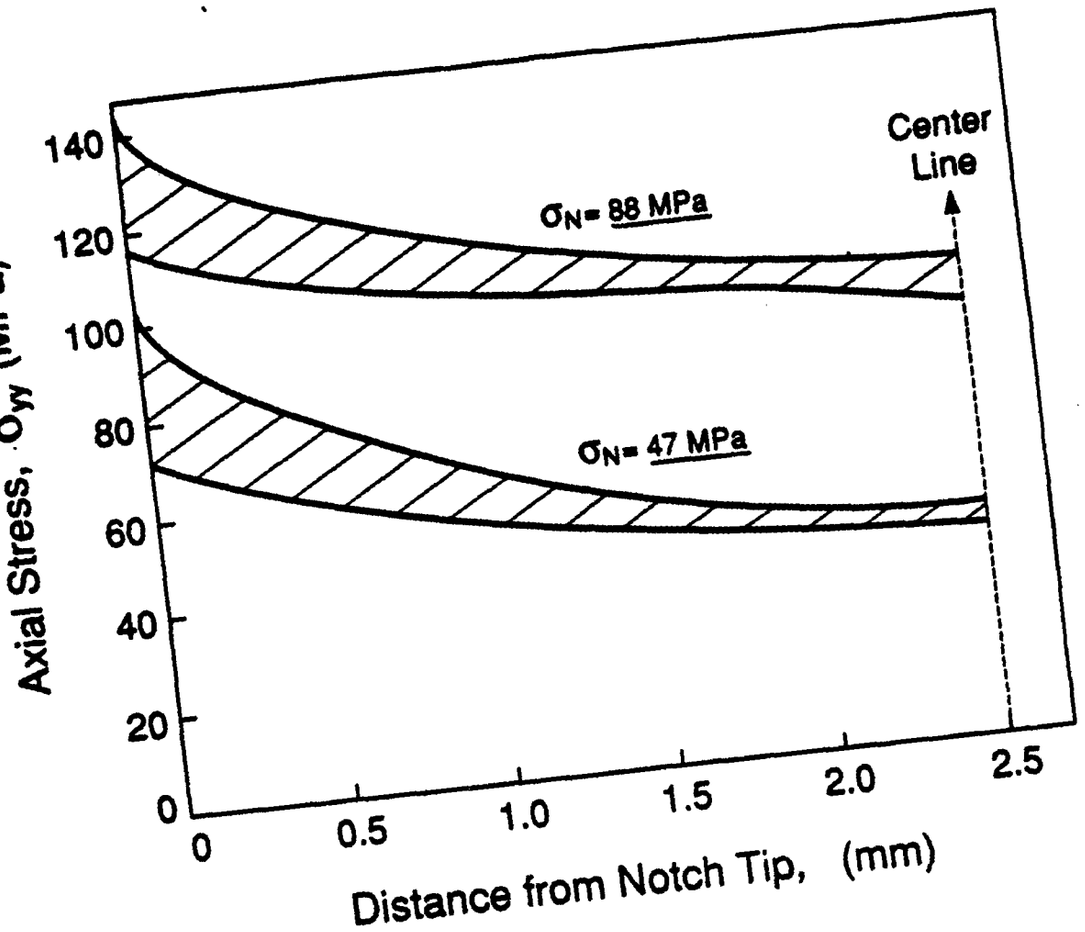
Center
Line
σ_N= 88 MPa
σ_N= 47 MPa
Axial Stress, σ_{yy} (MPa)
140
120
100
80
60
40
20
0
0
0.5
1.0
1.5
2.0
2.5
Distance from Notch Tip, (mm)

Figure 11

MATERIALS

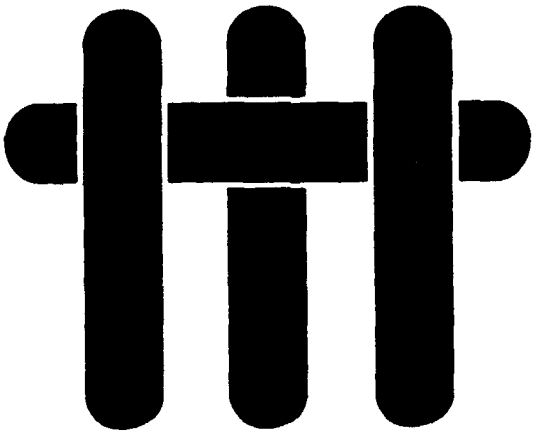

ON THE TENSILE PROPERTIES OF A FIBER REINFORCED TITANIUM MATRIX COMPOSITE II. INFLUENCE OF NOTCHES AND HOLES

S.J. Connell, F.W. Zok, Z.Z. Du and Z. Suo

Departments of Materials and Mechanical and
Environmental Engineering
University of California
Santa Barbara, California 93106

Submitted to Acta Metallurgica et Materialia

January, 1994

71:MS37(December 27, 1993)3:13 PM/mef

ABSTRACT

The effects of holes and notches on the ultimate tensile strength of a unidirectionally reinforced titanium matrix composite have been examined. During tensile loading, a narrow plastic strip forms ahead of the notch or hole prior to fracture, similar to that observed in thin sheets of ductile metals. Examination of the fibers following dissolution of the matrix indicates that essentially all the fibers within such a strip are broken prior to catastrophic fracture of the composite. The trends in notch-strength have been rationalized using a fracture mechanics-based model, treating the plastic strip as a bridged crack. The observations suggest that the bridging traction law appropriate to this class of composite is comprised of two parts. In the first, the majority of fibers are unbroken and the bridging stress corresponds to the unnotched tensile strength of the composite; in the second, the fibers are broken and the bridging stress is governed by the yield stress of the matrix, with some contribution derived from fiber pullout. This behavior has been modeled by a two-level rectilinear bridging law. The parameters characterizing the bridging law have been measured and used to predict the notch strength of the composite. A variation on this scheme in which the fracture resistance is characterized by an intrinsic toughness in combination with a rectilinear bridging traction law has also been considered and found to be consistent with the predictions based on the two-level traction law.

1. INTRODUCTION

Fiber-reinforced titanium matrix composites are being considered for structural applications in advanced aerospace engines[1]. It is envisioned that, in some applications, holes will be introduced for either fastening or cooling. The design of such structures will require an understanding of the damage processes occurring around the holes and the influence of damage on structural performance. The intent of the present article is to examine the nature of such processes and to assess the utility of non-linear fracture mechanics-based models for describing the influence of holes and notches on tensile strength.

It will become evident that the trends in strength with hole or notch size can be rationalized in terms of models based on crack bridging, analogous to those used to describe the notch sensitivity of monolithic ductile metals and ceramic matrix composites (CMCs). As a result, the following section provides a brief review of the existing crack bridging models. The review is followed by a description of the experimental portion of the study and comparisons with the model predictions.

2. BACKGROUND ON NOTCH SENSITIVITY

In brittle materials, the tensile strength $\bar{\sigma}$ of a panel containing a sharp, through-thickness *notch* can be described by the Griffith equation

$$\bar{\sigma} = \sqrt{\frac{E\Gamma}{\pi a_o}} \qquad (1)$$

where Γ is the toughness, E is Young's modulus‡ and $2a_o$ is the notch length. Alternatively, if the panel contains a circular hole with a radius a_o that is large in comparison to the intrinsic flaw size, c, the strength is given by

$$\bar{\sigma} = \frac{1}{3}\sqrt{\frac{E\Gamma}{\pi c}} \qquad (2)$$

In essence, the hole reduces the strength by a factor equivalent to the stress concentration factor ($k_t = 3$), independent of the absolute hole size*. Consequently, Eqn. 2 can be re-written as

$$\bar{\sigma} = \bar{\sigma}_o/3 \qquad (3)$$

where $\bar{\sigma}_o$ is the tensile strength in the absence of a hole or a notch.

Ductile materials, particularly in the form of thin sheet, behave differently. In the presence of a notch, tensile fracture is preceded by the development of a narrow zone of intense plasticity ahead of the notch[2]. Fracture occurs by the formation and propagation of a crack within the plastic zone. This process can be modeled by considering the tip of the plastic zone to be the tip of a hypothetical crack and the material within the plastic strip to be a "bridged zone"[3,4]. The tractions exerted by the bridged zone are taken to be equivalent to the yield stress of the metal, σ_y. Moreover, the intrinsic fracture energy, Γ_o, is taken to be zero, such that all the fracture resistance is derived from bridging. Using the J-integral, the contribution derived from bridging, Γ_b, can be expressed as[5]

$$\Gamma_b = \int_o^{\delta_c} \sigma_y \, d\delta = \sigma_y \, \delta_c \qquad (4)$$

‡ Corresponding to either plane stress or plane strain conditions, as appropriate.
* Neglecting the effects of volume on strength.

where δ is the crack opening displacement and δ_c is the critical value needed to fracture the metal. Moreover, the fracture stress varies with notch size according to the relation[4]

$$\frac{\bar{\sigma}}{\bar{\sigma}_o} = \frac{2}{\pi} \cos^{-1}\left(\exp \frac{-\pi}{8\alpha}\right) \tag{5a}$$

where α is a normalized measure of the notch size

$$\alpha \equiv \frac{a_o \bar{\sigma}_o^2}{\Gamma E} \tag{5b}$$

and the unnotched tensile strength, $\bar{\sigma}_o$, is taken to be the yield stress, σ_y. This approach is commonly referred to as the Dugdale-Barenblatt model.

The parameter used to normalize the notch size, $\Gamma E/\bar{\sigma}_o^2$, is a characteristic bridging length scale that governs the degree of notch sensitivity. When this length scale is large compared to the notch length, the tensile strength is reached after the plastic strip extends only a small amount and thus the steady-state toughness, given by Eqn. 4, is not fully realized. Conversely, when the bridging length scale is sufficiently small, the toughness is fully utilized prior to catastrophic fracture, whereupon the stress-notch length relation (Eqn. 5b) reduces to the Griffith relation (Eqn. 1).

More recently, models based on crack bridging have been developed for predicting the notch-strength characteristics of ceramic matrix composites (CMCs)[6-8]. The essential difference between these models and the one developed by Dugdale involves the functional form of the bridging traction law. The traction laws considered to date include linear softening, linear hardening and parabolic

hardening, in addition to the rectilinear law. Figure 1 shows three typical bridging traction laws and their effects on notch sensitivity. A notable feature here is that the notch sensitivity is governed predominantly by the parameter α, and is relatively insensitive to the shape of the traction law. Moreover, for large values of α ($\gtrsim 1$), the notch-strength follows the Griffith relation (Eqn. 1), with $\Gamma = \Gamma_b$.

An additional feature that has been incorporated into recent calculations is the intrinsic fracture energy, Γ_o[7,8]. This energy can be represented by a non-dimensional parameter, λ, defined by

$$\lambda = \Gamma_o/\Gamma_b \tag{6}$$

Some trends in notch strength with λ for the rectilinear traction law are illustrated in Fig. 2. The main effect of λ is to increase the strength for small values of α. At higher values of α, the notch-strength again follows the Griffith relation, with Γ replaced by the total fracture energy: $\Gamma = \Gamma_o + \Gamma_b$.

Calculations have also been performed to evaluate the strength of such materials in the presence of circular holes[7]. Figure 3 shows an illustrative example. For small values of α, the strength is similar to that corresponding to a sharp notch. However, for large values ($\alpha \gtrsim 1$) the strength asymptotically approaches the value predicted on the basis of the stress concentration factor, given by Eqn. 3.

3. EXPERIMENTS

3.1 Materials

The material used in this study was a Ti-6Al-4V matrix reinforced with unidirectional, continuous SiC fibers*, 100 μm in diameter. The composite panel was comprised of six plies, with a total thickness of 1.0 mm. The fiber volume fraction was 32%. Prior to consolidation, the fibers had been coated with ~ 1 μm of C, followed by ~ 1 μm of TiB_2. The TiB_2 coating serves as a diffusion barrier between the fiber and the matrix. During consolidation, the TiB_2 reacts with the matrix to form a layer of TiB needles, ~ 0.7 μm thick.

3.2 Tensile Tests

Uniaxial tensile tests were conducted on specimens containing either notches or circular holes, located at the specimen center. To minimize damage, the specimens were prepared using electrical discharge machining (EDM). The holes ranged in diameter from 0.6 mm to 6 mm. The notches were ~ 400 μm wide and ranged in length from 1.5 mm to 6 mm. The ratio of notch or hole size, $2a_o$, to specimen width, 2w, was fixed at 0.2. In one case, wherein the hole size was 0.6 mm, specimens with a_o/w ratios of 0.2 and 0.05 were prepared and tested. In all cases, the ratio of specimen length to specimen width was greater than 3.

Prior to testing, one face of each specimen was polished to a 1 μm finish. Beveled stainless steel tabs were bonded to the specimen ends with an epoxy adhesive. In some instances, a 0.8 mm strain gauge was attached immediately ahead of the notch or hole. The tests were conducted in a servohydraulic testing machine, using hydraulic wedge grips to load the specimen. The tests were conducted at a fixed displacement rate, between 0.005 and 0.03 mm/min. For comparison, uniaxial

* Sigma fiber, produced by British Petroleum.

tests were also conducted on straight (unnotched) tensile specimens, 6 mm wide, with axial strains measured using a 12.7 mm contacting extensometer. Additional details pertaining to the unnotched tensile strength of this material can be found in a companion paper[9].

3.3 Observations

During the tensile tests, the region immediately ahead of the notch or hole was monitored using a traveling stereo-microscope and recorded using a digital video camera. These observations were used to establish the extent of plasticity. In some cases, the tests were interrupted following the development of an extensive plastic zone (~ 1 to 3 mm), but prior to fracture. The extent of fiber fracture within this zone was determined by dissolving the matrix in the vicinity of the notch with a 49% HF solution and examining the underlying fibers in a scanning electron microscope (SEM). Some of the fracture surfaces were also examined in an SEM.

3.4 Toughness

The composite toughness, Γ, was evaluated using an edge-notched four-point work-of-rupture specimen[10,11], shown in the inset of Fig. 9. (For reasons described below, the notched tensile tests could not be used to obtain Γ.) The test was conducted at a displacement rate of 0.5 mm/min. The toughness (or fracture energy) was evaluated using the relation

$$\Gamma = \frac{\int_0^{u_c} P\,du}{t(w-a_o)} \tag{7}$$

where P is the load, u is the load point displacement, u_c is the displacement at fracture, and t is the specimen thickness.

3.5 Bridging Law Parameters

As detailed in a subsequent section, the effects of holes and notches on the tensile strength of this composite can be rationalized in terms of crack bridging models. One of the important parameters involved in the bridging traction law is the crack opening displacement at fracture, δ_c. This parameter was determined in the notched specimens from measurements of the notch width both before and after fracture. The post-fracture notch width was taken to be the sum of the normal distances from the notch surfaces to the tips of the fracture surface, as shown in the inset of Fig. 10. Similar measurements were made on specimens with small holes (0.6 and 1.5 mm diameter).

Another key parameter in the traction law is the displacement δ_f at the onset of fiber failure. This displacement can be estimated using the relation

$$\delta_f \approx h_p \varepsilon_f \tag{8}$$

where h_p is the width of the plastic zone measured parallel to the loading direction and ε_f is the failure strain of the fibers. The plastic zone size was measured off of micrographs of both sides of the fractured specimen, taken using Nomarski interference microscopy. At each notch tip, ~ 20-30 such measurements were made, starting immediately ahead of the notch tip and proceeding at intervals of ~ 0.2 mm.

Yet another parameter in the traction law is the strength of the composite following fiber fracture. This strength was measured using a two-step procedure. First, a specimen with a 6 mm notch was loaded in tension until plastic strips ~ 3 mm long had developed on both sides of the notch. SEM examinations of similar specimens indicated that all the fibers had indeed fractured within this strip. Narrow, longitudinal strips (~ 2 mm wide), passing through the plastic strips, were

then cut from the tested specimen. These strips were tested in tension, with a 10 mm clip gauge placed across the plastic strip to measure the local displacements.

4. EXPERIMENTAL RESULTS

Figures 4 and 5 show a typical stress-local strain response of a notched panel and a corresponding series of optical micrographs taken during the test. Initially, the response was linear, with non-linearity occurring at a stress of 450 MPa. At a slightly higher stress (590 MPa), a plastic zone was observed at the notch tip (Fig. 5a). Upon further loading, the length of the plastic strip increased stably, reaching ~ 3 mm at a stress of ~ 750 MPa. The specimen was subsequently unloaded for further examination. The local strain at the notch tip was ~ 5%: considerably higher than the fracture strain measured in the unnotched tensile specimens (~ 1%). The ultimate tensile strength of a similar specimen was ~ 850 MPa.

Examinations of specimens interrupted prior to fracture showed that *all* of the fibers contained within the plastic strips had been broken. Figure 6 shows one such example, from a specimen with a notch of length, $2a_0 = 3$ mm. In this case, both the plastic strip and the "plane" of fractured fibers follow the same, somewhat non-planar, path. The specimens containing circular holes exhibited similar patterns of plastic strips and fiber failure prior to catastrophic fracture.

Fractographic examinations showed that minimal fiber pullout occurs during the fracture process (Fig. 7). The pullout length is typically < 100 μm (i.e. one fiber diameter).

The trends in tensile strength $\bar{\sigma}$ with notch or hole size, $2a_0$, are summarized in Fig. 8. Evidently, the strength drops quickly with a_0 in the regime $0 < 2a_0 < 1.5$ mm. For larger values, $2a_0 \gtrsim 1.5$ mm, the strength continues to decrease, though at a much slower rate. The specimens containing holes exhibited similar

trends, though the strengths were slightly higher than those corresponding to notches of the same size, by ~ 6-7%.

The results of the work of rupture test are shown in Fig. 9. Combining these measurements with Eqn. 7 yields a toughness, $\Gamma = 72$ kJ m^{-2}. In this configuration, a similar process of plastic yielding was observed ahead of the notch tip. Once a crack had formed, it propagated stably across the specimen along a mode I path, resulting in a relatively smooth, continuous load-displacement curve.

The measurements of plastic zone width, h_p, and local displacement at fracture, δ_c, are summarized in Fig. 10. A typical optical micrograph used for measuring h_p and δ_c is shown in Fig. 11. The values of both parameters are independent of the specimen size and the specimen confirmation (notch vs. hole), with average values, $h_p \approx 0.9$ mm and $\delta_c \approx 80$ μm.

Figure 12 shows the results of a tensile test conducted on a specimen containing a plastic strip within which all fibers had been broken. The results are presented in the form of stress vs. displacement (not strain), since virtually all the inelastic strain was localized within the previously yielded strip. In this test, the response was essentially elastic-perfectly plastic, with a "yield stress" of ~ 800-850 MPa (approximately one half of the unnotched tensile strength). The inelastic displacement at fracture was ~ 40 μm. As expected, this value is lower than that measured on the notched tensile specimens (Fig. 10), a result of the prior inelastic deformation occurring during the development of the plastic strip.

5. ANALYSIS

5.1 Preliminary Assessment

A preliminary assessment of the trends in notch strength was made using two simple modeling approaches. The first was based on the Griffith relation

(Eqn. 1). Figure 8 shows the predicted trends in strength with notch size for values of Γ ranging from 5 to 30 kJ m^{-2}. The second approach was based on the classical Dugdale model (Eqn. 5). The predicted trends are also shown in Fig. 8, taking σ_o to be equal to the unnotched tensile strength ($\bar{\sigma}_o$ = 1590 MPa) and Γ to range between 5 and 30 kJ m^{-2}, as before. It is apparent that neither approach provides even a fair representation of the experimental measurements. This disparity between experiment and theory provides the motivation for the subsequent modeling effort. Moreover, it demonstrates that the trends in tensile strength with notch length cannot be used to infer the composite toughness.

5.2 Proposed Bridging Traction Law

The present measurements and observations suggest that the notch strength characteristics of the Ti/SiC composite can be rationalized in terms of a bridging traction law having the features shown on Fig. 13. In this law, the stress initially increases with displacement, analogous to the stress-strain response measured in a uniaxial tension test. At a critical stress, S_1, taken to be the unnotched tensile strength of the composite, $\bar{\sigma}_o$, the fiber bundle within the bridging zone fails, causing the stress to drop rather precipitously with increasing crack opening displacement. The corresponding critical displacement, δ_1, depends on the width of the plastic strip (being the effective gauge length) and the fiber failure strain, in accordance with Eqn. 8. Upon further crack opening, the bridging stress reaches a saturation level, dictated by the yield stress of the metal and the "pullout" contribution from broken fibers (detailed later). At a yet larger crack opening displacement, the local strain reaches the failure strain of the metal, leading to the formation of a matrix crack and a loss in bridging.

For modeling purposes, it is convenient to represent this behavior by a two level bridging traction law, shown schematically by the dashed lines in Fig. 13. Each

of the two parts of the traction law are characterized by a strength (S_1 or S_2) and a critical displacement (δ_1 or δ_2). The total (or steady state) fracture energy, obtained using the J-integral, is

$$\Gamma = \int_0^{\delta_2} \sigma_b \, d\delta = \Gamma_1 + \Gamma_2 \tag{9a}$$

where Γ_1 and Γ_2 are the areas contained within the top and bottom parts of the traction law, given by

$$\Gamma_1 = (S_1 - S_2)\delta_1 \tag{9b}$$

and

$$\Gamma_2 = S_2 \delta_2 \tag{9c}$$

A preliminary assessment of the proposed traction law can be made by comparing the total fracture energy, computed using Eqn. (9) along with the measured values of the traction law parameters, with the value obtained through the work-of-rupture test. The experimental measurements indicate that $S_1 = \overline{\sigma}_0 = 1590$ MPa, $S_2 = 850$ MPa (Fig. 12), and $\delta_2 = 80$ μm. Moreover, combining the plastic zone width, $h_p = 0.9$ mm, and the unnotched tensile fracture strain, $\varepsilon_f = 1\%$, with Eqn. 8 yields $\delta_1 \approx 9$ μm. Equation 9 thus predicts a fracture energy, $\Gamma = 71$ kJ m^{-2}, essentially identical to the value obtained experimentally ($\Gamma = 72$ kJ m^{-2}). This correlation provides some initial confidence in the proposed traction law.

5.3 Model of Notch Strength

For the purpose of modeling the notch-strength behavior of such a material, the two-level rectilinear law was incorporated into a fracture mechanics model, shown schematically in Fig. 14. In the model, the composite panel is taken to be infinitely large and contain a sharp, through-thickness notch of length, $2a_o$. The panel is loaded remotely with a uniform tensile stress, σ. The material is assumed to be linearly elastic, except within the plastic strips formed ahead of the notch tips. The stress intensity factor K at the tip of the plastic zone is taken to be zero, such that the material possesses no intrinsic toughness. Two relevant "crack lengths" are identified. The first, $2a_1$, represents the point at which the crack opening displacement δ reaches the critical value, δ_1. Ahead of this point, the tractions on the crack face are given by S_1, and behind it, by S_2. The total crack length (notch and plastic strip) is designated $2a_2$, and the crack opening displacement at the notch tip is designated D.

Two regimes are considered, governed by the value of D. In the first, $D < \delta_1$, such that the model reduces to the classical Dugdale-Barenblatt model, with a uniform bridging stress, S_1. The plastic strip thus extends according to[3,4]

$$\frac{\sigma}{S_1} = \frac{2}{\pi} \cos^{-1}\left(\frac{a_o}{a_1}\right) \tag{10}$$

with a crack opening displacement at the notch tip of

$$\frac{D E}{a_o S_1} = \frac{8}{\pi} \ell n \frac{a_1}{a_o} \tag{11}$$

The maximum stress is obtained by combining Eqns. 10 and 11 and setting $D = \delta_1$. In the second regime, D lies in the range $\delta_1 < D < \delta_2$, such that the plastic zone consists of two parts. Along the part of the crack plane defined by $a_o < |x| < a_1$, the bridging

stress is S_2, and, in that part defined by $a_1 < |x| < a_2$, the bridging stress is S_1, as noted earlier. The stress-crack length relations are obtained from handbook solutions of stress intensity factors and crack opening displacements[13]. In non-dimensional form, the relevant solutions can be expressed as

$$\frac{S_1 E}{\sigma a_o} = f_1 - f_2 \frac{S_1}{\sigma} - f_3 \frac{S_2}{\sigma} \tag{12}$$

$$\frac{K}{\sigma \sqrt{\pi a_o}} = g_1 - g_2 \frac{S_1}{\sigma} - g_3 \frac{S_2}{\sigma} \tag{13}$$

and

$$\frac{D E}{\sigma a_o} = h_1 - h_2 \frac{S_1}{\sigma} - h_3 \frac{S_2}{\sigma} \tag{14}$$

where the parameters f_i, g_i and h_i are functions of the crack length ratios, a_1/a_o and a_2/a_o, and are listed in the Appendix. Recognizing that $K = 0$ allows Eqn. 13 to be re-written as

$$\frac{\sigma}{S_1} = \frac{g_2}{g_1} + \frac{g_3}{g_1} \frac{S_2}{S_1} \tag{15}$$

which, combined with Eqn. 12, gives

$$\frac{\delta_1 E}{S_1 a_o} = \left(\frac{g_2}{g_1} + \frac{g_3 S_2}{g_1 S_1} \right) f_1 - f_2 - f_3 \frac{S_2}{S_1} \tag{16}$$

The stress-crack opening displacement curve is obtained by incrementally stepping through values of a_1/a_o, starting with the one evaluated using Eqn. 11 with

$D = \delta_1$. At each point, the ratio a_2/a_o is evaluated by numerically solving Eqn. 16, and the result then combined with Eqns. 12 and 14 to get σ and D, respectively.

Figure 15 shows illustrative examples of the trends in σ with D for a strength ratio, $S_1/S_2 = 2$, and a toughness ratio, $\Gamma_1/\Gamma_2 = 0.1$. For reasons that will become apparent in the subsequent section, the toughness ratio Γ_1/Γ_2 is designated λ, analogous to Eqn. 6. Three types of behavior are obtained, governed by the normalized notch length, α. (i) For very small notch lengths ($\alpha << 1$), the maximum stress is reached almost immediately after D exceeds δ_1. In this case, the ductility of the matrix (manifested in the critical displacement, δ_2) does not increase the notch strength of the composite. (ii) For intermediate sized notches, the maximum stress occurs at a value of D that is substantially larger than δ_1. Consequently, composite fracture does not occur immediately following the onset of fiber failure. Here, the matrix ductility provides some enhancement in tensile strength. (iii) For very long notches ($\alpha >> 1$), the maximum stress is obtained when the matrix fails, i.e. $D = \delta_2$. The relationship between strength, $\bar{\sigma}$, and notch length, α, is obtained from the maximum points in these curves.

Figure 16 shows the predicted trends in strength with notch length, for $S_1/S_2 = 2$ and Γ_1/Γ_2 ranging from 0 to 0.2. Also shown are the values obtained experimentally. The comparisons show that the predictions are in close agreement with the measurements for Γ_1/Γ_2 in the range ~ 0.03-0.1. The inferred value of Γ_1/Γ_2 is comparable to the one calculated using the values of S_1, S_2, δ_1 and δ_2 quoted above: $\Gamma_1/\Gamma_2 \sim 0.09$.

Because of the similarities in the strength characteristics of the specimen containing holes and notches, no calculations were conducted for holes. The similarities are consistent with previous calculations which show that the strength of materials that exhibit bridging is insensitive to the shape of the discontinuity, provided the bridging length scale is sufficiently large compared with a_o. Indeed, for

the entire range of hole and notch sizes used in this study, the normalized notch size lies in the range $\alpha \lesssim 0.5$ (Fig. 3).

5.4 An Alternate Approach

It is instructive to consider an alternate description of the fracture resistance: one that leads to a simpler solution to the notch sensitivity. For this purpose, it is noted that the energy dissipated in the top portion of the traction law is small in relation to the total. (i.e. $\Gamma_1/\Gamma_2 \sim 0.05$). Moreover, the critical displacement δ_1 is small in relation to δ_2. Consequently, the energy dissipated in the top portion can be lumped into an *intrinsic* fracture energy, Γ_o, whereupon

$$\Gamma_o = \Gamma_1 = (S_1 - S_2)\,\delta_1 \tag{17}$$

The fracture resistance can thus be characterized by Γ_o in combination with a single-level rectilinear bridging traction law, with a characteristic strength, S_2, and a critical displacement, δ_2. The toughness derived from bridging is thus

$$\Gamma_b \equiv \Gamma_2 = S_2\,\delta_2 \tag{18}$$

and the toughness ratio is again defined by $\lambda = \Gamma_o/\Gamma_b$.

The notch strength of such a system can be evaluated following the approach presented in the preceding section, with two modifications. First, since the stress along the entire bridged zone is uniform, a_1 is equivalent to a_o. Second, the crack tip stress intensity factor is finite and taken to be equal to the intrinsic fracture toughness, $\sqrt{\Gamma_o E}$. In this case, Eqns. 12-14 reduce to

$$\sqrt{\frac{\Gamma_o E}{\sigma^2 \pi a_o}} = \sqrt{\frac{a_2}{a_o}} - \frac{2}{\pi}\sqrt{\frac{a_2}{a_o}}\,\frac{S_2}{\sigma}\cos^{-1}\left(\frac{a_o}{a_2}\right) \tag{19}$$

and $$\frac{D E}{\sigma a_o} = 4\sqrt{\left(\frac{a_2}{a_o}\right)^2 - 1} - \frac{8}{\pi}\,\frac{S_2}{\sigma}\left(\sqrt{\left(\frac{a_2}{a_o}\right)^2 - 1}\,\cos^{-1}\left(\frac{a_o}{a_2}\right) - \ell n\,\frac{a_2}{a_o}\right) \tag{20}$$

The stress-crack opening relation is obtained by incrementally stepping through values of a_2/a_o, starting from zero. At each point, the stress σ is evaluated from Eqn. 19 and the result combined with Eqn. 20 to obtain D. Figure 15 shows comparisons of the predicted trends in σ vs. D with those obtained from the two-level rectilinear law. Evidently, the two solutions provide essentially the same results for $D/\delta_2 \gtrsim 0.1$.

Figure 16 shows the predicted trends in strength with notch length, again for values of λ ranging from 0 to 0.2. Over the range of interest ($\alpha \gtrsim 0.1$, $\lambda \lesssim 0.1$), the predictions are essentially identical to those of the two-level bridging law. For smaller values of α, the model predicts a strength-notch length relation of the form

$$\frac{\bar{\sigma}}{S_1} = \sqrt{\frac{E\Gamma_o}{\pi a_o S_1^2}} \tag{21}$$

in accordance with the Griffith equation. In this regime, the model strongly overestimates the notch-strength of the composite. Consequently, the two-level bridging law is required to capture the relevant trends.

It is of interest to note, parenthetically, that a conservative estimate of the notch strength can be obtained by assuming $\lambda = 0$, whereupon both models reduce to the Dugdale-Barenblatt model (Eqn. 5), with the bridging stress replaced by $S_2 = S_1/2$.

6. DISCUSSION

The present measurements allow some rudimentary connections to be established between the parameters involved in the traction law and the properties of the composite constituents. Such connections are important in understanding the role of microstructure in composite behavior and provide guidance for the development of new materials.

As noted previously, the peak stress, S_1, is equivalent to the unnotched composite tensile strength, $\bar{\sigma}_0$. This strength is controlled by the matrix yield stress and the *in-situ* fiber bundle strength, as described in a companion paper[9]. For this class of composite, the fiber bundle strength is *independent* of gauge length, provided the gauge length exceeds a critical value,

$$\ell_c = \left(\frac{S_o R L_o^{1/m}}{\tau} \right)^{m/(m+1)} \tag{22}$$

where τ is the interfacial sliding stress, R is the fiber radius, S_0 is the reference strength corresponding to a length L_0 in the Weibull distribution, and m is the Weibull modulus. In the Ti/SiC composite, the critical length is of the order, $\ell_c \approx 2$ mm: being approximately twice the relevant gauge length in the bridging process, namely, the plastic zone width, h_p. Simulations of fiber bundle failure for gauge lengths in the range $0.5 < \ell/\ell_c < 1$ suggest that the tensile strength is elevated only slightly (~ 5-10%) over the value corresponding to a long gauge length ($\ell/\ell_c \geq 1$)[12]. Consequently, S_1, is expected to be essentially the same as the tensile strength measured on a standard tensile coupon.

Bounds on the strength, S_2, characterizing the post-fiber failure regime, can be established in the following way. An upper bound estimate is obtained by taking the

average stress acting across a hypothetical crack plane passing through the middle of the plastic zone, whereupon

$$S_2 = (1-f)\,\sigma_m^y + f\,\hat{\sigma}_f \tag{23}$$

with $\hat{\sigma}_f$ being the average fiber stress resulting from fiber/matrix sliding following fiber fracture. For simplicity, the fiber failure sites are assumed to be randomly distributed within the plastic zone, with an average distance between the fracture sites and the hypothetical plane of ~$h_p/4$ (Fig. 17). Using a simple shear lag model, $\hat{\sigma}_f$ can be approximated by

$$\hat{\sigma}_f \approx \tau h_p/2R \tag{24}$$

Using the relevant measurements ($h_p \approx 800$ μm, R = 50 μm, τ = 130 MPa, σ_m^y = 1000 MPa) yields a value of strength, $S_2 \approx 1000$ MPa, somewhat higher than the measured value (850 MPa). This discrepancy may be attributed to the pullout distances being less than $h_p/4$ (~200 μm), as manifest in the relatively short pullout lengths measured on the fracture surface (<100 μm). A lower bound estimate is obtained by neglecting the pullout contribution derived from broken fibers, whereupon the strength reduces to

$$S_2 = (1-f)\,\sigma_m^y \tag{25}$$

This result predicts a value of strength, $S_2 \approx 680$ MPa, somewhat lower than the measured value.

The critical displacements, δ_1 and δ_2, are both expected to scale with the width of the plastic zone. As noted earlier, δ_1 is governed by the strain at fiber bundle

failure, in accordance with Eqn. 8. Similarly, δ_2 scales with the ductility of the matrix, $\bar{\varepsilon}_m$, according to the relation

$$\delta_2 \approx \varepsilon_m h_p \tag{26}$$

Combining the measured values, $\delta_2 \approx 80$ μm and $h_p \approx 0.9$ mm, with Eqn. 26 yields an estimate of the matrix ductility, $\bar{\varepsilon}_m \approx 9\%$, in agreement with values reported for similar Ti alloys [8– 10%][14].

The origin of the plastic zone width is presently not understood. It is speculated that it may be controlled by the panel thickness (≈ 1mm), as it is in thin ductile sheets[2]. This hypothesis requires experimental verification.

7. CONCLUDING REMARKS

The present study demonstrates that the notch-strength characteristics of fiber-reinforced Ti matrix composites can be described using crack bridging models, similar to those used to describe the behavior of ductile metals and ceramic matrix composites. The parameters controlling the bridging traction law have been measured and found to provide a consistent description of both the notch sensitivity and the steady state composite toughness. The two models considered here (one based on the two-level rectilinear bridging law and the other on the rectilinear law with a finite intrinsic toughness) yield similar predictions for notch sizes that are relevant in structural design ($2a_o \gtrsim 1$ mm). Owing to its simplicity, the latter model is preferred. The models are computationally relatively simple, making them amenable for use in design.

ACKNOWLEDGMENTS

Funding for this work was supplied by the DARPA University Research Initiative Program at UCSB under ONR contract N0014-92-J-1808.

Table I Summary of Tensile Test Results

	Hole or Notch Size, $2a_o$ (mm)	Specimen Width, 2W (mm)	Ratio, a_o/W	Ultimate Tensile Strength, σ_u (MPa)
Unnotched	—	6.0	—	1590 ± 100*
Hole	0.6	12.0	0.05	1210
Hole	0.6	3.0	0.20	1180
Hole	1.5	7.5	0.20	980
Hole	3.0	15.0	0.20	910
Hole	6.0	30.0	0.20	860
Notch	1.5	7.5	0.20	910
Notch	3.0	15.0	0.20	850
Notch	6.0	30.0	0.20	810

* Average and standard deviation from 8 tests.

REFERENCES

1. J. Doychak, *J. Metals*, **44** (1992), No. 6, 46-51.

2. D.S. Dugdale, *J. Appl. Mech.*, **8** (1960), 100-104.

3. B.A. Bilby, A.H. Cottrell and K.H. Swindon, *Proc. Royal Soc. London*, **A272**, 304-14.

4. A.H. Cottrell, Mechanics of Fracture, *Tewksbury Symposium on Fracture*, Jan. 1963, University of Melbourne Press.

5. J.R. Rice, *J. Appl. Mech.*, June, 1968, 379-86.

6. D.B. Marshall and B.N. Cox, *Acta Metall.* **35** (1987), 2607-19.

7. Z. Suo, S. Ho and X. Gong, *J. Eng. Mater. Tech.*, **115** (1993), 319-26.

8. G. Bao and F. Zok, *Acta Metall. Mater.*, **41** (1993), 3515-24.

9. C.H. Weber, X. Chen, S.J. Connell and F.W. Zok, submitted to *Acta Metall. Mater.*, (1993).

10. H.G. Tattersall and G. Tappin, *J. Mater. Sci.*, **1** (1966), 296-301.

11. J.I. Bluhm, *Eng. Fract. Mech.*, **7** (1975), 593-604.

12. F. Hild, J.M. Domergue, F.A. Leckie and A.G. Evans, *Int. J. Solids Struct.* (1993), in press.

13. H. Tada, P.C. Paris and C.R. Irwin, "The Stress Analysis of Cracks Handbook", Second Edition, Paris Productions Inc., St. Louis (1985).

14. Metals Handbook, Ninth Ed. (1990), Vol. 3, "Properties and Selection: Stainless Steels, Tool Materials and Special Purpose Metals, ASM, Metals Park, OH, pp. 388-91.

APPENDIX

The geometric parameters, f_i, g_i and h_i, in Eqns. 12-14 are given by[13]

$$f_1 = 4\sqrt{\eta_2^2 - \eta_1^2} \tag{A1}$$

$$f_2 = \frac{8}{\pi}\left[\sqrt{\eta_2^2 - \eta_1^2}\cos^{-1}\left(\frac{\eta_1}{\eta_2}\right) - \eta_1 \ln\left(\frac{\eta_2}{\eta_1}\right)\right] \tag{A2}$$

$$f_3 = \frac{8}{\pi}\left\{\sqrt{\eta_2^2 - \eta_1^2}\left[\sin^{-1}\left(\frac{\eta_1}{\eta_2}\right) - \sin^{-1}\left(\frac{1}{\eta_2}\right)\right] + \eta_1 \ln\left(\frac{\eta_2}{\eta_1}\right)\right\}$$
$$+\frac{8}{\pi}\left\{\eta_1 \tanh^{-1}\sqrt{\frac{(\eta_2/\eta_1)^2 - 1}{\eta_2^2 - 1}} - \tanh^{-1}\sqrt{\frac{\eta_2^2 - \eta_1^2}{\eta_2^2 - 1}}\right\} \tag{A3}$$

$$h_1 = 4\sqrt{\eta_2^2 - 1} \tag{A4}$$

$$h_2 = \frac{8}{\pi}\left[\sqrt{\eta_2^2 - 1}\cos^{-1}\left(\frac{\eta_1}{\eta_2}\right)\right]$$
$$+\frac{8}{\pi}\left[\coth^{-1}\sqrt{\frac{\eta_2^2 - 1}{(\eta_2/\eta_1)^2 - 1}} - \eta_1 \coth^{-1}\sqrt{\frac{\eta_2^2 - 1}{\eta_2^2 - \eta_1^2}}\right] \tag{A5}$$

$$h_3 = -\frac{8}{\pi}\left\{\sqrt{\eta_2^2 - 1}\left[\sin^{-1}\left(\frac{1}{\eta_2}\right) - \sin^{-1}\left(\frac{\eta_1}{\eta_2}\right)\right] + \ln \eta_2\right\}$$
$$+\frac{8}{\pi}\left\{-\coth^{-1}\sqrt{\frac{\eta_2^2 - 1}{(\eta_2/\eta_1)^2 - 1}} + \eta_1 \coth^{-1}\sqrt{\frac{\eta_2^2 - 1}{\eta_2^2 - \eta_1^2}}\right\} \tag{A6}$$

$$g_1 = \sqrt{\eta_2} \tag{A7}$$

$$g_2 = \frac{2}{\pi}\sqrt{\eta_2}\cos^{-1}\left(\frac{\eta_1}{\eta_2}\right) \tag{A8}$$

$$g_3 = \frac{2}{\pi}\sqrt{\eta_2}\left[\cos^{-1}\left(\frac{1}{\eta_2}\right) - \cos^{-1}\left(\frac{\eta_1}{\eta_2}\right)\right] \tag{A9}$$

where η_1 and η_2 are normalized crack lengths defined by

$$\eta_1 \equiv a_1/a_o \tag{A10}$$

and $$\eta_2 \equiv a_2/a_o \tag{A11}$$

NOMENCLATURE

$2a_o$	Notch width, or hole diameter
$2a_1$	Crack length at $\delta = \delta_1$
$2a_2$	Total length of notch and plastic strip
c	Flaw size
D	Crack opening displacement at notch tip
E	Young's modulus
f_i, g_i, h_i	Geometric parameters (Appendix)
h_p	Plastic zone width
K	Crack tip stress intensity factor
ℓ_c	Critical (transfer) length
L_o	Reference length (1 m)
m	Weibull modulus
P	Load
R	Fiber radius
S_o	Reference strength, corresponding to $L_o = 1$ m
S_1, S_2	Bridging stresses in two-level rectilinear law
t	Panel thickness
w	Half width (width for edge notched specimen)
α	Normalized notch length ($a_o\ \bar{\sigma}_o^2/\Gamma E$)
δ	Crack opening displacement (COD)
δ_1, δ_2	Critical values of δ in bridging traction law
δ_f	COD needed for fiber fracture
δ_c	COD needed for matrix fracture

ε_f	Fiber failure strain
ε_m	Matrix failure strain
Γ	Fracture energy
Γ_1, Γ_2	Components of fracture energies from bridging
Γ_b	Fracture energy derived from bridging
Γ_o	Intrinsic toughness
λ	Toughness ratio
	($\lambda=\Gamma_o/\Gamma_b$ for rectilinear law, $\lambda=\Gamma_1/\Gamma_2$ for two-level rectilinear law)
σ	Remote tensile stress
σ_o	Bridging stress
$\bar{\sigma}$	Notched tensile strength
$\bar{\sigma}_o$	Unnotched tensile strength
σ_m^y	Matrix yield stress
σ_y	Yield stress of monolithic metal
τ	Interfacial sliding stress

FIGURES

Fig. 1 Predicted trends in notch-strength with normalized notch size for several different forms of the bridging traction law.

Fig. 2 Influence of the intrinsic toughness Γ_o on the notch-strength characteristics for the rectilinear bridging traction law.

Fig. 3 Effects of circular holes vs. sharp notches on strength.

Fig. 4 The stress-local strain response of a specimen containing a 6 mm notch.

Fig. 5 Optical micrographs showing the progression of plastic strip development. The labels A, B, and C correspond to the stress levels shown in Fig. 4.

Fig. 6 Comparison of (a) the plastic strip ahead of a notch tip, with (b) the pattern of fiber fracture following matrix dissolution. The micrographs show identical regions of the specimen.

Fig. 7 SEM micrograph showing degree of fiber pullout.

Fig. 8 Trends in tensile strength with hole or notch size. Also shown for comparison are predictions based on the Griffith equation and the Dugdale model.

Fig. 9 Load-displacement curve measured on work-of-rupture specimen.

Fig. 10 Trends in (a) plastic zone width, h_p, and (b) local displacement at fracture, δ_c, with hole or notch size.

Fig. 11 Optical micrograph showing plasticity around the hole following fracture.

Fig. 12 Tensile tests of specimen containing plastic strip with broken fibers.

Fig. 13 Schematic diagram of the proposed traction law governing fracture in the Ti/SiC composite.

Fig. 14 Schematic diagram of the crack bridging model.

Fig. 15 Predicted stress-crack opening curves for the two traction laws: (i) the two-level rectilinear law, with no intrinsic toughness ($\Gamma_o = 0$), and (ii) the rectilinear law, with an intrinsic toughness, Γ_o.

Fig. 16 Comparisons between experimental measurements and predictions of models based on (i) the two-level rectilinear traction law, (ii) and the simple rectilinear law, with an intrinsic toughness Γ_o.

Fig. 17 Schematic diagram showing contribution from matrix yielding and fiber pullout on the composite strength in the post-fiber failure regime.

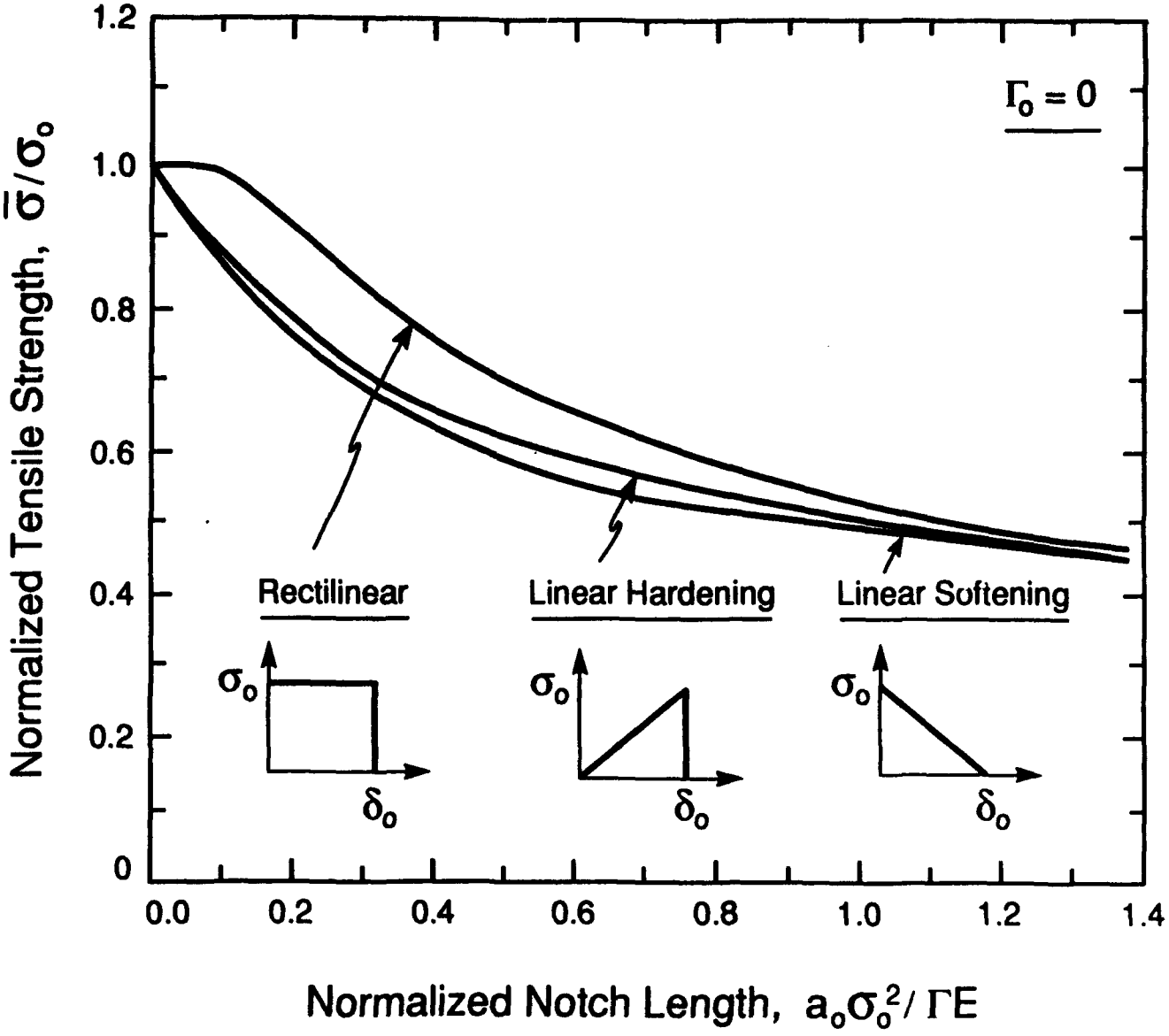
1.2
1.0
0.8
0.6
0.4
0.2
0
0.0
0.2
0.4
0.6
0.8
1.0
1.2
1.4
$\Gamma_o = 0$
Rectilinear
Linear Hardening
Linear Softening
σ_o
δ_o
Normalized Tensile Strength, $\bar{\sigma}/\sigma_o$
Normalized Notch Length, $a_o\sigma_o^2/\Gamma E$

Figure 1

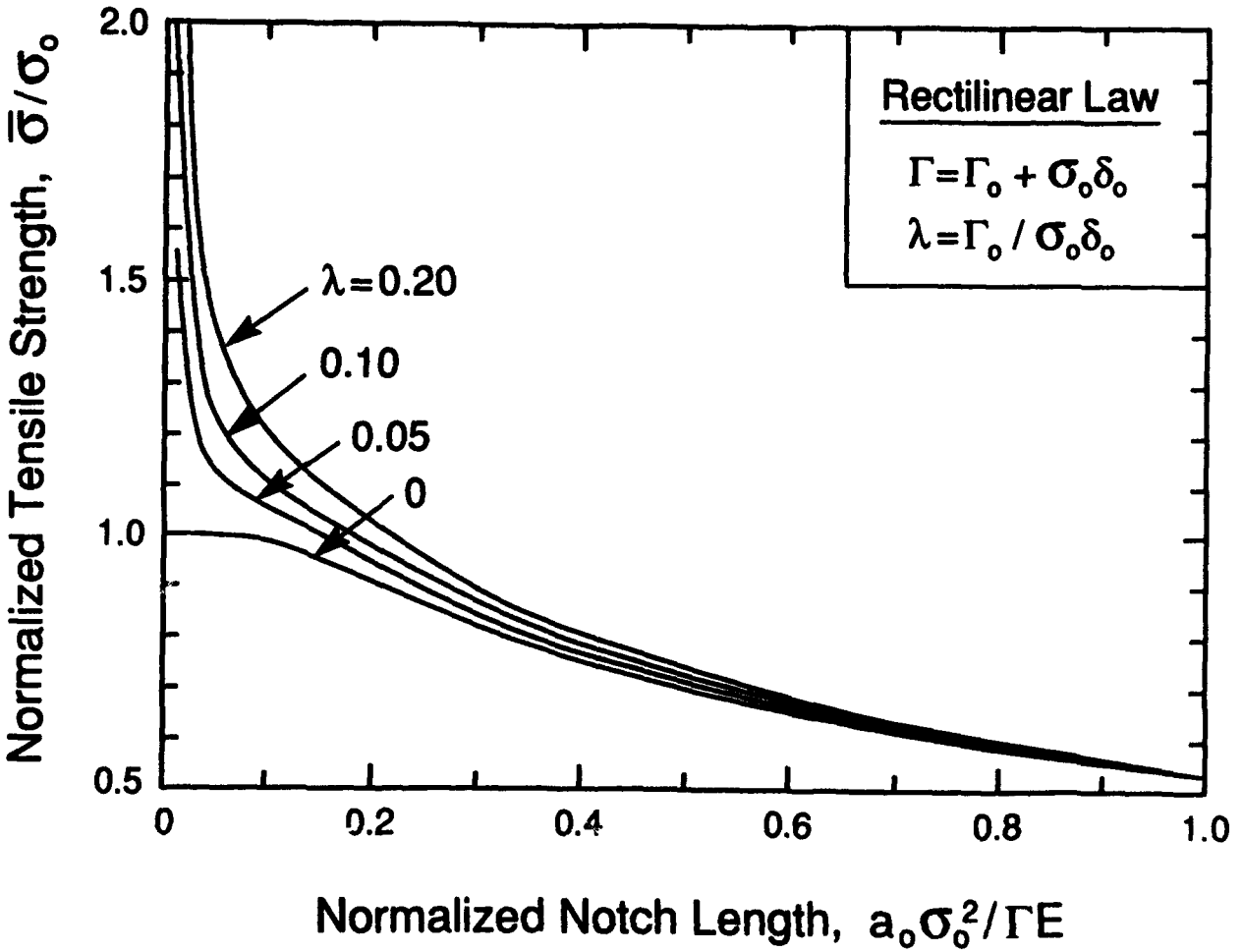
Rectilinear Law
$\Gamma=\Gamma_o+\sigma_o\delta_o$
$\lambda=\Gamma_o/\sigma_o\delta_o$
$\lambda=0.20$
0.10
0.05
0
Normalized Tensile Strength, $\bar{\sigma}/\sigma_o$
2.0
1.5
1.0
0.5
0
0.2
0.4
0.6
0.8
1.0
Normalized Notch Length, $a_o\sigma_o^2/\Gamma E$

Figure 2

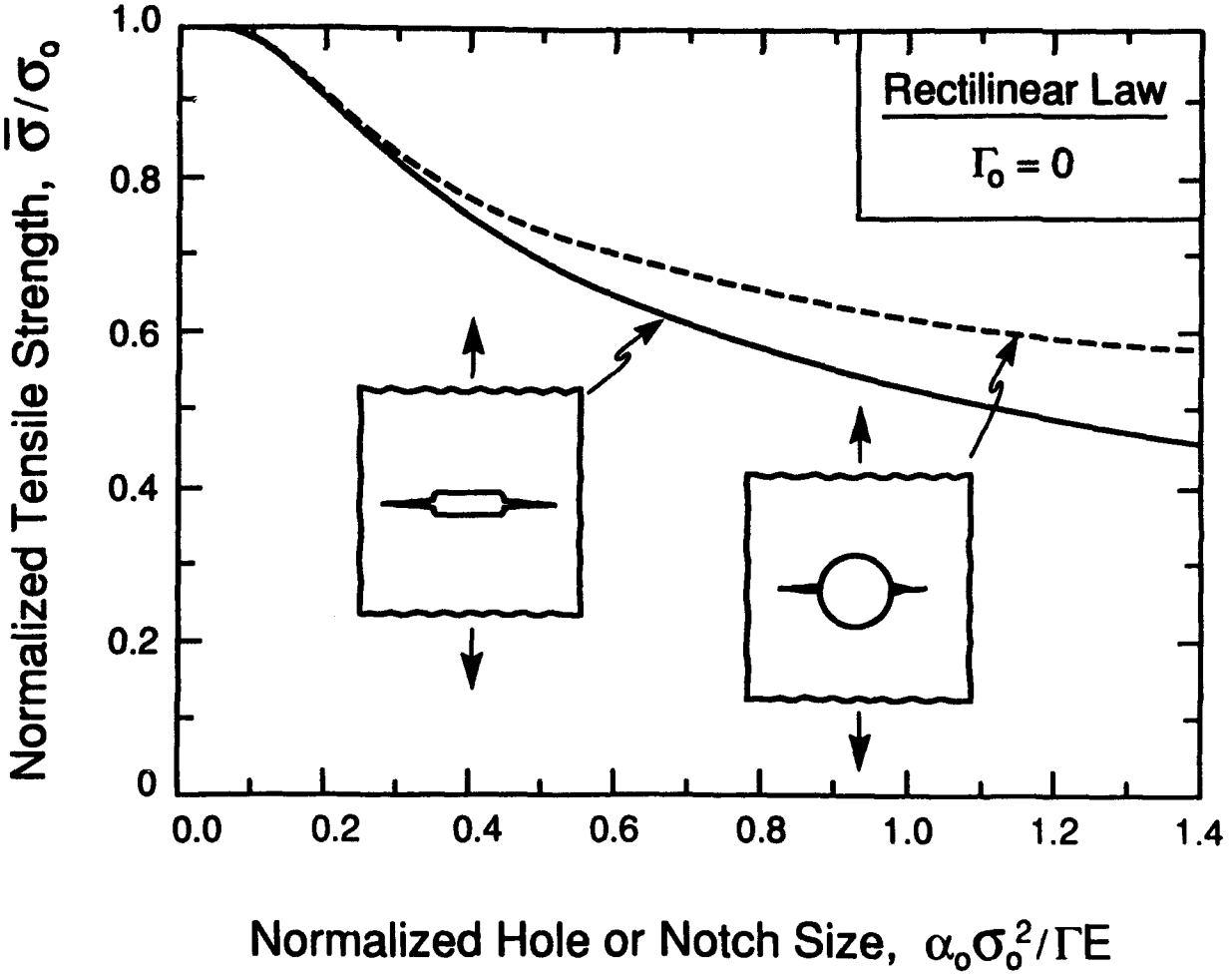
Rectilinear Law
$\Gamma_o = 0$
Normalized Tensile Strength, $\bar{\sigma}/\sigma_o$
1.0
0.8
0.6
0.4
0.2
0
0.0
0.2
0.4
0.6
0.8
1.0
1.2
1.4
Normalized Hole or Notch Size, $\alpha_o\sigma_o^2/\Gamma E$

Figure 3

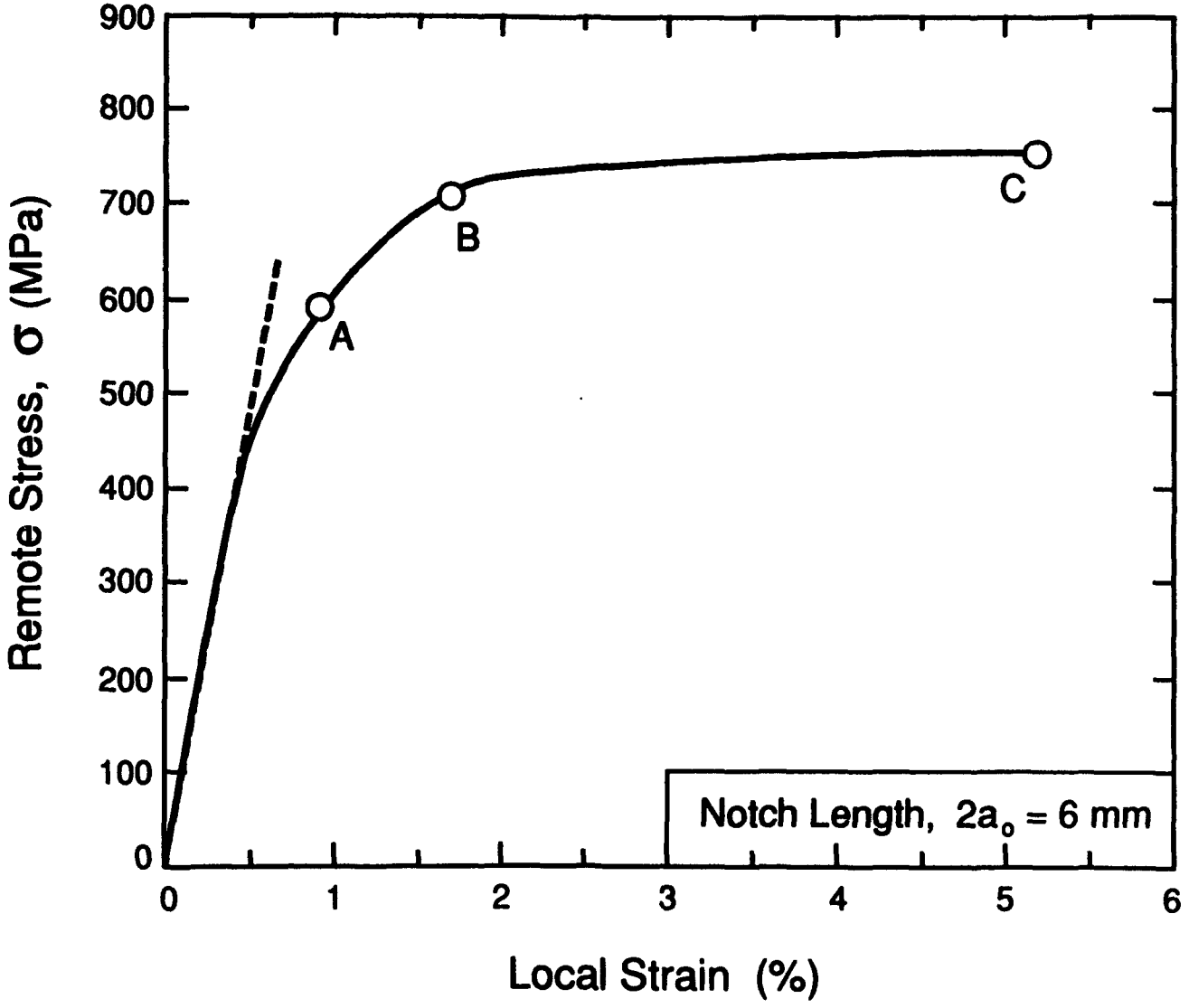
900
800
700
600
500
400
300
200
100
0
Remote Stress, σ (MPa)
A
B
C
Notch Length, $2a_o$ = 6 mm
0
1
2
3
4
5
6
Local Strain (%)

Figure 4

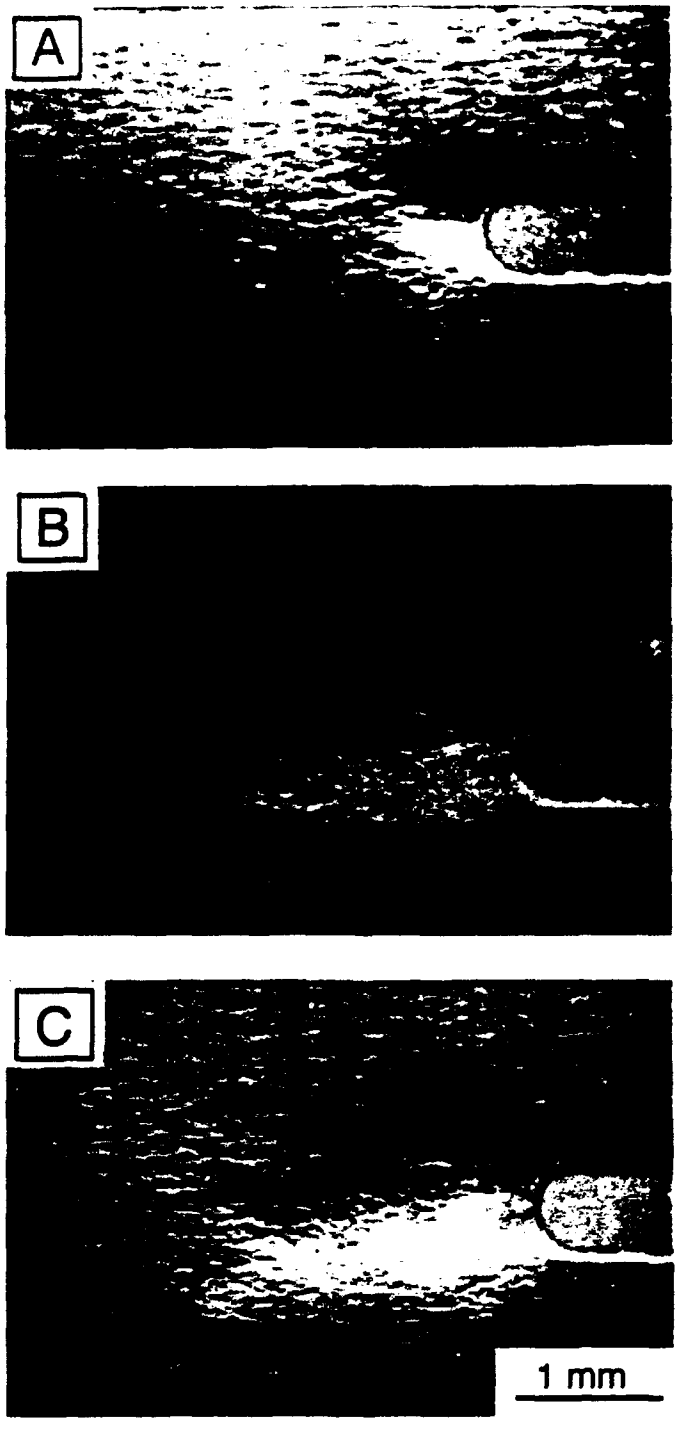

Figure 5

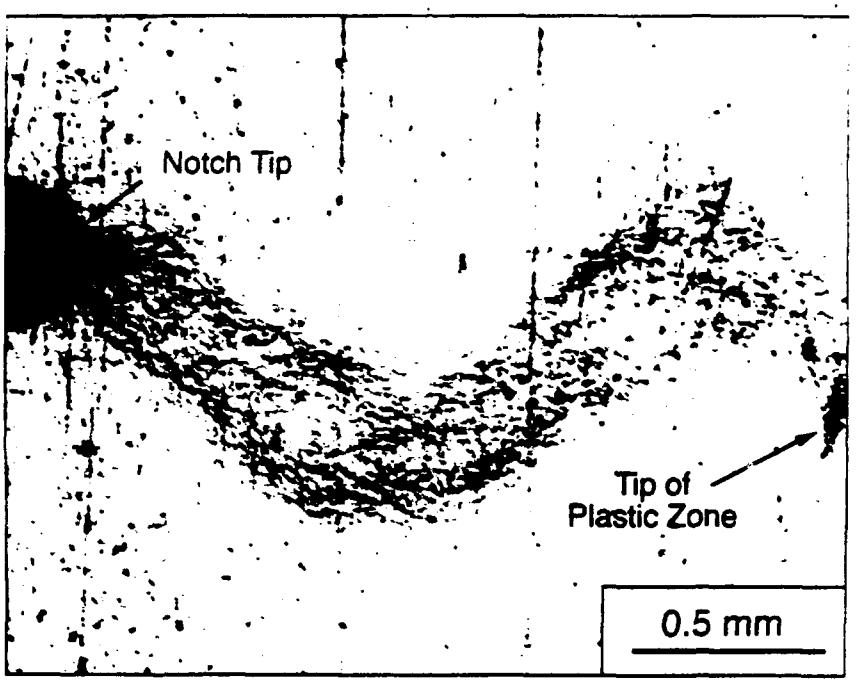

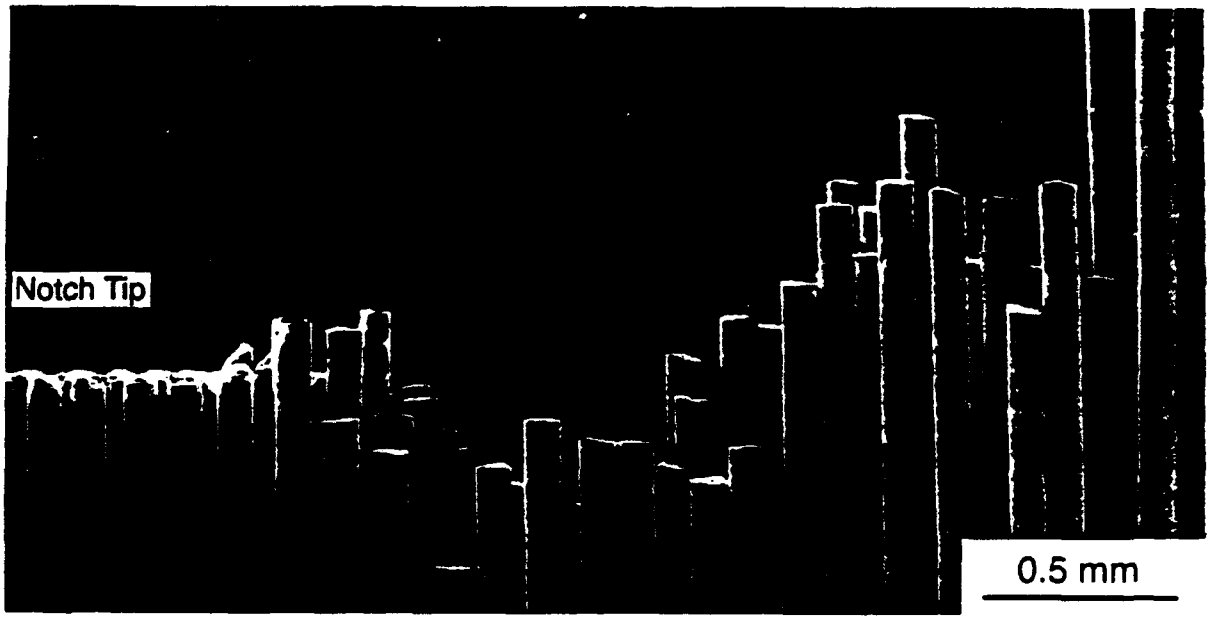

Figure 6

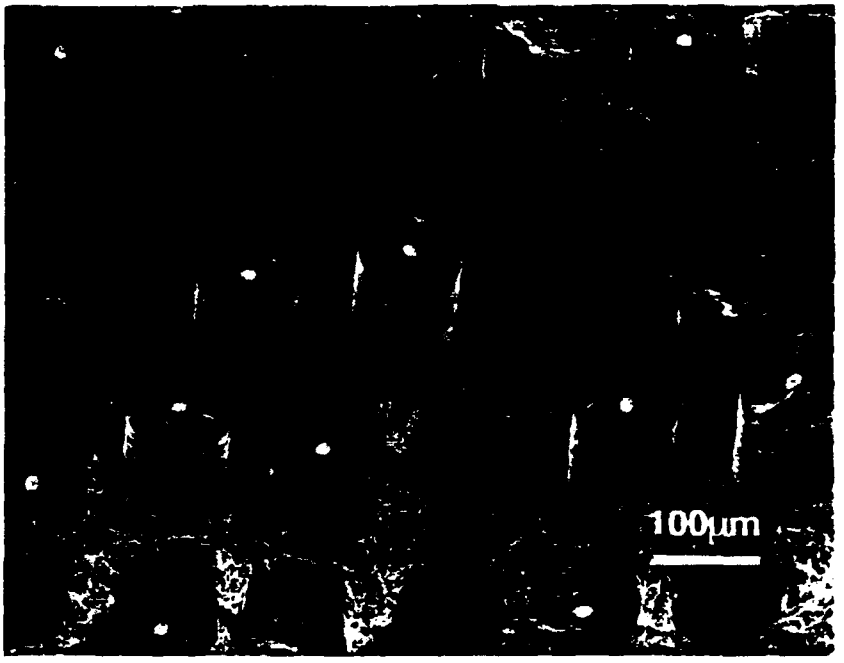

Figure 7

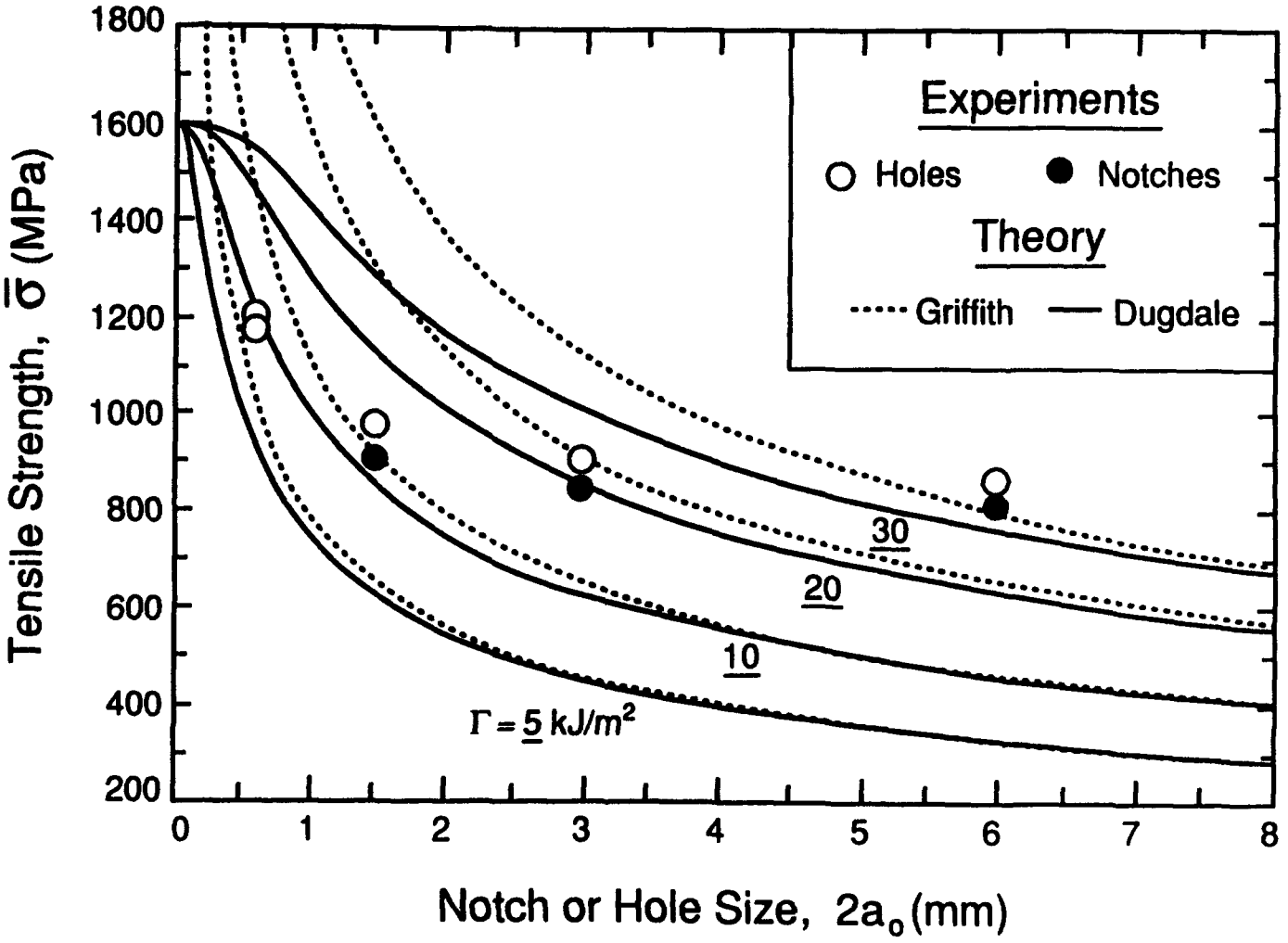
Experiments
Holes
Notches
Theory
Griffith
Dugdale
30
20
10
Γ = 5 kJ/m²
Tensile Strength, σ̄ (MPa)
Notch or Hole Size, 2a₀ (mm)
1800
1600
1400
1200
1000
800
600
400
200
0
1
2
3
4
5
6
7
8

Figure 8

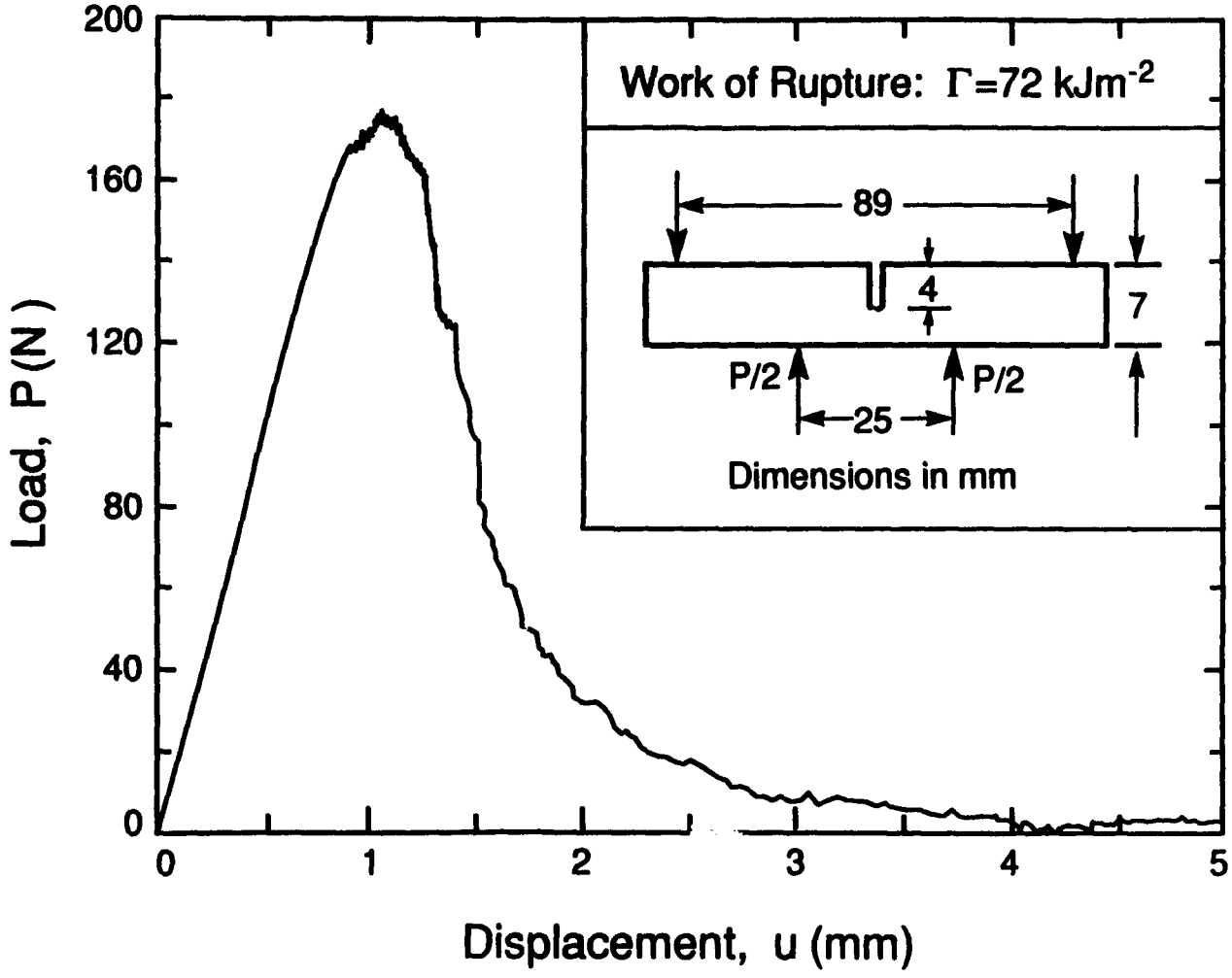
Work of Rupture: Γ=72 kJm-2
89
4
7
P/2
P/2
25
Dimensions in mm
Load, P(N)
200
160
120
80
40
0
0
1
2
3
4
5
Displacement, u (mm)

Figure 9

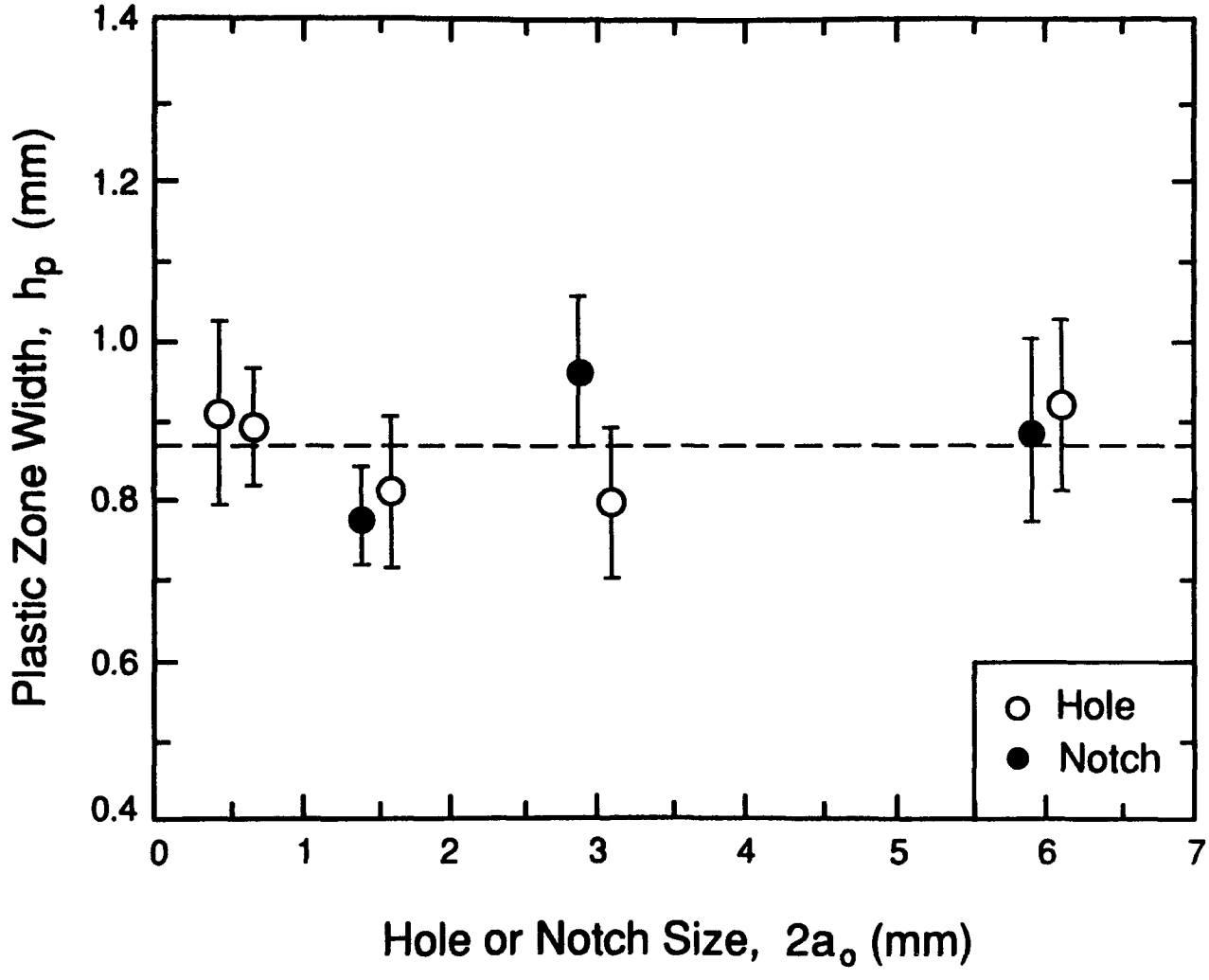
Plastic Zone Width, h_p (mm)
1.4
1.2
1.0
0.8
0.6
0.4
0
1
2
3
4
5
6
7
Hole or Notch Size, $2a_o$ (mm)
Hole
Notch

Figure 10(a)

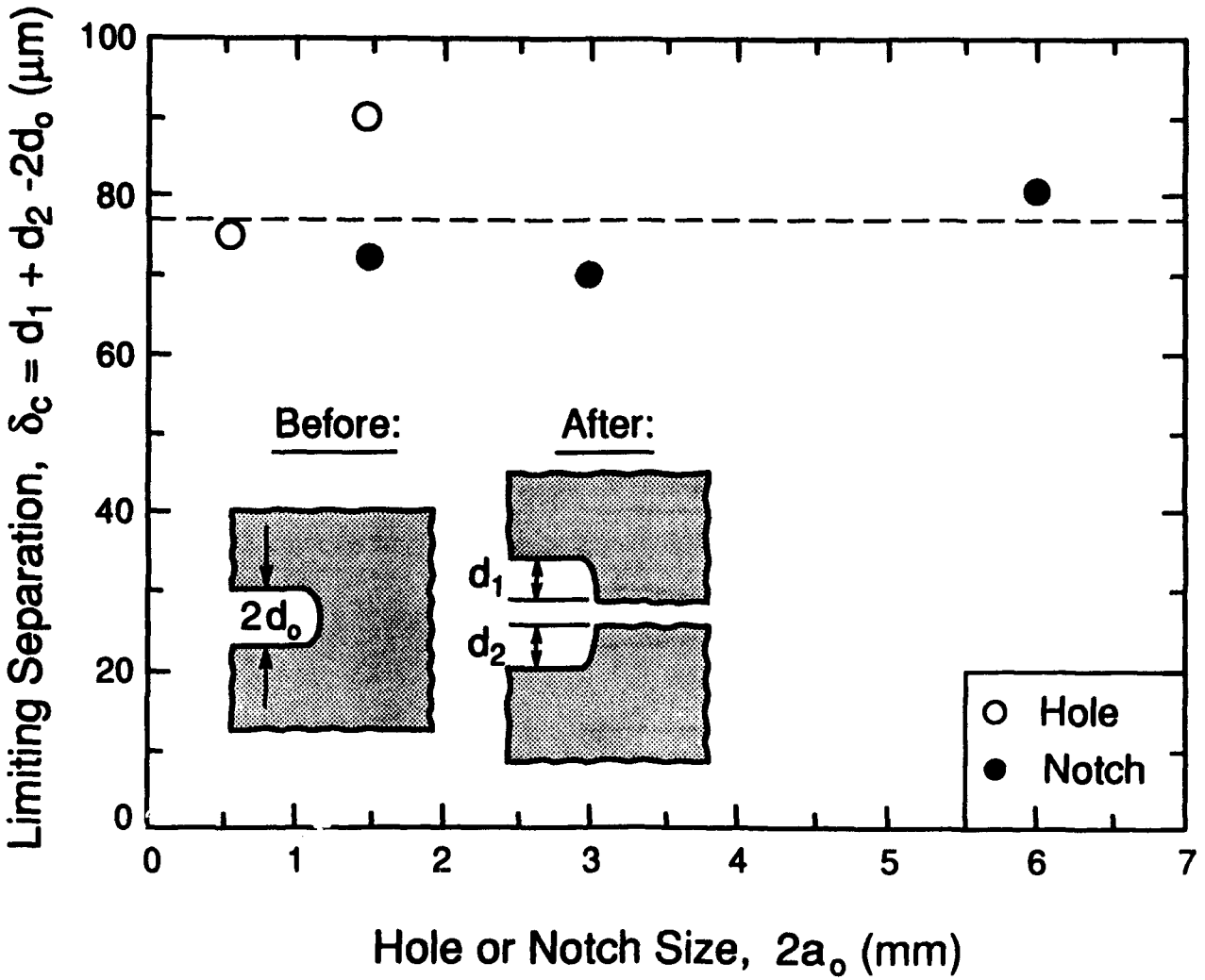
Limiting Separation, $\delta_c = d_1 + d_2 - 2d_o$ (μm)
100
80
60
40
20
0
0
1
2
3
4
5
6
7
Hole or Notch Size, $2a_o$ (mm)
Before:
After:
$2d_o$
d_1
d_2
Hole
Notch

Figure 10(b)

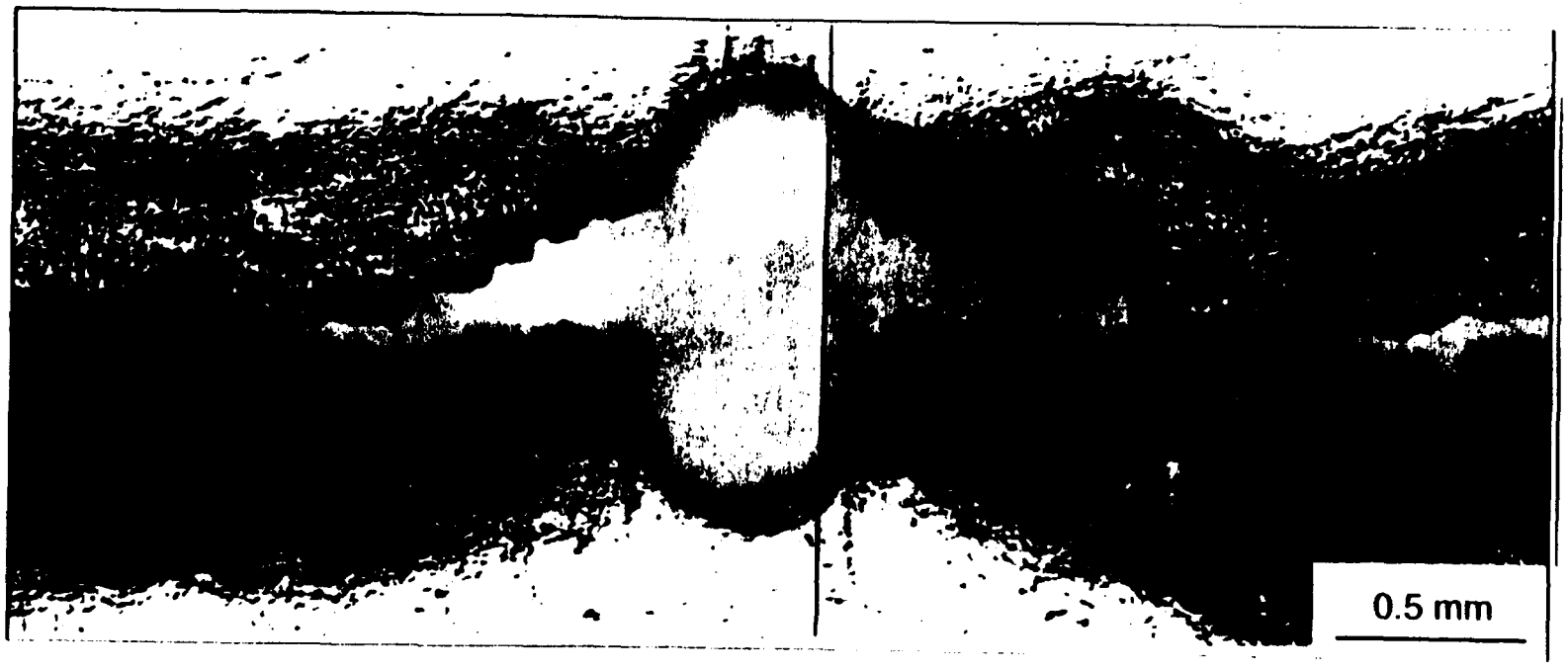

Figure 11

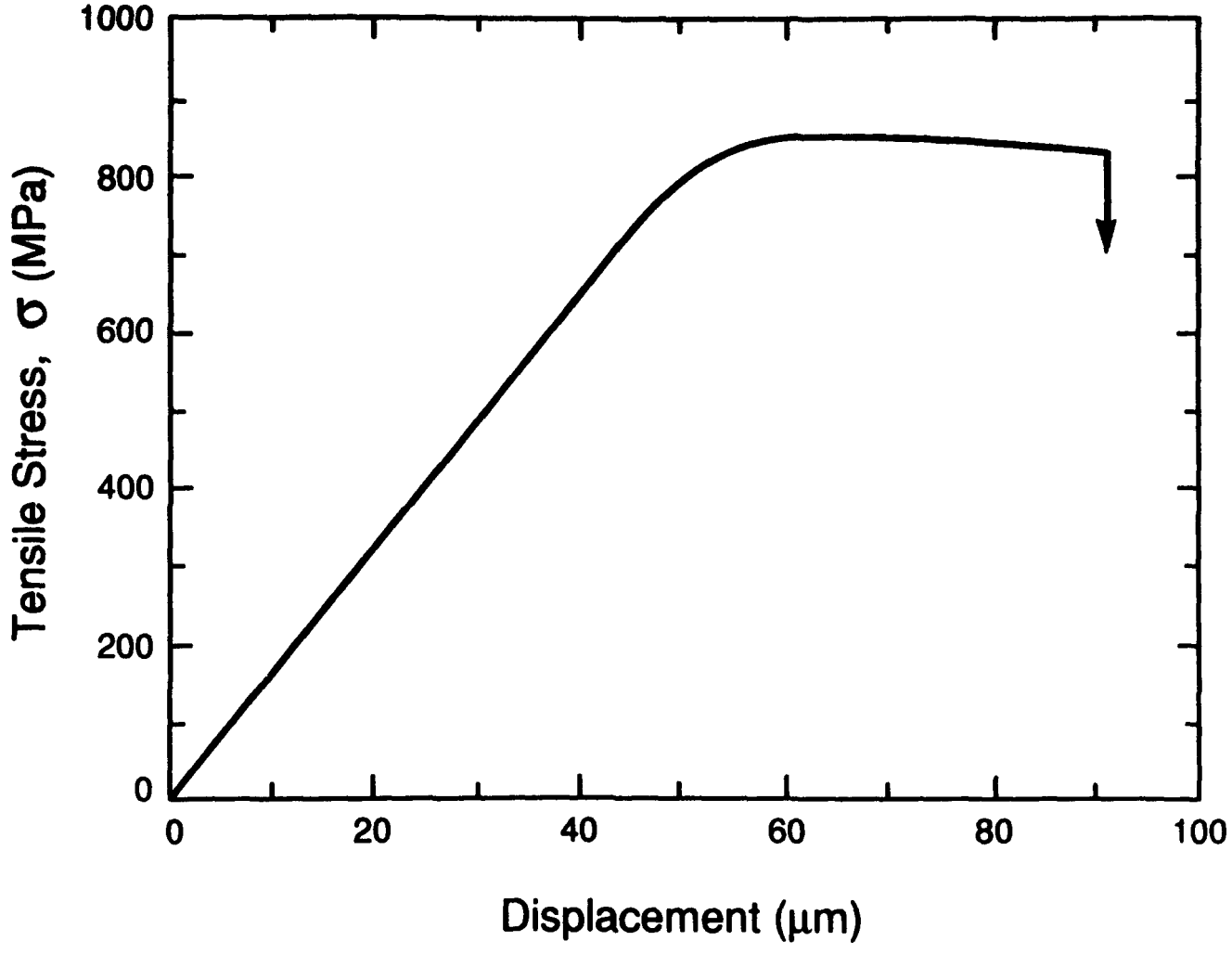
1000
800
600
400
200
0
Tensile Stress, σ (MPa)
0
20
40
60
80
100
Displacement (μm)

Figure 12

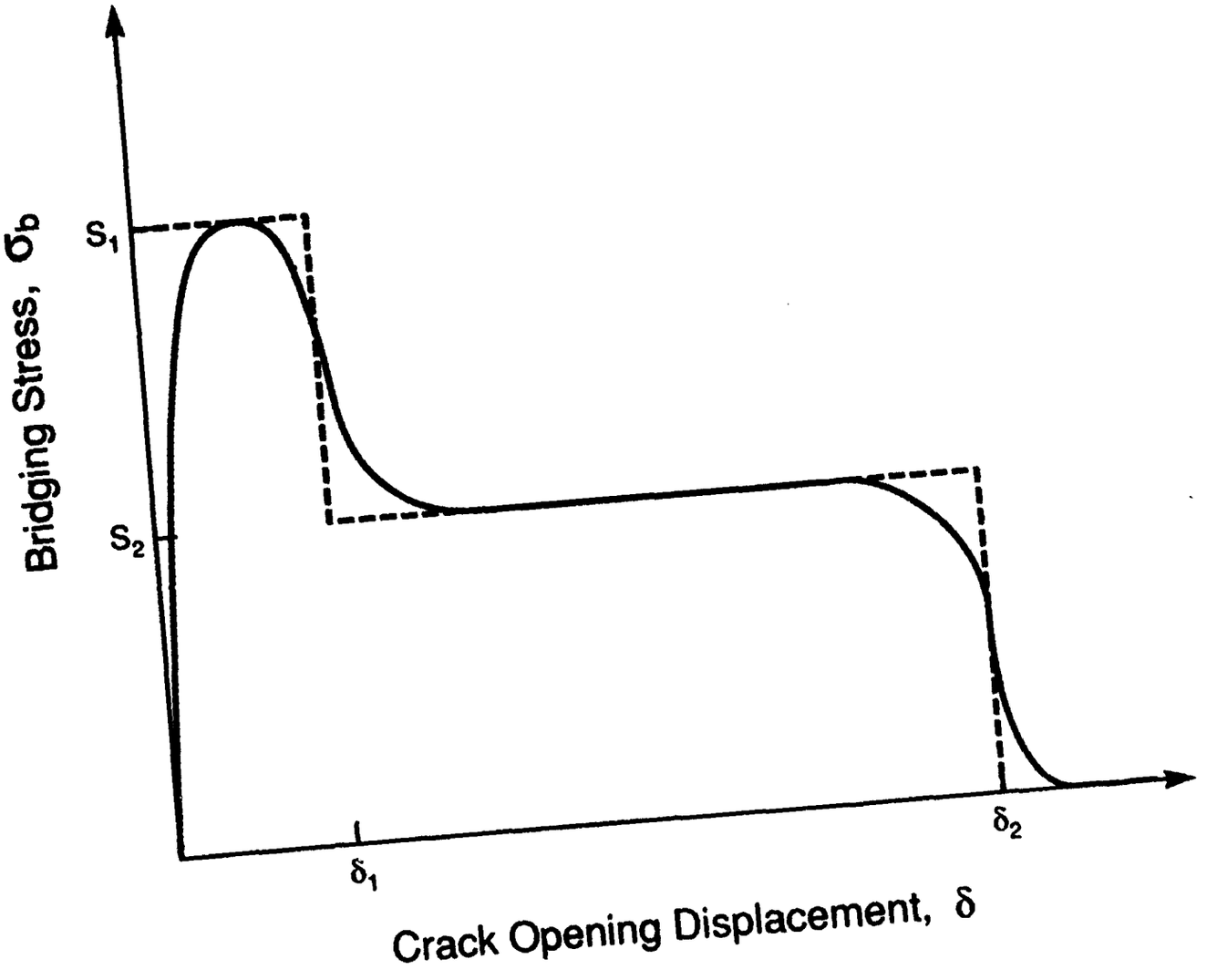
Bridging Stress, σ_b
S_1
S_2
δ_1
δ_2
Crack Opening Displacement, δ

Figure 13

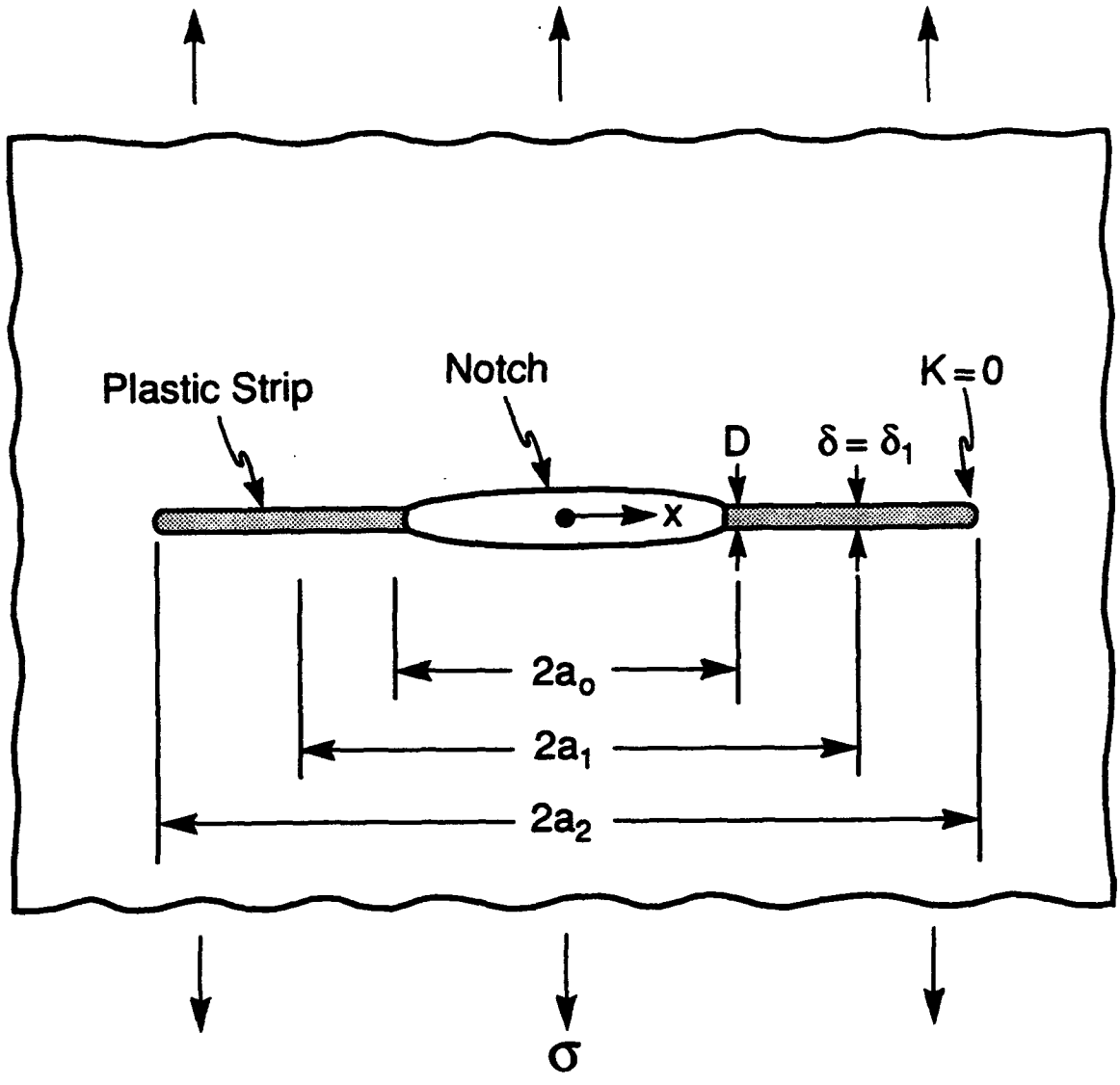

Figure 14

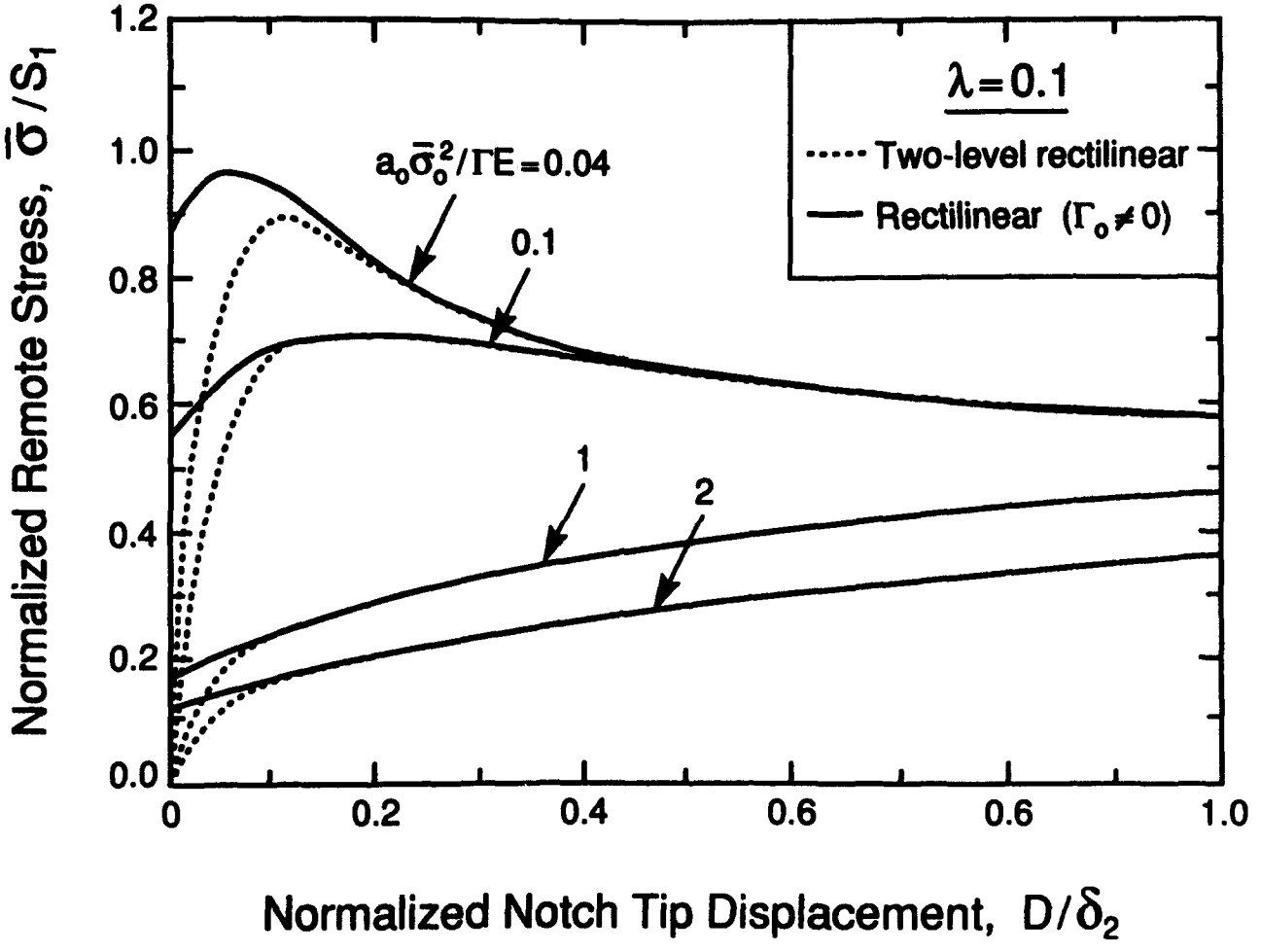
λ=0.1
Two-level rectilinear
Rectilinear (Γ₀≠0)
a₀σ̄₀²/ΓE=0.04
0.1
1
2
Normalized Remote Stress, σ̄/S₁
Normalized Notch Tip Displacement, D/δ₂
0.0
0.2
0.4
0.6
0.8
1.0
1.2
0
0.2
0.4
0.6
0.6
1.0

Figure 15

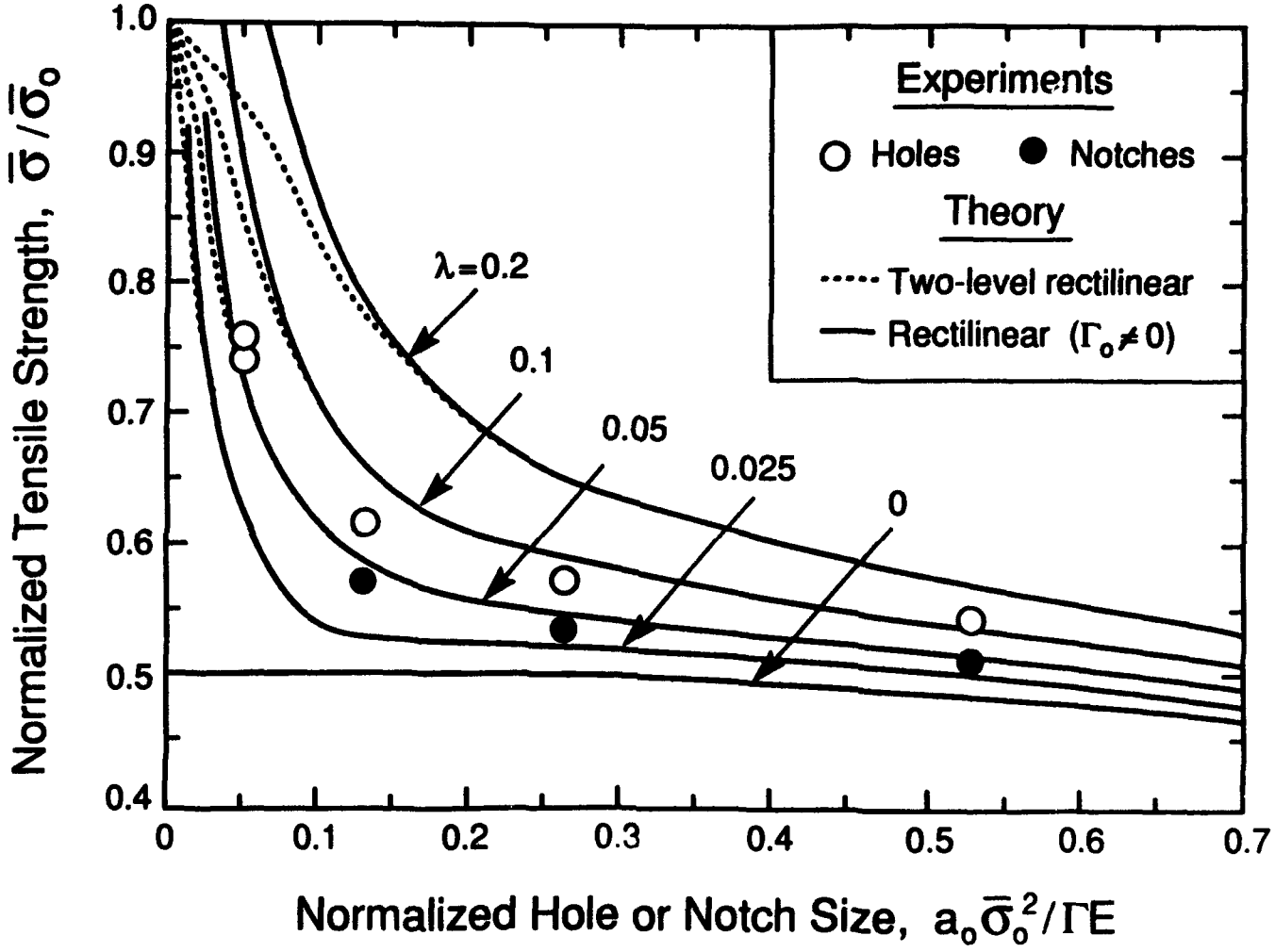
Experiments
Holes
Notches
Theory
Two-level rectilinear
Rectilinear ($\Gamma_o \neq 0$)
λ=0.2
0.1
0.05
0.025
0
Normalized Tensile Strength, $\bar{\sigma}/\bar{\sigma}_o$
Normalized Hole or Notch Size, $a_o\bar{\sigma}_o^2/\Gamma E$
1.0
0.9
0.8
0.7
0.6
0.5
0.4
0
0.1
0.2
0.3
0.4
0.5
0.6
0.7

Figure 16

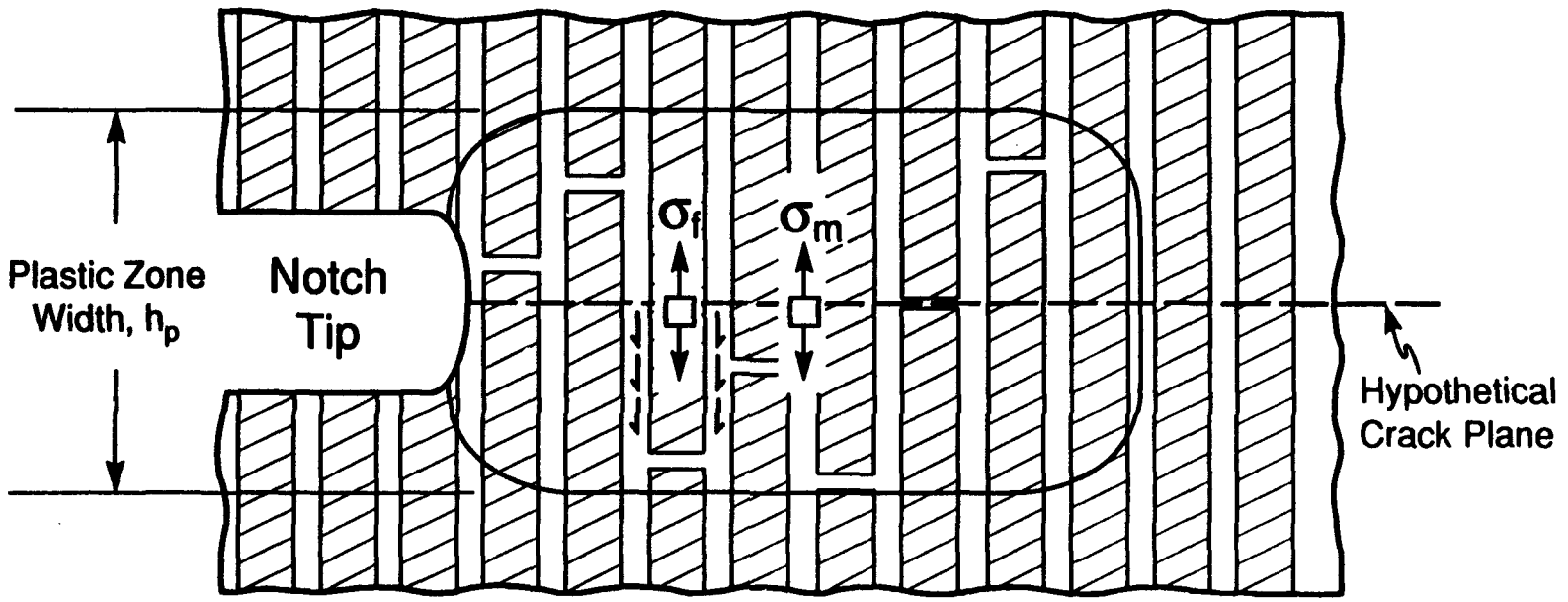
Plastic Zone
Width, h_p
Notch
Tip
σ_f
σ_m
Hypothetical
Crack Plane

Figure 17

To appear in J. Appl. Mech., accepted.

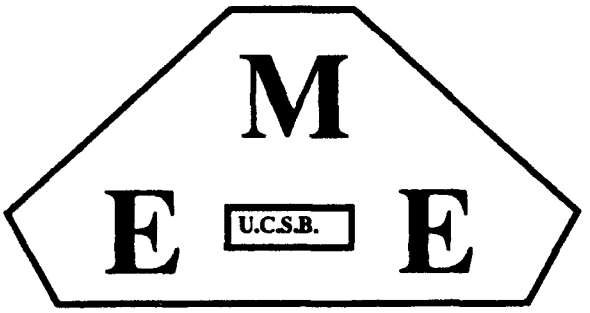

MECHANICAL AND ENVIRONMENTAL
ENGINEERING DEPARTMENT

LOCALIZATION DUE TO DAMAGE IN TWO DIRECTION FIBER REINFORCED COMPOSITES

François HILD[1]
Per-Lennart LARSSON[2]
Frederick A. LECKIE

Department of Mechanical and Environmental Engineering
University of California, Santa Barbara, CA 93106–5070, U.S.A.

[1]Visiting postgraduate researcher, also at Laboratoire de Mécanique et Technologie,
E.N.S. de Cachan/C.N.R.S./Université Paris 6
61 avenue du Président Wilson, F-94235 Cachan Cedex, France.
[2]Department of Solid Mechanics, Royal Institute of Technology,
S-100 44 Stockholm, Sweden.

LOCALIZATION DUE TO DAMAGE IN TWO DIRECTION FIBER REINFORCED COMPOSITES

François HILD
Per-Lennart LARSSON
Frederick A. LECKIE

Abstract: Fiber pull-out is one of the fracture features of fiber reinforced ceramic matrix composites. The onset of this mechanism is predicted by using Continuum Damage Mechanics, and corresponds to a localization of the deformations. After deriving two damage models from a uniaxial bundle approach, different configurations are analyzed through numerical methods. For one model some very simple criteria can be derived, whereas for the second one none of these criteria can be derived and the general criterion of localization must be used.

1. Introduction

Ceramic Matrix Composites (CMC's) can either be reinforced by fibers in one direction or by fibers in two directions. The aim of this paper is to study composites reinforced with fibers in two perpendicular directions by extending a previous study on CMC's with fibers in one direction (Hild et al., 1992).

The rupture of most of the CMC's involves two separate failure mechanisms. The first mechanism is matrix cracking. The matrix cracks develop and their density saturates as the load level increases. The second mechanism is fiber breakage accompanied with fiber pull-out. Enventually, the final rupture will take place around one of the matrix cracks: it correponds to *localized* fiber pull-out due to fiber breakage. The occurrence of this mechanism corresponds to the appearance of a macro-crack and will be described by a localization of the deformations. The initiation of macro-cracks in a structure during service often constitutes the early stage of the final failure of the structure. Starting from a material that is assumed free from any initial defect, the initiation of macro-cracks can be predicted using Continuum Damage Mechanics. The driving force is fiber breakage, which is accompanied by *distributed* pull-out. The approach using localization has successfully been used for ductile materials (Billardon and Doghri, 1989a,b; Doghri, 1989). The initiation stage is considered as the onset of a surface across which the velocity gradient is discontinuous. Under small deformation assumptions, this phenomenon is mainly driven by the damage mechanism that causes strain-softening. For CMC's, the damage mechanism is related to fiber breakage, and the damage variable describes the percentage of broken fibers (Hild et al., 1992).

Although localization can be studied at the scale of fibers bonded to a matrix through an interface (Benallal et al., 1991a), i.e. at a micro-level, localization also can be analyzed at a meso-level, when the material is assumed to be homogeneous. Continuum Damage Mechanics, which represents a local approach to fracture (Benallal et al., 1991b), constitutes an efficient tool for this purpose. The progressive deterioration of the material is modeled by internal variables defined at

the meso-level. These variables are called *damage* variables. The damage state and the evolution of these variables is obtained through a uniaxial study based on fiber breakage (Coleman, 1958; Curtin 1991). A 2-D plane stress analysis is performed based on an extended model. The loss of uniqueness and the localization are studied for shear free states. A criterion referring to a critical value of the damage or to a maximum normal stress can describe the localization, which constitutes an objective criterion, from a design point of view.

2. Localization and Loss of Uniqueness

The failure at a meso-level, with the initiation of a macro-crack, is defined as the bifurcation of the rate problem in certain modes, viz. the appearance of a surface across which the velocity gradient is discontinuous (Billardon and Doghri, 1989a). This phenomenon is referred to as *localization*, and corresponds to the failure of the elliptic condition. The condition of localization can also be compared to the loss of uniqueness of the rate problem.

Stationary waves were studied by Hadamard (1903) in elasticity, by Hill (1962) and Mandel (1962) in elasto-plasticity. Rice (1976) related the localization of plastic shear bands to jumps of the velocity gradient. Borré and Maier (1989) have given necessary and sufficient conditions for the onset of modes inside the body, who extended the results given by Rice (1976) and Rice and Rudnicki (1975, 1980).

Under small strain assumption and in elasticity coupled with damage, the behavior of a material is assumed to be described by the following piece-wise linear rate constitutive law

$$\dot{\sigma} = \begin{cases} \mathbf{E} : \dot{\varepsilon} & \text{if } \dot{D} = 0 \\ \mathbf{H} : \dot{\varepsilon} & \text{if } \dot{D} \neq 0 \end{cases} \qquad (1)$$

where $\dot{\sigma}$ and $\dot{\varepsilon}$ respectively denote the stress and strain rates, E and H are fourth rank tensors, E is assumed to be positive definite, and D is either a single damage variable or a set of damage variables.

Localization occurs *inside* the body, *if and only if* (Rudnicki and Rice, 1975; Borré and Maier, 1989; Benallal et al., 1991a)

$$\text{Det}(\mathbf{n}.\mathbf{H}.\mathbf{n}) = 0 \qquad \text{for a vector } \mathbf{n}\neq 0 \text{ and at a point inside a structure } \Omega \tag{2}$$

This criterion corresponds to the failure of the ellipticity condition of the rate equilibrium equation; it also can be used as an indicator of the local failure of the material, at a meso-scale (Billardon and Doghri, 1989a).

Furthermore, any loss of uniqueness, considered as bifurcation of the rate boundary value problem, is excluded provided

$$\dot{\sigma} : \dot{\varepsilon} > 0 \tag{3}$$

In this study, the quantity that defines loss of uniqueness and localization is the linear tangent modulus H. In the following, we analyze loss of uniqueness and loss of ellipticity (i.e. localization) for states when

$$\begin{cases} \varepsilon_{11} = \alpha\, \varepsilon_{22} \\ \varepsilon_{12} = 0 \end{cases} \tag{4}$$

The parameter α is referred to as the strain ratio and its inverse is denoted by β. These particular states only are considered. When the hypothesis of Eqn. (4) is satisfied, the non-vanishing components of the vector $\mathbf{n}$ are n_1 and n_2, and the matrix $A = \mathbf{n}.\mathbf{H}.\mathbf{n}$ reduces to (Ortiz et al., 1987)

$$\mathbf{A} = \begin{bmatrix} n_1^2 H_{1111} + n_2^2 H_{1212} & n_1 n_2 (H_{1212} + H_{1122}) \\ n_1 n_2 (H_{1212} + H_{2211}) & n_1^2 H_{1212} + n_2^2 H_{2222} \end{bmatrix} \tag{5}$$

If we rewrite $(n_1,n_2) = (\cos\theta,\sin\theta)$, $X = \tan^2\theta$, then the localization condition is equivalent to finding real positive roots of the following equation

$$a X^2 + b X + c = 0 \tag{6}$$

with

$$\begin{aligned} a &= H_{1212} H_{2222} \\ b &= H_{1111} H_{2222} - H_{1122} H_{2211} - H_{1122} H_{1212} - H_{2211} H_{1212} \\ c &= H_{1212} H_{1111} \end{aligned} \tag{7}$$

If real positive roots are found, then the localization direction is perpendicular to the vector $(n_1,n_2,0) = (\cos\theta,\sin\theta,0)$, characterized by the angle θ (Fig. 1). The values of H_{1111}, H_{2222}, H_{1122}, H_{2211} and H_{1212} are model dependent and specific models are now developed.

3. Constitutive Laws

This section is concerned with the development of two constitutive laws in the case of CMC's reinforced in two perpendicular directions. At constant temperature, the behavior of a CMC reinforced by unidirectional fibers in the x_2-direction (see Fig. 1) can be characterized by the Helmholtz free energy density ψ_2, which is a function of the state variables ε_{11}, ε_{22}, ε_{12}, and the damage variable D_2 in the x_2-direction

$$\rho\psi_2 = \rho\psi(\varepsilon_{11},\varepsilon_{22},\varepsilon_{12},D_2,f_2,k_2) \tag{8}$$

where D_2 represents the fiber degradation in the x_2-direction, E_2 the Young's modulus in the x_2-direction, ν_{12} the Poisson's ratio, k_2 the ratio of the Young's modulus in the fiber direction (E_2) to the Young's modulus in the transverse direction (E_1), and G_{12} the shear modulus. It is worth noting that the elastic quantities depend on the volume fraction of fibers. The expression for the general Helmholtz free energy density ψ is given by

$$\rho\psi(x,y,z,d,f,k) = \frac{E_2(f)}{2}\left[\frac{x^2 + 2\nu_{12}k(1-d)xy + ky^2}{k\left\{1-\nu_{12}^2 k(1-d)\right\}}\right] + 2G_{12}z^2 \tag{9}$$

where ρ is the material density, x,y,z are dummy variables representing strains, d damage, f volume fraction, and k Young's moduli ratio. The stresses and the thermodynamic force Y_2 associated to the damage variable D_2 are derived from the Helmholtz free energy density ψ_2 as follows

$$\sigma_{11} = \rho\frac{\partial\psi_2}{\partial\varepsilon_{11}} \qquad \sigma_{22} = \rho\frac{\partial\psi_2}{\partial\varepsilon_{22}} \qquad 2\sigma_{12} = \rho\frac{\partial\psi_2}{\partial\varepsilon_{12}} \tag{10}$$
$$Y_2 = \rho\frac{\partial\psi_2}{\partial D_2}$$

The explicit expressions for the stresses related to the strains and the damage variable modeling the fiber degradation in the x_2-direction are given by

$$\sigma_{11} = \frac{E_2}{k_2[1-\nu_{12}^2(1-D_2)k_2]}[\varepsilon_{11}+\nu_{12}(1-D_2)k_2\varepsilon_{22}]$$
$$\sigma_{22} = \frac{E_2(1-D_2)}{1-\nu_{12}^2(1-D_2)k_2}(\varepsilon_{22}+\nu_{12}\varepsilon_{11}) \tag{11}$$
$$\sigma_{12} = 2G_{12}\varepsilon_{12}$$

The damage state of fibers in the x_2-direction, D_2 can be related to the stress (and is denoted by $D_2^{(1)}$) or strain state (and is denoted by $D_2^{(2)}$). The relationship is either implicit in terms of the normal stress in the x_2-direction (model #1)

$$D_2^{(1)} = 1 - \exp\left[- \left\{ \frac{\sigma_{22}}{(1-D_2^{(1)}) f_2 \sigma_c} \right\}^{m+1} \right] \quad \text{if } \varepsilon_{22} > 0 \text{ and } \dot{\varepsilon}_{22} > 0 \tag{12}$$

where m is the shape parameter of a Weibull law (Weibull, 1939), σ_c the characteristic strength (Henstenburg and Phoenix, 1989), and f_2 is the volume fraction of fibers in the x_2-direction; or explicit in terms of the normal strain in the x_2-direction (model #2)

$$D_2^{(2)} = 1 - \exp\left[- \left(\frac{\varepsilon_{22}}{\varepsilon_c} \right)^{m+1} \right] \quad \text{if } \varepsilon_{22} > 0 \text{ and } \dot{\varepsilon}_{22} > 0 \tag{13}$$

where ε_c is related to the characteristic strength σ_c by $\sigma_c = E_F \varepsilon_c$ (E_F is the Young's modulus of the fibers). Both models describe the same material behavior when subjected to uniaxial tension. However the models give different predictions for multiaxial loading states (Hild et al., 1992). It is worth noting that the damage evolution laws are *a priori* independent of the volume, since we assume that the local behavior of the fiber degradation is not dependent on the total length of the fiber (Curtin, 1991). This type of behavior is observed when *distributed* pull-out happens in conjunction with fiber breakage, and it can be shown that in most practical cases, the statistics driving the fiber breakage is independent of the total length of the composite. On the other hand, if the composite length becomes very small, a length dependence is found again, and in this case the evolution of the damage variable is mainly given by a fiber-bundle-type of behavior, which leads to replacing m+1 by m, the characteristic strength σ_c by $\sigma_0 (L/L_0)^{1/m}$, where σ_0 is the scale parameter of a Weibull law, and the scale strain ε_c by $\varepsilon_0 (L/L_0)^{1/m}$, where L_0 is the gauge length at which the

scale parameter has been identified, and $\sigma_0 = E_F \varepsilon_0$. Since the results are the same for both damage evolution laws when the previous permutation is used, we will just express them in the case when the model is length independent, which is the most relevant in practice.

If the fibers are in the x_1-direction then the breakage can be modeled by a damage variable denoted by D_1. Using Eqn. (9), the Helmholtz free energy density $\rho\psi_1$ is given by

$$\rho\psi_1 = \rho\psi(\varepsilon_{22},\varepsilon_{11},\varepsilon_{12},D_1,f_1,k_1) \tag{14}$$

If the fibers are in both x_1- and x_2-directions, then we assume as a first approximation that the total specific Helmholtz free energy $\rho\psi_{12}$ is given by a law of mixture of the Helmholtz free energy densities in the x_1- and in the x_2-directions

$$\rho\psi_{12} = (1-f)\rho\psi_1 + f\rho\psi_2 \tag{15}$$

where f is the fraction of fibers in the x_2-direction ($f=f_2/(f_1+f_2)$, and where f_1 and f_2 are the volume fraction of fibers in the x_1- and x_2-direction, respectively). This assumption also corresponds to a Lin-Taylor Hypothesis. The evolution of the stresses is given by

$$\begin{aligned}
\sigma_{11} &= \rho \frac{\partial \psi_{12}}{\partial \varepsilon_{11}} = (1-f)S_{11} + fS_{12} \\
\sigma_{22} &= \rho \frac{\partial \psi_{12}}{\partial \varepsilon_{22}} = (1-f)S_{21} + fS_{22} \\
\sigma_{12} &= \rho \frac{\partial \psi_{12}}{\partial \varepsilon_{12}} = 2G_{12}\varepsilon_{12}
\end{aligned} \tag{16}$$

where the explicit expression for S_{ij} is given in appendix 1, and the corresponding thermodynamic forces associated to the two *independent* damage variables D_1 and D_2 are

$$Y_1 = \rho \frac{\partial \psi_{12}}{\partial D_1} = (1-f)\rho \frac{\partial \psi_1}{\partial D_1} \qquad (17)$$
$$Y_2 = \rho \frac{\partial \psi_{12}}{\partial D_2} = f\rho \frac{\partial \psi_2}{\partial D_2}$$

Again, the evolution of the damage variables can either be implicit in terms of the respective normal stresses (model #1)

$$D_1^{(1)} = 1 - \exp\left[-\left\{\frac{\sigma_{11}}{(1-D_1^{(1)})f_1\sigma_c}\right\}^{m+1}\right] \quad \text{if } \varepsilon_{11} > 0 \text{ and } \dot{\varepsilon}_{11} > 0 \qquad (18)$$
$$D_2^{(1)} = 1 - \exp\left[-\left\{\frac{\sigma_{22}}{(1-D_2^{(1)})f_2\sigma_c}\right\}^{m+1}\right] \quad \text{if } \varepsilon_{22} > 0 \text{ and } \dot{\varepsilon}_{22} > 0$$

or explicit in terms of the respective normal strains (model #2)

$$D_1^{(2)} = 1 - \exp\left[-\left(\frac{\varepsilon_{11}}{\varepsilon_c}\right)^{m+1}\right] \quad \text{if } \varepsilon_{11} > 0 \text{ and } \dot{\varepsilon}_{11} > 0 \qquad (19)$$
$$D_2^{(2)} = 1 - \exp\left[-\left(\frac{\varepsilon_{22}}{\varepsilon_c}\right)^{m+1}\right] \quad \text{if } \varepsilon_{22} > 0 \text{ and } \dot{\varepsilon}_{22} > 0$$

It is worth noting that we assume that the statistical properties of the fibers are supposed to be identical in both directions. This hypothesis will be maintained throughout the paper since generalization would be straightforward. Both models are studied for shear free states when the strain ratio α (see Eqn. (4)), and thus its inverse β are given.

3.1. Failure Criteria for Model #1

For model #1, the evolution of the damage variables is implicit in the sense that $D_1^{(1)}$ (respectively $D_2^{(1)}$) is a function of the normal stress σ_{11} (respectively σ_{22}) *and* the damage variable

$D_1^{(1)}$ (respectively $D_2^{(1)}$) itself. The evolution is therefore computed by a numerical scheme based upon a Newton method. To study localization and loss of uniqueness, we need to compute the tangent operator, which takes the following form

$$
\begin{aligned}
H_{1111} &= \frac{[(1-f)F_{11} + fF_{12}]\,(1 + fF_{52}F_{72}) - fF_{22}F_{72}\,[(1-f)F_{41} + fF_{42}]}{[1 + fF_{21}F_{72}\,](1 + fF_{52}F_{72}) - f(1-f)F_{22}F_{72}F_{51}F_{71}} \\
H_{2222} &= \frac{[(1-f)F_{61} + fF_{62}]\,[1 + (1-f)F_{21}F_{71}] - (1-f)F_{51}F_{71}\,[(1-f)F_{41} + fF_{42}]}{[1 + fF_{21}F_{72}\,](1 + fF_{52}F_{72}) - f(1-f)F_{22}F_{72}F_{51}F_{71}} \\
H_{1122} &= \frac{[(1-f)F_{41} + fF_{42}]\,(1 + fF_{52}F_{72}) - fF_{22}F_{72}\,[(1-f)F_{61} + fF_{62}]}{[1 + fF_{21}F_{72}\,](1 + fF_{52}F_{72}) - f(1-f)F_{22}F_{72}F_{51}F_{71}} \\
H_{2211} &= \frac{[(1-f)F_{41} + fF_{42}]\,[1 + (1-f)F_{21}F_{71}] - (1-f)F_{51}F_{71}\,[(1-f)F_{11} + fF_{12}]}{[1 + fF_{21}F_{72}\,](1 + fF_{52}F_{72}) - f(1-f)F_{22}F_{72}F_{51}F_{71}} \\
H_{1212} &= 2G_{12}
\end{aligned}
\tag{20}
$$

where the explicit expressions for F_{ij} are given in appendix 2.

The loss of uniqueness and localization are investigated when the fiber fraction f and the strain ratio α vary. Although analytical results cannot be derived from criterion (2) in the general case, some simple results can be found when f is equal to 0 or 1. In these cases, the criteria derived by Hild et al. (1992) apply. If f is equal to 0 (fibers only in the x_1-direction), then localization and loss of uniqueness occur at the same load level when

$$
\begin{aligned}
D_1^{(1)} &= D_c = 1 - \exp\left(\frac{-1}{m+1}\right) \\
\sigma_{11} &= \sigma_{u1} = f_1\,\sigma_c \left(\frac{1}{(m+1)e}\right)^{1/(m+1)} \\
Y_1 &= Y_c = \frac{\sigma_{u1}^2}{2E_1(1-D_c)^2}
\end{aligned}
\tag{21}
$$

where the stress σ_{u1} corresponds to the ultimate tensile strength in the x_1-direction. It is worth noting that the three previous criteria are easier to compute than the general criterion (2). The

direction of localization is $\theta = 0°$, i.e., a localization surface perpendicular to the fiber direction . If f is equal to 1, the same kind of result apply and the direction of localization is $\theta = 90°$, i.e., a localization surface again perpendicular to the fiber direction . When $f \neq 0$ and $f \neq 1$, these results cannot be proved. However the computations show that loss of uniqueness and localization can be described very accurately by the two following criteria

$$\text{Max}(D_1^{(1)}, D_2^{(1)}) = D_c = 1 - \exp\left(\frac{-1}{m+1}\right) \tag{22}$$

$$\sigma_{11} = \sigma_{u1} \quad \text{or} \quad \sigma_{22} = \sigma_{u2} \tag{23}$$

when the fiber properties are the same in the two directions. The maximum error is .5% in terms of criteria (22), and (23).

Criterion (22) shows that for model #1, maximum damage at localization depends only on the Weibull exponent of the fibers. Furthermore, criterion (23) shows that the maximum normal stress σ_{11} (respectively σ_{22}) depends only on the volume fraction of fibers in the x_1- (respectively x_2-) direction and on the fiber characteristics. This result is consistent with some experimental observations on woven carbon matrix composites reinforced with SiC (Nicalon) fibers (Heredia et al., 1992). On the other hand, the localization angle is dependent on the fiber percentage f (see Fig. 2). When the fiber percentage f and the sign of the strains ε_{11} and ε_{22} are constant, the variation of the localization angle is due to the fact that the maximum tensile stress is either reached in the x_1- or in the x_2-direction.

Moreover, if the strain ratio α is different from 0 and 1 then there is a complete symmetry of the results. If the strain ratio α, the strains ε_{11} and ε_{22} are positive, changing α into β, f_2 into f_1, changes f into 1–f, and alters the absolute value of the localization angle $|\theta|$ into $\pi/2 - |\theta|$ and keeps the maximum stresses and damage levels constant. These two properties are referred to as *symmetry properties*, and are mainly due to the features of Eqns. (4), (8), (14) and (15).

When the strain ratio α is equal to 1 and the fiber percentage f is equal to .5, the localization

angle is undetermined. This is due to the vanishing of the three constants a, b, and c in Eqn. (6), for $H_{1111} = H_{1122} = H_{2211} = H_{2222} = 0$. Any value of the angle θ satisfies Eqn (6). This phenomenon can be observed when the fiber percentage f is different from 1: if $\sigma_{11} = \sigma_{u1}$ and $\sigma_{22} = \sigma_{u2}$ simultaneously, then $D_1^{(1)} = D_2^{(1)} = D_c$, and $H_{1111} = H_{1122} = H_{2211} = H_{2222} = 0$. This particular result shows that in terms of this model, for a given strain ratio α, it is possible to optimize locally a CMC reinforced by fibers in two perpendicular directions. Indeed, in terms of fiber breakage, a condition $\sigma_{11} = \sigma_{u1}$ and $\sigma_{22} = \sigma_{u2}$ leads to an optimum of the fiber behavior in both directions.

Model #1 constitutes a straightforward generalization of the fiber bundle models studied by Krajcinovic and Silva (1982), and Hult and Travnicek (1983). Finally, a shear stress has no influence on all the previous results since we assumed no coupling between the damage variables and the shear strain or stress for both model #1 and #2.

3.2. Study of Localization with Model #2

For model #2, the evolution of the damage variables is explicit and therefore is easier to compute. The tangent operator takes the form

$$\begin{aligned} H_{1111} &= (1-f)(F_{11} - F_{21}\,F_{31}) + fF_{12} \\ H_{2222} &= (1-f)F_{62} + f(F_{42} - F_{52}\,F_{32}) \\ H_{1122} &= (1-f)F_{41} + f(F_{42} - F_{22}\,F_{32}) \\ H_{2211} &= (1-f)(F_{41} - F_{21}\,F_{31}) + fF_{42} \\ H_{1212} &= 2G_{12} \end{aligned} \qquad (24)$$

where the explicit expressions for F_i are given in appendix 2. As shown in the case of fibers in only one direction (Hild et al., 1992), the localization criterion cannot be described by some simple

criteria as those given by model #1. When fibers are in both directions the latter results are confirmed. A first consequence is that an optimization procedure can be performed since the maximum stress at localization, and the maximum damage at localization are dependent on both the strain ratio α and on the fiber percentage f.

Since the elastic law given in Eqns. (16) is identical for both models, the symmetry properties apply also for model #2 (see Figs. 3, 4, and 5). It can also be noticed that the maximum stress at localization varies with the fiber fraction f and with the strain ratio α.

In the experiments reported by Heredia et al. (1992) the stress at localization was given by the ultimate tensile strength corresponding to the volume fraction of fibers in the same direction. This is not found by using model #2. Indeed, in a tensile test, when $f_1 = f_2 = .5$ the maximum stress σ_{22} normalized by the ultimate tensile strength σ_{u2} is given by .63, whereas the same tensile test when $f_1 = .0$ and $f_2 = .5$ would give a normalized tensile strength σ_{22}/σ_{u2} equal to 1. On the other hand, the damage at localization D_2 normalized by the critical damage D_c is equal to 1.04 when $f_1 = .5$ and $f_2 = .5$ and is equal to 1. when $f_1 = .0$ and $f_2 = .5$.

It is too early to draw a final conclusion, but it seems that the predictions of model #1 correspond more to reality than those of model #2. On the other hand, model #2 turned out to give results very close to model #1 when applied to structures with fibers in one direction (Hild et al., 1992). This will be addressed in the case of structures with fibers in two perpendicular directions such as spinning discs.

4. Conclusions

Using a one-dimensional study of fiber breakage modeled by a single damage variable, two models are derived. Both of them are then generalized to a 2-D plane stress analysis, with fibers in two perpendicular directions. Whereas model #1 constitutes a straightforward generalization of the elementary study, model #2 exhibits different features. Indeed, loss of uniqueness and localization can be described by some very simple criteria referring to Continuum Damage Mechanics for

model #1. Conversely, these simple criteria do not apply for model #2. Physically, model #1 gives a better description of some experimental trends observed in the case of a carbon matrix reinforced with silicon carbide (Nicalon) fibers in two perpendicular directions. On the other hand, model #2 is easier to compute, and when applied to the study of spinning disc with fibers in one direction, it leads to load levels at localization of the same order of magnitude as model #1 (Hild et al, 1992).

Lastly, this study shows that the localization for model #1 can be described by using criterion (23) derived from the general criterion of localization (2). This criterion can also be used for a computation in elasticity and may turn out to be sufficient in first approximation to predict load levels at which at macro-crack initiates, instead of using a computation in elasticity coupled with damage. This work is still in progress and will be presented in a subsequent publication.

5. Acknowledgments

The authors gratefully acknowledge the financial support of the U.S. Air Force through contract AFOSR-90-0132 with the Department of Mechanical and Environmental Engineering, University of California at Santa Barbara, and the DARPA University Research Initiative at the University of California at Santa Barbara (ONR contract N00014-86-K0753).

References

Benallal, A., Billardon, R. and Geymonat, G. (1991a). Localization Phenomena at the Boundaries and Interfaces of Solids. 3rd Conference on Constitutive Laws for Engineering Materials: Theory and Applications, Tucson, AZ, January 1991.

Benallal, A., Billardon, R. and Lemaitre J. (1991b). Continuum damage mechanics and local approach to fracture: Numerical procedures. Comp. Meth. in Appl. Mech. and Eng., **92**, 141-155.

Billardon, R. and Doghri, I. (1989a). Prévision de l'amorçage d'une macro-fissure par la localisation de l'endommagement. C. R. Acad. Sci. Paris **308** [II], 347-352.

Billardon, R. and Doghri, I. (1989b). Localization Bifurcation Analysis for Damage Softening Elasto-Plastic Materials. *Strain Localization and Size Effect due to Cracking and Damage.* J. Mazars and Z.P. Bazant eds. Elsevier, 295-307.

Borré, G. and Maier, G. (1989). On Linear versus Nonlinear Flaw Rules in Strain Localization Analysis. Meccanica **24**, 36-41.

Coleman, B.D. (1958). On the Strength of Classical Fibers and Fiber Bundles. J. Mech. Phys. Solids **7**, 60-70.

Curtin, W.A., (1991). Theory of Mechanical Properties of Ceramic-Matrix Composites. J. Am. Ceram. Soc., **74** [11], 2837-2845.

Doghri, I. (1989). Etude de la localisation de l'endommagement. Thèse de l'Université Paris 6, May 1989.

Hadamard, J. (1903). Leçon sur la propagation des ondes et les équations de l'hydrodynamique. Paris.

Heredia, F.E., Spearing, S.M., Evans, A.G., Mosher, P., and Curtin, W.A. (1992). Mechanical Properties of Carbon Matrix Composites Reinforced with Nicalon Fibers. J. Am. Ceram. Soc., **75** [11], 3017-3025.

Henstenburg, R.B. and Phoenix, S.L. (1989). Interfacial Shear Strength Using Single-Filament-Composite Test. Part II: A Probability Model and Monte-Carlo Simulations. Polym. Comp., **10** [5], 389-406.

Hild, F., Larsson, P.-L., and F.A. Leckie (1992). Localization due to Damage in Fiber Reinforced Composites. Int. J. Solids Struct., **29** [24], 3221-3238.

Hill, R. (1962). Acceleration Waves in Solids. J. Mech. Phys. Solids **10**, 1-16.

Hult, J. and Travnicek, L. (1983). Carrying Capacity of Fiber Bundles with Varying Strength and Stiffness. Journal de Mécanique Théorique et Appliquée **2** [2], 643-657.

Krajcinovic, D. and Silva, M.A.G. (1982). Statistical Aspects of the Continuous Damage Theory.

Int. J. Solids Structures **18** [7], 551-562.

Mandel, J. (1962). Ondes plastiques dans un milieu indéfini à trois dimensions. J. de Mécanique **1** 1, 3-30.

Ortiz, M., Leroy, Y. and Needelman, A. (1987). A Finite Element Method for Localized Failure Analysis. Comput. Meths Appl. Engrg. **61**, 189-214.

Rice, J.R. and Rudnicki, J.W. (1980). A Note on Some Features of the Theory of Localization of Deformation. Int. J. Solids Struct. **16**, 597-605.

Rice, J.R. (1976). The Localization of Plastic Deformations. *Theoretical and Applied Mechanics*, edited by W.T. Koiter (North-Holland), 207-220.

Rudnicki, J.W. and Rice, J.R. (1975). Conditions for Localization of Deformation in Pressure-Sensitive Dilatant Materials. J. Mech. Phys. Solids **23**, 371-394.

Weibull, W., (1939). A Statistical Theory of the Strength of Materials. Ingeniörsvetenskapakademiens, Handlingar Nr 151.

Appendix 1

$$k_1 = \frac{E_2(f_1)}{E_1}$$
$$k_2 = \frac{E_2(f_2)}{E_1}$$

$$S_{11} = \frac{E_2(f_1)(1-D_1)}{1-\nu_{12}^2(1-D_1)k_1}(\varepsilon_{11}+\nu_{12}\varepsilon_{22})$$
$$S_{12} = \frac{E_2(f_2)}{k_2[1-\nu_{12}^2(1-D_2)k_2]}[\varepsilon_{11}+\nu_{12}(1-D_2)k_2\varepsilon_{22}]$$
$$S_{21} = \frac{E_2(f_1)}{k_1[1-\nu_{12}^2(1-D_1)k_1]}[\varepsilon_{22}+\nu_{12}(1-D_1)k_1\varepsilon_{11}]$$
$$S_{22} = \frac{E_2(f_2)(1-D_2)}{1-\nu_{12}^2(1-D_2)k_2}(\varepsilon_{22}+\nu_{12}\varepsilon_{11})$$

Appendix 2

$$F_{11} = \frac{E_2(f_1)(1-D_1)}{1-\nu_{12}^2(1-D_1)k_1} \qquad F_{12} = \frac{E_2(f_2)}{k_2(1-\nu_{12}^2(1-D_2)k_2)}$$

$$F_{21} = \frac{E_2(f_1)(\nu_{12}\varepsilon_{11}+\varepsilon_{22})}{(1-\nu_{12}^2(1-D_1)k_1)^2} \qquad F_{22} = \frac{E_2(f_2)\nu_{12}(\nu_{12}\varepsilon_{11}+\varepsilon_{22})}{(1-\nu_{12}^2(1-D_2)k_2)^2}$$

$$F_{41} = \frac{E_2(f_1)\nu_{12}(1-D_1)}{1-\nu_{12}^2(1-D_1)k_1} \qquad F_{42} = \frac{E_2(f_2)\nu_{12}(1-D_2)}{1-\nu_{12}^2(1-D_2)k_2}$$

$$F_{51} = \frac{E_2(f_1)\nu_{12}(\nu_{12}\varepsilon_{11}+\varepsilon_{22})}{(1-\nu_{12}^2(1-D_1)k_1)^2} \qquad F_{52} = \frac{E_2(f_2)(\nu_{12}\varepsilon_{11}+\varepsilon_{22})}{(1-\nu_{12}^2(1-D_2)k_2)^2}$$

$$F_{61} = \frac{E_2(f_1)}{k_1(1-\nu_{12}^2(1-D_1)k_1)} \qquad F_{62} = \frac{E_2(f_2)(1-D_2)}{1-\nu_{12}^2(1-D_2)k_2}$$

$$F_{31} = \frac{m+1}{\varepsilon_c}\left(\frac{\varepsilon_{11}}{\varepsilon_m}\right)^m \exp\left[-\left(\frac{\varepsilon_{11}}{\varepsilon_c}\right)^{m+1}\right] \qquad F_{32} = \frac{m+1}{\varepsilon_c}\left(\frac{\varepsilon_{22}}{\varepsilon_m}\right)^m \exp\left[-\left(\frac{\varepsilon_{22}}{\varepsilon_c}\right)^{m+1}\right]$$

$$F_{71} = \frac{\frac{m+1}{f_1\sigma_c}\left[\frac{\sigma_{11}}{(1-D_1)f_1\sigma_c}\right]^m}{1-(m+1)\left[\frac{\sigma_{11}}{(1-D_1)f_1\sigma_c}\right]^{m+1}} \qquad F_{72} = \frac{\frac{m+1}{f_2\sigma_c}\left[\frac{\sigma_{22}}{(1-D_2)f_2\sigma_c}\right]^m}{1-(m+1)\left[\frac{\sigma_{22}}{(1-D_2)f_2\sigma_c}\right]^{m+1}}$$

Figure Caption

Figure 1: Localization mode.

Figure 2: Absolute value of the localization angle in degrees at localization for model #1, the main caption of the axes corresponds to the case where $f_2 = .5$, $f_1 = .0,.125,.333,.5$, and the captions in brackets correspond to the cases where $f_1 = .5$, $f_2 = .0,.125,.333,.5$.

Figure 3: Normalized maximum stress at localization for model #2, the main caption of the axes corresponds to the case where $f_2 = .5$, $f_1 = .0,.125,.333,.5$, and the captions in brackets correspond to the cases where $f_1 = .5$, $f_2 = .0,.125,.333,.5$.

Figure 4: Absolute value of the localization angle in degrees for model #2, the main caption of the axes corresponds to the case where $f_2 = .5$, $f_1 = .0,.125,.333,.5$, and the captions in brackets correspond to the cases where $f_1 = .5$, $f_2 = .0,.125,.333,.5$.

Figure 5: Maximum normalized damage value at localization (m=4.) for model #2, the main caption of the axes corresponds to the case where $f_2 = .5$, $f_1 = .0,.125,.333,.5$, and the captions in brackets correspond to the cases where $f_1 = .5$, $f_2 = .0,.125,.333,.5$.

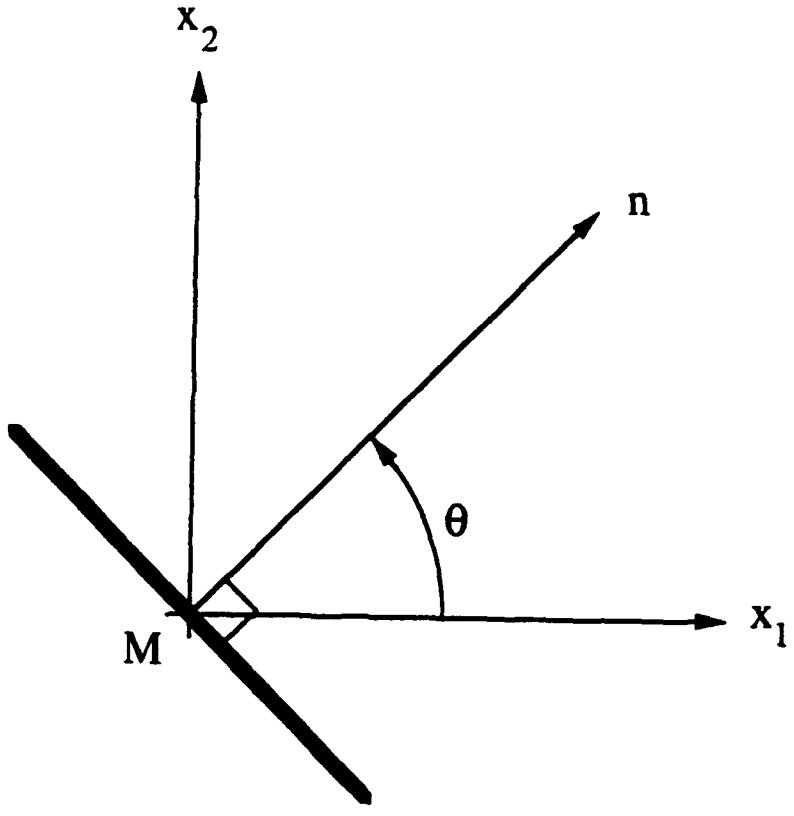

Fig. 1

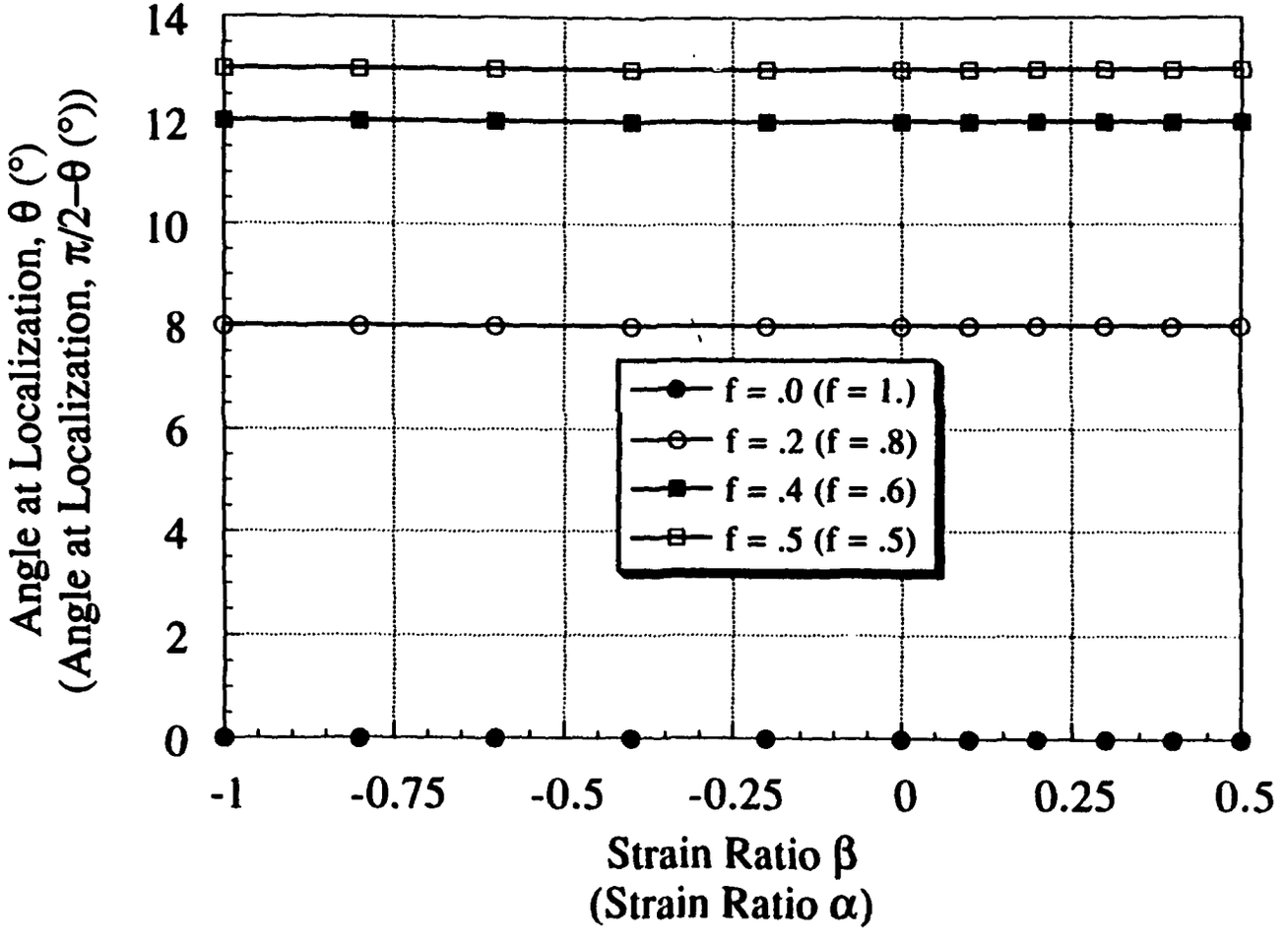
14
12
10
8
6
4
2
0
-1
-0.75
-0.5
-0.25
0
0.25
0.5
Angle at Localization, θ (°)
(Angle at Localization, π/2–θ (°))
Strain Ratio β
(Strain Ratio α)
f = .0 (f = 1.)
f = .2 (f = .8)
f = .4 (f = .6)
f = .5 (f = .5)

Fig. 2

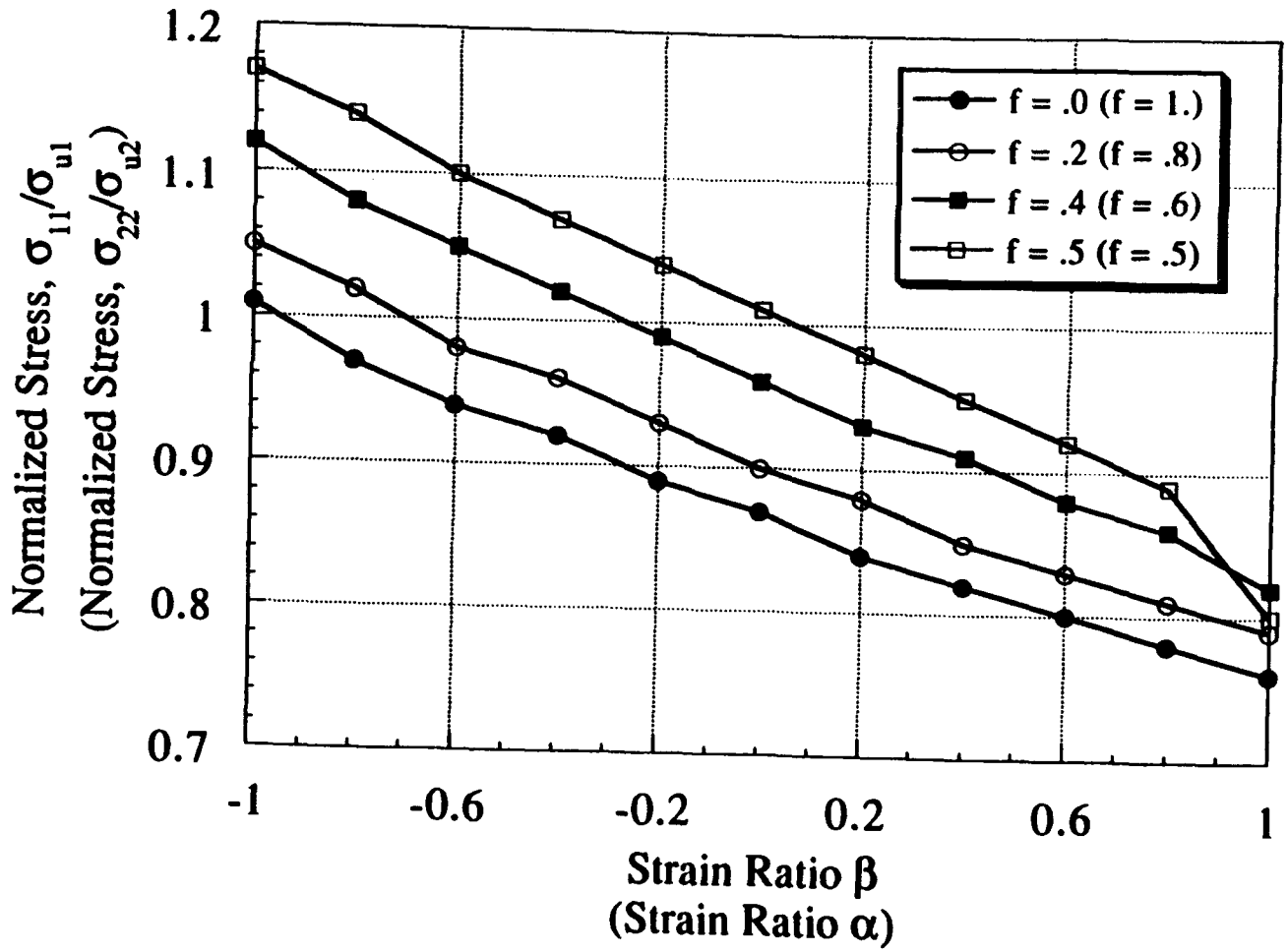
1.2
1.1
1
0.9
0.8
0.7
-1
-0.6
-0.2
0.2
0.6
1
Normalized Stress, σ_{11}/σ_{u1}
(Normalized Stress, σ_{22}/σ_{u2})
Strain Ratio β
(Strain Ratio α)
f = .0 (f = 1.)
f = .2 (f = .8)
f = .4 (f = .6)
f = .5 (f = .5)

Fig. 3

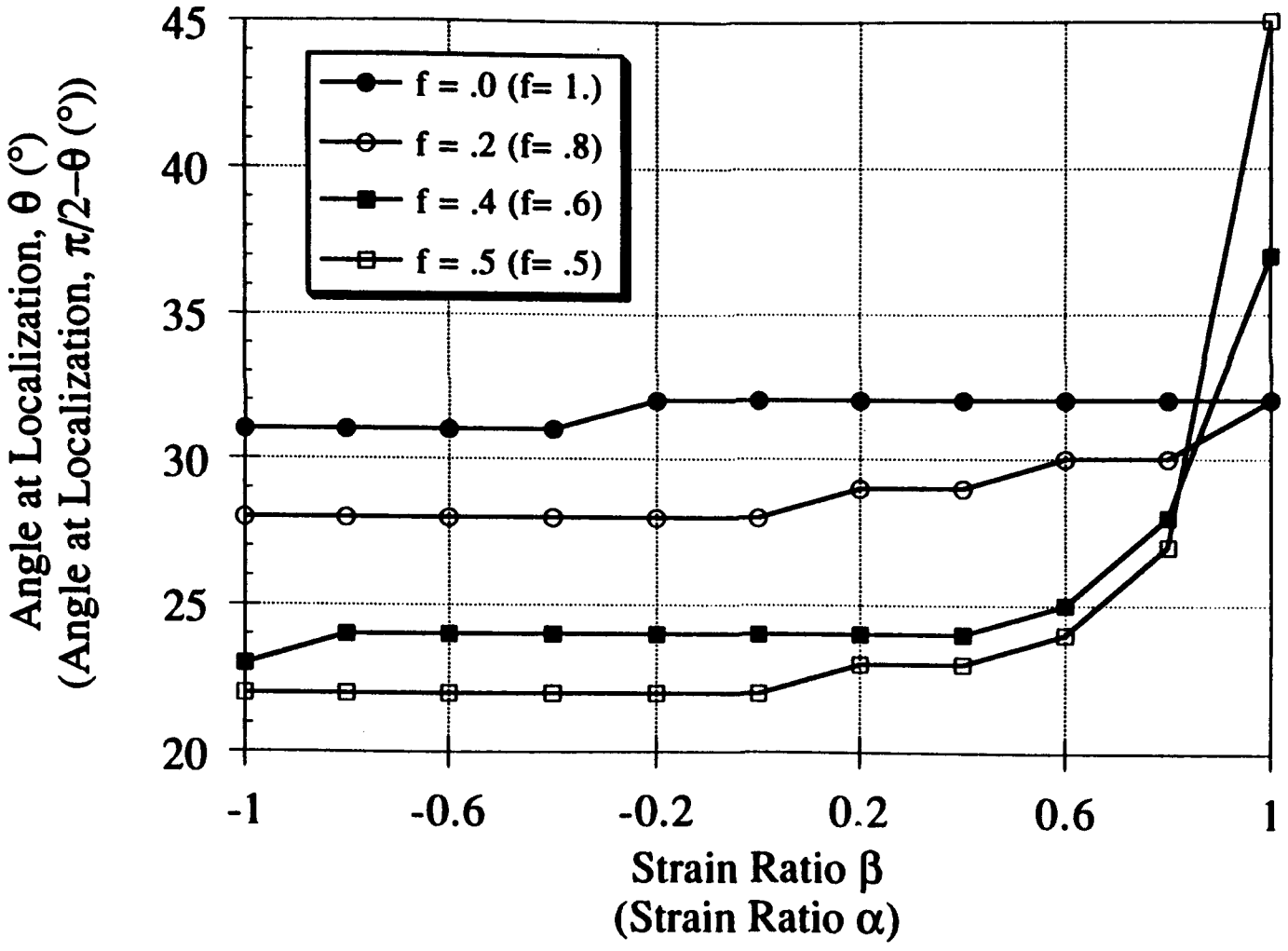
Angle at Localization, θ (°)
(Angle at Localization, π/2−θ (°))
45
40
35
30
25
20
f = .0 (f= 1.)
f = .2 (f= .8)
f = .4 (f= .6)
f = .5 (f= .5)
-1
-0.6
-0.2
0.2
0.6
1
Strain Ratio β
(Strain Ratio α)

Fig. 4

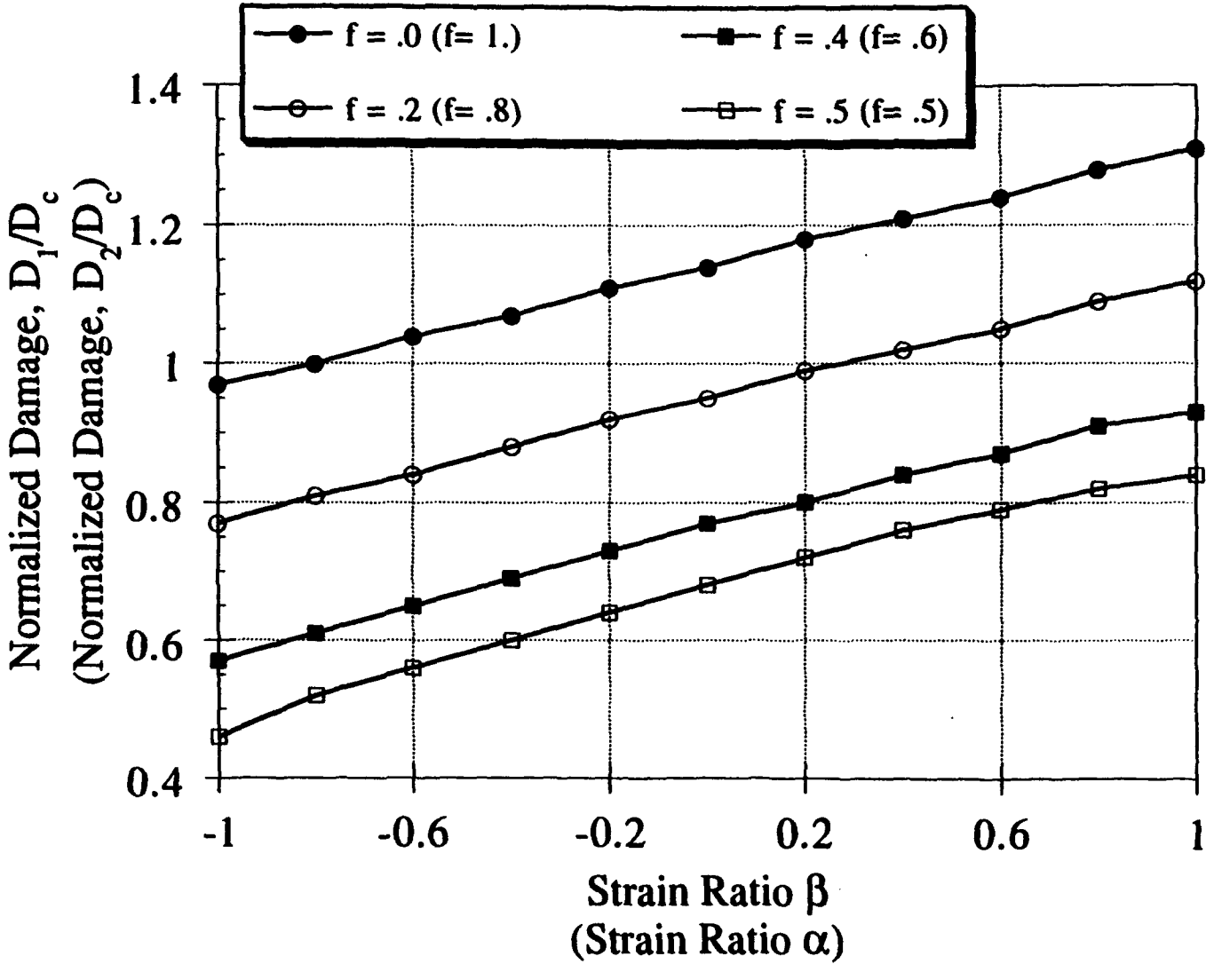
f = .0 (f= 1.)
f = .4 (f= .6)
f = .2 (f= .8)
f = .5 (f= .5)
1.4
1.2
1
0.8
0.6
0.4
Normalized Damage, D_1/D_c
(Normalized Damage, D_2/D_c)
-1
-0.6
-0.2
0.2
0.6
1
Strain Ratio β
(Strain Ratio α)

Fig. 5

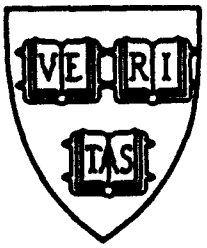

MECH-211

AN ELLIPTICAL INCLUSION EMBEDDED IN AN ANISOTROPIC BODY

Yingqing Lawrence Cui

Division of Applied Sciences
HARVARD UNIVERSITY
Cambridge, Massachusetts 02138

June 1993

AN ELLIPTICAL INCLUSION EMBEDDED IN AN ANISOTROPIC BODY

Yingqing Lawrence Cui
Division of Applied Sciences
Harvard University
Cambridge, MA 02138

ABSTRACT

This paper presents a general method for the plane problems of an anisotropic elliptical inclusion embedded in an anisotropic matrix. The analysis is based upon the use of a conformal mapping technique and a Laurant series expansion. The solutions for an infinite anisotropic matrix containing a perfectly bonded anisotropic elliptical inclusion are constructed by using the corresponding solutions of an infinite homogeneous material subjected to the same loading. The general solution is presented in terms of infinite series. Closed form solutions are obtained for the special cases of an elliptical hole and a rigid elliptical inclusion.

INTRODUCTION

Most engineering materials contain some defects and imperfections in the form of cracks, voids, inclusions, or secondary particles. These inhomogeneities play an important role in the mechanical behavior of engineering structures. The elastic response of a material with such inhomogeneities is a basic problem in solid mechanics, and has been a topic of extensive studies. One fascinating aspect of the inclusion problems is the interactions of inhomogeneities with singularities like concentrated forces and dislocations. Elastic solutions for interactions of singularities with material inhomogeneities not only provide the kernel functions for singular integral equations and Green's functions for the boundary element method, but also provide a direct tool to study the phenomena like matrix cracking in composites, ductile/brittle transition of an interface with impurity segregation, strain hardening in metal alloys, and toughening and strengthening of metal matrix composites.

During the past decades, many researchers studied the problems of a dislocation interacting with an inhomogeneity within the frame-work of isotropic elasticity. The problem of a circular inclusion interacting with an edge dislocation inside the matrix was studied by Dundurs and Mura (1964) via a semi-inverse method. The problem for a

dislocation inside a circular inclusion was solved by Durdurs and Senderky (1965). Due to its flexibility to cover a wide variety of cases ranging from line to circular defects, the elliptic inclusion has received more attention recently. Warren (1983) solved the problem of a dislocation inside an elliptic inclusion. Stagni and Lizzio (1983) obtained the solution for an elliptic inclusion interacting with an edge dislocation inside the matrix. Santare and Keer (1986) revisited the problem and obtained a closed form solution for the special case of a rigid elliptical inclusion.

Although a substantial amount of work has also been reported on the inclusion problems within the frame-work of anisotropic elasticity, these studies mostly deal with the problem under uniform remote loading. The anisotropic elastic solutions for the interaction of singularity with an elliptical inclusion have not been reported in the literature. The present study is partially motivated by the author's interest in modeling the problem of matrix cracking in the presence of an elliptic hole, and the problem of splitting tangent to an elliptic hole.

The purpose of the present study is to provide a general method to the plane problems of an anisotropic elliptical inclusion inside a general anisotropic matrix. The analysis is based upon the use of a conformal mapping technique and a Laurant series expansion. We shall show that solutions for an infinite anisotropic matrix containing a perfectly bonded elliptical anisotropic inclusion can be constructed by using the corresponding solutions of an infinite homogeneous material subjected to the same loading. In other words, one can build the solution with an elliptical inclusion as long as one has the solution of an infinite solid under the same loading. The derivation is valid for general anisotropic materials. The anti-plane deformation is also considered in the analysis. As two very useful cases of an elliptical hole and a rigid elliptical inclusion, the solutions are obtained in a closed form, provided that the solution for the corresponding homogeneous problem is readily available.

We start with a concise review of the basic results of anisotropic elasticity on the basis of Lekhnitskii-Eshelby representation and then present a general solution procedure. Finally, we give a few specific examples.

BASIC RESULTS OF ANISOTROPIC ELASTICITY

Consider the two-dimensional elasticity problem of a general anisotropic material. The Hooke's law for the material can be written as

$$\varepsilon_i = \sum_{j=1}^{6} s_{ij}\sigma_j \qquad (1)$$

where

$$\{\varepsilon_i\} = \left[\varepsilon_{xx}, \varepsilon_{yy}, \varepsilon_{zz}, \gamma_{yz}, \gamma_{zx}, \gamma_{xy}\right]^T \tag{2}$$

$$\{\sigma_i\} = \left[\sigma_{xx}, \sigma_{yy}, \sigma_{zz}, \tau_{yz}, \tau_{zx}, \tau_{xy}\right]^T \tag{3}$$

with superscript T denoting the transpose. The 6x6 matrix S is the standard compliance matrix.

It has been shown by Lekhnitskii (1963) and Eshelby et al. (1953) that, under the assumption that all displacements are independent of the direction normal to the x,y-plane, the general solution of the problem can be expressed in terms of three analytic functions, $f_1(z_1)$, $f_2(z_2)$ and $f_3(z_3)$, with three complex variables given by $z_1 = x + \mu_1 y$, $z_2 = x + \mu_2 y$ and $z_3 = x + \mu_3 y$. The following algebraic equation has six roots:

$$l_2(\mu)\, l_4(\mu) - \left[l_3(\mu)\right]^2 = 0 \tag{4}$$

where

$$l_2(\mu) = s_{55}\mu^2 - 2s_{45}\mu + s_{44} \tag{5}$$

$$l_3(\mu) = s_{15}\mu^3 - (s_{14} + s_{56})\mu^2 + (s_{25} + s_{46})\mu - s_{24} \tag{6}$$

$$l_4(\mu) = s_{11}\mu^4 - 2s_{16}\mu^3 + (2s_{12} + s_{66})\mu^2 - 2s_{26}\mu \tag{7}$$

The parameters μ_1, μ_2 and μ_3 are the three distinct roots whose imaginary parts are positive.

In terms of $f_1(z_1)$, $f_2(z_2)$ and $f_3(z_3)$, the displacements u_i, the stresses σ_{ij} and the resultant forces on an arc T_i are given by

$$u_i = 2\,\mathrm{Re}\left[\sum_{j=1}^{3} A_{ij} f_j(z_j)\right], \qquad T_i = -2\,\mathrm{Re}\left[\sum_{j=1}^{3} L_{ij} f_j(z_j)\right] \tag{8}$$

$$\sigma_{2i} = 2\,\mathrm{Re}\left[\sum_{j=1}^{3} L_{ij} f_j'(z_j)\right], \qquad \sigma_{1i} = -2\,\mathrm{Re}\left[\sum_{j=1}^{3} L_{ij}\mu_j f_j'(z_j)\right] \tag{9}$$

where Re[] denotes the real part of a complex quantity and $(\,)'$ stands for the derivative with respect to the associated variables. The elements of the matrices A and L can be expressed in terms of elastic constants as

$$\mathbf{L} = \begin{bmatrix} -\mu_1 & -\mu_2 & -\mu_3\eta_3 \\ 1 & 1 & \eta_3 \\ -\eta_1 & -\eta_2 & -1 \end{bmatrix} \tag{10}$$

and

$$A_{1\alpha} = s_{11}\mu_\alpha^2 + s_{12} - s_{16}\mu_\alpha + \eta_\alpha(s_{15} - \mu_\alpha - s_{14}) \tag{11}$$

$$A_{2\alpha} = s_{21}\mu_\alpha + s_{22}/\mu_\alpha - s_{26} + \eta_\alpha(s_{25} - s_{24}/\mu_\alpha) \tag{12}$$

$$A_{3\alpha} = s_{41}\mu_\alpha + s_{42}/\mu_\alpha - s_{46} + \eta_\alpha(s_{45} - s_{44}/\mu_\alpha) \tag{13}$$

for $\alpha = 1, 2$ and

$$A_{13} = \eta_3\left(s_{11}\mu_3^2 + s_{12} - s_{12}\mu_3\right) + s_{15}\mu_3 - s_{14} \tag{14}$$

$$A_{23} = \eta_3\left(s_{21}\mu_3 + s_{22}/\mu_3 - s_{26}\right) + s_{25} - s_{24}/\mu_3 \tag{15}$$

$$A_{33} = \eta_3\left(s_{41}\mu_3 + s_{42}/\mu_3 - s_{46}\right) + s_{45} - s_{44}/\mu_3 \tag{16}$$

where $\eta_\alpha = -l_3(\mu_\alpha)/l_2(\mu_\alpha)$, $\alpha = 1,2$ and $\eta_3 = -l_3(\mu_3)/l_4(\mu_3)$

If we introduce the following vectors:

$$\mathbf{u} = [u_1, u_2, u_3]^T, \quad \mathbf{T} = [T_1, T_2, T_3]^T, \quad \mathbf{f} = [f_1(z_1), f_2(z_2), f_3(z_3)]^T \tag{17}$$

Eqs. (8) and (9) can be recast into the form

$$\mathbf{u} = \mathbf{A}\mathbf{f}(z) + \overline{\mathbf{A}}\,\overline{\mathbf{f}(z)} \qquad \mathbf{T} = \mathbf{L}\mathbf{f}(z) + \overline{\mathbf{L}}\,\overline{\mathbf{f}(z)} \tag{18}$$

It is important to note that the vector $\mathbf{f}(z)$ has component f_j with the understanding that z is to be replaced for f_j by z_j.

All the above equations hold for the plane stress problem, but they are equally valid as well for the plane strain counterpart if the following substitution of compliance is made

$$s_{ij} = s_{ij} - s_{i3}\,s_{j3}/s_{33} \tag{19}$$

THE GENERAL SOLUTION FOR AN INFINITE ANISOTROPIC SOLID WITH AN ELLIPTIC INCLUSION

Formulation

We now construct the general solutions for the problem of an infinite anisotropic plane with an elliptical inclusion. Let the matrix material occupy the space specified by $x^2/a^2 + y^2/b^2 > 1$, and the inclusion occupy the rest of the plane. The inclusion and the matrix are assumed to be bonded perfectly together, so that

$$\mathbf{u}^m = \mathbf{u}^i \qquad \mathbf{T}^m = \mathbf{T}^i \qquad \text{on} \quad x^2/a^2 + y^2/b^2 = 1 \tag{20}$$

The superscripts m and i of u and T refer to materials in the matrix and in the inclusion respectively. Throughout this paper, whenever necessary, explicit superscripts and subscripts m and i will be reserved to signify quantities for the matrix and the inclusion respectively. We will find the stress potentials $f_j(z_j)$ for z_j both in the matrix and in the inclusion. Without loss of generality, we assume that loading is applied in the matrix, but the same procedure can be applied to the case that loading is applied in the inclusion. Denote the stress potential vector for the corresponding problem of an infinite homogeneous matrix subjected to the same loading condition as $\mathbf{f}^0(z)$. Then the potentials in the presence of an elliptical inclusion may be written as

$$\mathbf{f}(z) = \begin{cases} \mathbf{f}^i(z), & z \text{ in the inclusion} \\ \mathbf{f}^m(z) + \mathbf{f}^0(z), & z \text{ in the matrix} \end{cases} \tag{21}$$

Here both $f^i(z)$ and $f^m(z)$ are analytical in their respective regions. The function $f^0(z)$ may have singularities due to concentrated loading or dislocations.

Substituting (21) into (20) via (18), one obtains

$$L_i f^i(z) + \overline{L_i}\,\overline{f^i(z)} = L_m\left[f^m(z) + f^0(z)\right] + \overline{L_m}\left[\overline{f^m(z)} + \overline{f^0(z)}\right] \tag{22}$$

$$A_i f^i(z) + \overline{A_i}\,\overline{f^i(z)} = A_m\left[f^m(z) + f^0(z)\right] + \overline{A_m}\left[\overline{f^m(z)} + \overline{f^0(z)}\right] \tag{23}$$

Eqs. (22) and (23) hold for every point on the interface $x^2/a^2 + y^2/b^2 = 1$. We shall solve for $f^i(z)$ and $f^m(z)$ in terms of $f^0(z)$ from these two equations.

Before presenting the general solution procedure, we note that

$$z_j^m = x + \mu_j^m y = X_j^m + iY_j^m \qquad j = 1,2,3 \tag{24}$$

$$z_j^i = x + \mu_j^i y = X_j^i + iY_j^i \qquad j = 1,2,3 \tag{25}$$

are affine transformations which map points in the z plane into affine points in z_j^i and z_j^m planes. The ellipse $x^2/a^2 + y^2/b^2 = 1$ in the z plane (physical plane) corresponds to six ellipses in the planes z_j^m, z_j^i, $j = 1,2,3$.

The mixed boundary value problem defined by Eqs. (22) and (23) may be handled by a conformal mapping technique. We introduce mapping functions

$$z_j^m = \frac{a + i\mu_j^m b}{2}\varsigma_j^m + \frac{a - i\mu_j^m b}{2\varsigma_j^m} \qquad j = 1,2,3 \tag{26}$$

which map the areas outside the ellipses in z_1^m, z_2^m and z_3^m planes onto the areas inside the unit circles in ς_1^m, ς_2^m, and ς_3^m planes respectively; and

$$z_j^i = \frac{a + i\mu_j^i b}{2}\varsigma_j^i + \frac{a - i\mu_j^i b}{2\varsigma_j^i} \qquad j = 1,2,3 \tag{27}$$

For each given value of j, mapping function given by (27) maps the area inside the ellipse in the z_j^i plane onto the annular region between the unit circles $\left|\varsigma_j^i\right| = 1$ and $\left|\varsigma_j^i\right| = \rho_j = \left|\sqrt{\left(a - i\mu_j^i b\right)/\left(a + i\mu_j^i b\right)}\right|$, which corresponds to a straight line connecting points $z_j^i = -\sqrt{a^2 + \left(\mu_j^i b\right)^2}$ and $z_j^i = \sqrt{a^2 + \left(\mu_j^i b\right)^2}$ in the z_j^i plane.

It is important to note that for every point P on the contour $x^2/a^2 + y^2/b^2 = 1$, there are six corresponding affine points $P^1, P^2, \cdots\cdots, P^6$. However, the conformal mapping functions defined by (26) and (27) map all these affine points into a single point on the contour of the unit circle given by $\varsigma = e^{i\theta}$, where θ is connected to the parametric equations of the interface via

$$\begin{cases} x = a\cos\theta \\ y = -b\sin\theta \end{cases} \tag{28}$$

Therefore, for each point (x,y) on the interface, the corresponding transformed points are

$$\varsigma_j^i = \varsigma_j^m = \varsigma = e^{i\theta} \qquad j = 1,2,3 \tag{29}$$

With transformation functions (26), (27) and identities (29), we can rewrite Eqs. (22) and (23) as

$$\mathbf{L}_i \mathbf{f}^i(\varsigma) + \overline{\mathbf{L}_i}\,\overline{\mathbf{f}^i(\varsigma)} = \mathbf{L}_m\left[\mathbf{f}^m(\varsigma) + \mathbf{f}^0(\varsigma)\right] + \overline{\mathbf{L}_m}\left[\overline{\mathbf{f}^m(\varsigma)} + \overline{\mathbf{f}^0(\varsigma)}\right] \qquad \varsigma = e^{i\theta} \tag{30}$$

$$\mathbf{A}_i \mathbf{f}^i(\varsigma) + \overline{\mathbf{A}_i}\,\overline{\mathbf{f}^i(\varsigma)} = \mathbf{A}_m\left[\mathbf{f}^m(\varsigma) + \mathbf{f}^0(\varsigma)\right] + \overline{\mathbf{A}_m}\left[\overline{\mathbf{f}^m(\varsigma)} + \overline{\mathbf{f}^0(\varsigma)}\right] \qquad \varsigma = e^{i\theta} \tag{31}$$

where $f_j^i(\varsigma)$, $f_j^m(\varsigma)$, and $f_j^0(\varsigma)$ represent $f_j^i\left[z_j^i(\varsigma)\right]$, $f_j^m\left[z_j^m(\varsigma)\right]$, and $f_j^0\left[z_j^m(\varsigma)\right]$ respectively. In addition, the following condition must be satisfied by $f_j^i(\varsigma)$:

$$f_j^i(\varsigma_j) = f_j^i\left(\overline{\varsigma_j} e^{2i\phi_0}\right) \qquad \text{on} \quad \varsigma_j^i = \sqrt{\frac{\left(a - i\mu_j^i b\right)}{\left(a + i\mu_j^i b\right)}}\; e^{i\theta} = \rho_j e^{i\phi_0} e^{i\theta} \tag{32}$$

since on $\varsigma_j^i = \rho_j e^{i\phi_0} e^{i\theta}$, points ς_j and $\overline{\varsigma_j} e^{2i\phi_0}$ correspond to one and the same point on the cut from $z_j^i = -\sqrt{a^2 + \left(\mu_j^i b\right)^2}$ to $z_j^i = \sqrt{a^2 + \left(\mu_j^i b\right)^2}$ in the z_j^i plane.

We note that once the solutions for $\mathbf{f}^i(\varsigma)$ and $\mathbf{f}^m(\varsigma)$ are obtained, one may proceed to find the final solutions for stresses and displacements via Eqs. (8) and (9) as follows. The vector $\mathbf{f}^m(z)$ can be obtained by first replacing ς with ς_j^m, and then substituting ς_j^m by

$$\varsigma_j^m = \frac{z_j^m - \sqrt{\left(z_j^m\right)^2 - a^2 - \left(\mu_j^m b\right)^2}}{a + i\mu_j^m b} \tag{33}$$

for the jth component f_j^m. The vector $\mathbf{f}^i(z)$ can be obtained similarly by first replacing ς with ς_j^i, and then substituting ς_j^i by

$$\varsigma_j^i = \frac{z_j^i - \sqrt{\left(z_j^i\right)^2 - a^2 - \left(\mu_j^i b\right)^2}}{a + i\mu_j^i b} \tag{34}$$

for the jth component f_j^i.

General solution procedure

Now, we try to solve the boundary value problem defined by Eqs. (30) and (31). Recall that function $f_j^m(\varsigma)$ is holomorphic in $|\varsigma| < 1$, and that function $f_j^i(\varsigma)$ is holomorphic in the annular region $1 < |\varsigma| < \rho_j$. Furthermore, if $\varsigma_s = \rho_0 e^{i\phi}$ is the singular point whose distance to $|\varsigma| = 1$ is the shortest among all singular points of $f_j^0(\varsigma)$, then function $f_j^0(\varsigma)$ is holomorphic in the region $0 < \rho_0 < |\varsigma| \le 1$. Therefore, one can expand these potentials in terms of infinite series as

$$f_j^i(\varsigma) = \sum_{k=0}^{\infty} a_{jk}\left[\varsigma^k + \left(\frac{a - i\mu_j^i b}{a + i\mu_j^i b}\right)^k \Big/ \varsigma^k\right] \tag{35}$$

$$f_j^m(\varsigma) = \sum_{k=0}^{\infty} c_{jk}\varsigma^k \tag{36}$$

$$f_j^0(\varsigma) = \sum_{k=0}^{\infty}\left[d_{jk}\varsigma^k + e_{jk}/\varsigma^k\right] \tag{37}$$

Here the continuity condition (Eq. (32)) across the straight line connecting points $z_j^i = -\sqrt{a^2 + (\mu_j^i b)^2}$ and $z_j^i = \sqrt{a^2 + (\mu_j^i b)^2}$ in the z_j^i plane has been satisfied. To proceed, we denote

$$\mathbf{a}_k = [a_{1k}, a_{2k}, a_{3k}]^T, \quad \mathbf{c}_k = [c_{1k}, c_{2k}, c_{3k}]^T \tag{38}$$

$$\mathbf{d}_k = [d_{1k}, d_{2k}, d_{3k}]^T, \quad \mathbf{e}_k = [e_{1k}, e_{2k}, e_{3k}]^T \tag{39}$$

and

$$\mathbf{I}_c^k = \begin{bmatrix} \left(\frac{a - i\mu_1^i b}{a + i\mu_1^i b}\right)^k & 0 & 0 \\ 0 & \left(\frac{a - i\mu_2^i b}{a + i\mu_2^i b}\right)^k & 0 \\ 0 & 0 & \left(\frac{a - i\mu_3^i b}{a + i\mu_3^i b}\right)^k \end{bmatrix} \tag{40}$$

Substitution of (35), (36) and (37) into (30) and (31) and then comparing the coefficients of ς^k lead to algebraic equations

$$\mathbf{L}_l\mathbf{a}_k + \overline{\mathbf{L}_l}\,\overline{\mathbf{I}_c^k}\,\overline{\mathbf{a}_k} = \mathbf{L}_m\mathbf{c}_k + \mathbf{L}_m\mathbf{d}_k + \overline{\mathbf{L}_m}\,\overline{\mathbf{e}_k} \tag{41}$$

$$\mathbf{A}_l\mathbf{a}_k + \overline{\mathbf{A}_l}\,\overline{\mathbf{I}_c^k}\,\overline{\mathbf{a}_k} = \mathbf{A}_m\mathbf{c}_k + \mathbf{A}_m\mathbf{d}_k + \overline{\mathbf{A}_m}\,\overline{\mathbf{e}_k} \tag{42}$$

Solving for $\mathbf{a}_k$, $\mathbf{c}_k$ from the above equations in terms of $\mathbf{d}_k$ and $\mathbf{e}_k$, one obtains the complete solution for the inclusion problem.

Special cases of holes or rigid inclusions

For the special cases of holes and rigid inclusions, the solutions can be obtained in a compact and closed form. The boundary conditions (30) and (31) reduce to

$$\mathbf{L}_m\left[\mathbf{f}^m(\varsigma) + \mathbf{f}^0(\varsigma)\right] + \overline{\mathbf{L}_m}\left[\overline{\mathbf{f}^m(\varsigma)} + \overline{\mathbf{f}^0(\varsigma)}\right] = 0 \qquad \varsigma = e^{i\theta} \tag{43}$$

for an open hole; and

$$\mathbf{A}_m\left[\mathbf{f}^m(\varsigma) + \mathbf{f}^0(\varsigma)\right] + \overline{\mathbf{A}_m}\left[\overline{\mathbf{f}^m(\varsigma)} + \overline{\mathbf{f}^0(\varsigma)}\right] = \mathbf{u}^i \qquad \varsigma = e^{i\theta} \tag{44}$$

for a rigid inclusion.

To illustrate the solution procedure, we assume that $z_{j0}^m = x_0 + \mu_j^m y_0$ is a singular point of $f_j^0\left(z_j^m\right)$. For any affine point corresponding to the interface boundary, one has

$$z_j^m(\varsigma) - z_{j0}^m = \frac{a + i\mu_j^m b\left(\varsigma - \eta_{j1}^i\right)\left(\varsigma - \eta_{j1}^0\right)}{2 \qquad \varsigma} \tag{45}$$

and

$$\overline{z_j^m(\varsigma)} - \overline{z_{j0}^m} = \frac{a + i\overline{\mu_j^m} b\left(\varsigma - \eta_{j2}^i\right)\left(\varsigma - \eta_{j2}^0\right)}{2 \qquad \varsigma} \tag{46}$$

where

$$\eta_{j1}^I = \frac{z_{j0}^m - \sqrt{\left(z_{j0}^m\right)^2 - a^2 - \left(\mu_j^m b\right)^2}}{a + i\mu_j^m b} \tag{47}$$

$$\eta_{j1}^0 = \frac{z_{j0}^m + \sqrt{\left(z_{j0}^m\right)^2 - a^2 - \left(\mu_j^m b\right)^2}}{a + i\mu_j^m b} \tag{48}$$

$$\eta_{j2}^I = \frac{\overline{z_{j0}^m} - \sqrt{\left(\overline{z_{j0}^m}\right)^2 - a^2 - \left(\overline{\mu_j^m} b\right)^2}}{a + i\overline{\mu_j^m} b} \tag{49}$$

$$\eta_{j2}^0 = \frac{\overline{z_{j0}^m} + \sqrt{\left(\overline{z_{j0}^m}\right)^2 - a^2 - \left(\overline{\mu_j^m} b\right)^2}}{a + i\overline{\mu_j^m} b} \tag{50}$$

Here we have chosen the branch such that $\left|\eta_{j\beta}^I\right| < 1, \left|\eta_{j\beta}^0\right| > 1\ (\beta = 1,2)$.

Recall that both $f_j^0\left(z_j^m\right)$ and $\overline{f_j^0\left(z_j^m\right)}$ are singular at $z_j^m = z_{j0}^m$. Therefore function $f_j^0(\varsigma) \equiv f_j^0\left[z_j^m(\varsigma)\right]$ is singular at $\varsigma = \eta_{j1}^I, \eta_{j1}^0$, and function $\overline{f_j^0(\varsigma)} \equiv \overline{f_j^0\left[z_j^m(\varsigma)\right]}$ is singular at $\varsigma = \eta_{j2}^I, \eta_{j2}^0$. The most frequently encountered singularities of $f_j^0\left(z_j^m\right)$ are either of the type $\ln\left(z_j^m - z_{j0}^m\right)$ or of the type $\left(z_j^m - z_{j0}^m\right)^{-n}$, where n is a positive integer. With the use of (45) and (46), one may decompose each singular term into two separate parts so that each part contains only one singular point with respect to ς. Therefore one may rewrite $f_j^0(\varsigma)$ and $\overline{f_j^0(\varsigma)}$ in the form

$$f_j^0(\varsigma) = f_j^{0i}\left(\frac{\varsigma - \eta_{j1}^I}{\varsigma}\right) + f_j^{0m}\left(\varsigma - \eta_{j1}^0\right) + \text{constant} \tag{51}$$

$$\overline{f_j^0(\varsigma)} = g_j^{0i}\left(\frac{\varsigma - \eta_{j2}^I}{\varsigma}\right) + g_j^{0m}\left(\varsigma - \eta_{j2}^0\right) + \text{constant} \tag{52}$$

where functions f_i^{0i}, g_j^{0i} are analytical for $|\varsigma| > 1$, but functions f_j^{0m} and g_j^{0m} are analytical for $|\varsigma| < 1$, since $|\eta_{j\beta}^I| < 1, |\eta_{j\beta}^0| > 1\ (\beta = 1,2)$. Substituting (51) and (52) into (43) and (44), one obtains:

$$\mathbf{L}_m\left[\mathbf{f}^m(\varsigma) + \mathbf{f}^{0m}(\varsigma) + \mathbf{f}^{0i}(\varsigma)\right] + \overline{\mathbf{L}_m}\left[\overline{\mathbf{f}^m(\varsigma)} + \mathbf{g}^{0m}(\varsigma) + \mathbf{g}^{0i}(\varsigma)\right] = 0 \tag{53}$$

$$\mathbf{A}_m\left[\mathbf{f}^{(m)}(\varsigma) + \mathbf{f}^{0m}(\varsigma) + \mathbf{f}^{0i}(\varsigma)\right] + \overline{\mathbf{A}_m}\left[\overline{\mathbf{f}^m(\varsigma)} + \mathbf{g}^{0m}(\varsigma) + \mathbf{g}^{0i}(\varsigma)\right] = \mathbf{u}^i \tag{54}$$

Define $\mathbf{f}_*^m(\varsigma) = \overline{\mathbf{f}^m\left(\frac{1}{\varsigma}\right)}$, then on $|\varsigma| = 1$, $\mathbf{f}_*^m(\varsigma) = \overline{\mathbf{f}^m(\varsigma)}$. Since $\mathbf{f}^m(\varsigma)$ is analytical for $|\varsigma| \geq 1$, $\mathbf{f}_*^m(\varsigma)$ is regular for $|\varsigma| > 1$. Regrouping Eqs. (53) and (54), one obtains

$$\mathbf{L}_m\left[\mathbf{f}^m + \mathbf{f}^{0m}\right] + \overline{\mathbf{L}_m}\mathbf{g}^{0m} = -\overline{\mathbf{L}_m}\mathbf{f}_*^m(\varsigma) - \mathbf{L}_m\mathbf{f}^{0i}(\varsigma) - \overline{\mathbf{L}_m}\mathbf{g}^{0i}(\varsigma) \tag{55}$$

$$\mathbf{A}_m\left[\mathbf{f}^m + \mathbf{f}^{0m}\right] + \overline{\mathbf{A}_m}\mathbf{g}^{0m} = -\overline{\mathbf{A}_m}\mathbf{f}_*^m(\varsigma) - \mathbf{A}_m\mathbf{f}^{0i}(\varsigma) - \overline{\mathbf{A}_m}\mathbf{g}^{0i}(\varsigma) + \mathbf{u}^i \tag{56}$$

The above equations hold on the circle $|\varsigma| = 1$. The left-hand side of these equations are analytic inside the circle $|\varsigma| < 1$, while those on the right-hand side are analytic outside the circle $|\varsigma| > 1$. Analytic continuation arguments lead to equations:

$$\mathbf{L}_m\left[\mathbf{f}^m + \mathbf{f}^{0m}\right] + \overline{\mathbf{L}_m}\mathbf{g}^{0m} = \text{constant} \qquad |\varsigma| < 1 \tag{57}$$

$$\mathbf{A}_m\left[\mathbf{f}^m + \mathbf{f}^{0m}\right] + \overline{\mathbf{A}_m}\mathbf{g}^{0m} = \text{constant} \qquad |\varsigma| < 1 \tag{58}$$

Solving for $\mathbf{f}^m(\varsigma)$, one finds

$$\mathbf{f}(\varsigma) = \mathbf{f}^0(\varsigma) - \mathbf{f}^{0m}(\varsigma) - \mathbf{L}_m^{-1}\overline{\mathbf{L}_m}\,\mathbf{g}^{0m}(\varsigma) + \text{constant} \qquad |\varsigma| \leq 1 \tag{59}$$

for an open hole; and

$$\mathbf{f}(\varsigma) = \mathbf{f}^0(\varsigma) - \mathbf{f}^{0m}(\varsigma) - \mathbf{A}_m^{-1}\overline{\mathbf{A}_m}\,\mathbf{g}^{0m}(\varsigma) + \text{constant} \qquad |\varsigma| \leq 1 \tag{60}$$

for a rigid inclusion.

EXAMPLES

Elliptical inhomogeneity subjected to uniform loading at infinity

Consider now the problem of an elliptical inclusion in an infinite matrix subjected to uniform stresses σ_{2j}^{∞} and σ_{1j}^{∞} at infinity. The solution for the corresponding homogeneous matrix is

$$\mathbf{f}^0(z) = \left[p_1 z_1, p_2 z_2, p_3 z_3\right]^T + \left[q_1 z_1, q_2 z_2, q_3 z_3\right]^T \tag{61}$$

where vectors $\mathbf{q} = \{q_j\}$ and $\mathbf{p} = \{p_j\}$ are given by

$$\mathbf{L}_m\mathbf{q} + \overline{\mathbf{L}_\mu}\,\overline{\mathbf{q}} = \{\sigma_{2j}\} \qquad \mathbf{L}_m\mathbf{I}_\mu\mathbf{p} + \overline{\mathbf{L}_m}\,\overline{\mathbf{I}_\mu}\,\overline{\mathbf{p}} = -\{\sigma_{1j}\} \tag{62}$$

Here $\mathbf{I}_\mu$ is a diagonal matrix given by

$$\mathbf{I}_\mu = \begin{bmatrix} \mu_1 & & \\ & \mu_2 & \\ & & \mu_3 \end{bmatrix} \tag{63}$$

Introducing diagonal matrices

$$\mathbf{I}_q = \begin{bmatrix} q_1 & & \\ & q_2 & \\ & & q_3 \end{bmatrix} \qquad \mathbf{I}_p = \begin{bmatrix} p_1 & & \\ & p_2 & \\ & & p_3 \end{bmatrix} \tag{64}$$

one can rewrite Eq. (61) as

$$\mathbf{f}^0(z) = \mathbf{I}_q z + \mathbf{I}_p z \tag{65}$$

The expansion of $\mathbf{f}^0(\varsigma)$ is

$$\mathbf{f}^0(\varsigma) = \left(\mathbf{I}_q + \mathbf{I}_p\right)\left(\mathbf{h}_1\varsigma + \mathbf{h}_2\varsigma^{-1}\right) \tag{66}$$

where $\mathbf{h}_1 = \frac{1}{2}\left\{a_j + i\mu_j^m b\right\}$ and $\mathbf{h}_2 = \frac{1}{2}\left\{a_j - i\mu_j^m b\right\}$. Substitution of Eq. (66) into Eqs. (41) and (42) yields

$$a_k = c_k = 0 \qquad k \geq 2 \tag{67}$$

Therefore, the potentials are

$$f^m(\varsigma) = c_1\varsigma \qquad f_j^i(\varsigma) = a_{j1}\left[\varsigma + \frac{\left(a - i\mu_j^i b\right)/\left(a + i\mu_j^i b\right)}{\varsigma}\right] \tag{68}$$

which gives

$$f_j^i\left(z_j^i\right) = \frac{2a_{j1}}{\left(a + i\mu_j^i b\right)} z_j^i \tag{69}$$

The linear form of $f_j^i\left(z_j^i\right)$ indicates that the stresses are constant inside the elliptical inclusion, a well known result first discovered by Eshelby (1957).

A concentrated force and a dislocation interacting with an elliptical hole or a rigid elliptical inclusion

As a second example, we consider the interactions of an elliptical hole and a rigid elliptical inclusion with a concentrated force **p** and a dislocation with Burger's vector **b**, both located at $x = x_0$ and $y = y_0$. The potentials $f_j^0(z_j)$ for the corresponding homogeneous problem are (Eshelby et al. 1953)

$$f_j\left(z_j\right) = q_j \ln\left(z_j - z_{j0}\right) \qquad z_{j0} = x_0 + \mu_j y_0 \tag{70}$$

where $\mathbf{q} = \left\{q_j\right\}$ is a complex vector to be determined in terms of **b** and **p**. Since $\ln\left(z_j - z_{j0}\right)$ is a multivalued function with a branch point at z_{j0}, we introduce a branch cut

in the negative x direction. By definition, (70) satisfies the conditions

$$\mathbf{b} = \mathbf{u}^+ - \mathbf{u}^- \qquad \mathbf{p} = \mathbf{T}^+ - \mathbf{T}^- \tag{71}$$

which lead to

$$\mathbf{b} = 2\pi i\left(\mathbf{A}\mathbf{q} - \overline{\mathbf{A}}\,\overline{\mathbf{q}}\right) \qquad \mathbf{p} = 2\pi i\left(\mathbf{L}\mathbf{q} - \overline{\mathbf{L}}\,\overline{\mathbf{q}}\right) \tag{72}$$

Solving for q from the above equations, one obtains the solution for the singularities in an infinite homogeneous matrix.

A direct application of the formula (59) and (60) gives the solutions for the interaction problems as

$$\begin{Bmatrix} f_1(\varsigma) \\ f_2(\varsigma) \\ f_3(\varsigma) \end{Bmatrix} = \begin{Bmatrix} q_1 \ln\left[z_1(\varsigma) - z_{10}\right] \\ q_2 \ln\left[z_2(\varsigma) - z_{20}\right] \\ q_3 \ln\left[z_3(\varsigma) - z_{30}\right] \end{Bmatrix} - \begin{Bmatrix} q_1 \ln\left(\varsigma - \eta_{11}^0\right) \\ q_2 \ln\left(\varsigma - \eta_{21}^0\right) \\ q_3 \ln\left(\varsigma - \eta_{31}^0\right) \end{Bmatrix} - \mathbf{L}_\infty^{-1}\overline{\mathbf{L}_\infty} \begin{Bmatrix} q_1 \ln\left(\varsigma - \eta_{12}^0\right) \\ q_2 \ln\left(\varsigma - \eta_{22}^0\right) \\ q_3 \ln\left(\varsigma - \eta_{32}^0\right) \end{Bmatrix} \tag{73}$$

for an open hole; and

$$\begin{Bmatrix} f_1(\varsigma) \\ f_2(\varsigma) \\ f_3(\varsigma) \end{Bmatrix} = \begin{Bmatrix} q_1 \ln\left[z_1(\varsigma) - z_{10}\right] \\ q_2 \ln\left[z_2(\varsigma) - z_{20}\right] \\ q_3 \ln\left[z_3(\varsigma) - z_{30}\right] \end{Bmatrix} - \begin{Bmatrix} q_1 \ln\left(\varsigma - \eta_{11}^0\right) \\ q_2 \ln\left(\varsigma - \eta_{21}^0\right) \\ q_3 \ln\left(\varsigma - \eta_{31}^0\right) \end{Bmatrix} - \mathbf{A}_\infty^{-1}\overline{\mathbf{A}_\infty} \begin{Bmatrix} q_1 \ln\left(\varsigma - \eta_{12}^0\right) \\ q_2 \ln\left(\varsigma - \eta_{22}^0\right) \\ q_3 \ln\left(\varsigma - \eta_{32}^0\right) \end{Bmatrix} \tag{74}$$

for a rigid inclusion.

ACKNOWLEDGMENT

The author is very grateful to Professors B. Budiansky and J.W. Hutchinson for their encouragement and comments on this work. This work was partially supported by the DARPA University Research Initiative (Subagreement P.O. # VB38639-0 with the University of California, Santa Barbara, ONR Prime Contract N00014-86-K-0753 and Subagreement P.O. # KK3007 with the University of California, Santa Barbara, ONR Prime Contract N00014-92-J-1808), the Office of Naval Research (Contract N00014-90-J-1377), and by the Division of Applied Sciences, Harvard University.

REFERENCE

Dundurs, J. and Mura, T. (1964). "Interaction between an edge dislocation and a circular inclusion," J. Mech. Phys. Sol., **12**, pp. 177-189.

Durdurs, J. and Senderky, G.P. (1965). "Edge dislocation inside a circular inclusion," J. Mech. Phys. Sol., **13**, pp. 141-147.

Eshelby, J.D., Read, W.T. and Shockley, W. (1953). Acta Met., **1**, pp. 251-259.

Eshelby, J.D. (1957). Proc. Roy. Soc., A **241**, 376-396.

Gong, S.X. and Meguid, S.A. (1992). "A general treatment of the elastic field of an elliptical inhomogeneity under antiplane shear," ASME Journal of Applied Mechanics, **59**, pp. 131-135

Hwu, C. and Ting, T.C.T. (1989). "Two-dimensional problems of the anisotropic elastic solid with an elliptic inclusion," Mech. appl. Math., **42**, pp. 553-572.

Lekhnitskii, S.G. (1963). "Theory of elasticity of an anisotropic body," Holden-Day, Inc.

Santare, M.H. and Keer, L.M. (1986). "Interaction between an edge dislocation and a rigid elliptical inclusion," ASME Journal of Applied Mechanics, **53**, pp. 382-385.

Stagni, L. and Lizzio, R. (1983). "Shape effects in the interaction between an edge dislocation and en elliptical inhomogeneity," Appl. Phys., **A30**, pp. 217-221.

Stroh, A.N. (1958). Phil. Mag., **7**, pp. 625-646.

Tewary, V.K., Wagoner, R.H. and Hirth, J.P. (1989). "Elastic Green's function for a composite solid with a planar interface," J. Mater. Res., **4**, pp. 113-120.

Warren, W.E. (1983). "The edge dislocation inside an elliptical inclusion," Mechanics of Materials, **2**, pp 319-330.

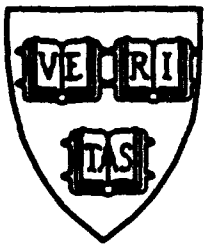

MECH-217

ON THE STRENGTH OF FIBER REINFORCED CERAMIC COMPOSITES CONTAINING AN ELLIPTIC HOLE

Yingqing Lawrence Cui

Division of Applied Sciences
HARVARD UNIVERSITY
Cambridge, Massachusetts 02138

September 1993

ON THE STRENGTH OF FIBER REINFORCED CERAMIC COMPOSITES CONTAINING AN ELLIPTIC HOLE

Yingqing Lawrence Cui
Division of Applied Sciences
Harvard University
Cambridge, MA 02138

ABSTRACT

This paper studies the tensile strength of a fiber reinforced ceramic composite containing a hole. The strength is determined on the basis of a full analysis of matrix cracking in the presence of the hole and the failure of crack bridging fibers. The crack bridging fibers are assumed to undergo large amounts of slipping relative to the matrix and modeled as an array of springs. The dependence of the composite tensile strength on fiber tensile strength, orthotropic parameters, hole size and shape parameters, and frictional shear stress at the fiber-matrix interface is determined and described in terms of a universal set of nondimensional parameters. The effects of compressive residual stress in the fibers upon strength are also discussed.

INTRODUCTION

Fiber reinforced ceramic composites containing through-the-fiber cutouts in the form of notches and circular holes have many design applications. The tensile fracture strength is one of the important mechanical properties of fibrous ceramic composites when either notches or holes are present. It provides information not only necessary for practical design but is also very useful to predict the trends in notch properties. A rigorous understanding of the relationship between such a design limiting feature and the constituent properties is essential for further improvement of the composite. For a brittle unreinforced ceramic containing a hole subjected to uniaxial load, the tensile strength is given as $\sigma_s = \bar{\sigma}/\kappa$, where $\bar{\sigma}$ is the strength of the material in the absence of the hole and κ is the stress concentration factor. However, for a fiber reinforced ceramic, the tensile strength can only be determined by a full analysis of a process involving nucleation of matrix cracking from flaw near the hole or notch boundary, matrix crack growth, frictional sliding of the fiber-matrix interface, and failure of crack bridging fibers.

Although a substantial amount of work has been reported on the mechanical behaviour of unidirectional fiberous composites with or without through-the-fiber cutouts,

these studies mostly deal with either the effects of matrix cracking or fibrous toughening. Relatively less has been done to evaluate the tensile strength of composites with cutouts. A recent effort in this direction has been presented by Budiansky and Cui (1993). They studied the tensile strength of fiber ceramic composites containing a through-the-fiber crack. The dependence of the composite tensile strength on fiber tensile strength, matrix toughness, crack-size, and frictional shear stress at the fiber-matrix interface was determined and described in terms of three basic stress parameters.

Experimental observations show that the tensile strength of fibrous composites containing a circular hole depends on hole size. Such a phenomenon can not be explained on the basis of classical stress concentration factor, which predicts no size effects. The purpose of this paper is to predict the tensile strength of unidirectional fibrous ceramic composites containing holes, and to provide the answer to the question: how does the tensile strength of a unidirectional fibrous ceramic composite containing a hole depend on hole size? We shall study the configuration shown in Fig. 1, where an infinite, two dimensional, aligned-fiber reinforced ceramic body containing an elliptical hole is subjected to uniform remote tension in the fiber direction. More specifically, the major semi-axis of the ellipse is in the direction normal to the direction of fibers and is of length a, and the minor semi-axis of length b is in the direction of fibers. As in most previous studies the fibers are assumed to be held by friction, that is, sliding between the fibers and the matrix is suppressed only if the interface frictional shear is less than some limiting stress τ. The effects of crack bridging fibers are taken into account by means of a spring model. Failure of the composite is assumed to be associated with the growth of a single mode I matrix crack and the fracture of crack bridging fibers. We assume that no longitudinal splitting takes place in the vicinity of hole boundary. Splitting is found to be very effective in relieving the high stress concentration ahead of the tips of cracks or at the boundaries of holes (Cui, 1993a), but we neglect it in the present study. We also assume that there is no statistical variation in fiber strength. In addition, we assume that an initial matrix crack along the direction of the major axis emanates from both poles of the hole before loading is applied.

ORTHOTROPIC PARAMETERS

Consider the plane strain deformation of an orthotropic material. Following Lekhnitskii (1963), if x and y axes are coincident with the principal axes of the material, the Hooke's law for the material can be written as:

$$\varepsilon_{xx} = b_{11}\sigma_{xx} + b_{12}\sigma_{yy} \tag{1}$$

$$\varepsilon_{yy} = b_{12}\sigma_{xx} + b_{22}\sigma_{yy} \tag{2}$$

$$\gamma_{xy} = b_{66}\tau_{xy} \tag{3}$$

It has been shown by Savin (1961) that the general solutions of the above plane strain problem can be expressed in terms of two analytic functions, $\phi(z_1)$ and $\psi(z_2)$ with two complex variables given by $z_1 = x + s_1 y$ and $z_2 = x + s_2 y$. The parameters s_1 and s_2 are the two roots of the algebraic equation

$$b_{11}s^4 + (2b_{12} + b_{66})s^2 + b_{22} = 0 \tag{4}$$

with positive imaginary parts.

In terms of $\phi(z_1)$ and $\psi(z_2)$, the stresses and displacements are given by

$$\sigma_{xx} = 2\mathrm{Re}\left[s_1^2\phi'(z_1) + s_2^2\psi'(z_2)\right] \tag{5}$$

$$\sigma_{yy} = 2\mathrm{Re}\left[\phi'(z_1) + \psi'(z_2)\right] \tag{6}$$

$$\tau_{xy} = -2\mathrm{Re}\left[s_1\phi'(z_1) + s_2\psi'(z_2)\right] \tag{7}$$

$$u_x = 2\mathrm{Re}\left[p_1\phi(z_1) + p_2\psi(z_2)\right] \tag{8}$$

$$u_y = 2\mathrm{Re}\left[q_1\phi(z_1) + q_2\psi(z_2)\right] \tag{9}$$

where Re[ ] denotes the real part of a complex quantity, $\phi' = \dfrac{\partial\phi}{\partial z_1}$, and

$$p_\alpha = b_{11}s_\alpha^2 + b_{12} \quad , \quad q_\alpha = b_{22}/s_\alpha + b_{12}s_\alpha \qquad \alpha = 1,2 \tag{10}$$

After introducing two nondimensional quantities (Suo , 1990)

$$\lambda = b_{11}/b_{22}, \qquad \rho = \left(b_{12} + \frac{1}{2}b_{66}\right)\Big/(b_{11}b_{22})^{\frac{1}{2}} \tag{11}$$

one can express the parameters s_1 and s_2 as

$$s_1 = \frac{i(n+m)}{\lambda^{1/4}}, \quad s_2 = \frac{i(n-m)}{\lambda^{1/4}} \qquad \text{for } \rho > 1 \tag{12}$$

where

$$n = \sqrt{\frac{1+\rho}{2}} \quad , \quad m = \sqrt{\frac{\rho-1}{2}} \tag{13}$$

For ceramic composites, both λ and ρ are generally greater than 1. We therefore will only consider the case $\rho > 1$ and $\lambda > 1$ in this paper.

It is useful to introduce another orthotropic parameter. For a Mode I crack lying along the x-direction, the energy release rate can be expressed in terms of stress intensity factor K_I as (Suo, 1990)

$$G = nb_{22}\lambda^{1/4}K_I^2 \tag{14}$$

On the other hand, by introducing an orthotropic factor, A, (Budiansky and Amazigo, 1989), one can write

$$G = \frac{1-\nu^2}{AE}K_I^2 \tag{15}$$

where E is the Young's module in the fiber direction, and ν is the Poisson's ratio of the

composite. It follows from (14) and (15) that

$$A = \frac{1-\nu^2}{nEb_{22}\lambda^{1/4}} \tag{16}$$

For an aligned fiber composite with matrix Young's module E_m, fiber Young's module E_f, and fiber volume concentration c_f, if we ignore the difference between the Poisson's ratios of the fibers and the matrix ($\nu_f = \nu_m = \nu$), the Young's module E of the composite is given by the role of mixture formula $E = c_f E_f + (1-c_f)E_m$. The dependence of the nondmensional orthotropic parameters A, λ, and ρ on E_f, E_m, and c_f for $\nu_f = \nu_m$ may be calculated on the basis of the Hill (1965) self-consistent estimates. The results for A vs. c_f have been presented in the work of Budiansky and Cui (1993). Plotted in Fig. 2 is the results of λ vs. c_f for various values of E_f/E_m. Fig. 3 shows ρ for serval values of E_f/E_m. It is seen that for reasonable values of E_f/E_m, both λ and ρ are greater than but not far from 1. However, it is important to note that the above calculations are under the assumption that fibers and matrix are bounded together perfectly. Since the fiber-matrix interface is assumed to undergo large amounts of debonding and sliding in the present analysis, the orthotropic effects, as represented by the parameters λ, ρ, and A, may have been seriously underestimated.

REVIEW OF THE RESULTS FOR A CRACK LIKE FLAW

In the absence of through the fiber flaws, if we ignore the statistical variations in the fiber tensile strength, the tensile strength of a unidirectional fiber composite in the fiber direction is simply the base fibers only strength, $c_f S$. When a tensile stress σ is applied to a unidirectional ceramic composite in the fiber direction, failure due to a preexisting, through the fiber crack always begins with the growth of the crack in the matrix and ends with the fracture of crack bridging fibers. Due to stress concentration at the oringial flaw tips, the bridging stress at the flaw tip is always the maximum. This nonuniformity in bridging stress distribution causes bridging fiber at original flaw tip to fracture at a remote load less than $c_f S$. According to Budiansky and Cui (1993), the ratio of the tensile strength, σ_s, to $c_f S$ under the degrading influence of a crack of length 2a takes the following nondimensional form:

$$\frac{\sigma_s}{c_f S} = F\left(\overline{a_0}, \frac{\sigma_{mc}}{c_f S}\right) \tag{17}$$

where σ_{mc} is the steady-state matrix cracking stress, and $\overline{a_0}$ is a nondimensional flaw index given by

$$\overline{a_0} = \alpha\left[\frac{a\tau}{RS}\right] \tag{18}$$

Here

$$\alpha = \frac{6\pi\left(1-\nu^2\right)c_f E E_f}{A\left(1-c_f\right)^2 E_m^2} \tag{19}$$

The results in the form of (17) have been summarized in Fig. 4. Note that the flaw index $\overline{a_0}$ is independent of the matrix toughness K_m. For a fixed value of the parameter $\overline{a_0}$, changing values of $\sigma_{mc}/c_f S$ reflects changing values of K_m. The curve for $\sigma_{mc}/c_f S = 0$, corresponding to $K_m = 0$, is of special interest. For $K_m = 0$, the matrix crack will crack out to infinity as soon as loa ' is applied, and then the strength is given by the critical load required to produce fiber fracture at oringinal flaw tip for a configuration of two semi infinite elastic blocks connected by bridging fibers, except for the crack of length 2a. As indicated in Fig 4, the results for $K_m = 0$ provide not only a lower bound but also a fairly good approximation to the strength, since only modest increases above this value are obtained for reasonable finite values of $\sigma_{mc}/c_f S$. Suo et al (1993) have done similar calculations on the basis of Dugdale and linear type bridging laws and developed a unified representation for strength over a wide range of bridging laws via energy concepts.

FORMULATION AND ANALYSIS

Encouraged by previous findings on through-the-fiber crack, we further assume that the matrix toughness, K_m, is zero. Under this assumption, the preexisting matrix cracks (see Fig. 1) will crack out to infinity as soon as load is applied, as discussed in the previous section. The strength of the composite therefore equals the strength of the fully cracked configuration shown in Fig. 5.

The analysis of the stress concentration problem illustrated in Fig. 5 is now taken up. We smear out the fibers and the matrix, and treat the composite as a homogeneous orthotropic solid. The mechanics problem can be stated as foliows:

Denote the net normal and shear traction by N(x,y) and S(x,y); the boundary conditions for the open hole are

$$S(x,y) = 0 \qquad N(x,y) = 0 \quad \text{on the hole boundary} \quad \frac{x^2}{a^2} + \frac{y^2}{b^2} = 1 \tag{20}$$

The boundary condition on the matrix crack faces is

$$\sigma_{yy}(x,0) = p(x) \qquad a < |x| < \infty \tag{21}$$

where p(x) is the smeared-out stress on the crack faces induced by bridging fibers, and p(x) must be connected appropriately to the crack-face displacement. As in previous studies the crack bridging fibers are modeled as an array of springs, and the smeared-out

bridging fiber stress p(x) is related to the crack-opening displacement v(x) by

$$p(x) = \beta\sqrt{v(x)} - \sigma_R \tag{22}$$

where σ_R is the compressive residual stress imposed by the matrix upon the fibers and the spring constant β is given as

$$\beta = \left\{ \frac{4c_f^2 E_f E^2 \tau}{R(1-c_f)^2 E_m^2} \right\}^{\frac{1}{2}} \tag{23}$$

The relation (22) follows from the assumption that the frictional resisitance at the fiber matrix interface is low enough to permit long slip lengths adjacent to the matrix crack faces compared with the fiber diameter, as elaborated by Aveston et al (1971); Budiansky et al (1986); Budiansky and Amazigo (1989); Hutchinson and Jenson (1991).

The matrix cracks may be regarded as continuously distributed dislocations:

$$b_y(x) = \lim_{\varepsilon \to 0} \left[\frac{\partial v(\varepsilon, x)}{\partial x} - \frac{\partial v(-\varepsilon, x)}{\partial x} \right] \qquad a \le |x| \le \infty \tag{24}$$

The above boundary value problem may be solved by superposing two states of plane-strain orthotropic elasticity for an infinite body with an elliptic hole, with the stress free conditions on the hole boundary automatically satisfied, produced as follows:

(i) apply the uniform remote loading $\sigma_{yy} = \sigma^{\infty}$.

(ii) subject the matrix crack to the distributed dislocations $b_y(x)$, given by (24).

For each problem, we shall calculate the normal stress $\sigma_{yy}(0,x)$. The superposition of the solutions of the two problems should satisfy the boundary condition (22) on the matrix crack faces.

Problems (i) and (ii) may be readily handled by the complex-stress-potential method introduced in the previous section in conjunction with a conformal mapping technique. The mapping functions

$$z = \omega(\varsigma) = \frac{a-b}{2}\varsigma + \frac{a+b}{2}\frac{1}{\varsigma} \tag{25}$$

$$z_\alpha = \omega_\alpha(\varsigma) = \frac{a+is_\alpha b}{2}\varsigma + \frac{a-is_\alpha b}{2}\frac{1}{\varsigma} \qquad \alpha = 1,2 \tag{26}$$

map the areas outside ellipses in z=x+iy, $z_\alpha = x + s_\alpha y$ $(\alpha = 1,2)$ planes into the areas inside unit circles in ς, ς_1, ς_2 planes respectively. The stress potentials for problem (i) have been given by Savin (1961) as

$$\phi^{\infty}(\varsigma_1) = \frac{a\sigma^{\infty} s_2}{2(s_1 - s_2)}\varsigma_1 \tag{27}$$

$$\psi^{\infty}(\varsigma_2) = -\frac{a\,\sigma^{\infty} s_1}{2(s_1 - s_2)}\varsigma_2 \tag{28}$$

The longitudinal stress on the matrix crack plane due to the uniform remote tension in the presence of an elliptic hole, calculated on the basis of (27) and (28), is

$$\sigma_{yy}^{(i)} = \frac{\sigma^{\infty}}{2m} F(x/a, \rho, e) + \sigma^{\infty} \tag{29}$$

where $e = b/\left(a\lambda^{1/4}\right)$, and the function F is listed in Appendix A.

The solution of problem (ii) may be written on the basis of the fundamental plane-strain solution for a single dislocation interacting with an open hole. The stress potentials for an edge dislocation with Burgers vectors b_y at a point (x_0, y_0) in an infinite orthotropic body are

$$\phi_0(z_1) = A\ln(z_1 - z_{10}) \qquad z_{10} = x_0 + s_1 y_0 \tag{30}$$

$$\psi_0(z_2) = B\ln(z_2 - z_{20}) \qquad z_{20} = x_0 + s_2 y_0 \tag{31}$$

where

$$A = -\frac{B_y}{\lambda^{1/4}(m+n)}, \quad B = \frac{B_y}{\lambda^{1/4}(n-m)} \tag{32}$$

with

$$B_y = \frac{b_y}{16\pi mnb_{22}} \tag{33}$$

In the presence of an open hole, the stress potentials of an edge dislocation may be constructed by writing ϕ^d and ψ^d in the form

$$\phi^d = \phi_0 + \phi_h \quad , \quad \psi^d = \psi_0 + \psi_h \tag{34}$$

The stress potentials ϕ_h and ψ_h have been derived by Cui (1993b). In terms of B_y, these potentials can be cast into the form

$$\phi_h = F_{1y}(z_1, z_{10}, z_{20})B_y \tag{35}$$

$$\psi_h = F_{2y}(z_2, z_{10}, z_{20})B_y \tag{36}$$

The F functions are listed in Appendix B. Integrating ϕ^d and ψ^d over the two matrix cracks (see Fig. 5), one obtains the stress potentials for the problem (ii).

It follows from (34)---(36) that the longitudinal stress on the matrix crack plane due to the dislocation array is

$$\sigma_{yy}^{(ii)}(x) = \frac{1}{4\pi n\lambda^{1/4} b_{22} a} \int_a^{\infty} G(x/a, t/a, \rho, e) \frac{\partial v(t)}{\partial t} dt \tag{37}$$

The function G is also listed in Appendix A. In terms of the orthotropic factor A introduced earlier, Eq. (37) can be written as

$$\sigma_{yy}^{(ii)}(x) = \frac{AE}{4\pi\left(1-\nu^2\right)a} \int_a^{\infty} G(x/a, t/a, \rho, e) \frac{\partial v(t)}{\partial t} dt \tag{38}$$

The sum of (29) and (38) gives the crack-face stress p(x) to be substituted into the

condition (22), which becomes

$$\frac{AE}{4\pi(1-\nu^2)a}\int_a^{\infty} G(x/a,t/a,\rho,e)\frac{\partial v(t)}{\partial t}dt+\frac{\sigma^{\infty}}{2m}F(x/a,\rho,e)+\sigma^{\infty}=\beta\sqrt{v(x)}-\sigma_R \quad (39)$$

The above integral equation may be nondimensionalized by introducing the non-dimensional quantities

$$\xi=x/a,\quad \eta=t/a,\quad \overline{v(\xi)}=v(x)/v_f,\quad \Sigma=\sigma^{\infty}/(c_fS),\quad \Sigma_R=\sigma_R/(c_fS) \quad (40)$$

where

$$v_f=\frac{(c_fS)^2}{\beta^2} \quad (41)$$

The resulting nondimensionalized equation may be written as

$$\frac{3}{8\overline{a_0}}\int_1^{\infty} G(\xi,\eta,\rho,e)\frac{\partial\overline{v(\eta)}}{\partial\eta}d\eta+\frac{\Sigma}{2m}F(\xi,\rho,e)+\Sigma=\sqrt{\overline{v(\xi)}}-\Sigma_R \quad (42)$$

Here the nondemsional flaw size parameter, $\overline{a_0}$, has the same definition as it does in Eq. (17). Note that at $x=\infty$, the stress in the bridging springs should be equal to the stress σ^{∞} applied remotely. Thus the nondimensional displacement of the upper face of the matrix crack is given by (see Fig. 5)

$$\overline{v(\infty)}=\frac{\beta^2 v(\infty)}{(c_fS)^2}=\frac{(p(\infty)+\sigma_R)^2}{(c_fS)^2}=\left(\frac{\sigma^{\infty}+\sigma_R}{c_fS}\right)^2=(\Sigma+\Sigma_R)^2 \quad (43)$$

Now consider fiber fracture that leads to the overall failure of the composite. Note that the smeared-out bridging stress distribution p(x) always achive a maximum value p(a) at the intersection of the hole boundary and the matrix crack. Therefore first fiber fracture occurs when the condition

$$p(a)=c_fS \quad (44)$$

is satisfied. In terms of crack bridging displacement, this condition takes the following nondimensional form:

$$\overline{v(1)}=(1+\Sigma_R)^2 \quad (45)$$

In addition, we have found that the failure process of crack bridging fibers is an unstable process. In orther words, the first-fiber-failure results in the failure of all bridging fibers in the matrix crack plane, and therefore the separation of the composites. Consequently, we conclude that the critical remote stress corresponding to first-fiber-failure, denoted as $\sigma^{\infty}=\sigma_s$, is the maximum load the flawed composite can carry and is therefore the strength of the composite.

Equations (42), (43), and (45) suggest that the solution for the tensile strength depends on the nondemensonal flaw size parameter $\overline{a_0}$, the orthotropic parameter ρ, the

shape parameter e, the fiber strength, and the residual stress σ_R. In terms of nondimensional variables, the strength σ_s, nondimensionlized by the base fibers only strength, $\Sigma_s = \sigma_s/(c_f S)$, takes the following form:

$$\Sigma_s = f(\overline{a_0}, \rho, e, \Sigma_R) \tag{46}$$

RESULTS AND DISCUSSIONS

On the basis of discussions described in the previous sections, we now present the final results for the strength σ_s. The results will be presented in terms of the nondimensional representation (46). The physical implications of the representation will be discussed in full details. In the discussions that follow, the results for zero residual stress is presented first. The effects of residual stress are then disscussed. We start with the special case of a very large hole.

For the case of a very large hole, the relaxation effects of crack bridging fibers upon stress concentration is negligible, the strength can be extracted from the stress concentration factor. The stress concentration factor is

$$\kappa = 1 + 2n\lambda^{1/4}\frac{a}{b} \tag{47}$$

which may be obtained by substituting Eqs. (27) and (28) into (5).

When a composite contains a very large hole, the bridging stress at the intersection of matrix cracks and the hole boundary corresponding to the failure of the composite may be well approximated by $p(a) \approx \sigma_s \kappa$. Setting $p(a_0) = c_f S$, one obtains

$$\sigma_s = \frac{c_f S}{\kappa} \tag{48}$$

Therefore the tensile strength for aligned fibrous ceramic composites containing a very large hole equals the strength of the composite in the absence of the hole divided by the stress concentration factor κ. Note that result (48) is valid regardless of the presence of compressive residual stress in the bridging fibers.

We now present the strength in the form of (46). Consider first the case of $\sigma_R = 0$. Fig. 6 shows how the strength $\sigma_s/(c_f S)$ varies with the size of the ellipse, for several values of parameter e, and $\rho = 1$. The curve for e=0, corresponding to the special case of a through-the-fiber crack, reproduces the curve for $\sigma_{mc}/(c_f S) = 0$ in Fig. 4. At a fixed value of $\overline{a_0}$, the curves in Fig. 6 should be interpreted as displaying the effects of the

aspect ratio b/a on the strength σ_s. For small values of $\overline{a_0}$, the strength is little influenced by the aspect ratio. However, at $\overline{a_0} = 25$, as b/a is increased from 0 to $\lambda^{1/4}$, the strength is increased by about 60%. Note that at $\overline{a_0} = 0$, $\sigma_s = c_f S$. The results presented in Fig. 6, displaying the ratio $\sigma_s/(c_f S)$ as the dependent variable, provide the answer to the question: how much has the base fibers only strength, $c_f S$, been reduced under the degrading influnce of a hole?

To give strength σ_s over a full range of the sizes of the ellipse, we present the results in terms of $1/\sqrt{\overline{a_0}}$. Plotted in Fig. 7 are the results of $\sigma_s/c_f S$ vs. $1/\sqrt{\overline{a_0}}$, for $\rho = 1$ and several values of the parameter e. Note that at $1/\sqrt{\overline{a_0}} = 0$, which corresponds to the case $\overline{a_0} = \infty$, the strength is $\sigma_s/c_f S = 1/\kappa$, as discussedd earlier. This result may be obtained by taking the limit $\overline{a_0} \to \infty$ in the governing equation (42) and then making use of Eq. (43). This limit has been defined as the notch-brittle regime of the composite (Suo et al, 1993). The salient feature of Fig. 6 is that it shows how the ductility of a composite increases with the parameter $1/\sqrt{\overline{a_0}} = \alpha^{-1/2}[RS/(a\tau)]^{1/2}$. It is clear that regardless of the values of the aspect ratio $b/(a\lambda^{1/4})$ the ductility increases with increasing values of R and S, but decreases with increasing values of a and τ. An inspection of Fig. 4 indicates that as $1/\sqrt{\overline{a_0}} = \alpha^{-1/2}[RS/(a\tau)]^{1/2}$ is increased from 0 to 1 the enhancement of ductility decreases with the increasing values of the aspect ratio $b/(a\lambda^{1/4})$.

Now consider the effects of ρ. Note that the orthotropic factor A depends on the parameter ρ, and so does the parameter $\overline{a_0}$. Substitution of (16) and (19) into the expression of $\overline{a_0}$ leads to

$$\frac{\overline{a_0}}{n} = \frac{6\pi c_f E^2 E_f \lambda^{1/4} b_{22}}{(1-c_f)^2 E_m^2}\left(\frac{a\tau}{RS}\right) = \beta\left(\frac{a\tau}{RS}\right) \tag{49}$$

Therefore the quantity $\overline{a_0}/n$ is independent of the parameter ρ. Thus it is more useful to plot the strength $\sigma_s/(c_f S)$ as a function of $\overline{a_0}/n$ rather than as a function of $\overline{a_0}$. Shown in Fig. 8 are the results of $\sigma_s/(c_f S)$ vs. $\overline{a_0}/n$, for $b/a\lambda^{1/4} = 1$, and several values of ρ. At a fixed value of $\overline{a_0}/n$, it is seen that the strength decreases with increasing values of ρ.

The tensile strength σ_s also depends on the residual stress parameter, σ_R. The effects of compressive residual stresss in the fibers upon the tensile strength σ_s are shown in Fig. 9 and Fig. 10 for $\rho = 1$, and various values of the nondimensional parameter $\sigma_R/(c_f S)$, with $b/a = 0$ and $b/a = \lambda^{1/4}$ respectively. These Figs. clearly indicate that compressive residual stresses in the fibers enhance the tensile strength of flawed composits. An inspection of Fig. 9 and Fig.10 suggests that the enhancement for a through the fibers crack is greater than for a circular hole of the same size. Note that at

both $\overline{a_0} = 0$ and $\overline{a_0} \to \infty$, the strength of the composites is independent of residual stresses. The maximum enhancement always occurs at a finite value of the size parameter $\overline{a_0}$.

Finally, it is important to note that for a through-the-fiber crack the strength obtained under the assumption $K_m = 0$ constitutes a lower bound of this property, and that finite values of K_m in the practical range provide only modest increases over this bound. The same conclusion can be made for the case of holes. Therefore the solution obtained in this paper is a fairly good approximation of the strength of unidirectional ceramic composites with holes.

ACKNOWLEDGMENT

The author is very grateful to Professor Bernard Budiansky for many useful discussions and for reading the manuscript. This work was partially supported by the DARPA University Research Initiative (Subagreement P.O. # VB38639-0 with the University of California, Santa Barbara, ONR Prime Contract N00014-86-K-0753 and Subagreement P.O. # KK3007 with the University of California, Santa Barbara, ONR Prime Contract N00014-92-J-1808), the Office of Naval Research (Contract N00014-90-J-1377), and by the Division of Applied Sciences, Harvard University.

REFERENCES

Aveston, J., Cooper, G.A. and Kelly, A. (1971). "The properties of fiber composites," pp. 15-26. Conference proceedings, National Physical Laboratory, Guildford. IPC Science and Technology Press Ltd.

Budiansky, B. and Amazigo J C. (1989). "Toughening by aligned, frictionally constrained fibers," J. Mech. Phys. Solids. **37**, pp 93-109.

Budiansky, B and Cui, Y.L. (1993). "On the tensile strength of a fiber-reinforced ceramic composite containing a crack-like flaw," J. Mech. Phys. Solids. *in press.*

Budiansky, B., Hutchinson, J.W. and Evans, A.G. (1986). "Matrix fracture in fiber-reinforced ceramics," J. Mech Phys Solids **34**, pp 167-189.

Cui, Y. L. (1993a). "Mechanics of splitting in orthotropic materials," Submitted to Int. J. of Solids and Structures.

Cui, Y. L. (1993b). "An elliptical inclusion in an anisotropic plane," Submitted to J. Appl. Mech.

Erdogan, F., and Gupta, G.D. (1972). "On the numerical solution of singular integral equations," Quart. Appl. Math. **29**, 525-534.

Hill, R. (1965). "Theory of mechanical properties of fiber-strengthened materials: III. Self

consistent model," J. Mech. Phys. Solids **13**, pp 189-198.

Hutchinson, J.W. and Jensen, H.M. (1990). "Models of fiber debonding and pullout in brittle-composites with friction," Mech. Mater. **9**, 139-163.

Lekhnitskii, S.G. (1981). Theory of Elasticity of an Anisotropic Body. Mir Publishers, Moscow.

Savin, G.N. (1961). "Stress concentration around holes," Pergamon Press Ltd.

Sih, G. C., Paris, P. C., and Irwin, G. R., (1965). "On Cracks in Rectilinearly Anisotropic Bodies," Int. J. Fracture Mech. **1**, pp. 189-203.

Suo Z. (1990). "Delamination specimens for orthotropic materials," J. Appl. Mech. **57**, pp 627-634

Suo, Z., Ho, S. and Gong X. (1992). "Notch ductile-to-brittle transition due to localized inelastic band," ASME J. Engr. Mat. Tech. **115**, pp 319-326

APPENDIX A

In this Appendix, we list the functions used in Eqs. (29) and (37). The function F is

$$F(x/a,\rho,e)=\frac{(n-m)}{1-(n+m)e}F_1-\frac{(n+m)}{1-(n-m)e}F_2 \tag{A1}$$

where

$$F_1=1-\frac{x/a}{\sqrt{(x/a)^2-1+(n+m)^2e^2}} \tag{A2}$$

and

$$F_2=1-\frac{x/a}{\sqrt{(x/a)-1+(n-m)^2e^2}} \tag{A3}$$

With the use of the following expressions:

$$\varsigma_\alpha=\frac{x/a-\sqrt{(x/a)^2-1+s_\alpha^2e^2}}{1-s_\alpha e} \qquad \alpha=1,2 \tag{A4}$$

$$\eta_{\alpha1}^0=\frac{t/a+\sqrt{(t/a)^2-1+s_\alpha^2e^2}}{1-s_\alpha e} \qquad \alpha=1,2 \tag{A5}$$

$$\eta_{\alpha2}^0=\frac{t/a+\sqrt{(t/a)^2-1+s_\alpha^2e^2}}{1+s_\alpha e} \qquad \alpha=1,2 \tag{A6}$$

$$Dx_\alpha=-\frac{\varsigma_\alpha}{\sqrt{(x/a)^2-1+s_\alpha^2e^2}} \qquad \alpha=1,2 \tag{A7}$$

$$SA=\frac{s_2}{\varsigma_1-\eta_{11}^0}-\frac{ns_2}{(\varsigma_1-\eta_{12}^0)m}+\frac{1}{m(\varsigma_1-\eta_{22}^0)} \tag{A8}$$

$$SB=\frac{s_2}{\varsigma_1+\eta_{11}^0}-\frac{ns_2}{(\varsigma_1+\eta_{12}^0)m}+\frac{1}{m(\varsigma_1+\eta_{22}^0)} \tag{A9}$$

$$SC=-\frac{s_1}{\varsigma_2-\eta_{21}^0}-\frac{ns_1}{(\varsigma_1-\eta_{22}^0)m}+\frac{1}{m(\varsigma_1-\eta_{12}^0)} \tag{A10}$$

$$SD=-\frac{s_1}{\varsigma_2+\eta_{21}^0}-\frac{ns_1}{(\varsigma_1+\eta_{22}^0)m}+\frac{1}{m(\varsigma_1+\eta_{12}^0)} \tag{A11}$$

where $s_1=n+m$ and $s_2=n-m$, the function G can be expressed as

$$G(x/a,t/a,\rho,e)=\frac{2}{x/a+t/a}-\frac{2}{x/a-t/a}-\frac{(SA-SB)Dx_1+(SC-SD)Dx_2}{m} \tag{A12}$$

APPENDIX B

In this Appendix, we list the stress functions used in Eqs. (35) and (36) in the text. With the use of the following expressions

$$\varsigma_\alpha = \frac{z_\alpha - \sqrt{z_\alpha^2 - a^2 - s_\alpha^2 b^2}}{a + is_\alpha b} \quad \alpha = 1,2 \tag{B1}$$

$$\eta_{\alpha 1}^0 = \frac{z_\alpha^0 + \sqrt{(z_\alpha^0)^2 - a^2 - s_\alpha^2 b^2}}{a + is_\alpha b} \quad \alpha = 1,2 \tag{B2}$$

$$\eta_{\alpha 2}^0 = \frac{\bar{z}_\alpha^0 + \sqrt{(\bar{z}_\alpha^0)^2 - a^2 - \bar{s}_\alpha^2 b^2}}{a - is_\alpha b} \quad \alpha = 1,2 \tag{B3}$$

$$D\varsigma_\alpha = -\frac{\varsigma_\alpha}{\sqrt{z_\alpha^2 - a^2 - s_\alpha^2 b^2}} \quad \alpha = 1,2 \tag{B4}$$

where $z_\alpha = x + s_\alpha y$, $z_\alpha^0 = x_0 + s_\alpha y_0$, and $\bar{z}$ denotes the complex conjugate of a complex variable z, one can express these functions as follows

$$F_{1y}(z_1, z_{10}, z_{20}) = \lambda^{-\frac{1}{4}}\left[\frac{1}{(n+m)}\ln(\xi_1 - \eta_{11}^0) - \frac{n}{m}\frac{1}{(n+m)}\ln(\xi_1 - \eta_{12}^0) + \frac{1}{m}\ln(\xi_1 - \eta_{22}^0)\right] \tag{B5}$$

$$F_{2y}(z_2, z_{10}, z_{20}) = \lambda^{-\frac{1}{4}}\left[-\frac{1}{n-m}\ln(\varsigma_2 - \eta_{21}^0) - \frac{n}{m(n-m)}\ln(\varsigma_2 - \eta_{22}^0) + \frac{1}{m}\ln(\varsigma_2 - \eta_{12}^0)\right] \tag{B6}$$

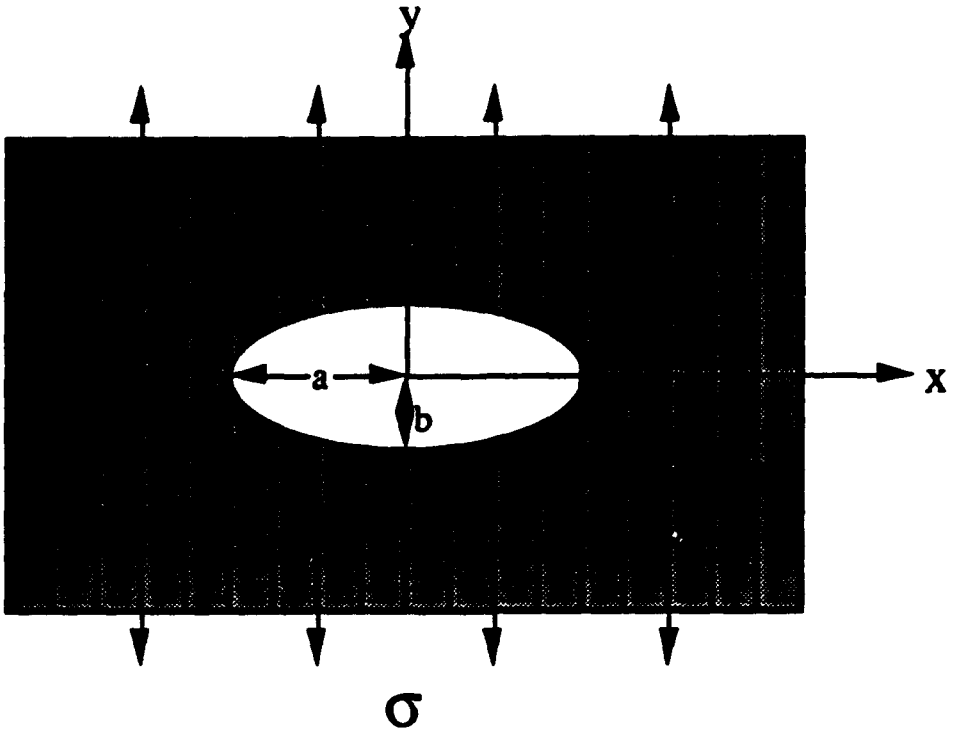

Fig. 1. Problem statement.

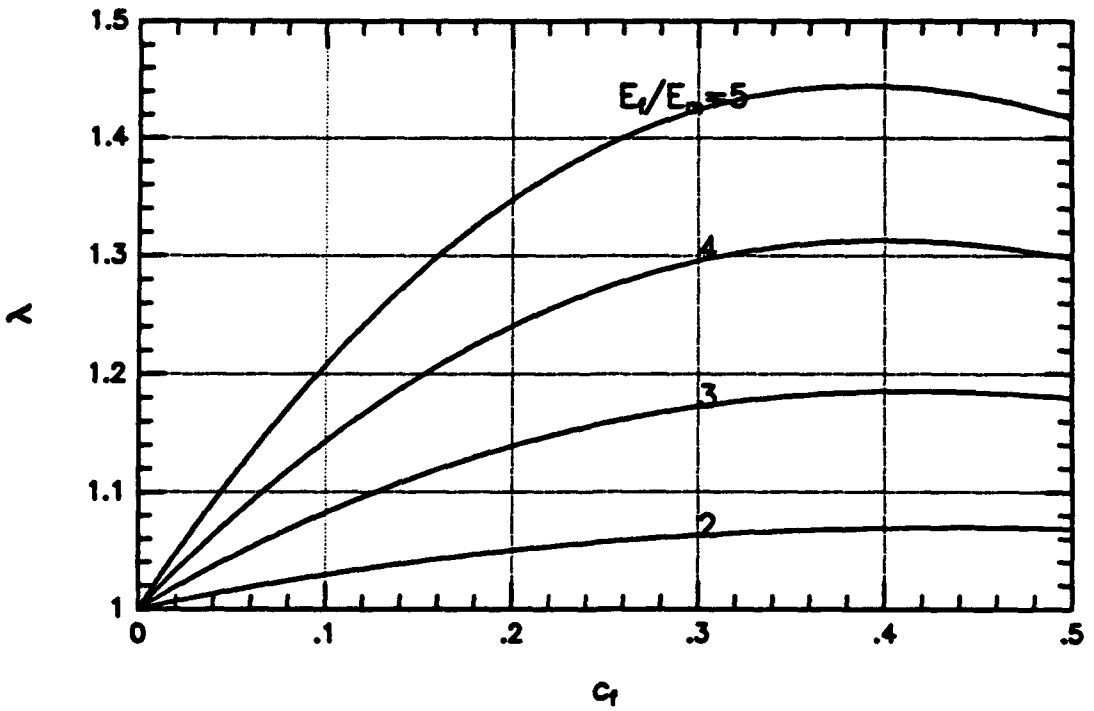

Fig. 2. Orthotropic parameter λ vs. c_f for various values of E_f/E_m.

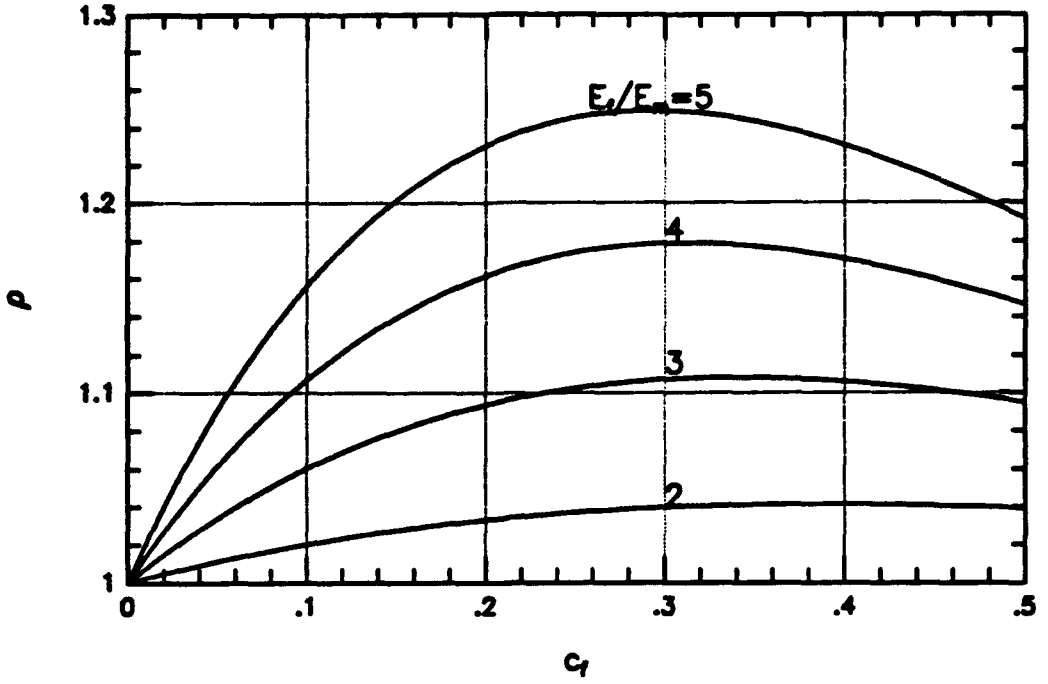

Fig. 3. Orthotropic parameter ρ vs. c_f for various values of E_f/E_m.

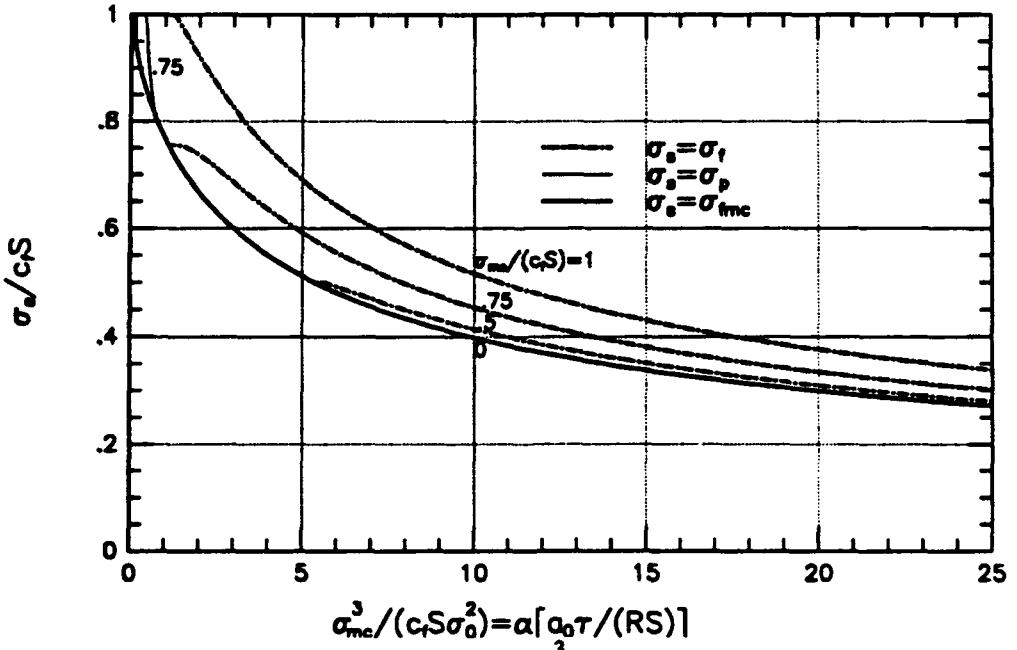

Fig. 4. Strength ratio $\sigma_e/(c_fS)$ vs. $\bar{a}_0 \equiv \frac{\sigma_{mc}^3}{c_fS\sigma_0^2}$ for various values of $\sigma_{mc}/(c_fS)$.

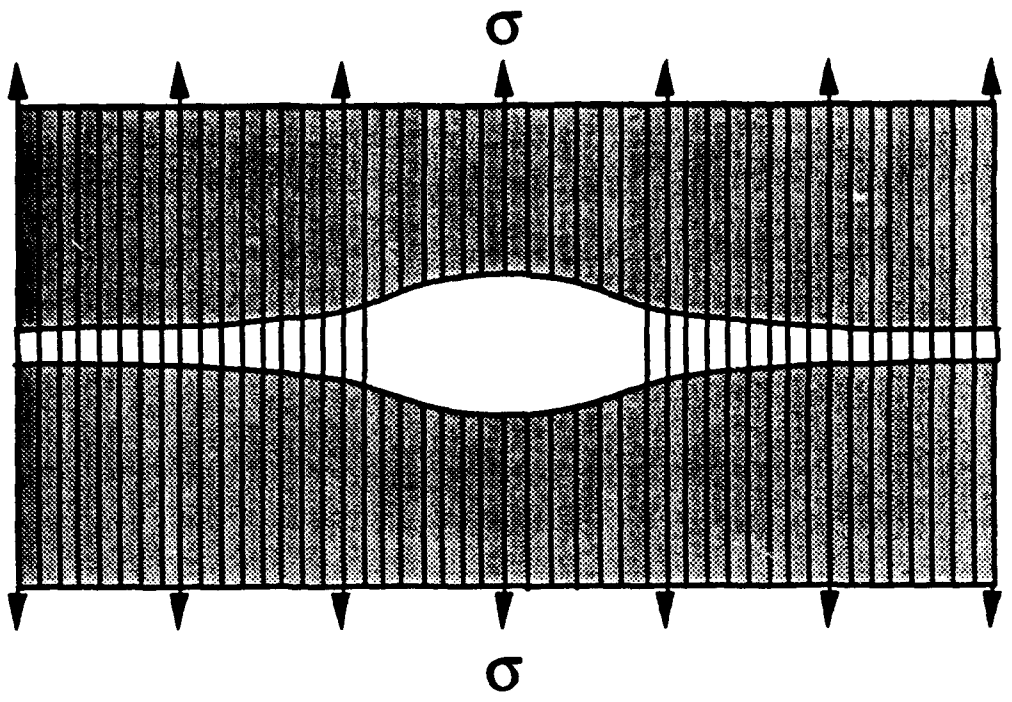

Fig. 5. Fully cracked matrix.

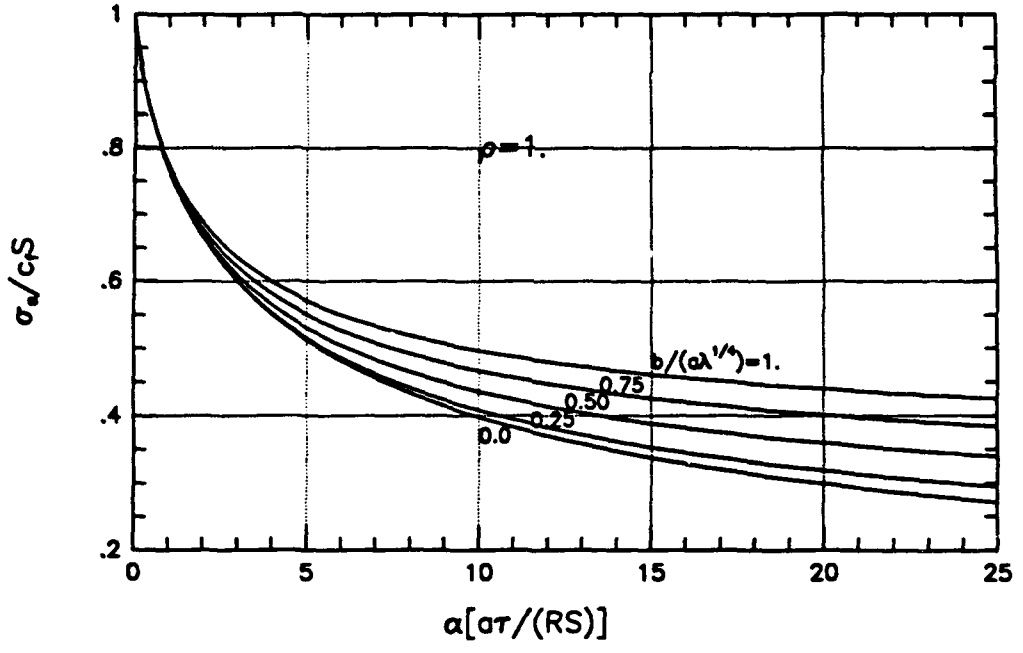

Fig. 6. Strength $\sigma_s/(c_f S)$ vs. $\overline{a_0} = \alpha[a\tau/RS]$ for various values of $b/\left(a\lambda^{1/4}\right)$, with $\sigma_R = 0$.

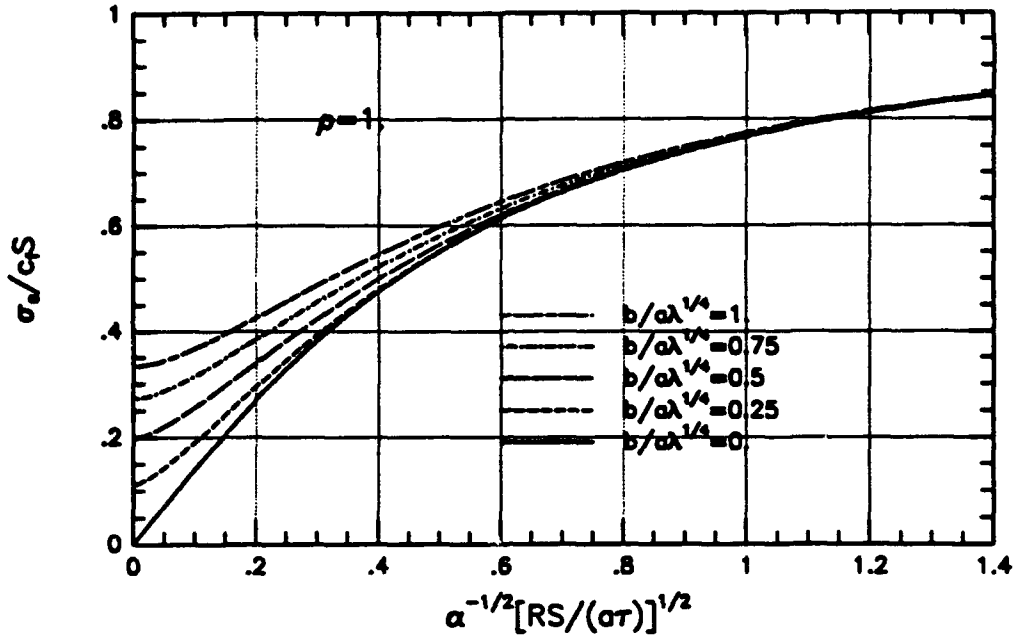

Fig. 7. Strength $\sigma_s/(c_f S)$ vs. $\left(\overline{a_0}\right)^{-1/2} = \alpha^{-1/2}[RS/(a\tau)]^{1/2}$ for various values of $b/\left(a\lambda^{1/4}\right)$, with $\sigma_R = 0$.

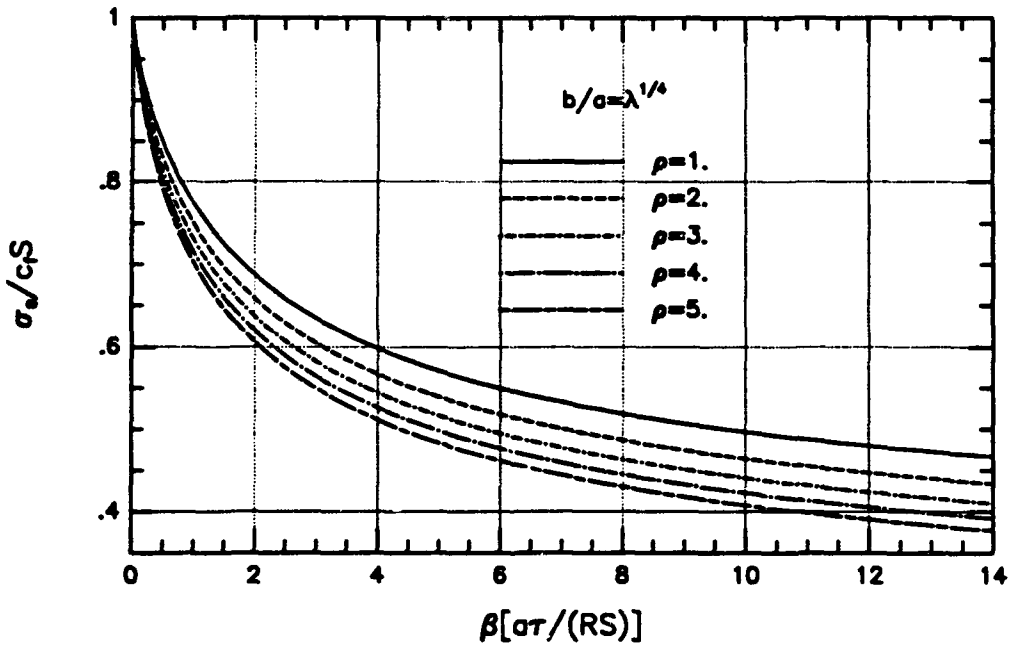

Fig. 8. Strength $\sigma_s/(c_f S)$ vs. $\overline{a_0}/n = \beta[a\tau/RS]$ for various values of ρ, with $\sigma_R = 0$.

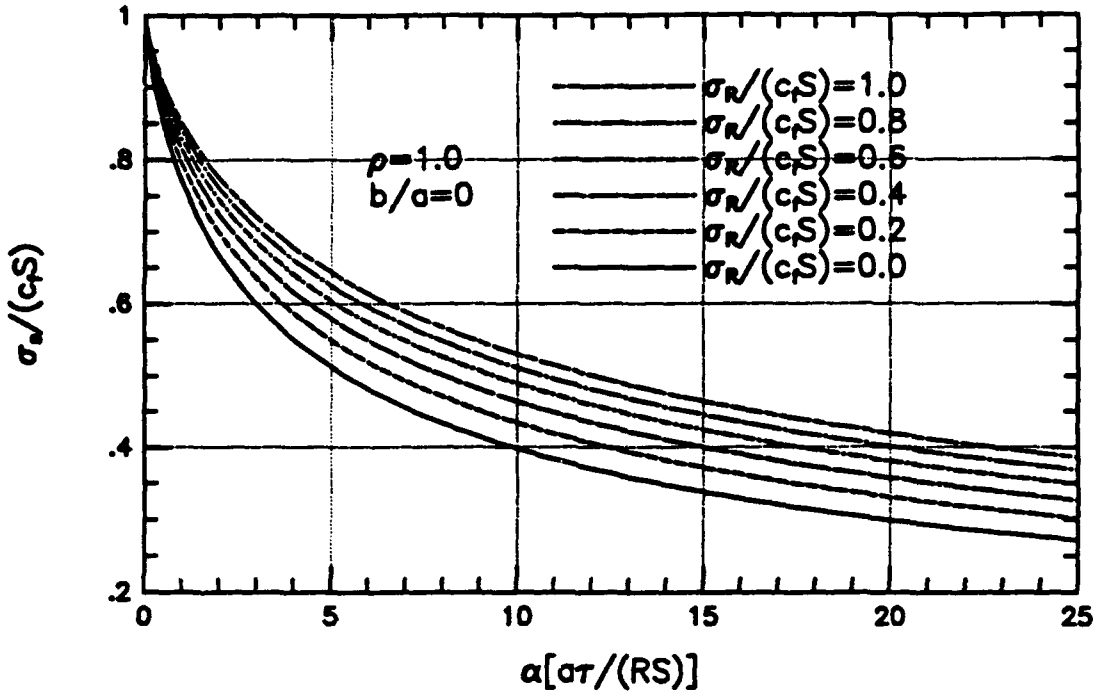

Fig. 9. Strength $\sigma_s/(c_fS)$ vs. $\overline{a_0} = \alpha[a\tau/RS]$ for various values of $\sigma_R/(c_fS)$, with $b/a = 0$.

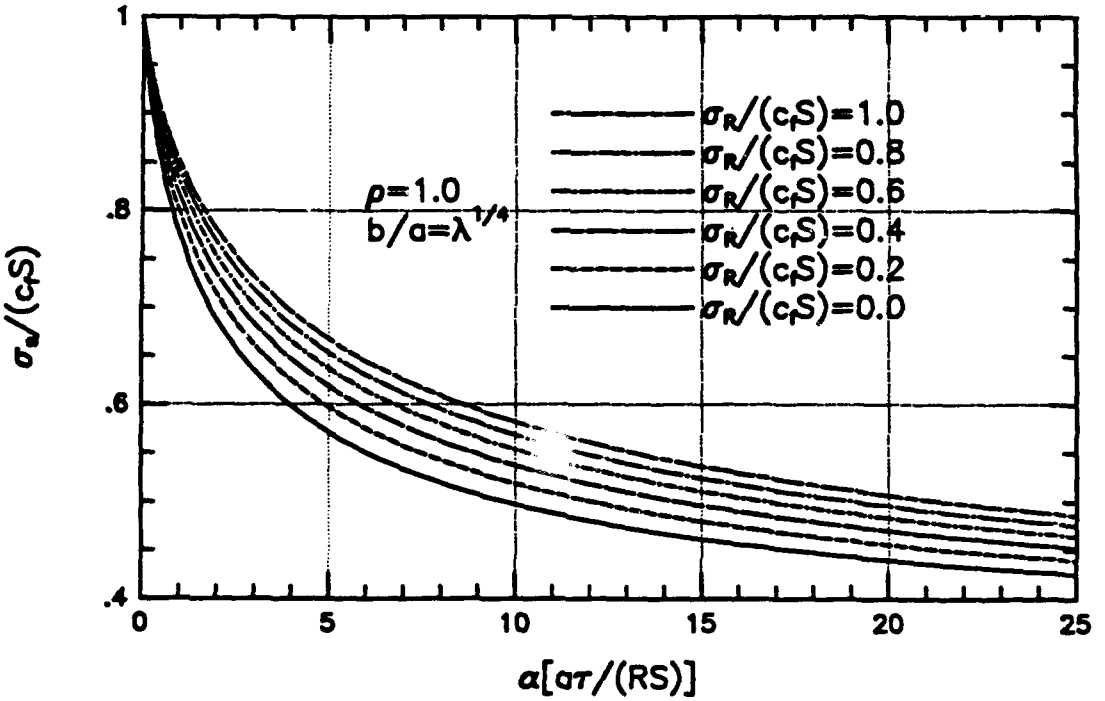

Fig. 10. Strength $\sigma_s/(c_fS)$ vs. $\overline{a_0} = \alpha[a\tau/RS]$ for various values of $\sigma_R/(c_fS)$, with $b/a = \lambda^{1/4}$.

MECH-216

ON THE THEORETICAL TOUGHNESS AND STRENGTH OF CERAMIC COMPOSITES

BERNARD BUDIANSKY

To be published in Proceedings of IUTAM Symposium on Fracture of Brittle Disordered Materials: Concrete, Rock, Ceramics
September 20-24, 1993, Brisbane

Division of Applied Sciences
HARVARD UNIVERSITY
Cambridge, Massachusetts 02138

August 1993

ON THE THEORETICAL TOUGHNESS AND STRENGTH OF CERAMIC COMPOSITES

BERNARD BUDIANSKY
Division of Applied Sciences, Harvard University, Cambridge, Massacusetts, USA

Abstract
Fracture studies of ceramics reinforced by phase-transforming particles, ductile particles, or ceramic fibers are reviewed. The concepts of mode-I fracture toughness and tensile strength of such composites are contrasted. Fracture toughness may be regarded as a material property for a composite only if the fracture process zone is small relative to crack size and representative body dimensions; the strength of a composite as a function of flaws of finite size is a more significant measure of its structural performance. Following descriptions of the individual effects on toughness and strength of each type of reinforcement, the interaction of fibers and transforming particles is discussed. A few more topics in fiber-ceramic composite fracture theory are discussed briefly, including the effects of fiber-matrix debonding toughness, and aligned short fibers. Some final remarks are made on deficiencies of the underlying fracture theory.
Keywords: Ceramics, Composites, Fracture, Toughness, Strength, Micromechanics.

1 Introduction

The low fracture toughness of ceramic materials constitutes the primary barrier to their use in high-temperature structures. Considerable attention has therefore been directed to the development of ceramic composites, in which various kinds of reinforcements toughen and strengthen a ceramic matrix in the presence of flaws.

In this paper, a review is given of the micromechanics of fracture of ceramics reinforced by phase-transforming particles, ductile particles, or ceramic fibers, with the main emphasis on the last of these. A recurrent theme is the distinction between a conventionally defined mode-I fracture *toughness*, which is limited in its applicability to fracture of a ceramic composite with long cracks, for which the fracture process zone is small relative to crack size and other relevant geometrical dimensions, and tensile fracture *strength*, which must be determined independently as a function of finite flaw size. Several special topics concerned with fiber composites will also be addressed briefly.

2 Transformation toughening and transformation strengthening

The seminal paper "Ceramic steel" by Garvie et al (1975) showed that the apparent fracture toughness of a ceramic could be increased by the introduction of tetragonal zirconia (ZrO_2) particles. Based on experimental observations of a tetragonal-to-monoclinic phase transformation of the particles in the wake of a growing crack, many theoretical studies of the so-called transformation toughening of long cracks have since been made. In the most elementary modeling of this phenomenon (e.g., McMeeking and Evans, 1982; Budiansky et al, 1983; Rose, 1986; Amazigo and Budiansky, 1988), a long

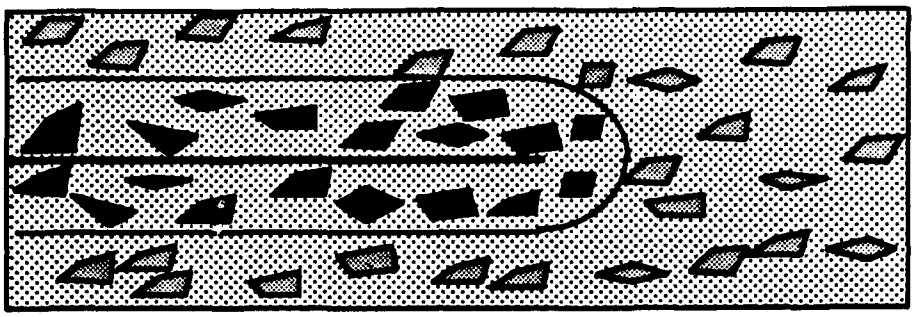

Fig. 1. Zone of transformed particles (black).

crack is presumed to be propagating steadily under an applied, far-field, mode-I stress-intensity-factor (SIF) equal to K (see Fig. 1). The ZrO_2 particles, having a volume concentration c (and possibly containing a dopant that tends to inhibit their transformation), are assumed to undergo phase transformation to the monoclinic state when they experience a mean stress σ_m equal to a critical value σ_m^c. A continuous distribution of permanent volumetric dislocation $c\theta$ is imposed within the transformed zone, where θ is the "stress-free" phase dilatation that would have occurred if the particles were unconstrained. (The tetragonal-to-monoclinic phase change of a free crystal also involves a shear deformation $\gamma \approx .16$, but this is ignored in the continuum analysis, with the excuse that the transformed zirconia inclusions exhibit multiple bands of twinned monoclinicity, so the net shear strain is small.) The location of the transformed region, as well as the magnitude of the applied K, are then determined mathematically when the crack-tip SIF is maintained at the value K_m equal to the toughness of the matrix, assumed to be the same as that of the particles. The consequent value of the toughening ratio K/K_m has been calculated, and its reciprocal is shown by the upper curve in Fig. 2 as a function of the toughening parameter (Budiansky and Amazigo, 1988a)

$$\omega = \left(\frac{1+\nu}{1-\nu}\right)\frac{Ec\theta}{\sigma_m^c} \tag{1}$$

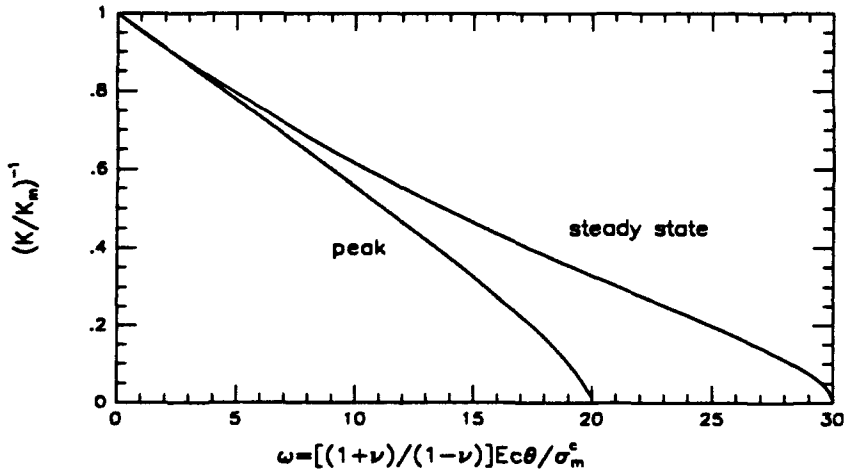

Fig. 2. Reciprocal of transformation-toughening ratio; steady-state and peak.

Here E and ν are Young's modulus and Poisson's ratio, assumed to be the same for the matrix and the particles. Note that the toughening ratio becomes infinite at the "lock-up' value $\omega = 30$; the lock-up phenomenon was discovered by Rose (1986).

In contrast to this steady-state crack growth analysis, the transient growth of an initially long crack was studied by Stump and Budiansky (1989a), with the results for the non-dimensional resistance curves shown in Fig. 3. Here, for several values of ω, K/K_m is plotted versus the crack extension Δa, normalized by the characteristic length

$$L = \frac{2}{9\pi}\left[\frac{K_m(1+\nu)}{\sigma_m^c}\right]^2 \tag{2}$$

Unexpectedly, K/K_m approaches its steady state value in an oscillatory fashion, and so the long-crack toughness is actually given by the peak magnitude K_{max} attained during the approach to steady state. The reciprocals of these peaks are shown as a function of ω in Fig. 2 by the lower curve, which approaches lock-up at $\omega = 20$.

Now consider an isolated 2D crack of initial finite length 2a, subjected to remote tension σ normal to its faces. If the crack is sufficiently long, the tensile strength in the presence of transforming particles is given simply by $\sigma_s = K_{max}/\sqrt{\pi a}$, and since the strength of the unreinforced ceramic is $\sigma_0 = K_m/\sqrt{\pi a}$, the strengthening ratio σ_s/σ_0 would then be the same as the toughening ratio K_{max}/K_m. But for cracks of arbitrary initial size a separate transient crack-growth analysis is needed to determine the strengthening ratio, and this leads to the results in Fig. 4 (Stump and Budiansky, 1989b; Stump, 1991a). The parameter

$$t = \frac{Ec\theta\sqrt{a}}{(1-\nu)K_m} \tag{3}$$

is a measure of the initial crack size, so the curves show how the long-crack toughening ratio becomes increasingly less valid an indicator of transformation strengthening as crack size decreases. For c=.3, values of a in the range .01–1 mm give t roughly between 3 and

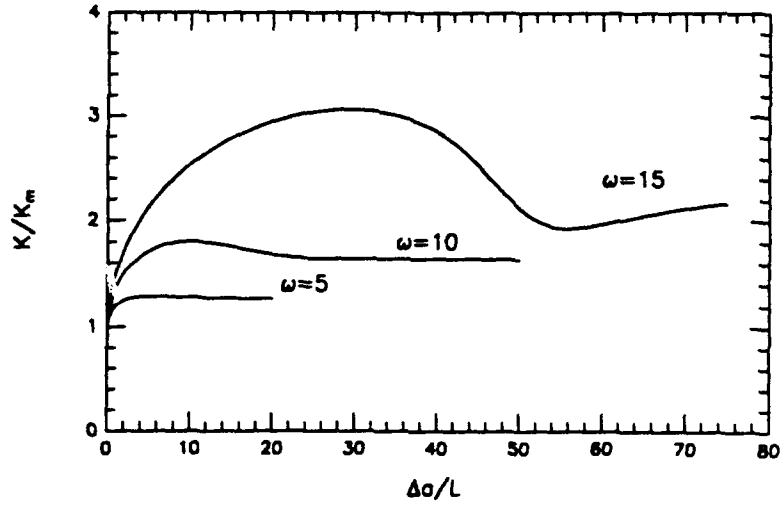

Fig. 3. Long-crack resistance curves.

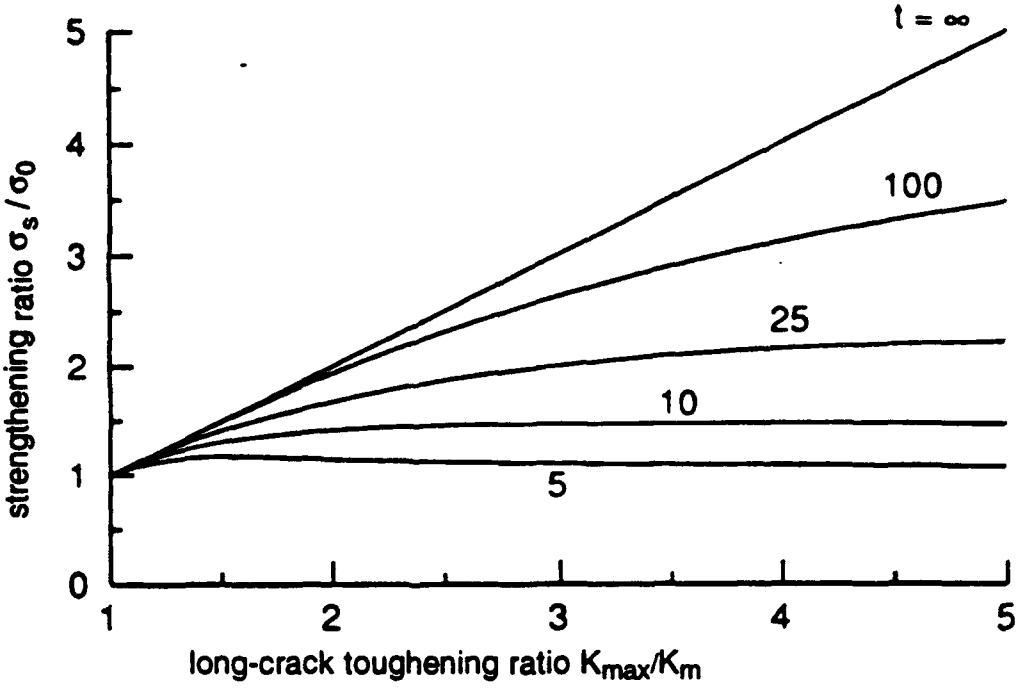

Fig. 4. Transformation strengthening vs. transformation toughening.

30, so a ceramic having only very small flaws would not be helped much by transformation strengthening; but then it might not need help.

This summarizes the consequences of the most primitive form of the theory of transformation toughening, based on an arbitrary, certainly highly oversimplified rule for the stress dependence of the phase changes in the zirconia inclusions. Calculations based on the assumption that shear stresses as well as the mean stress near the crack tip induce a dilatational transformation have recently been made by Stump (1992), with some startling predictions of strangely shaped transformed regions. But reliable rules governing the activation of the phase transformation of zirconia under complex states of stress remain to be established. Budiansky and Truskinovsky (1993) speculate about this.

3 Ductile-particle toughening and strengthening

Ductile particles embedded in a brittle matrix tend to impede crack growth by the mechanism of crack-bridging, but only if the crack is attracted into the particles as it advances, so that they pin together opposite sides of the crack face (Krstic, 1983). Likely requirements for such crack attraction are that the particle stiffness be less than that of the matrix, and that the particle-matrix bond be tough enough to prevent the crack from going completely around the particle through the interface. But the bond should not be *too* good; a certain amount of interface debonding is desirable to permit plastic deformation in the particle that might otherwise tend to be inhibited by the lateral constraint induced by perfect bonding (Mataga, 1989).

Let c be the volume concentration of particles. Fig. 5 shows a sketch of the pinned crack faces near a crack tip; a thought experiment to define crack-face opening displacements as a function of nominal particle tension σ_p; and a schematic sketch of σ_p vs. δ, the local opening *averaged* over the appropriate, local vicinity of the particle. Failure of the particle occurs at $\delta=\delta_F$, with $\sigma_p = 0$ for $\delta>\delta_F$.

Now let E_m and ν_m be the Young's modulus and Poisson's ratio of the matrix, while

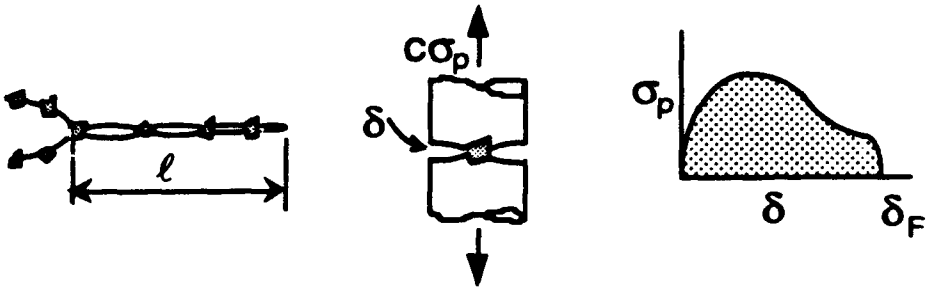

Fig. 5. Particle bridging, and particle stress vs. local crack opening.

E and ν correspond to the homogenized composite. If the critical SIF for the matrix material is K_m, an equivalent critical crack-tip K_c for the composite may be defined by

$$K_c^2(1-\nu^2)/E^2 = K_m^2(1-c)(1-\nu_m^2)/E_m^2 \tag{4}$$

wherein the conventional expression for crack-tip in a homogeneous isotropic material is equated to the energy-release-rate of the growing, bridged matrix crack. The (1-c) factor takes into account the reduced length of the matrix crack edge due to the presence of the bridging particles.

Now contemplate a long, initially unbridged crack subjected to a remote K-field in the homogenized composite. Bridged-crack growth will occur when K exceeds K_c, with the crack-tip SIF of the composite maintained at K_c. If the particle bridging stresses are smeared out along the crack faces, an application of the Rice (1968) J-integral then provides the relation (Budiansky et al, 1988; Sigl et al, 1988)

$$\frac{K^2(1-\nu^2)}{E} = \frac{K_c^2(1-\nu^2)}{E} + c\int_0^{\delta}\sigma_p(\delta')d\delta' \tag{5}$$

between K and the stretch δ at the end of the bridged zone. The maximum value of K is reached for $\delta = \delta_F$, giving the long-crack toughness ratio

$$\Lambda = \frac{K_{max}}{K_c} = \sqrt{1+\frac{cE\int_0^{\delta_F}\sigma_p d\delta}{K_c^2(1-\nu^2)}} \tag{6}$$

This, via Eq. (4), is close to the toughening ratio K_{max}/K_m between the long-crack composite toughness and the toughness of the unreinforced matrix.

Since δ may be expected to scale like the particle size, it follows from Eq. (6) that for a given volume concentration, bigger particles are better, as long as the smeared-out continuum approximation remains valid.

Even though it is not very realistic, an idealized Dugdale law of the form σ_p=S for $0<\delta<\delta_F$ and σ_p=0 for $\delta>0$, provides a basis for some useful insights. For this law, Λ can be related to the particle strength S and the final bridge length by

$$\Lambda = \sqrt{1+\frac{cES\delta_F}{K_c^2(1-\nu^2)}} = 1+\frac{cS}{K_c}\sqrt{\frac{8\ell}{\pi}} \tag{7}$$

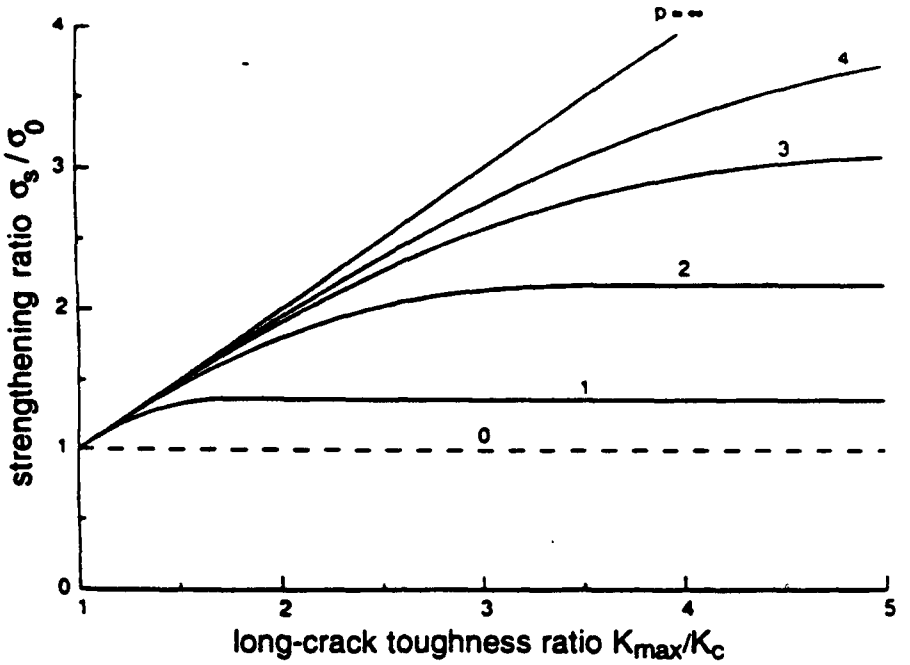

Fig. 6. Ductile-particle strengthening vs. toughening.

Consider the possibility of using the long-crack toughness ratio Λ to estimate the tensile strength of a composite containing an isolated, unbridged 2D crack of length 2a. The crack-growth initiation stress (not too different from the strength of the unreinforced matrix) is $\sigma_0 = K_c/\sqrt{\pi a}$, and if the long-crack toughness ratio is applicable, the strength σ_s would be given by $\Lambda\sigma_0$, and the bridge length at each crack tip would be

$$\frac{\ell}{a} = \frac{\pi^2(\Lambda-1)^2}{8}\left(\frac{\sigma_0}{cS}\right)^2 \tag{8}$$

But the long-crack results are only valid for *small-scale bridging*, wherein the bridge length is small relative to the initial crack length. Thus, the estimate $\sigma_s = \Lambda\sigma_0$ is reliable only if the long-crack toughening ratio, the crack size (via σ_0), and the particle strength S give a sufficiently small value for ℓ/a in Eq. (8).

Some direct calculations of the strengthening ratio based on the Dugdale model were made by Stump (1991). For various magnitudes of the initial crack-size parameter $p=cS/\sigma_0$, the applied stress was tracked versus crack growth, and the strength σ_s of the composite was set either by the attainment of a smooth maximum in the applied stress as the crack grew, or by failure of the particles at the ends of the bridging zones. The results for σ_s/σ_0 are plotted against the long-crack toughening ratio Λ in Fig. 6, and they show that no matter how large Λ may be, σ_s/σ_0 can only get to be comparable to $p=cS/\sigma_0$. For example, with c=.3, K_m=3 MPa$\sqrt{m}$, and a=1mm, $\sigma_0 \approx$ 30 MPa, and so to get the p parameter into the range $p > 2$, ductile particles of strength S greater than 200 Mpa, as well as a toughening ratio $\Lambda > 3$, would be needed.

4 Aligned-fiber toughening and strengthening

Considerable attention has been devoted to the tensile cracking behavior of ceramics

reinforced by long, aligned ceramic fibers. Although such an extremely anisotropic composite would usually be impractical, a theoretical understanding of aligned-fiber composite fracture would appear to be a necessary precursor to the rational design and analysis of the more isotropic laminates or weaves that would probably be exploited. Consider the load-body configuration sketched in Fig. 7a, wherein the infinite, aligned-fiber composite contains a sharp 2D crack of length $2a_0$ that initially cuts through the fibers, and ask the question: what is the tensile strength σ_s? This question received early study from Marshall and Cox (1987), and was given a detailed reexamination recently by Budiansky and Cui (1993), the results of which are summarized here.

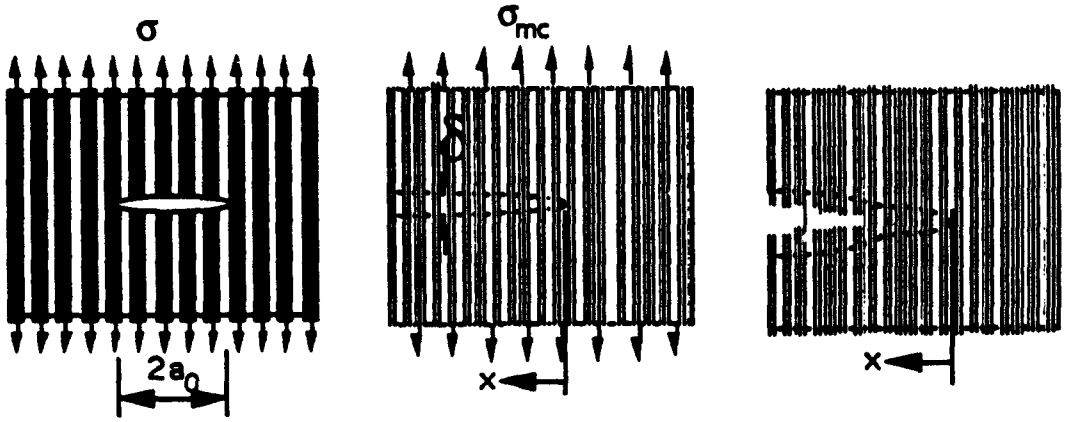

Fig. 7. (a) Through-the-fibers crack. (b) Steady matrix cracking. (c) Long initial crack

The fibers, of radius R and volume concentration c_f, are assumed to be prevented from axial sliding with respect to the matrix by frictional stresses if they do not exceed a limiting value τ. The frictional shear stress is then assumed to stay equal to τ during relative longitudinal motion at the fiber-matrix interface. Initial stresses are ignored for now, as is any interface debonding fracture energy (but more about these later). The axial moduli are E_f, E_m, and E for the fibers, matrix, and homogenized composite, respectively, and the corresponding Poisson's ratios (for the ratios of transverse contraction to longitudinal extension) are ν_f, ν_m, and ν. The matrix fracture toughness is K_m.

The results for σ_s are going to be expressed in terms of three basic stress quantities that characterize the composite. These are:

- $c_f S$, the base fibers-only strength,
- σ_{mc}, the steady-state matrix-cracking stress; and
- σ_0, the critical applied stress for the initiation of matrix cracking in the composite containing the initial through-the-fibers crack.

The first of these, with the fiber strength S considered to be a deterministic quantity, is self-explanatory. The matrix cracking stress σ_{mc} is that required to keep a long matrix crack propagating steadily around and past intact fibers (Fig. 7b), and has the classical value

$$\sigma_{mc} = \left[\frac{6c_f^2\left(1-\nu_m^2\right)K_m^2\tau E_f}{(1-c_f)RE}\right]^{\frac{1}{3}}\frac{E}{E_m} \tag{9}$$

found by Aveston et al (1971); see also Budiansky et al (1986). (A pervasive population of initial matrix cracks grows into many closely spaced long matrix cracks throughout an aligned-fiber ceramic composite at stresses in vicinity of σ_{mc}.) The formula (9) is based on the assumption that the slip length along the fibers is large relative to R.

The stress σ_0 at which a through-the-fibers crack starts to grow into the matrix is

$$\sigma_0 = K_c/\sqrt{\pi a_0} \tag{10}$$

where now K_c, the critical SIF for the homogenized, orthotropic composite, satisfies

$$K_c^2(1-\nu^2)/(AE^2) = K_m^2(1-c)(1-\nu_m^2)/E_m^2 \tag{11}$$

Here A is an orthotropy factor, somewhat smaller than unity (see Budiansky et al, 1993). Note that σ_0 should be fairly close to the strength $K_m/\sqrt{\pi a_0}$ of the unreinforced matrix containing a crack of the same size.

The determination of the strength of the initially flawed composite of Fig. 7a follows from a detailed study of the history of the applied stress and the fiber stress at the original crack tip during matrix crack growth, as well as subsequent to growth of the matrix crack all the way through the material. But first, as in the earlier studies of this review, we can determine the toughness associated with a very long initial crack (Fig. 7c). The constraining effects of fibers bridging the crack are represented by springs that relate the locally smeared-out fiber stress p to the crack-face opening displacement δ=2v according to the law

$$p(x) = \beta\sqrt{v(x)} \tag{12}$$

where

$$\beta = \left\{\frac{4c_f^2E_fE^2\tau}{R(1-c_f)^2E_m^2}\right\}^{\frac{1}{2}} \tag{13}$$

Equivalently,

$$\delta = \left(\frac{3K_c^2(1-\nu^2)}{AE}\right)\left(\frac{p^2}{\sigma_{mc}^3}\right) \tag{14}$$

This is consistent with the analyses of Aveston et al (1971), Budiansky et al (1986), and Budiansky and Amazigo (1989). Suppose that a far-field $K=K_{max}$ keeps the configuration of Fig. 7c propagating with a tip SIF in the composite equal to K_c, while simultaneously the last bridging fibers are fracturing at $p=c_fS$; then a J-integral (analogous to the one used in Eq. (5) for bridging particles) gives

$$\frac{K_{max}^2(1-\nu^2)}{AE} = \frac{K_c^2(1-\nu^2)}{AE} + \int_0^{p=c_fS} p(\delta)d\delta \tag{15}$$

Hence the long-crack toughening ratio is simply (Budiansky and Amazigo (1989)

$$\Lambda = \frac{K_{max}}{K_c} = \sqrt{1+2\left(\frac{c_fS}{\sigma_{mc}}\right)^3} \tag{16}$$

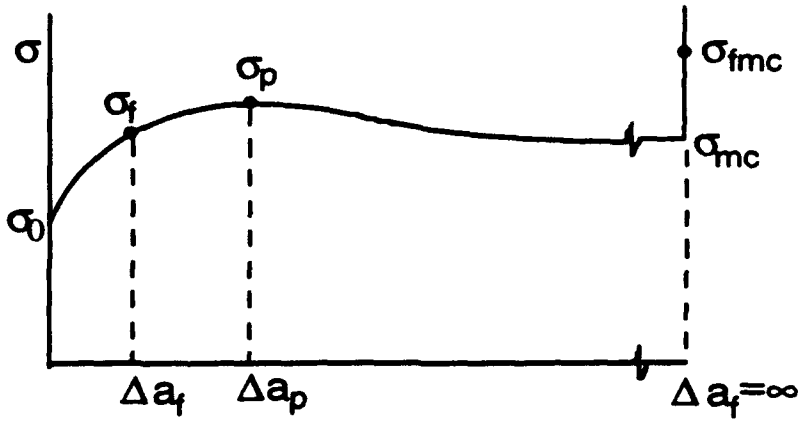

Fig. 8. Applied stress vs. matrix crack growth.

Note that the toughening ratio increases as the matrix cracking stress decreases; thus, for a fixed fiber volume fraction, lowering the frictional resistance τ, or increasing the fiber radius R, raises the toughening ratio. Again, as in the earlier toughening studies, the strength ratio σ_s/σ_0 equals Λ only for sufficiently long initial cracks.

The history of matrix crack growth in the case of an initial through-the-fibers crack of finite size is sketched schematically in Fig. 8, on the assumption that fiber failure does not occur. The curve of σ vs. Δa, the matrix crack growth from each end of the original crack, approaches the classical matrix cracking stress σ_{mc} as the matrix crack grows to

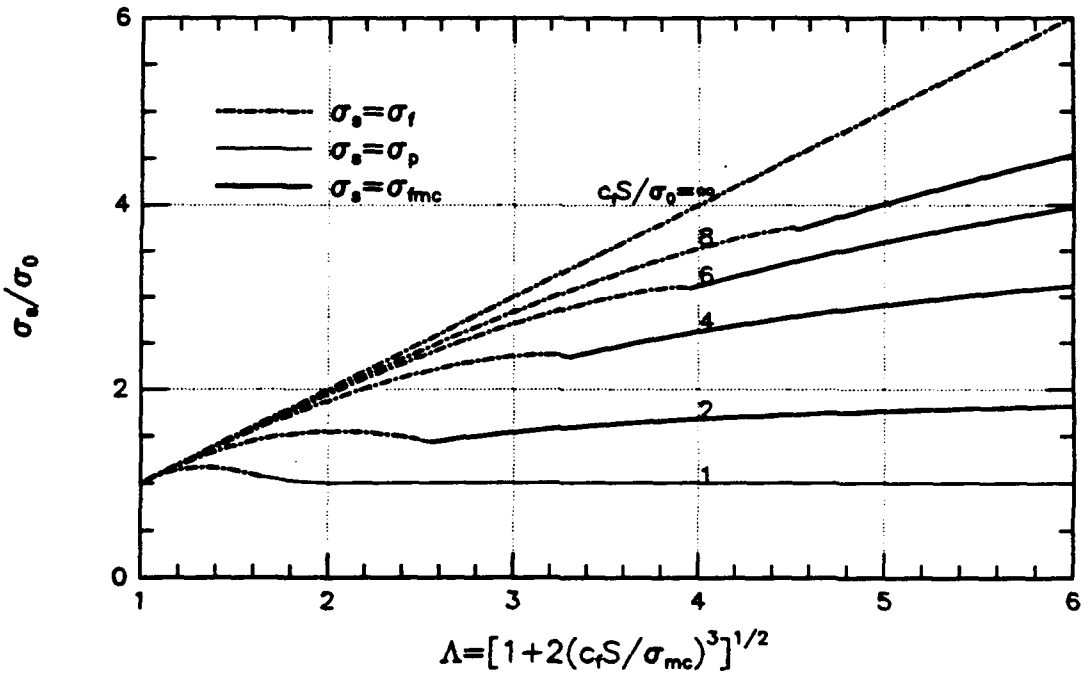

Fig. 9. Modified strengthening ratio σ_s/σ_0 for various values of c_fS/σ_0.

infinity. The strength σ_s of the composite corresponds to one of three distinguished stresses along the curve: if fiber failure at the original crack tip occurs for $\sigma=\sigma_f$ before a local peak σ_p is reached, then $\sigma_s=\sigma_f$; if the matrix crack gets to infinity without fiber failure, but then, with further loading, fiber failure occurs at $\sigma=\sigma_{fmc}$, where $\sigma_{fmc}>\sigma_p$, then $\sigma_s=\sigma_{fmc}$; otherwise, $\sigma_s=\sigma_p$.

Crack growth histories and fracture strengths have been determined from numerical solutions of an integral equation (Budiansky and Cui, 1993a) based on the spring model, with results for the strength ratio σ_s/σ_0 versus the long-crack toughening ratio Λ shown in Fig. 9, for various values of the crack-size parameter c_fS/σ_0. The failure mode that determined σ_s is indicated by the key to the varying line-type of the curves; except for the very smallest cracks (i.e., values of σ_s/σ_0 less than 2) σ_p defines failure in only tiny ranges between σ_f and σ_{fmc}. As expected, σ_s/σ_0 is well approximated by Λ for large values of c_fS/σ_0; estimates of the effects of the sizes of various parameters on the strength ratio are readily made from the information in Fig. 9. In contrast to most ductile particles, fiber strengths can be of the order of 2 GPa, so c_fS/σ_0 can get to be high (e.g., larger than 8) even for cracks in the 100 μm range.

The results in the ranges where σ_s is given by σ_{fmc}, the failure stress after the matrix is fully cracked, are of particular interest. Here the failure strength does not depend on the fracture toughness of the matrix, and comes from the solution of the auxiliary problem of the strength of two half-spaces connected by springs outside of the region of the original crack. Because of the concentration of bridging stress at the original crack tips, this strength is necessarily smaller than c_fS. This suggests that an alternative point of view might be appropriate for assessing the strength of the composite: rather than asking how much the matrix material is strengthened by fiber reinforcement, determine the extent

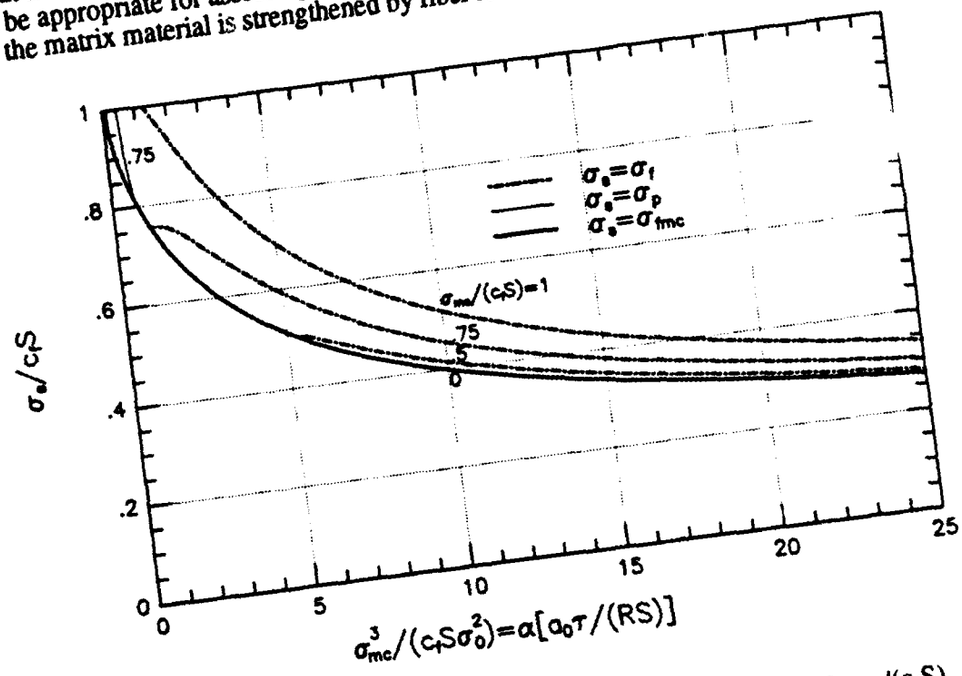

Fig. 10. Strength ratio $\sigma_s/(c_fS)$ vs. $\bar{a}_0 \equiv \dfrac{\sigma_{mc}^3}{c_fS\sigma_0^2}$ for various values of $\sigma_{mc}/(c_fS)$.

to which σ_s differs from the fibers-only strength c_fS in the presence of an initial flaw. Accordingly, the results of Fig. 9 have been replotted in Fig. 10, wherein, for various values of the parameter $\sigma_{mc}/(c_fS)$, the ratio $\sigma_s/(c_fS)$ is shown as a function of the crack-size parameter

$$\bar{a}_0 \equiv \frac{\sigma_{mc}^3}{c_f S \sigma_0^2} = \alpha\left[\frac{a_0\tau}{RS}\right] \tag{17}$$

where

$$\alpha = \left[\frac{6\pi(1-\nu^2)c_f E E_f}{A(1-c_f)^2 E_m^2}\right] \tag{18}$$

The bottom curve, for $\sigma_{mc}=0$, is actually the result for $\sigma_{fmc}/(c_fS)$, which is the strength ratio not only in the case of zero matrix toughness, but also in all ranges of $\bar{a}_0$ and $\sigma_{mc}/(c_fS)$ for which σ_s is defined by σ_{fmc}. (For example, $\sigma_s = \sigma_{fmc}$ for $\sigma_{mc}/(c_fS)$ between .5 and .75, and $\bar{a}_0$ between 2 and 5.) Clearly, σ_{fmc} constitutes a lower bound to σ_s, and a fairly close one except for extremely small crack sizes.

For large values of $\bar{a}_0$, the long-crack toughening formula (16) and the relation $\sigma_s \approx \Lambda\sigma_0$ provide the asymptotic approximation (quite accurate for $\bar{a}_0 > 25$)

$$\frac{\sigma_s}{c_f S} \approx \sqrt{\frac{2+(\sigma_{mc}/c_f S)^3}{\bar{a}_0}} \tag{19}$$

These strength predictions are not very cheerful. For silicon carbide (SiC) fibers in a calcium-alumino-silicate (CAS) matrix, and the nominal numbers c_f=.4, R=7 μm, τ=20 MPa, and S=2 GPa (suggested by A.G. Evans, private communication) we find that $\sigma_s/(c_fS)$ would be only around 1/3 for a crack of length $2a_0$=2 mm. A similar estimate for SiC/SiC composites, with τ=150 MPa, gives $\sigma_s/(c_fS) \approx 1/10$. But, as we shall see in the remarks at the end of this review, several idealizations underlying the present theory of aligned-fiber composite fracture may be quite conservative. Furthermore, it has not yet been decreed as a design requirement that composites *should* be able to tolerate through-the-fiber flaws of a particular size.

4 Addenda

4.1 Interactive effects of fibers plus transforming particles

In principle, two or more of the reinforcement types discussed can be combined, for whatever advantages doing so may provide. Becher and Tiegs (1987) studied experimentally the toughening effects of a combination of ZrO_2 particles plus whiskers; and several theoretical papers have been published on the combined effects of transforming and ductile particles (Amazigo and Budiansky, 1988b; Stump, 1991). Here we mention the results of two more recent analyses of the interacting effects of aligned fibers and transforming particles.

If steady state matrix cracking of an aligned-fiber composite is contemplated (Cui and Budiansky, 1993), the addition of a volume concentration c_t of transforming particles increases the steady state matrix-cracking stress from σ_{mc}^0 to a larger value σ_{mc}, as shown in Fig. 11. Here the ratio $\sigma_{mc}/\sigma_{mc}^0$ is plotted against the long-crack, steady-state

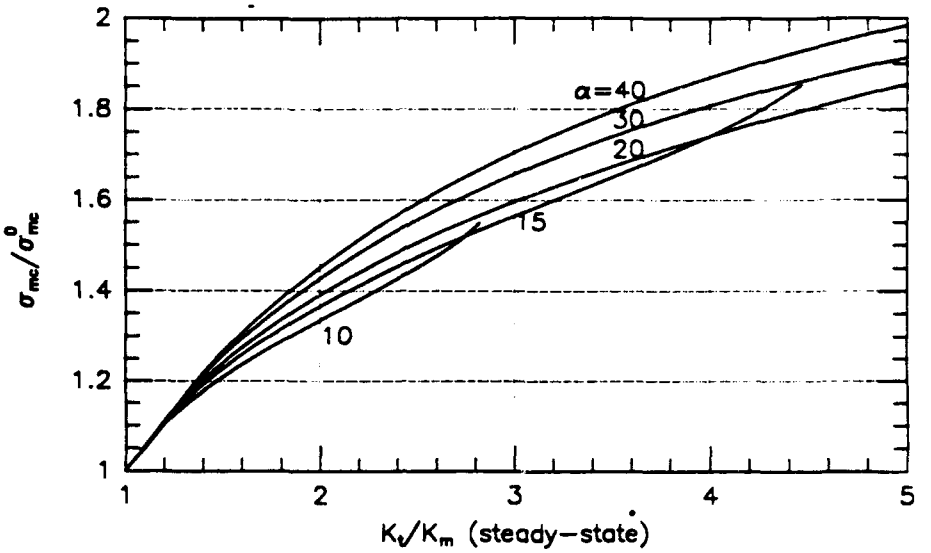

Fig. 11. Matrix-cracking stress ratio vs. steady-state transformation-toughening ratio; $\alpha = c_t\theta/[(1-\nu)\varepsilon_{mc}^0]$, where $\varepsilon_{mc}^0 = \sigma_{mc}^0/E$.

transformation-toughening ratio K_t/K_m that would be provided by the particles alone. The parameter α on the individual curves is defined by $\alpha = c_t\theta/[(1-\nu)\varepsilon_{mc}^0]$, where $\varepsilon_{mc}^0 = \sigma_{mc}^0/E$ is the original matrix cracking strain due to just the fibers. (In the analysis, moduli differences among matrix, fibers, and transforming particles were ignored, and any change in the sliding resistance τ that might be induced by the dilating particles was also neglected.) Evidently, only modest increases in the cracking stress would be produced by a sprinkling of zirconia.

With the same simplifying assumptions, Cui (1992) also studied interaction effects on long-crack toughening. Here a key parameter is $\rho = (1+\nu)c_f S/\sigma_m^c$, and Cui found that for $\rho \to \infty$, the combined toughening ratio becomes simply the product of the toughening ratio K_{max}/K_m given by Eq. (16) for the fibers alone, and the steady-state transformation-toughening ratio K_t/K_m (Fig. 2) due to just the particles. Further, numerical calculations showed that for $K_{max}/K_m < 4$, this limiting result is well approximated for $\rho > 2$.

4.2 Fiber-matrix debonding toughness and residual stress

Potentially significant effects on both the matrix cracking stress and toughening in an aligned-fiber composite are provided by residual stresses as well as debonding toughness $\mathcal{G}_D$ at the fiber-matrix interface, acting in addition to the frictional sliding resistance τ. A current study by Budiansky et al (1993), based on a simplified version of the analyses by Hutchinson and Jensen (1990), provides the results in Fig. 12 for matrix cracking. The quantity σ_D, the remote applied stress needed to initiate debonding at a crack-bridging fiber, is given by

$$\sigma_D = \sqrt{\frac{4c_f^2 E_f E \mathcal{G}_D}{(1-c_f)E_m R}} \qquad (20)$$

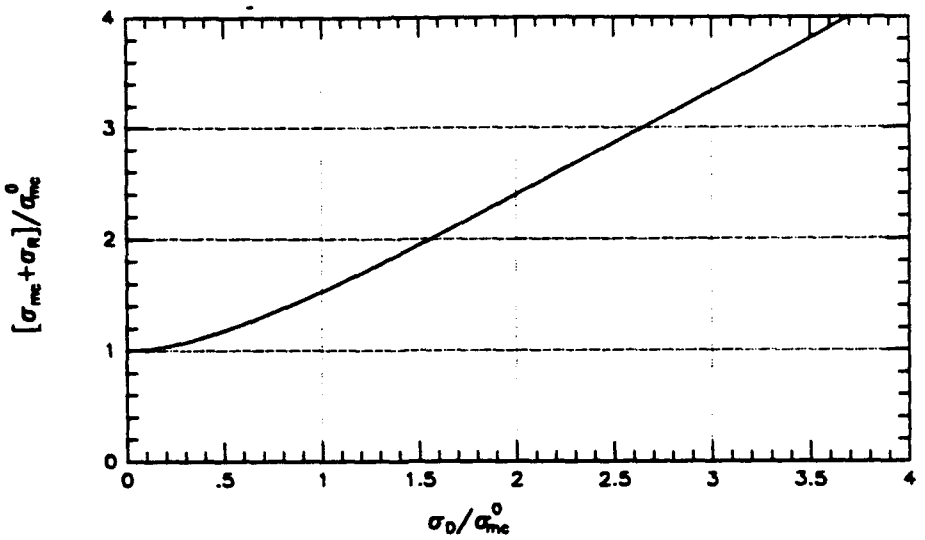

Fig. 12. Influence of debonding toughness and initial stress on matrix cracking stress.

and σ_R is an initial stress quantity defined by $(E/E_m)\sigma_m^I$, where σ_m^I is the initial longitudinal stress in the matrix. As before, σ_{mc}^0 is the base matrix cracking stress (9).

Estimates of the ratio σ_D/σ_{mc}^0 for SiC/CAS and SiC/SiC configurations currently under study are in the range .6 – .9, implying a modest effect of debonding toughness on matrix cracking; but initial stress effects can be important.

4.3 Fiber-strength statistics, pullout, and toughening

At least passing reference should be made here to the important studies by Thouless and Evans (1988) and Sutcu (1989), who observe that because the fiber strength S is actually a stochastic property, fibers may fail at various locations within the matrix rather than at the crack faces where each fiber stress is a maximum. Then, even if the average strength of the fibers is lowered by the strength dispersion, their toughening effects may increase substantially because of the additional energy (see Eq. (15)) needed to pull the fractured fibers out of the matrix. In this sense, worse is better! It remains to be seen whether a reliance on toughening that depends on a guaranteed nonuniformity of strength will find engineering acceptability.

4.4 Aligned short fibers

Instead of depending on fiber strength dispersion to get interior fiber fractures, why not try to use randomly arrayed, but aligned short fibers whose length is so chosen that pullout will occur before fracture, no matter where along their axes a propagating matrix crack intersects them. The largest fiber length that ensures pullout is ℓ_f=SR/τ, and for this length the average pullout work is much bigger than that given by the long-fiber integral in Eq. (15). For the case K_m=0, an elementary calculation provides the simple long-crack approximation

$$\frac{\sigma_s(\text{short fiber})}{\sigma_s(\text{long fiber})} = \frac{E}{2(1-c_f)E_m}\sqrt{\frac{1}{\varepsilon_f}} \quad \text{for } a_0 \to \infty \tag{21}$$

in terms of the fiber fracture strain $\varepsilon_f = S/E_f$, assumed to be the same for the short and long fibers. Although this strength ratio is big, more detailed calculations (Budiansky and Cui, 1993b) indicate less spectacular chopped-fiber improvements in strength at finite crack lengths in the millimeter range. Furthermore, short fibers may induce strength *degradation* at smaller crack sizes. For K_m=0, it is clear that for fibers of the critical length ℓ_f, $\sigma_s \to c_f S/2$ for $a_0 \to 0$, in contrast to the limit $c_f S$ (see Fig. 10) for long fibers. So, besides the processing questions that arise, it is not yet clear whether aligned chopped-fiber composites merit preference over long fibers of the same strength. But short fibers (or whiskers) having intrinsic strengths superior to those of long fibers, and endowed with well-tailored lengths and interfaces, could be very attractive.

5 Critiques of the aligned-fiber micromechanical model for fracture

There are at least two ways in which the bridging-fiber/brittle-matrix model may be seriously deficient, leading to unduly pessimistic strength estimates. First, in the analysis of the fiber stresses associated with the matrix crack growing out of an initial through-the-fibers crack , the possibility of multiple matrix cracking, and consequent changes in effective composite properties, have been ignored. This could be particularly important if inclined matrix cracks driven by shear as well as tension in the vicinity of the last bridging fibers at the original crack tip lead to concentrated shearing deformations that would tend to reduce the fiber stress concentration . The material could then be relatively notch insensitive (Evans et al, 1993).

Further, the spring model for bridging fibers is really based on the presumption that the neighbors of an individual fiber share essentially the same stress environment. But this is not consistent with the high lateral fiber-stress gradients near the most highly loaded fibers. Current calculations (Hutchinson and Xia, unpublished) based on a more realistic model of the fiber-matrix interaction at the matrix crack face predict substantially smaller fiber stress concentrations, and hence higher strengths, than those of the spring model.

6 Acknowledgments

This work was partially supported by an ARPA University Research Initiative (Subagreement P.O. #KK3007 with the University of California, Santa Barbara, ONR Prime Contract N00014-92-J-1808) and by the Division of Applied Sciences, Harvard University.

7 References

Amazigo, J.C. and Budiansky, B. (1988) Steady-state crack growth in supercritically transforming materials. **Int. J. Solids Structures**, 24, 751-755.

Aveston, J., Cooper, G.A. and Kelly, A. (1971) Single and multiple fracture, in **The Properties of Fiber Composites**, Proc. National Physical Laboratory, Guildford, IPC Science and Technology, U.K., pp. 15-26.

Budiansky, B., Amazigo, J.C., and Evans, A.G. (1988) Small-scale crack bridging and the fracture toughness of particulate-reinforced ceramics. **J. Mech. Phys. Solids**, 36, 167-187.

Budiansky, B. and Amazigo, J.C. (1989). Toughening by aligned, frictionally constrained fibers. **J. Mech. Phys. Solids**, 37, pp 93-109.

Budiansky, B. and Cui, Y.L. (1993a) On the tensile strength of a fiber-reinforced ceramic composite containing a crack-like flaw. **J. Mech. Phys. Solids**, in press.

Budiansky, B. and Cui, Y.L. (1993b) Toughening of ceramics by short aligned fibers. To be published.

Budiansky, B., Evans, A.G. and Hutchinson, J.W. (1993) Fiber-matrix debonding effects on cracking in aligned-fiber ceramic composites. To be published.

Budiansky, B., Hutchinson, J.W. and Evans, A.G. (1986) Matrix fracture in fiber-reinforced ceramics. **J. Mech Phys Solids, 34**, 167-189.

Budiansky, B., Hutchinson, J.W. and Lambropoulos, J.C. (1983) Continuum theory of dilatant transformation toughening in ceramics. **Int. J. Solids Structures, 19**, pp 337-356.

Budiansky, B., and Truskinovsky, L. (1993) On the mechanics of stress-induced phase transformation in zirconia. **J. Mech Phys. Solids**, 41, 1445-1459.

Cui, Y.L. (1992) Interaction of fiber and transformation toughening. **J. Mech Phys. Solids**, 40, 1837-1850.

Cui, Y.L.,and Budiansky, B. (1993) Steady-state matrix cracking of ceramics reinforced by aligned fibers and transforming particles. **J. Mech Phys. Solids**, 41, 615-630.

Evans, A.G., Domergue, J.M., and Vagaggini, E. (1993) A methodology for relating the tensile constitutive behavior of ceramic composites to constituent properties. To be published.

Garvie, R.C., Hannink, R.H.J. and Pascoe, R.T. (1975). Ceramic steel, **Nature**, 258, 695-708.

Hutchinson, J.W. and Jensen, H.M. (1990). Models of fiber debonding and pullout in brittle composites with friction. **Mech. Mater.**, 9, 139-163

Krstic, V.D. (1983) On the fracture of brittle-matrix/ductile particle composites. **Phil. Mag. A**, 48, 695-708.

Marshall, D.B. and Cox, B.N. (1987). Tensile fracture of brittle matrix composites: influence of fiber strength. **Acta. Met.**, 35, pp 2607-2619.

Mataga, P.A. (1989) Deformation of crack-bridging ductile reinforcements in tough brittle materials. **Acta. Metall.** 37, 3349-59.

McMeeking, R.M. and Evans, A.G. (1982). Mechanics of transformation toughening in brittle materials. **J. Am. Ceram. Soc.**, 65, 242-246.

Rice, J.R. (1968) A path-independent integral and the approximate analysis of strain concentration by notches and cracks. **J. Appl. Mech.**, 35, 379-386.

Rose, L.R.F. (1986). The size of the transformed zone during steady-state cracking in transformation toughened materials, **J. Mech. Phys. Solids**, 34,. 609-616.

Sigl, L.S., Mataga, P.A., Dalgleish, B.J., McMeeking, R.M. and Evans, A.G. (1988) On the toughness of brittle materials reinforced with a ductile phase. **Acta. Metall.**, 36, 945-953.

Stump, D.M. (1991a) Toughening and strengthening of ceramics reinforced by dilatant transformations and ductile particles. **Int. J. Solids Structures**, 25, 669-689.

Stump, D.M. (1991b) The role of shear stresses and shear strains in transformation-toughening. **Phil. Mag. A**, 64, 879-902.

Stump, D.M. and Budiansky, B. (1989a). Crack growth resistance in transformation toughened ceramics. **Int. J. Solids Structures**, 25, 635-646.

Stump, D.M. and Budiansky, B. (1989b). Finite cracks in transformation-toughened ceramics, **Acta. Met.**, 37, 3297-3304.

Sutcu, M. (1989) Weibull statistics applied to fiber failure in ceramic composites and work of fracture. **Acta. Metall.**, 37, 651-661.

Thouless, M.D. and Evans, A.G. (1988) Effects of pull-out on the mechanical properties of ceramic-matrix composites. **Acta. Metall.**, 36, 517-522.

MICROLAMINATED HIGH TEMPERATURE INTERMETALLIC COMPOSITES

R. G. Rowe, D. W. Skelly and M. Larsen

GE Corporate Research and Development, Schenectady, NY 12309

and

J. Heathcote, G. R. Odette and G. E. Lucas

University of California at Santa Barbara, Materials Dept., Santa Barbara, CA

ABSTRACT

Microlaminated composites of Nb_3Al-Nb and Cr_2Nb-Nb(Cr) were synthesized by high rate Magnetron® sputtering with 2 and 6 μm lamination thicknesses and tested at room temperature to determine the effect of metal layers on mechanical properties. The Nb_3Al-Nb microlaminate with 2 μm layer thickness had a fracture strength of 476 MPa at room temperature and a steady state fracture toughness of 10 MPa$\sqrt{m}$. The Cr_2Nb-Nb(Cr) microlaminates with 2 μm layer thickness had a fracture strength of 725 MPa and a limiting fracture toughness of about 17-22 MPa$\sqrt{m}$. The same microlaminate with 6μm layers had a higher fracture toughness but a shallower slope in the resistance curve, and had a room temperature fracture strength of 475 MPa. The resistance curve behavior and fracture strength could be modeled in terms of characteristic stress-displacement functions for the constrained metal layers. The higher toughness of the Cr_2Nb-Nb(Cr) microlaminates appears to be largely a result of the higher strength of the Nb(Cr) reinforcement. The shallower resistance curve slope of 6 μm Cr_2Nb-Nb(Cr) microlaminate and the lower toughness of the Nb_3Al-Nb microlaminate result in lower fracture strengths. The demonstrated toughening of these high temperature intermetallics by compositing may lead to their utilization and a significant increase in aircraft engine turbine performance. High temperature property measurements are now needed to determine the limits of their elevated temperature performance.

INTRODUCTION

The thrust to weight ratio of aircraft engines is limited by the density and elevated temperature capability of high temperature turbine materials. Single crystal superalloys, which are the current state-of-the-art in high temperature turbine blade materials, have limited potential for further increases in temperature capability. High temperature intermetallics offer the advantage of higher specific strength and higher temperature capability, but lack ductility and fracture toughness below 1000°C. By compositing these very high temperature intermetallics with ductile metals, toughening may be improved to the point [1-7] where the composites have applicability in aircraft engine turbine sections.

Lamination of ductile metals with continuous intermetallic layers offers one means of producing such composites. Small lamellae thicknesses may have advantages related to intrinsic defect sizes and the effectiveness of ductile reinforcements in load-controlled applications where strength is important. Intermetallic composites will require a refractory metal for toughening because of the need for metal strength at temperatures above 1100°C. Niobium-base alloys were selected as the toughening layer in this study because of their low density compared to superalloys, experience with oxidation-resistant niobium alloys [8] and the existence of metal-intermetallic systems in equilibrium at high temperatures [4, 9, 10]. Two microlaminated composite systems, Nb_3Al-Nb and Cr_2Nb-Nb(Cr) were chosen for microstructural and mechanical property evaluation. This choice of systems was based upon well established knowledge of phase relations between the metal and the intermetallic compositions.

COMPOSITE SYNTHESIS

Intermetallic laminated composites were synthesized in-situ [11]. Metal and intermetallic alloys were alternately vapor deposited by Magnetron® sputtering with 2 and 6 μm thick metal and intermetallic layers to produce microlaminated composite sheets approximately 0.15 mm thick [11]. The as-deposited compositions and composite parameters of the two microlaminated composite systems, Nb_3Al-Nb and Cr_2Nb-Nb(Cr), are shown in Table 1(a). Pure Nb was used as the metal layer in the Nb_3Al-Nb microlaminate to maximize room temperature ductility of the metal layer. The metal and intermetallic compositions of the Cr_2Nb-Nb(Cr) microlaminate were displaced to the Nb rich side of high temperature equilibrium compositions. Samples of the Nb_3Al-Nb microlaminates were annealed 2 hr. 1000°C to produce a composite with metal (bcc) and Nb_3Al (A15) lamellae, as shown in Figure 1(a). The compositions of the metal and intermetallic layers after annealing are shown in Table 1(b). The Cr_2Nb-Nb(Cr) microlaminates L17, which had 2 μm layer thicknesses, and L60, which had 6 μm laminations, were annealed 2 h at 1200°C to produce metal layers with the bcc structure and intermetallic layers with a two phase equiaxed Cr_2Nb + bcc metal grain structure; these are shown in Figures 1(b) and (c). All microlaminates exhibited a low density of conical growth defects ranging in size from part-

through 10 μm diameter defects to through-thickness 100 μm diameter defects [11].

Transmission electron microscopy (TEM) was used to examine sections across the metal and intermetallic layers of microlaminates L8, the 2 μm layered Nb_3Al-Nb microlaminate, and L17, the 2 μm layered Cr_2Nb-Nb(Cr) microlaminate. Representative micrographs are shown in Figures 2 (a) and (b), respectively. The metal layers in both microlaminates retained columnar bcc microstructures and the intermetallic layers had two-phase fine equiaxed intermetallic microstructures after annealing. The Nb_3Al-Nb microlaminates had a single phase A15 Nb_3Al intermetallic layer containing small Al_2O_3 precipitates along columnar grain boundaries. The intermetallic layers in the Cr_2Nb-Nb(Cr) microlaminates consisted of Cr_2Nb containing bcc Nb(Cr) particles. The volume fraction of bcc Nb(Cr) particles within the Cr_2Nb intermetallic layers was estimated by backscattered electron imaging, X-ray intensity measurements and transmission electron microscopy to be approximately 25%. Fine bubbles, presumably Ar-stabilized voids, were observed in the matrix and along grain boundaries in the metal and intermetallic layers of both Nb_3Al-Nb and Cr_2Nb-Nb(Cr) microlaminates. The Nb_3Al composite had a higher oxygen impurity content (≈700wppm O) than the Cr_2Nb (≈ 100-200wppm O) composites.

Table 1(a) Microlaminated Composite Deposited Compositions and Layer Count[1]

Microlaminate No.	Intermetallic Composition (atom %)	Metal Composition (atom %)	Layer Thickness (μm)	Number of IM Layers	Number of Metal Layers
L8,L9	Nb-18.3Al	Nb	2	32	33
L17	Cr-40.5Nb	Nb-4.7Cr	2	32	33
L60	Cr-42.2Nb	Nb-3.3Cr	6	11	11

Table 1(b) Metal and Intermetallic Layer Compositions after Annealing

ID No.	Intermetallic LayerComposition (in atom %)	Metal Layer Composition (in atom %)	Annealing Temperature 2 hrs. (°C)
L8	Nb-22.6AlAl	Nb-2.2Al	1000
L17	Cr-33.1Nb matrix plus Nb-6.9Cr precipitates	Nb-4.7Cr	1200

Room Temperature Fracture Strength

Sheet tensile specimens, 0.15 mm thick with gage sections 4.2 mm wide and 12.5 mm long were formed by electric discharge machining and were annealed in argon for 2 hours at 1000°C and 1200°C for the Nb_3Al-Nb and Cr_2Nb-Nb(Cr) composites, respectively. They were tested in tension at room temperature at a strain rate of $7x10^{-4}$/s. Most samples failed at the first cracking event, but a few exhibited microcracking before failure. Microcracks appeared to be associated with the conical growth defects.

The room temperature tensile strengths are listed in Table 2. The average fracture strengths were 476, 735 and 475 MPa for the the Nb_3Al-Nb (L8), the 2 μm layer Cr_2Nb-Nb(Cr) (L17), and the 6 μm layer Cr_2Nb-Nb(Cr) microlaminate (L60), respectively.

Table 2. Room Temperature Fracture Strengths of Three Microlaminated Composites

L8, 2 μm Layer Nb_3Al-Nb		L17, 2 μm Layer Cr_2Nb-Nb(Cr)		L60, 6 μm Layer Cr_2Nb-Nb(Cr)	
Heat Treatment	Fracture Stress (MPa)	Heat Treatment	Fracture Stress (MPa)	Heat Treatment	Fracture Stress (MPa)
1000°C/2 h	501	1200°C/2 h	750	1200°C/2 h	500
1000°C/2 h	451	1200°C/2 h	731[a]	1200°C/2 h	441
		1200°C/2 h	725	1200°C/2 h	484[b]
avg. ± s.d.	476 ±25	avg. ± s.d.	735 ± 15	avg. ± s.d.	475 ± 35

[a] Through crack 0.39 mm average width at final fracture. [b] Cone growth defect halfway through thickness.

Fracture Toughness, Resistance Curves, and Fractography

One of the Cr_2Nb-Nb(Cr) L17 micromlaminates (2 μm layer thickness) exhibited cracking and crack arrest prior to final fracture, the others fractures with no prior cracking. The engineering stress versus strain curve for the sample that exhibited subcritical cracking, shown in Figure 3, was derived from the load-time curve (at constant crosshead speed) of

[1] As noted later, the intermetallic layers are initially deposited as metastable solid solutions. Annealing at elevated temperatures transforms them to the stable intermetallic structure. For convenience, we will refer to them as the "intermetallic" layers throughout the text.

the specimen. An arrested crack was subsequently measured by fractography to have an average through-thickness length of 0.39 mm before final fracture. Using a linear elastic fracture mechanics analysis for an off-center through crack in a finite width sheet [12], the room temperature fracture toughness of microlaminate L17 was estimated to be about 22 MPa$\sqrt{m}$.

SEM fractographs of the microlaminates that were fractured in tension at room temperature are shown in Figures 4 (a-c). Chisel-point necking of the Nb layers such as that shown in Figure 4(a) was observed in all tensile fractures of the Nb_3Al-Nb microlaminate. In all cases, the Nb layer fractured with the appearance of highly restrained metal failure [13] and little or no metal-intermetallic delamination was observed. Intermetallic Nb_3Al layers failed by brittle cleavage. The Al_2O_3 particles that were observed in the intermetallic layers did not appear to have affected the fracture path. The tensile fracture surfaces of the Cr_2Nb-Nb(Cr) microlaminates L17 (2 μm) and L60 (6 μm) are shown in Figures 4 (b) and (c), respectively. Fracture appearance was of two types. Most of the fracture surface of the Nb(Cr) layers failed by very local fluted dimpling parallel to the columnar grain structure of the Nb(Cr) layer. This was distinctly different from the failure appearance of the Nb_3Al-Nb metal layer. The Cr_2Nb intermetallic layer fractured by flat cleavage, but the angle of fracture and smoothness of the intermetallic fracture surface in L17 (2 μm) appeared to be related to features within the Nb(Cr) layers. The intermetallic layers of L60 (6 μm) were flatter. Both L17 and L60 Cr_2Nb-Nb(Cr) microlaminate intermetallic layers showed evidence of the bcc second phase particles that were observed in metallographic sections. In the one instance where crack arrest was evident in the tensile sample (L17, the fracture appearance within the region corresponding to the arrested crack was different; the intermetallic layers still fractured by flat cleavage, but the Nb(Cr) layers showed evidence of microvoid growth and coalescence along a chisel-point ridge formed by necking -- like the Nb_3Al-Nb microlaminate.

Fracture resistance curves were determined for Nb_3Al-Nb microlaminate L9 and for Cr_2Nb-Nb(Cr) microlaminates L17 (2 μm) and L60 (6 μm) using a frame bending technique. A side notched 2.5 cm x 0.787 cm panel of the microlaminate was glued onto an aluminum support frame which provided a loading surface and prevented buckling. The compound specimen was tested in three-point bending with the direction of crack propagation within the plane of the sheet so that the crack cut across all lamellae simultaneously. The effect of the frame was taken into account in the calculation of stress intensity. Fracture resistance curves were determined as stress intensity K vs crack length Δa and are shown in Figure 5.

Fractography was also performed on the three point bend fracture resistance specimens. The fracture surface of the Nb_3Al-Nb three-point bend fracture specimen was similar to the tensile specimen; that is, chisel point failure of the Nb layers and cleavage of the Nb_3Al layers, with little sign of debonding between the two. The fracture surface of the Cr_2Nb-Nb(Cr) microlaminate L17 (2 μm) again had different features in the regions of stable and unstable crack propagation. Failure of the Nb(Cr) layers in the fast fracture region was by very local fluted dimpling parallel to the columnar grain structure of the Nb(Cr) layer and the Cr_2Nb intermetallic layer fractured by cleavage, similar to the tensile specimen fracture surfaces. In the region of stable crack growth, however, the failure of the Nb(Cr) layer looked much more like the Nb_3Al-Nb microlaminate, with evidence of microvoid growth and coalescence along a chisel-point ridge formed by necking. Again, the metal layers appeared to be tightly bonded to the matrix at the fracture surface.

The resistance curves of Figure 5 were analyzed using a combination of confocal microscopy measurements of the critical extensions of the ductile ligaments at failure, solid mechanics modeling of the bridged cracks, and microhardness measurements. Details of the complete analysis will be presented elsewhere. However, the most salient points can be summarized here. All three microlaminates exhibited increasing toughness with crack extensions (Δa) following initiation at $K_o \approx 5$ MPa$\sqrt{m}$. The resistance curve in the 2 μm Nb_3Al-Nb (L9) samples saturated at about 10 MPa$\sqrt{m}$ following about 60μm of crack growth. After about 100μm of crack growth, fracture toughness in specimen L17, the 2μm thick layer Cr_2Nb-Nb(Cr) microlaminate, aproached a steady-state value of about 17 MPa$\sqrt{m}$, similar to the value estimated from the tensile test. The resistance curve for L60, the 6μm thick layer Cr_2Nb-Nb(Cr) microlaminate, manifested a shallower slope but appeared to cross over the resistance curve of the corresponding 2 μm layer specimen at a crack extension of about 150 μm. This specimen fractured prior to steady state due to crack instability; but based on a solid mechanics model analysis, a continued increase in toughness to a steady state value of about 21 MPa$\sqrt{m}$ would be expected at a Δa of about 300 μm.

The differences in the resistance curves are a consequence of differences in the constrained ductile layer stress-extension functions S(u). These are shown schematically in Figure 6, where S(u) is a sawtooth function with a maximum stress S_{max} and a critical extension to failure u*. In all cases the resistance curves were generally consistent with this sawtooth form, which has been found in previous studies on other materials as well [5-7]. Moreover, the maximum toughness values were close to those associated with small scale bridging conditions; that is, $\Delta K_{max}^2 \approx K_{max}^2 - K_o^2 \approx Ef\chi$, where E is the plane strain elastic modulus, f is the volume fraction of ductile phase and χ is the value of S(u) integrated over u from 0 to u*.[1,5] Values of u* normalized by the layer thickness t were estimated to average about $u^*/t \approx 0.95 \pm 0.15$. This is in agreement with previous observations on TiAl reinforced by Nb

and TiNb ductile phases [5-7]. Diamond pyramid microhardness (DPH) measurements of the ductile layers indicated that the Nb(Cr) layers in L17 and L60 were about 1.7 times as strong as the nominally pure Nb in L9. This is of the same order as the ratio of S_{max} in L17 and L60 ($\approx$ 2750±300 MPa) to S_{max} in L9 ($\approx$ 1500±300 MPa). Moreover, these values of S_{max} are about 2.7±0.3 times higher than the nominal tensile strength σ_u of the metal layer as determined by σ_u(MPa) $\approx$ 3 DPH (kg/mm^2). Such high values of constraint ($M = S_{max}/\sigma_u \approx 2.7\pm0.3$) are consistent with the fractographic observations of a tightly bonded matrix. These values of constraint are somewhat larger than estimates of $M \leq 2.5$ for thicker TiNb reinforcements found in TiAl composites, but again this is consistent with observations of increasing constraint with decreasing layer thickness and a theoretical upper bound of 3.[14]

DISCUSSION OF RESULTS

As noted previously, the differences in the resistance curve behavior of the microlaminates are consistent with bridging mechanics models and are mediated by the stress-extension function as described previously. The higher toughness of the 2 μm layer thick Cr_2Nb-Nb(Cr) versus the Nb_3Al-Nb microlaminate can be attributed to the higher strength of the Nb(Cr) reinforcement. The thicker 6 μm reinforcements in L60 versus L17 produce a higher toughness after crack extensions greater than about 150 μm, but the slope of the resistance curve is shallower.

These differences in resistance curve behavior may also rationalize the differences in fracture strength as well. Here strength is believed to be limited by the unstable propagation of pre-existing or nucleated (unbridged) microcracks during tensile testing. Where observable, it appears the cracks in the tensile samples nucleate at conical growth defects which range in size up to 100 μm in diameter. Under these conditions fracture strength is determined by the stress at which both

$$K_a = K_r \qquad \text{and} \qquad dK_a/da = dK_r/da \tag{1}$$

where K_a is the nominal applied stress intensity and K_r is the material fracture toughness at a given value of crack length a as determined by the resistance curve. [13] First estimates of fracture stresses for the three microlaminates L9, L17, and L60 were made by assuming a large pre-existing microcrack in a 100μm diameter growth defect at the center of the tensile specimen -- for which K_a can be determined from handbook stress intensity functions for a center cracked panel -- and taking K_r(a) from the measured resistance curves. The estimated fracture stress for L17 was about 775 MPa, in good agreement with the measured value of about 735 MPa. However, the instability was predicted to occur at a total crack length of about 200 μm, which is only about 50% of the observed value in the one tensile specimen that showed apparent crack arrest. Further, the corresponding predicted fracture stresses for L60 and L9 were 675 and 625, respectively, about 40% higher than the experimentally observed values.

Of course, using resistance curves from three point bend specimens to predict instability in center cracked specimens is not strictly correct. This can be corrected by using the S(u) functions to predict resistance curves for center-cracked panels; when this is done, however, predicted fracture stresses are generally higher -- about 950, 850 and 600 MPa for L17, L60 and L9, respectively. These estimates might decrease for more realistic crack/specimen geometries (e.g., eccentric cracks), however, the overpreictions of fracture stress are likely due to other effects such as multiple cracks, microcracking-induced modulus changes and stress redustributions, varying growth defect size, etc. Nonetheless, this approach correctly predicts the observed trends, including the higher strength level in the L17 microlaminate.

CONCLUSIONS

- In-situ vapor phase synthesis by Magnetron® sputtering was used successfully to synthesize metal-intermetallic laminated composites with independent control over the composition, spacing and volume fraction of the layers.
- The Nb_3Al-Nb microlaminate with 2 μm layer thickness had a fracture strength of over 476 MPa at room temperature and a steady state fracture toughness of 10 MPa$\sqrt{m}$ after about 60μm of crack growth.
- Cr_2Nb-Nb(Cr) microlaminates with 2 μm layer thickness had a fracture strength of over 725 MPa at room temperature. Its limiting fracture toughness was determined to be about 17-22 MPa$\sqrt{m}$. The same microlaminate with 6μm layers had a higher fracture toughness but a shallower slope in the resistance curve and a room temperature fracture strength of only 475 MPa.
- There was a difference in the fast fracture failure mode of the metal layers in the Nb_3Al-Nb and Cr_2Nb-Nb(Cr) microlaminates. The Nb layer in Nb_3Al-Nb microlaminate failed in fast fracture by chisel-point necking while the Nb(Cr) layer in Cr_2Nb-Nb(Cr) separated with a fluted ductile dimpling pattern. Under stable crack growth conditions, both types of metal layers failed by chisel-point necking with evidence of void growth and coalescence along the necking ridge. Little debonding between metal and intermetallic layers was evident.
- The resistance curve behavior and fracture strength could be modeled in terms of characteristic stress-displacement functions for the constrained metal layers. The higher toughness of the Cr_2Nb-Nb(Cr) microlaminates appears to be largely a result of the higher strength of the Nb(Cr) reinformcement. The shallower resistance curve slope of 6 μm Cr_2Nb-Nb(Cr) microlaminate and the lower toughness of the Nb_3Al-Nb microlaminate result in crack instabilities at

lower values of applied stress and hence lower fracture strengths.

REFERENCES

1. Déve, H.E., et al., "Ductile Reinforcement Toughening of Gamma-TiAl: Effects of Debonding and Ductility" Acta Metall. Mater, 38, 1491-1502, (1990).
2. Sigl, L.S., et al., "On the Toughness of Brittle Materials Reinforced with a Ductile Phase", Acta Metall. Mater. 36, 945-953, (1988).
3. Cao, H.C. and A.G. Evans, "On Crack Extension in Ductile/Brittle Laminates", Acta Metall. Mater, 39, 2997-3005, (1991).
4. Anton, D.L. and D.M. Shah, "Ductile Phase Toughening of Brittle Intermetallics", Mat. Res. Soc. Symp. Proc., 194, 45-52, (1990).
5. Odette, G. R., Chao, B. L. Sheckherd, J. W., and Lucas, G. E., "Ductile Phase Toughening Mechanisms in a TiAl-TiNb Laminate Compoite," Acta metall. mater., 40 (1992) 2381.
6. Venkateswara, K. T., Odette, G. R., and Ritchie, R. O., "On the Contrasting Role of Ductile Phase Reinforcements in the Fracture Toughness and Fatigue Crack Propagation Behavior of TiNb/γ-TiAl Intermetallic Matrix Composites," Acta metall. mater., 40 (1992) 353/
7. Venkateswara, K. T. Odette, G. R., and Rigchie, R. O., "Ductile-Reinforcement Toughening in γ-TiAl Matrix Composites: Effects on Fracture Toughness and Fatigue-Crack Propagation Resistance," Acta metall. mater. (1993) in press.
8. Jackson, M.R., et al., "Response of Nb-Ti Alloys to High Temperature Air Exposure". in Refractory Metals Extraction, Processing and Applications, Edited by K.C. Liddell, S. D.R., andR.G. Batista, TMS, Warrendale, PA, 1991, 335-346.
9. Massalski, T.B., Binary Alloy Phase Diagrams. ASM International, Metals Park, OH, 1986.
10. Thoma, J.D. and J.R. Perepezko, "An Experimental Evaluation of the Phase Relationships and Solubilities of the Chromium-Niobium System", Mat'ls. Sci. & Engrg., A156, 97-108, (1992).
11. Rowe, R.G. and D.W. Skelly, "The Synthesis and Evaluation of Nb_3Al-Nb Laminated Composites", Mat. Res. Soc. Conf. Proc., 273, 411-416, (1992).
12. Rooke, D.P. and D.J. Cartwright, Compendium of Stress Intensity Factors. Her Majesty's Stationery Office, London, 1976.
13. Bannister, M. and M.F. Ashby, "The Deformation and Fracture of Constrained Metal Sheets", Acta Metall. Mater., 39, 2575-2582, (1991).
14. Johnson, M., Odette, G. R., Lucas. G. E., University of California at Santa Barbara, Santa Barbara, CA, unpublished work.

ACKNOWLEDGMENTS

This work was partially funded by the U.S. Air Force, Wright Research and Development Center, Wright-Patterson AFB, OH under contract F33615-91-C-5613. The authors would like to acknowledge the contributions of Mr. R. Nardi and Ms. K Denike in sputter deposition and processing of the microlaminated composites.

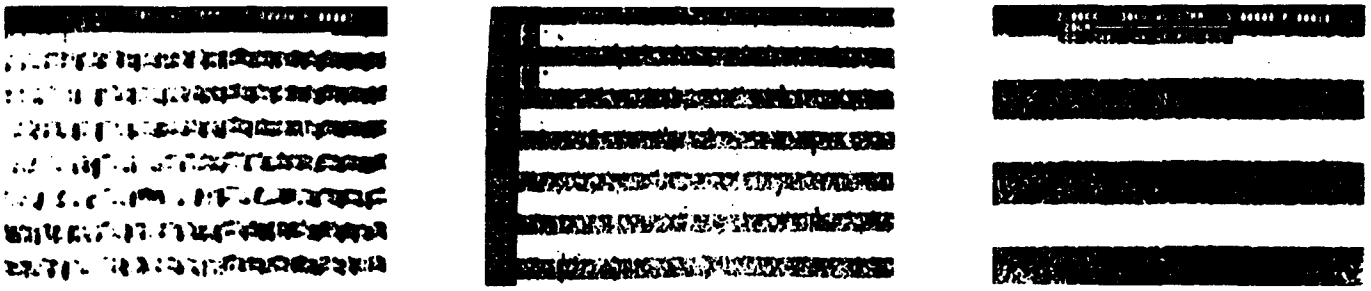

FIG. 1. Backscattered electron micrographs of (a) L9 (NB_3Al-Nb) after 1000°C 2hr. in argon. (b) L17 (Cr_2Nb-Nb. 2 micron layers) after 1200°C 2hr. in argon. and (c) L60 (Cr_2Nb-Nb. 6

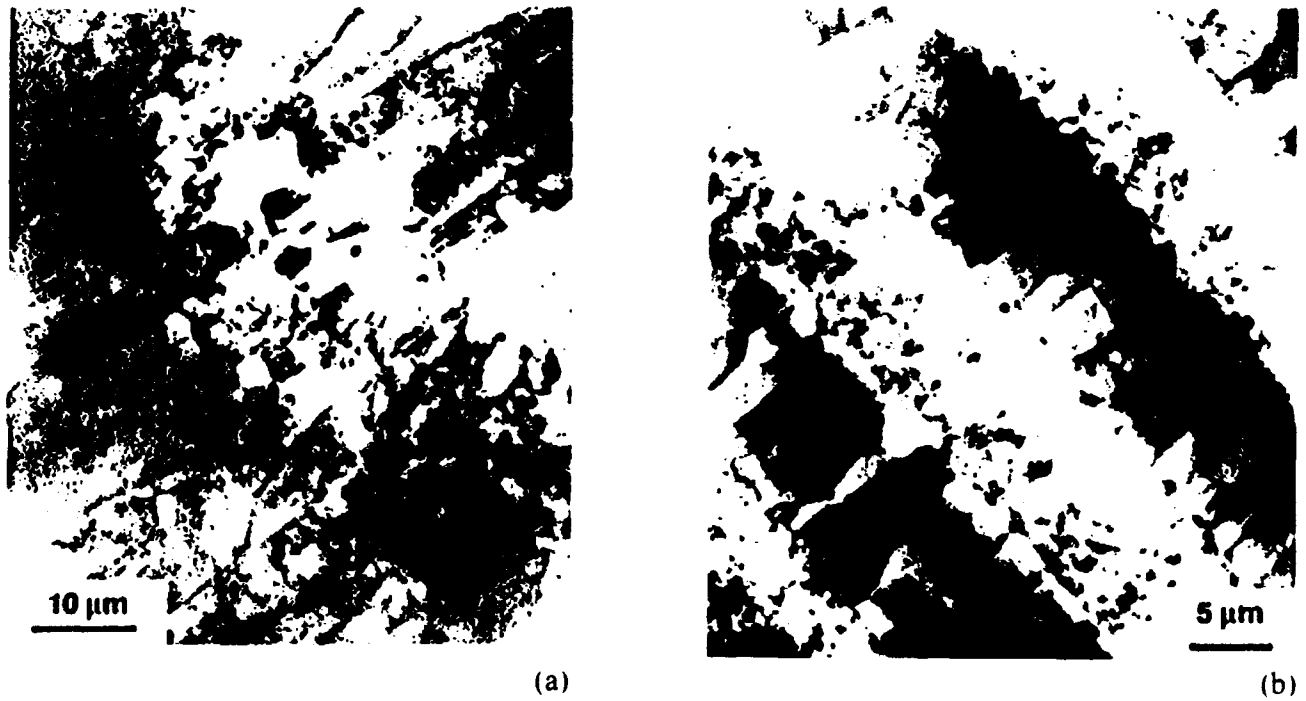

FIG. 2. TEM micrograph of (a) the microlaminate L8 (Nb_3Al-Nb) after 1000°C 2 hr in argon and (b) microlaminate L17 (Cr2Nb-Nb) after 1200°C 2 hr in argon.

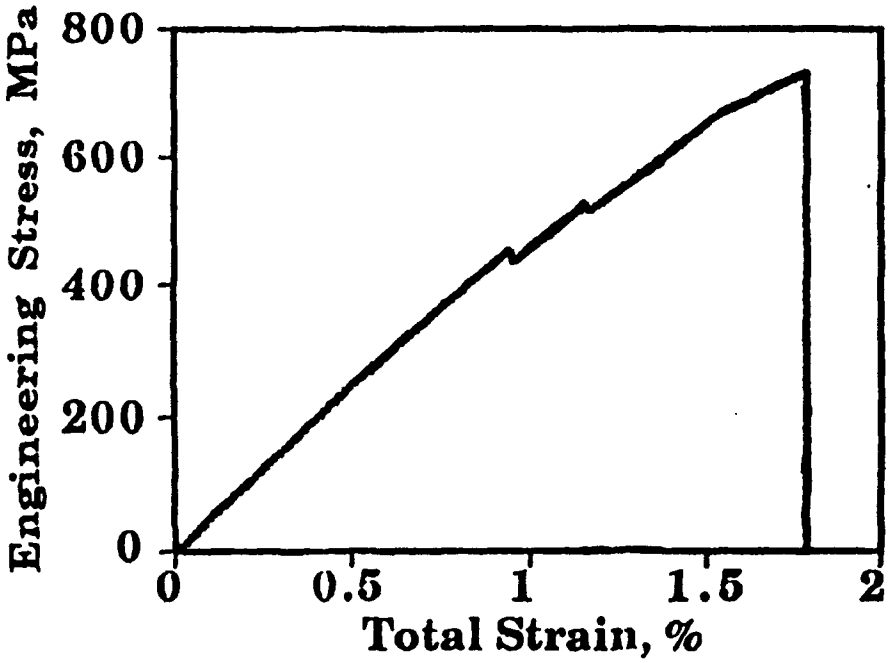

FIG. 3. Stress-strain curve for the L17 tensile test that exhibited subcritical cracking.

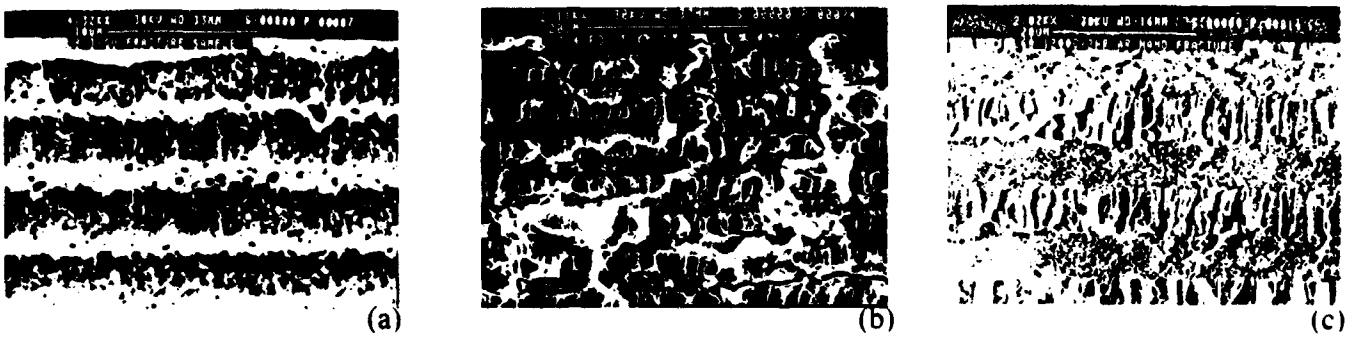

FIG. 4. SEM fractographs of tensile specimens fractured at room temperature: a) Nb_3Al-Nb annealed at 1000°C, b) Cr_2Nb-Nb(Cr) with 2 micron layers annealed at 1200°C and c) Cr_2Nb-Nb(Cr) with 6 micron layers annealed at 1200°C.

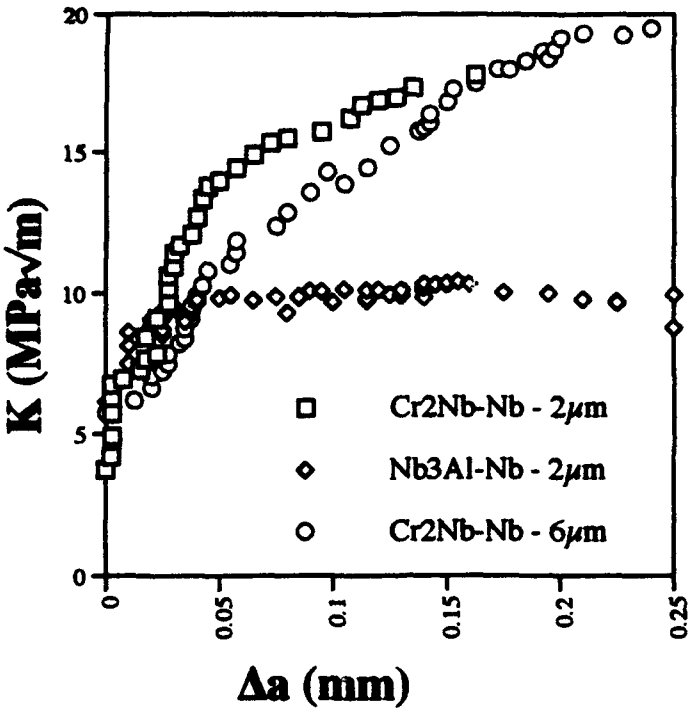

FIG. 5. Fracture resistance curves -- stress intensity vs. crack length -- for L9, L17, and L60.

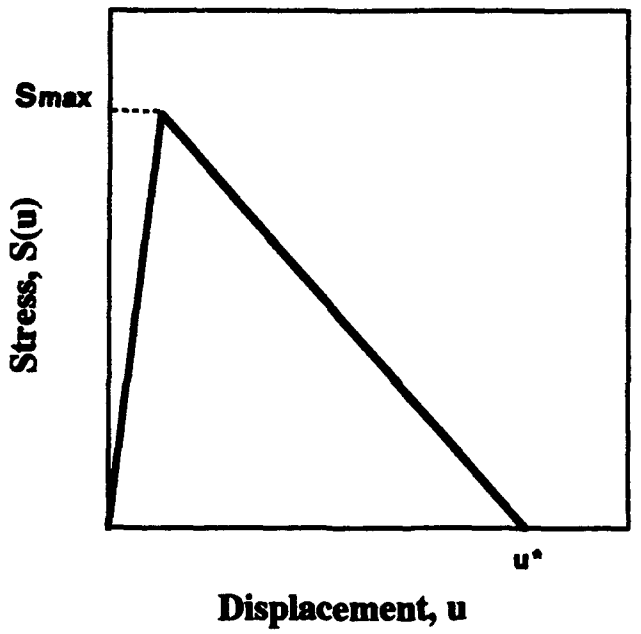

FIG. 6. Schematic stress-extension function determined for the constrained metal layers in the microlaminate composites.

Fracture Toughness of Al-4% Mg/Al_2O_3p Composites

R.H. Pestes*, S.V. Kamat** and J.P. Hirth**

*Hewlett-Packard
Camus, WA 98607

**Mechanical and Materials Engineering Department
Washington State University
Pullman, WA 99164-2920

Abstract

Fracture toughness tests were carried out on Al-4%Mg/Al_2O_3p composites containing different sizes and volume fractions of alumina particulates. The results indicated that the fracture toughness was dependent on the interparticle spacing provided the particulate size was below a critical size. The critical particulate size corresponds to the situation wherein the energy release rate on particulate cracking is sufficient to trigger dynamic unstable crack extension.

1. Introduction

Particulate reinforced metal matrix composites have attracted considerable attention in recent years because of their high specific strengths and stiffnesses as well as the relative ease of fabrication and secondary processing. The applications for these composites have, however, been limited because of their low ductility and fracture toughness. An understanding of the effect of microstructural parameters, such as volume fraction and particle size of the reinforcement, on the fracture toughness of these composites is essential for improving their damage tolerance. Unfortunately, only a few studies on the influence of microstructural parameters on the fracture toughness of particulate reinforced MMC's have been reported in the literature [1-7]. These studies have shown that the fracture toughness was dependent on both volume fraction and particle size and could be correlated to the interparticle spacing. However, the particle sizes used in most studies varied in a very narrow range.

The objectives of the present investigation were to study the effect of particle size, in a much wider range of sizes (3μm-165μm), on the fracture toughness of Al-4%Mg/Al_2O_3p composite and to use a bimodal mixture of particle sizes to separate the particle spacing and particle size variables.

2. Experimental Procedure

The composite materials were obtained from University of California at Santa Barbara in the form of 50mm × 50mm × 12mm blocks. The matrix for all the composites was a binary aluminum alloy containing 4 wt% magnesium and the reinforcements were roughly equiaxed alumina particulates. The composites contained alumina particulates varying from 3μm to 165μm and the volume fraction of the reinforcements was in the range 45-54%. Two of the composites had a bimodal mixture of two particulate sizes. Lists of the composites studied in this investigation and the particulate

characteristics are given in Table 1. A representative scanning electron micrograph for one of the composites (Al-4%Mg+165μm, 54% Al_2O_3p) is shown in Fig. 1. One can see that the distribution of the alumina particulates was nominally uniform and that the surrounding matrix was also free of voids.

Mode I fracture toughness tests were performed on these composites with the matrix in the annealed condition. The fracture toughness specimen design is illustrated in Fig. 2. The design was based on the standard compact tension specimen design recommended by ASTM E-399 [8], the only difference being that the w/B ratio was 4 instead of 2, which is within acceptable limits. The fracture toughness specimens were fatigue precracked and tested in an Instron 1361 testing machine at a crosshead speed of 0.5 mm/min. A clip gauge was used to measure the load-line displacements and load versus load-line displacements were recorded with the help of a HP x-y plotter. The broken compact tension specimens were examined under the scanning electron microscope.

3. Results

Load versus load-line displacement plots for the composites are shown in Figs. 3 a) and b). Fig. 3 b) is representative for the composite with 165μm size reinforcement whereas Fig. 3a is representative for all the other composites studied. The conditional fracture toughness (K_{IQ}) was calculated from the following relationship

$$K_{IQ} = \frac{P_Q}{Bw^{1/2}} f(a/w) \qquad (1)$$

where P_Q is the 5% secant offset load, B the thickness, w the width, a the crack length and f(a/w) the geometric factor. The calculated values of K_{IQ} for all the composites investigated are tabulated in Table 2. In most cases the condition for plane strain $B \geq 2.5(K_{IQ}/\sigma_{ys})^2$ was not satisfied. Hence, the fracture toughness values obtained in this investigation are conditional and not plane

strain values. However, comparison of the fracture toughness values across the study is justified because the thicknesses for all specimens were identical. It is evident from Table 2 that the fracture toughness values do not exhibit any correlation with the volume fraction.

SEM fractographs for the composites are shown in Figs. 4 a) and b) Figure 4 b) is representative of the composite with 165μm Al_2O_3 particle size whereas Fig. 4 a) is representative of all the other composites. Figure 4 a) shows that for all the composites except the one containing 165μm size alumina particles, fracture occurred by a locally ductile mechanism. The fracture surface essentially consisted of large flat dimples associated with the alumina particles and fine dimples associated with the ductile fracture of the aluminum alloy matrix. These observations are consistent with those observed for other particulate reinforced aluminum alloy matrix composites [1, 9-11]. The observation of stereo pairs of the broken particle surfaces showed smooth planar surfaces which indicate that the alumina particulates are cut rather than decohered. This is consistent with expectations since these composites have a large interfacial bond strength because of the formation of $MgAl_2O_4$ spinel at the interface [12-13]. In the case of the composite with 165μm size alumina particulates, the fracture surface (Fig. 4b) contains numerous cut alumina particulates. However, there is very limited evidence of small dimples associated with the ductile fracture of the matrix alloy.

4. Discussion

In the case of composites other than the one with 165μm size particles, the fractographic features [Fig. 4a] demonstrate that fracture is governed by the linkage of the microcracks or voids, formed because of particulate fracture, with the main crack. This linkage occurs by the ductile fracture of the matrix. Hence, one would expect the fracture toughness to be limited by interparticle spacing. In an earlier study on 2014 and 2024 aluminum alloys reinforced

with alumina particulates, Kamat *et al* [3] have suggested that the fracture toughness in particulate reinforced MMC's is given by a Rice-Johnson type relationship [14]:

$$J_{IC} = \sigma_f \lambda \tag{2}$$

where σ_f is the flow stress and λ the interparticle spacing, corresponding to the mean edge-edge free path.

The interparticle spacing for composites containing a single m: value particle size distributions can be theoretically calculated from t: expression [15]

$$\lambda = D\left[\left(\frac{\pi}{6V_F}\right)^{1/2} - \frac{2}{\pi}\right] \tag{3}$$

where D is the particle size and V_F the volume fraction of the reinforcement. This expression can be modified for composites containing bimodal particle sizes to the form:

$$\lambda = \lambda_{cc} - \frac{2}{\pi}(x_s D_s + x_b D_b) \tag{4}$$

where the subscripts b and s represent properties of the larger and smaller particles, respectively. Here λ_{cc} is the centre to centre spacing of the particles given by

$$\lambda_{cc} = \left[\frac{\pi D_b^2 D_S^2}{6(V_{fb} D_S^2 + V_{fs} D_b^2}\right]^{1/2} \tag{5}$$

Also, x_b and x_s, the number fraction of the total reinforcement contributed by the larger and smaller particles, respectively, are as follows.

$$x_b = \frac{c_s V_{fb}}{c_s V_{fb} + c_b V_{fs}} \tag{6}$$

$$x_s = \frac{c_b V_{fs}}{c_s V_{fb} + c_b V_{fs}} \tag{7}$$

where c is the volume of an individual particle. The theoretically calculated interparticle spacings are listed in Table 3.

In order to test the applicability of the Rice-Johnson type model to the composites tests in this investigation, the K_{IQ} values were converted to J_{IQ} by the relation

$$J_{IQ} = \frac{K_{IQ}^2}{E(1-\nu^2)} \tag{3}$$

where E is Young's modulus and υ is Poisson's ratio. If the data were to fit the Rice-Johnson model, (J_{IQ}/σ_f) should scale linearly with λ. A plot of experimentally determined J_{IQ}/σ_f versus the theoretically calculated λ is shown in Fig. 5. One can see that the agreement with the Rice-Johnson line is fairly good for small λ, although the experimental values of J_{IQ}/σ_f tend to be smaller than those predicted by the Rice-Johnson model. The deviation from the Rice-Johnson line is attributed to the fact that the theoretical calculation of λ assumes a perfectly homogeneous distribution of the particles in the matrix, whereas in the actual case there are some regions of clustering which would then act as preferential sites for crack extension. The interparticle spacing in this region would be smaller than the theoretical λ which would then reduce the deviation from the Rice-Johnson model. Thus, it is apparent that in composites which fail by a locally ductile mechanism, the fracture toughness can be increased by increasing the interparticle spacing. It is also evident that the presence of a bimodal particle size has only an indirect effect on the fracture toughness through its effect on interparticle spacing.

In the case of the composite with 165μm size alumina particulates which exhibits unstable crack growth (Fig. 3b), one would expect a behavior analogous to that discussed by Evans [16] for steels below the ductile-brittle transition temperatures. The initial crack begins to blunt and the stress ahead of the crack is increased because of the plastic flow and hydrostatic stress elevation. A particle in the deformed region cracks and if the local energy release rate is sufficient, runs back to the main crack and triggers unstable crack growth. Kamat *et al* [3] have suggested that for such a situation, the

local expected stress intensity factor for the propagation of the microcracked particle into the matrix, which is approximately equal to $10\sigma_f\sqrt{D}$, should correlate with the dynamic fracture toughness of the matrix alloy. The static fracture toughness of the Al-4%Mg alloy is approximately equal to $31MPa\sqrt{m}$ [17] and one would expect the dynamic fracture toughness to be lower than this value. The value of $10\sigma_f\sqrt{D}$ for A1-4%Mg alloy with D-165 μm and f=0.54 is $22MPa\sqrt{m}$ which is 71% of the static value of matrix fracture toughness and in the expected range for the matrix dynamic fracture toughness. That is, the dynamic crack arrest critical stress intensity factor exceeds the static value [18] so that an applied value of the stress intensity factor that does not lead to static crack propagation can produce dynamic crack propagation. Hence, in the regime where the composite fails by unstable crack growth, an increase in the particle size results in an enhancement of the stress intensity factor ahead of the cracked particle, thereby, resulting in an earlier fracture of the composite and lower fracture toughness.

5. Summary

The fracture toughness of the Al_2O_3 particulate reinforced Al-4%Mg alloy matrix composites can be increased by increasing the interparticle spacing provided that the particle size is below a critical size which corresponds to the size required for unstable crack extension of the microcrack into the matrix. One can increase the interparticle spacing by either decreasing the volume fraction or increasing the particle size of the reinforcement. The only significant effect of the presence of two markedly different particle sizes on the fracture toughness is the indirect one manifested by the attendant change in interparticle spacing. However, once the particle size exceeds a critical value, a further increase in particle size results in a decrease in the fracture toughness of the composite.

6. Acknowledgment

The authors are grateful for the support of this research by the Office of Naval Research under ONR Contract N00014-93-I-0213 with the University of California, Santa Barbara. They also are grateful to R. Mehrabian for supplying the composite.

References

[1] J.J. Lewandowski, C. Liu and W.H. Hunt Jr. in "Processing and Properties of Powder Metallurgy composites," P. Kumar, K. Vedula and A. Ritter eds, *Metallurgical Society of AIME*, Warrendale PA. (1988), 117.

[2] Y. Flom and R.J. Arsenault, *Acta Metall.*, Vol. 37, (1989), 2413.

[3] S.V. Kamat, J.P. Hirth and R. Mehrabian, *Acta Metall.*, Vol. 37, (1989), 2395.

[4] J.J. Lewandowski, C. Liu and W.H. Hunt Jr., *Materials Sci. and Engng. A*, Vol. 107, (1989) 241.

[5] M. Manoharan, C. Liu and J.J. Lewandowski in "Proc. Int. Conf. on Fracture VII," K. Salama, K. Ravi-Chander, D.M.R. Taplin and P. Rama Rao eds., Pergamon, Oxford, (1989) 2977.

[6] M. Manoharan and J.J. Lewandowski, *Acta Metall*, Vol. 38, (1990) 489.

[7] M. Manoharan and J.J. Lewandowski, *Materials Sci and Engng A*, Vol. A150, (1992) 179.

[8] ASTM E-399, Annual Book of ASTM Standards, American Society for Testing and Materials, V. 301, (1993) 509.

[9] C.P. You, A.W. Thompson and I.M. Bernstein, *Scripta Metall*, Vol. 21, (1987) 181.

[10] C.R. Crowe and R.A. Gray, in "Failure Mechanisms in High Performance Materials, Proc. 39th meeting of High Performance Group, Gaithersburg, (1984) 157.

[11] M. Manoharan and J.J. Lewandowski, *Scripta Metall*, Vol. 24, (1990) 2357.

[12] B.F. Quigley, G.J. Abbaschian, R. Wunderlin and R. Mehrabian, *Metall Trans*, Vol. 13A, (1982) 93.

[13] G.G. Levi, G.J. Abbaschian and R. Mehrabian, *Metall. Trans.*, Vol. 9A, (1978) 697.

[14] J.R. Rice and M.A. Johnson, in "Inelastic Behavior of Solids," M.F. Kanninen *et al* eds., McGraw Hill, New York, (1969) 641.

[15] S.V. Kamat, A.D. Rollet and J.P. Hirth, *Scripta Metall. Mater*, Vol. 25, (1991) 27.

[16] A.G. Evans, *Metal Trans.*, Vol. 14A, (1983) 1349.

[17] M.V. Ravichandran, R. Krishna Prasad and E.S. Dwarkadasa, *J. of Mater. Sci. Let.*, Vol. 11, (1992) 452.

[18] M.F. Kanninen and C.H. Popelar, "Advanced Fracture Mechanics," Oxford Univ. Press, 1985

Table 1: List of composites investigated. The matrix is Al-4%Mg Alloy and the reinforcement is alumina particulates. Cases 1 and 2 represent the bimodal particle distributions.

Composite No.	Total Vol. fraction %	1		2	
		Part. Size μm	Vol. fract. %	Part. Size μm	Vol. fract. %
1	47	3	26	30	21
2	46	3	41	30	5
3	45	3	45	-	-
4	47	45	47	-	-
5	50	9	50	-	-
6	53	30	53	-	-
7	54	165	54	-	-

Table 2: Fracture toughness of the composites investigated

Composite No.	Fracture Toughness $K_{IQ}, MPa\sqrt{m}$
1	11.5
2	8.1
3	3.2
4	17.5
5	10.5
6	12.7
7	9.9

Table 3: Comparison of Experimentally obtained J_{IQ} / σ_f μm with interparticle spacing

Composite No.	J_{IQ} / σ_f μm	λ μm
1	4.12	3.13
2	1.90	2.32
3	0.51	1.10
4	11.35	18.80
5	3.02	3.50
6	5.37	10.7
7	5.30	57.4

List of Figures

Figure 1

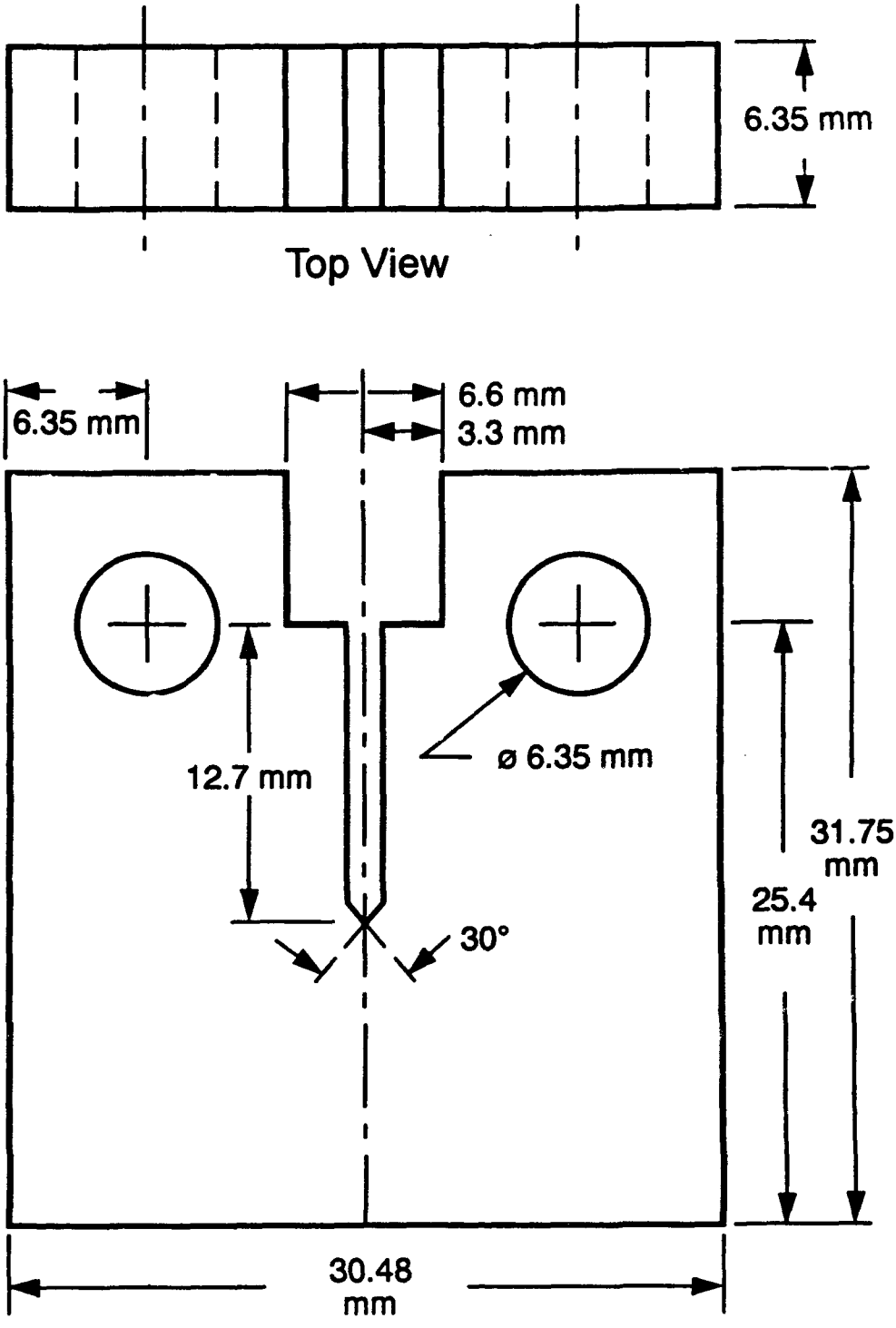
6.35 mm
Top View
6.35 mm
6.6 mm
3.3 mm
12.7 mm
ø 6.35 mm
31.75 mm
25.4 mm
30°
30.48 mm
Side View

Figure 2

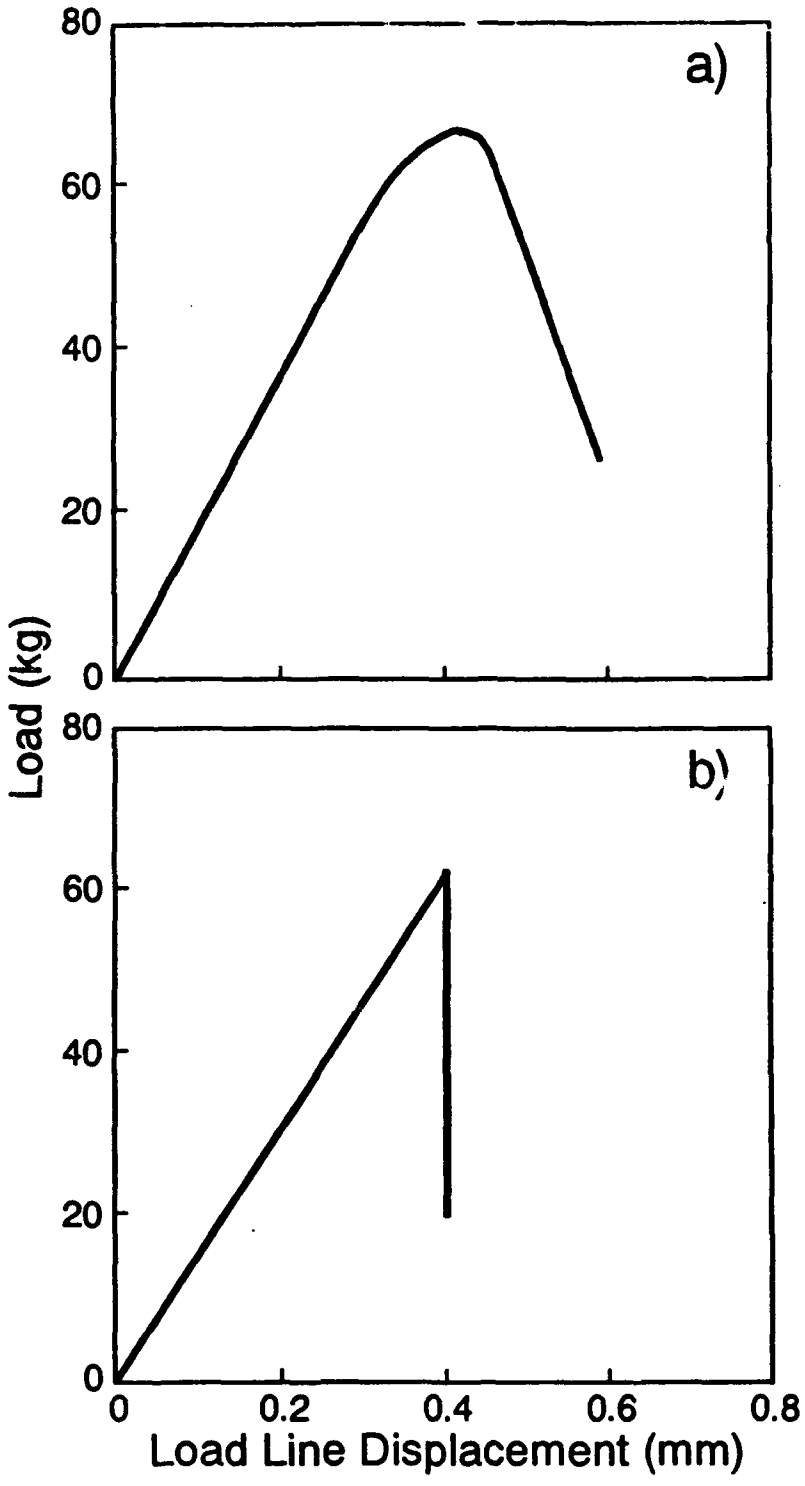
80
60
40
20
0
a)
Load (kg)
80
60
40
20
0
b)
0
0.2
0.4
0.6
0.8
Load Line Displacement (mm)

Figure 3

a)

b)

Figure 4

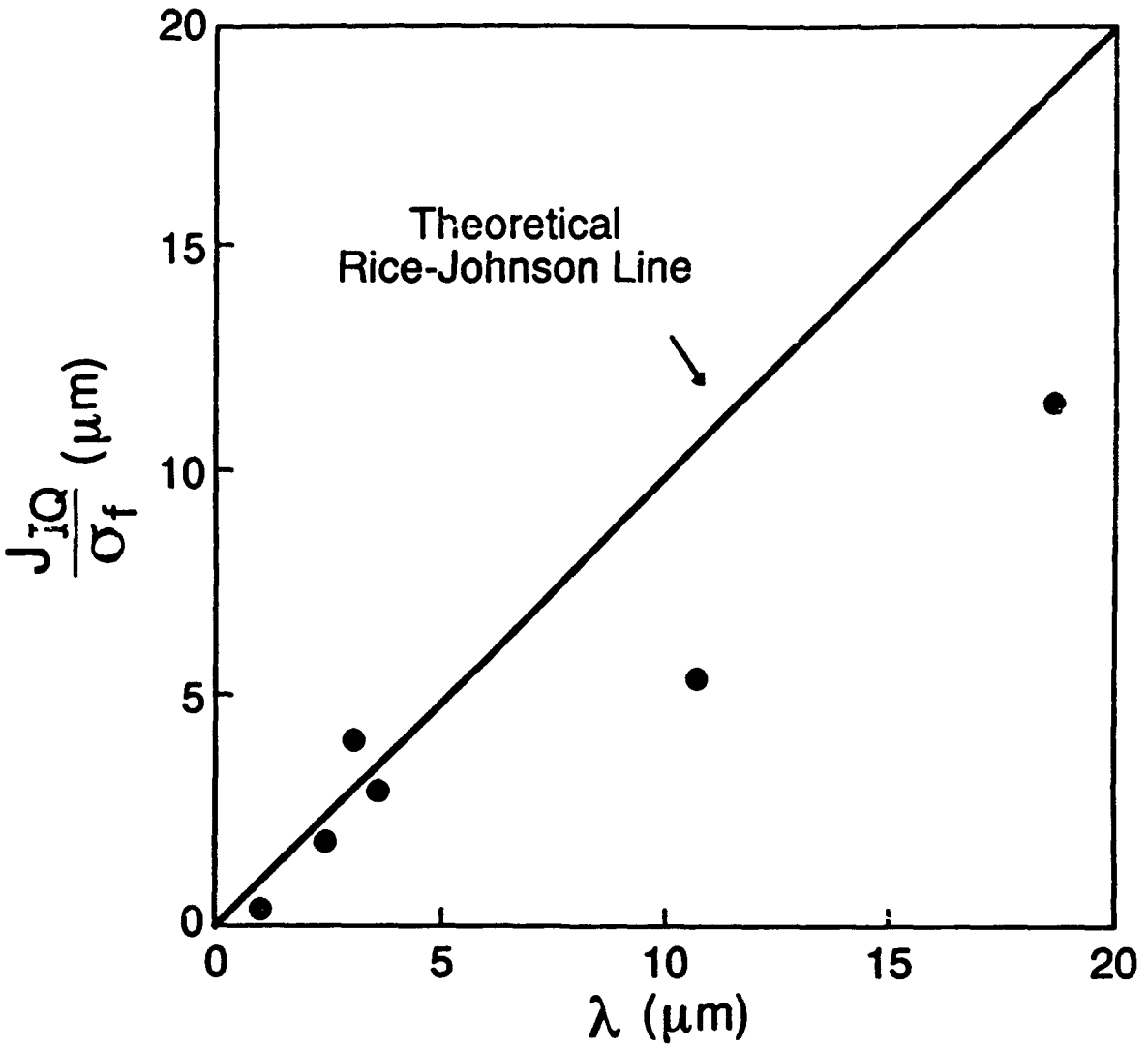
20
15
10
5
0
0
5
10
15
20
Theoretical
Rice-Johnson Line
$\frac{J_{iQ}}{\sigma_f}$ (μm)
λ (μm)

Figure 5